ABSTRACT

Title of Dissertation: STRUCTURE-FUNCTION RELATIONSHIPS OF OXIDIZERS FOR FUEL OXIDATION

Xizheng Wang, Doctor of Philosophy, 2018

Dissertation directed by: Professor Michael R. Zachariah, Department of Chemistry and Biochemistry and Department of Chemical and Biomolecular Engineering

Nanothermite is a class of composite that combines nanoscale fuel and metal oxide to allow for the rapid release of large amounts of energy through redox reaction. The use of nanomaterials has been illustrated to increase reactivity by multiple orders of magnitude as a result of the larger specific surface area and reduced diffusion length scales. However for this seemingly simple oxygen exchange process, there can be large differences in initiation temperatures among different fuel-metal oxide formulations. The large numbers of variables among metal oxides have limited our understanding of what properties of metal oxide control the initiation and reaction kinetics. For my dissertation, I have employed mainly two systematic doped metal oxides as oxidizers that minimize numbers of variables, allowing to probe the transport of solid-state oxygen for fuel oxidation with the goal of understanding the fundamental reaction mechanisms.

Doped perovskite oxides synthesized by aerosol spray pyrolysis with the same crystal structure, morphology and size distribution were used as oxidizers mixed with Al as fuel. Ignition temperatures were measured by temperature-jump/time-of-flight mass spectrometer (T-Jump/TOFMS). Remarkably we found a linear relationship between average bond energy and electronegativity with ignition temperature.

Doped δ-Bi_2O_3 with high oxygen ion conductivity is another systematic oxidizer with even higher oxygen reactivity. The oxygen ion transports of doped δ-Bi_2O_3 were measured by impedance spectroscopy and it was found that oxygen ion transport from oxidizer controls the reaction initiation. Similar trend between average bond energy, oxygen vacancy concentration ($[V_O^{\cdot\cdot}]$) and ignition temperature was found for Al/doped δ-Bi_2O_3. With boron as fuel, the ignition temperature and combustion reactivity (pressurization rate and burn time) can also be correlated with the average bond energy and $[V_O^{\cdot\cdot}]$ of doped δ-Bi_2O_3.

By employing fuels with different melting points for core/passivation layers (Al, B, Ta) and carbon that with no shell and two systematic doped metal oxides (doped perovskite oxides and doped δ-Bi_2O_3), in general, within each systematic metal oxide, I found linear relationships between average bond energy, $[V_O^{\cdot\cdot}]$, electronegativity of the metal oxides with initiation temperature for all four fuels, despite their very different physical/chemical properties. These results indicate that it is generic that intrinsic microscopic properties of metal oxide control the fuel-metal oxide reaction initiation.

In addition, the reaction kinetics between carbon and doped δ-Bi_2O_3 in the application for chemical looping combustion (CLC) was measured by *in-operando*

synchrotron X-ray diffraction. Again, I found lower metal-oxygen bond energy and higher $[V_O^{\cdot\cdot}]$ of doped δ-Bi_2O_3 led to lower onset temperature, faster reaction rate and smaller activation energy for carbon oxidation.

Finally, size-tunable uniform metal iodates were synthesized by electrospray co-precipitation method. Common nano metal iodates including $Mn(IO_3)_2$, $Zn(IO_3)_2$, $Cr(IO_3)_3$, $Bi(IO_3)_2$, $Fe(IO_3)_3$, and $Ni(IO_3)_2$ were synthesized successfully. In addition, by tuning the experimental parameters in electrospray co-precipitation setup, $Bi(IO_3)_3$ nanoparticles of size ranges 10 nm to 200 nm could be successfully prepared.

STRUCTURE-FUNCTION RELATIONSHIPS OF OXIDIZERS FOR FUEL OXIDATION

by

Xizheng Wang

Dissertation submitted to the Faculty of the Graduate School of the
University of Maryland, College Park, in partial fulfillment
of the requirements for the degree of
Doctor of Philosophy
2018

Advisory Committee:
Professor Michael R. Zachariah, Chair
Professor Chunsheng Wang
Professor Eric Wachsman
Professor Dongxia Liu
Professor Liangbing Hu, Dean's Representative

Dedication

To

My Parents

Xueqin Wang and Minghui Tian

And my fiancé

Chao Gao.

Thank you for your unconditional love and support.

Acknowledgements

I am grateful for all the people who helped make this dissertation possible over these past 5 years.

First and foremost, I would like to thank my advisor, Dr. Michael Zachariah for his patience, encouragement and support throughout my PhD study. I truly enjoy working in a research environment that stimulate original think guided by Dr. Zachariah. His advice and example have taught me so much about how to be not only a professional researcher but also a good person.

I would also like to thank all members from the Zachariah group for both contributing the work in this dissertation and making my graduate study at the University of Maryland enjoyable, particularly Dr. Wenbo Zhou, Dr. Garth Egan, Dr. Haiyang Wang, Dr. Lu Liu, Dr. Jeffery Delisio, Dr. Phillip Guerieri, Dr. Rohit Jacob, Dr. Haihan Chen, Tao Wu and Yong Yang for their invaluable efforts, expertise and supports in the collaborative work. Thanks to Rishvi Jayathilake and Dr. Daniel Taylor from Dr. Rodriguez's group for their collaborative for the chemical looping combustion work. Also thanks to Dr. Sz-Chian Liou and Dr. Wen-An Chiou of the UMD Nanocenter's AIMLab.

Finally, I'd like to acknowledge my advisory committee for their time and advice. I'd also like to thank the Army Research Office and the Defense Threat Reduction Agency for financial support of my projects.

Table of Contents

List of Tables

List of Figures

List of Abbreviations

ABE	Average Bond Energy
APS	Advanced Photon Source
CLC	Chemical Looping combustion
DSC	Differential Scanning Calorimetry
EDS/EDX	Energy Dispersive X-ray Spectroscopy
EELS	Electron Energy Loss Spectroscopy
FWHM	Full Width at Half Maximum
M-O bond energy	Metal-Oxygen Bond Energy
MCP	Microchannel Plates
RDX	Cyclotrimethylenetrinitramine
SEM	Scanning Electron Microscopy/Microscope
SOEC	Solid Oxide Electrolysis Cells
SOFC	Solid Oxide Fuel Cells
SXRD	Synchrotron X-Ray Diffraction
TEM	Transmission Electron Microscopy/Microscope
TGA	Thermogravimetric Analysis
T-Jump	Temperature Jump
TNT	2, 4, 6-trinitrotoluene
TOFMS	Time-of-Flight Mass Spectrometer
$[V_O^{\cdot\cdot}]$	Oxygen Vacancy Concentration
XRD	X-ray Diffraction

YSB15	$(Y_{0.15}Bi_{0.85})_2O_3$
YSB30	$(Y_{0.3}Bi_{0.7})_2O_3$
YSB40	$(Y_{0.4}Bi_{0.6})_2O_3$
WSB5	$(W_{0.05}Bi_{0.95})_2O_{3.15}$
WSB10	$(W_{0.1}Bi_{0.9})_2O_{3.3}$
WSB15	$(W_{0.15}Bi_{0.85})_2O_{3.45}$
WSB20	$(W_{0.2}Bi_{0.8})_2O_{3.6}$
ESB15	$(Er_{0.15}Bi_{0.85})_2O_3$
DSB15	$(Dy_{0.15}Bi_{0.85})_2O_3$
DWSB10	$(Dy_{0.1}W_{0.05}Bi_{0.85})_2O_{3.15}$
DWSB5	$(Dy_{0.05}W_{0.1}Bi_{0.85})_2O_{3.3}$
DNSB	$(Dy_{0.05}Nb_{0.10}Bi_{0.85})_2O_{3.2}$

Chapter 1: Introduction

1.1. Energetic materials

Energetic materials are a class of materials that when ignited, a large amount of stored chemical energy will be released through redox reaction with intensive light emission, high pressure rise and shock generation. The heat released will further propagate the unreacted materials and lead to a self-sustained reaction. Energetic materials have been widely used as propellants, explosives, and pyrotechnics and fuel applications due to their generated high temperature flames upon combustion. In general, energetic materials can be divided into two categories: homogeneous energetic materials with fuel and oxidizer within one molecule, such as 2, 4, 6-trinitrotoluene (TNT), cyclotrimethylenetrinitramine (RDX), etc.; and heterogeneous energetic materials with phase separated fuel and oxidizer. The earliest heterogeneous energetic materials are gunpowder (black powder), a composition of sulfur and charcoal as fuel and potassium nitrate as oxdizer.[1] Compared with monomolecular energetic materials in which fuel and oxidizer exist in one molecule linked by chemical bond, the heterogeneous energetic materials suffer from increased mass diffusion length and thus significantly lower energy release rate.[2] However, the energy density of monomolecular energetic materials is limited, due to the limitation on the physical density of the materials and their chemical stability.[3]

The metal-based energetic materials were reported to have high energy density. The enthalpy of combustion of monomolecular energetic materials and common metals in stoichiometric pure gaseous oxygen are compared in Figure 1.1a.[3] Apparently solid metal fuels show both higher gravimetric and volumetric enthalpies

than those of monomolecular compounds. However, although the energy density of the fuel is high, the overall density of the fuel and gaseous oxygen is low because oxygen is a gaseous reactant, requiring high pressures to speed up the reaction kinetics. This is not ideal for many applications.

Substantial studied have been focused on a type of heterogeneous energetic materials called thermite, which is usually a physically mixed reactive fuel (metal for most cases) and solid oxidizer (commonly metal oxides). A typical exothermic thermite reaction is shown as below:

$$A + MO \rightarrow AO + M + \Delta H$$

where A is a reactive metal, MO is metal oxide and ΔH is the enthalpy of the reaction. The reaction is exothermic because the produced metal oxide, AO is more stable than the oxidizer, MO. It was reported that compared with monomolecular energetic explosives, thermite composites have similar gravimetric energy densities and much higher volumetric energy densities and greater stability as shown in Figure 1.1b.[4] For instance, aluminum-based thermite composites have >1.5 times higher volumetric energy density than the best monomolecular energetic materials, i.e., CL-20.

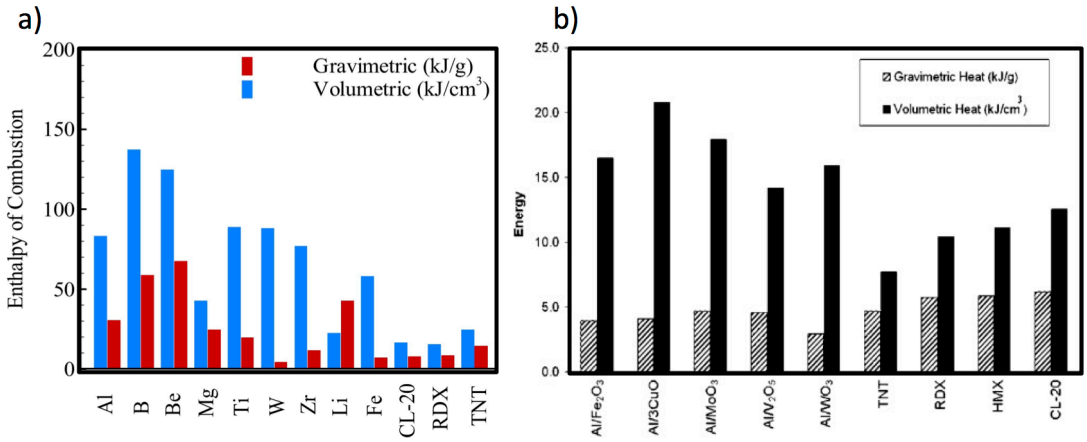

Figure 1.1. Volumetric and gravimetric energy densities of a) some metals and monomolecular energetic materials in pure oxygen at stoichiometric conditions.[3] b) some thermites and conventional monomolecular explosives.[4]

1.2.Nanothermite

Although thermites have the advantages of high energy density, they suffer from slow energy release rate due to the significant mass diffusion length between the reactants. One way to increase the mass transfer rate would be employing reactants in nanoscale, i.e., nanothermite. It is widely known that nanoscale materials offer enhanced reactivity due to the increased surface to volume ratio. A comparison of thermite in micro-size and nano-size is shown in Figure 1.2. The presence of a large number of atoms on the surface and decreased diffusion length enhance the combustion reactivity regarding to the enhanced flame propagation rate and energy release rate.[5-8]. Nano Al based thermites have shown ~1000X increased reaction rates than thermite in micron size and with much less energy needed for reaction initiation.[9-10] Young et al. found ~800X reduced burn time of boron nanoparticles compared with micron sized boron.[11]

Besides the reactivity, the particle size of fuel was reported to affect the ignition temperature. The ignition temperature of Al based thermite is found to be particle size dependent with a trend that ignition temperature decreased with particle size from 1000-2100 °C at 1-100 microns to ~630 °C at 100 nm.[12]

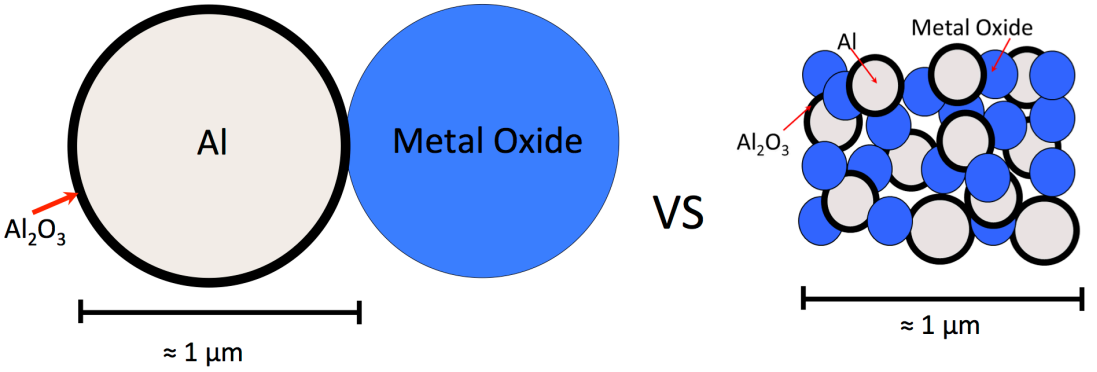

Figure 1.2. A scale illustration of the difference in diffusion distances between micron particles and nanoparticles.

The high energy release rate of nanothermite along with their high energy density have made them of interest in the energetic materials field. Another advantage of nanothermites is their high tunability in terms of the particle size, composite combination, stoichiometry and packing. Since nanothermites release energy in fast explosion process that is within several microseconds, ultrafast heating rate measurements are required. By applying time-resolved high heating rate and in-situ tools, we have studied several important aspects regarding of the ignition mechanism and reaction kinetics of nanothermites. Detailed introductions of these tools are provided in Chapter 2.

1.3. Fuels in Nanothermites

Elemental metal (e.g., Al, Mg, Ti, Fe, W), metalloid (e.g., B, Be) and nonmetals (e.g., C) can be employed as fuels.

By far the most commonly employed fuel is Al due to the high enthalpy of reaction and its ready availability[4, 13]. Aluminum has a naturally occurring thin Al_2O_3 shell (~2-5 nm), which prevents direct contact between aluminum and metal oxide.[14-15] The reaction between aluminum and oxidizer is complicated by the existence of this Al_2O_3 shell. Substantial efforts have been devoted to studying the mechanism and parameters that govern the initiation reaction between nano aluminum and oxidizer. It was generally believed that the prerequisite for ignition is the existence of molten aluminum.[16-17] However, Stamatis et al. reported the ignition temperature of Al/MoO_3 is lower than the melting point of aluminum (633 ˚C) resulting from amorphous alumina to a crystalline polymorph ~500 ˚C.[18] Sullivan et al. proposed Al/WO_3 undergoes a reactive sintering mechanism, whereby initiation of the reaction occurs only when condensed-phase reactants have an interfacial contact.[19]

Boron is theoretically better due to its higher energy density shown in Figure 1.1a.[5] Unlike aluminum, which has a low melting point of ~ 660 °C and a high melting point native oxide shell (~ 2072 °C), boron has a high melting point (~ 2076 °C) while its oxide, B_2O_3, melts at a low temperature (~ 450 °C). In particular upon heating, molten B_2O_3 coats the solid boron core and inhibits the further oxidation of boron, which delays ignition and combustion,[20-21] greatly limiting the performance of boron as a fuel. Studies on modifying the surface of boron particles to oxide-free and air-stable boron particles to improve ignition behavior have been investigated.[22-23] It

is generally accepted that the combustion of micron sized boron particles occurs in two stages,[24-25]: the first stage involves removal of the boron oxide shell, followed by a second stage of burning of the boron core. The transition from the first to the second stage requires the removal of boron oxide shell. Dreizin et al. studied the ignition of boron filaments in air and argon/oxygen mixtures and found that a phase change from α to β rhombohedral boron, triggered first stage ignition.[26] In recent years more efforts have been devoted to the ignition and combustion of nano boron as the reduced length scale offers the potential to significantly reduce the energy release time and enhance the reactivity. Sullivan et al. found that adding nano boron as a minor component in an Al/CuO thermite could enhance the thermite reactivity, but micro boron did not, and attributed this result to the fast melting of nano boron particles.[21] Other studies have primarily focused on macroscopic properties, i.e., particles size, crystallization of boron, etc.[27-28]

While aluminum and boron are nominally the fuels of choice, for the purposes of tweezing out mechanistic information I will also study both carbon and tantalum as fuels. Based on previous work in our group with carbon black as a fuel,[29] the C based thermite system, although not violent, offers a valuable mechanistic perspective, in that the carbon nanoparticle, unlike aluminum, has no oxide shell, thus no barrier for the oxygen species migration that leads to ignition. Additionally, C will remain solid and thus not particularly mobile. Therefore, the ignition of C based thermite is expected to be controlled by the transport of oxygen from the oxidizer. Tantalum is another candidate as a high energy density fuel due to the high negative enthalpy of formation of tantalum oxide.[30] Similar to aluminum, tantalum also has a surface

passivating amorphous oxide shell. However, tantalum has a very high melting temperature (~3000 °C),[31] which lies far above the ignition temperature. DeLisio et al. investigated the oxidation mechanism of tantalum nanoparticles by in-situ high heating rate TEM and found that the Ta_2O_5 shell crystallization led to cracks through which oxygen ion can migrate.[32] Thus I have four different fuels, one (Al) with a low melting point core and a high melting point passivating shell, one (B) with a high melting core and a low melting point shell, one (Ta) with a high melting point core and a high melting point passivating oxide shell and one (C) with a high melting point with no passivating oxide shell. It can be foreseen that varying fuels with different melting points for core/passivation layers (Al, B, Ta) and carbon that does not have passivation oxide can enhance the understanding of nanothermite reaction mechanisms and tuning the function of the energetic materials. In chapter 6, I will examine the thermite ignition with these different fuels.

1.4. Common Oxidizers and Possible Reaction Mechanisms

Very often the oxidizer is an oxygen donor that can be intimately packed together with the fuel. Typically, this is a metal oxide, which can under appropriate condition lead to very rapid redox reactions. CuO, Fe_2O_3, Bi_2O_3, MoO_3 and WO_3 are commonly used as oxidizers in nanothermite as they lead to high adiabatic reaction temperature high heat of reaction or significant gas production.[33] But even for the same fuel, there are large differences on thermite ignition/combustion with diverse ignition temperatures and combustion reactivity when different metal oxides are used. This indicates some parameters of metal oxide govern the ignition/combustion.

Substantial effort has been devoted to studying the mechanism and parameters that govern the initiation reaction between nano fuel and metal oxide. The most direct measure of the onset of runaway violent reaction is the ignition temperature. Ignition temperature is defined as the critical temperature at which the heat supply rate overcomes the heat consumption rate so the reaction can sustain and induce observable phenomena such as a burst of flame or light. More generally, the initiation mechanism of the thermite reaction is being explored by several research groups.[34-37] The basic questions at hand are, what species initiate the reaction, what form are they in, and how is it transported? Answering this question could lead to a better understanding on how best to choose oxidizers. Jian et al. investigated whether gas phase oxygen generation from an oxidizer is an essential prerequisite to ignition under rapid heating rate conditions, and found large differences in ignition temperatures among different nanothermite formulations involving aluminum and metal oxides shown in Figure 1.3.[37] For instance, many formulations (e.g., Al-CuO and Al-Fe_2O_3) have ignition temperatures slightly higher than the decomposition temperatures of the oxidizers, suggesting gas-phase oxygen generation may be necessary for the ignition. However, some formulations (e.g., Al-Bi_2O_3) have ignition temperatures lower than the decomposition temperatures of oxidizers, suggesting a condensed phase reaction mechanism that is not governed by the release of gas-phase oxygen. Thus in general there are two possible reaction mechanisms of nanothermites: gas-condensed heterogeneous reaction and condensed phase interfacial reaction.

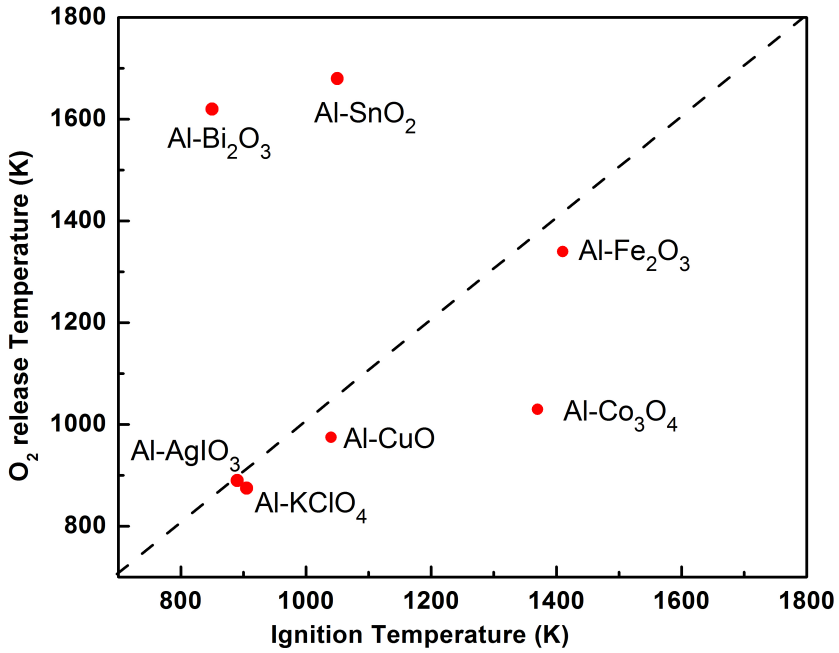

Figure 1.3. Ignition temperature of Al/oxidizer vs O_2 release temperature from bare oxidizer. [37]

For the gas-condensed heterogeneous reaction, the release of O_2 from the decomposition of oxidizer controls the ignition. For this mechanism, the reaction between the oxidizer and fuel would be limited either by the release of O_2 from the oxidizer or the reaction between O_2 with the fuel. Zhou et al. has discussed in detail about the reaction mechanisms of potassium oxysalts with aluminum and carbon.[34] Potassium oxysalts can easily decompose and have low decomposition temperature, lower than the melting point of aluminum. When the O_2 release temperature is lower than the melting point of aluminum, the reaction is dominated by the melting of aluminum shown in Figure 1.4a. While carbon doesn't have oxide shell, when O_2 is released, carbon can readily react with and they found a linear correlation between the O_2 release temperatures from the oxidizers with the ignition temperatures of carbon-based thermite composites. This is the gas-condensed heterogeneous reaction

mechanism shown in Figure 1.4c. However they also found cases that the composite was ignited without the revolution of O_2 and this is the condensed phase interfacial reaction (Figure 1.4b).

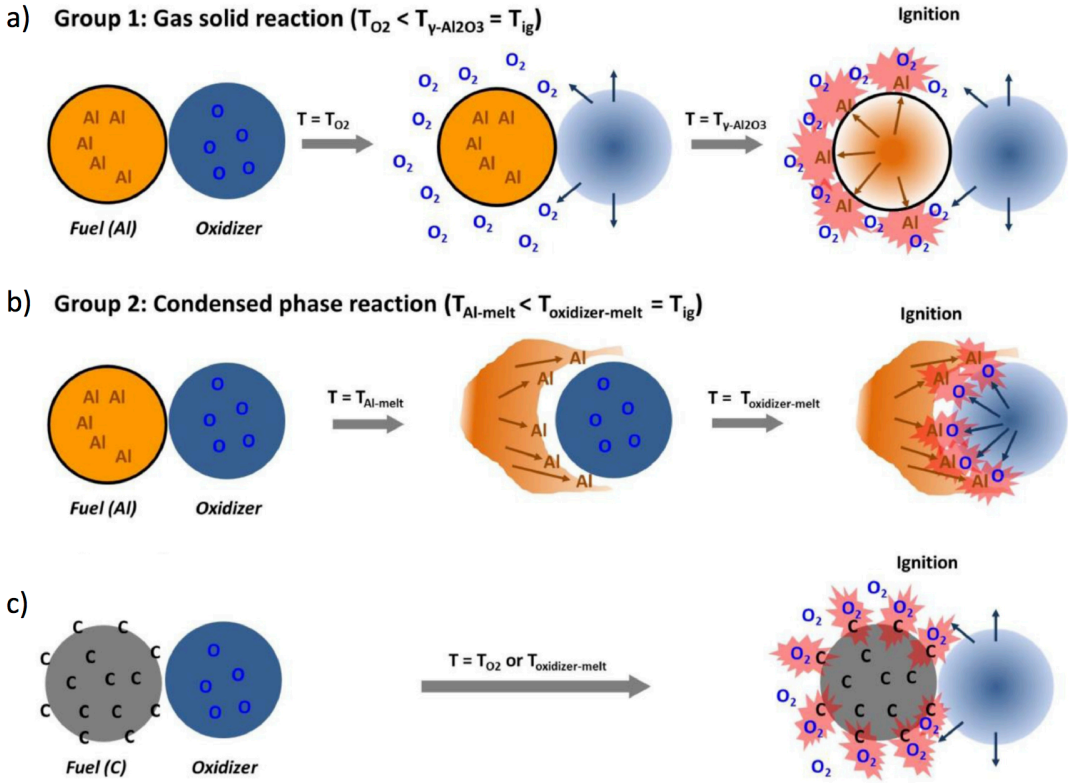

Figure 1.4. Ignition mechanisms for the a-b) Al–oxysalt thermites and c) C–oxysalt thermites. [34] T_{O2} is the O_2 release temperature from oxidizer, $T_{\gamma\text{-}Al2O3}$ is the phase transfer temperature of Al_2O_3, T_{ig} is the ignition temperature, $T_{Al\text{-}melt}$ is the melting temperature of aluminum, and $T_{oxidizer\text{-}melt}$ is the melting temperature of oxysalt..

The condensed phase interfacial mechanism assumes the oxidation occurs between the condensed phase fuel and solid-state oxygen. In this case, the reaction between the oxidizer and fuel would be limited either by solid fuel diffusion through the oxide shell and across the interface between fuel and oxidizer or solid oxygen diffusion across the interface to react with fuel. In whichever cases, the direct contact between solid-state fuel and oxygen is prerequisite. As discussed in Figure 1.3a, the ignition temperature of Al/Bi_2O_3 is lower than the decomposition temperatures of

Bi_2O_3, suggesting a condensed phase initiation mechanism. Piekiel et al. investigated the initial reaction of Al/Bi_2O_3 and C/Bi_2O_3 and found strong evidences that support the condensed phase initiation mechanism.[29] The initiation temperature of Al/Bi_2O_3 is ~630 °C, below the melting point of either Bi_2O_3 (823°C) or aluminum (660°C). However it is not clear why Bi_2O_3 behaves so unique as oxidizer and there are limited studies on the condensed phase thermite initiation. Some basic questions for condensed phase thermite initiation at hand are not answered: what species initiate the reaction, what form are they in, and how is it transported?

It is the properties of the oxidizers on ignition that is very much an open question, as it is well known that reactivity and ignition behavior do not correlate well with overall reaction enthalpy or the metal-oxygen bond energy of the common metal oxides as shown in Figure 1.5a and b, respectively. In summary, when considering the totality of the research into initiation of metal-metal oxide redox reaction to the point of ignition, it is still difficult to say what fundamental properties of the oxidizer determine ignition.

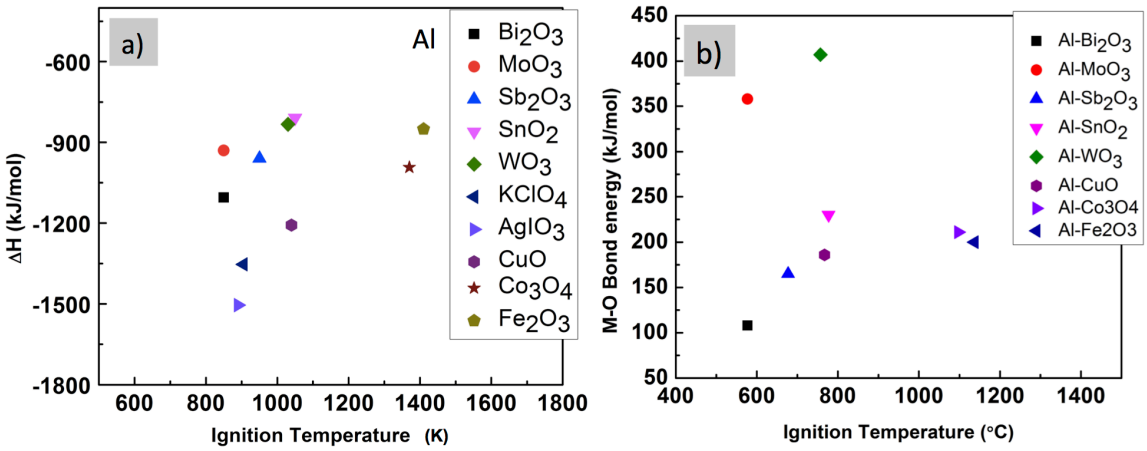

Figure 1.5. Ignition temperature of Al/oxidizer vs. a) enthalpy of reaction and b) metal-oxygen bond energy of oxidizer.

In part the problem is due to the large number of variables comprising an oxidizer that might impact ignition including, bond energy, oxygen mobility, crystal structure, reaction interface area, thermal conductivity, heat capacity and thermal contact, etc. For example, CuO (sigma-Aldrich, <50nm), Fe_2O_3 (sigma-Aldrich, <50nm) and Bi_2O_3 (sigma-Aldrich, <50nm) have completely different crystal structure as shown in Figure 1.6a and it is unknown if the difference in crystal structure would affect their performance. In addition, even for Co_3O_4 (sigma-Aldrich) and Fe_3O_4 (sigma-Aldrich, <50nm) that share the same crystal structure in the same space group (Fd-3m, spinel structure), they have completely different morphologies shown in Figure 1.6b. In order to deal with this complexity a system is needed in which most of the dependent variables can be held constant. Two such classes of material that offers the opportunity for such a study are doped perovskite oxides and doped Bi_2O_3.

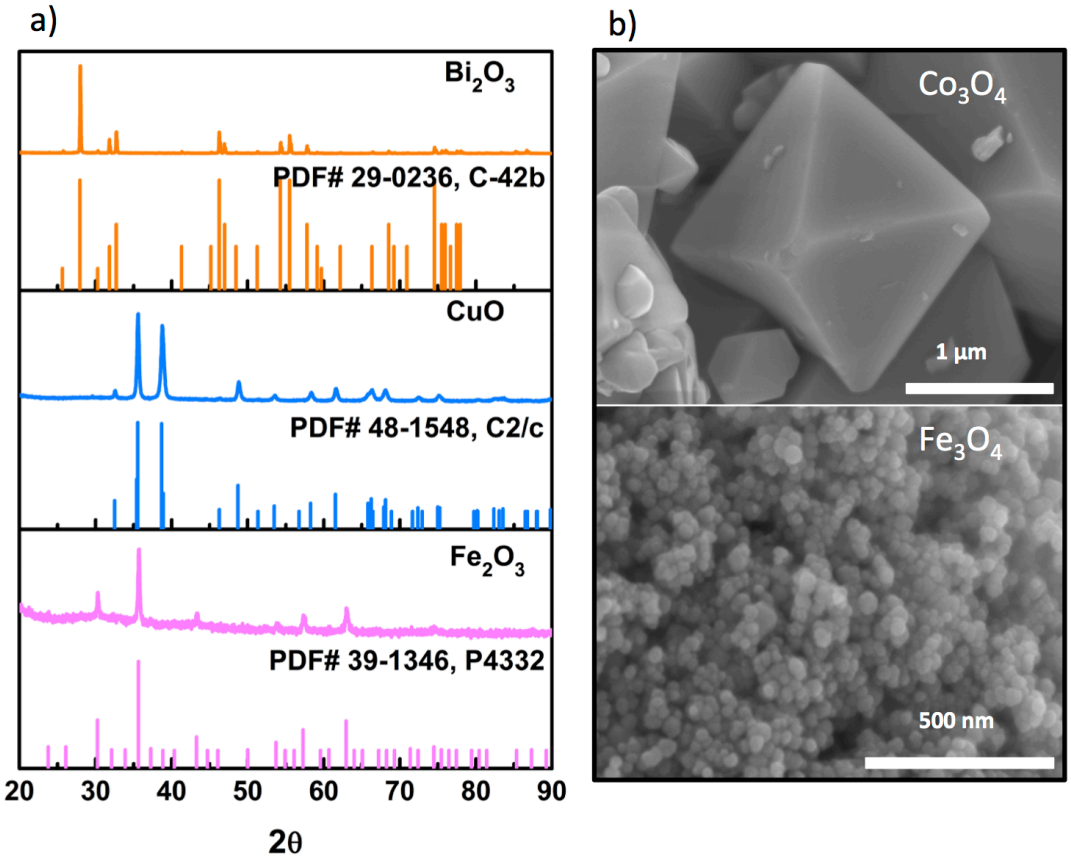

Figure 1.6. a) Crystal structure of common oxidizer: CuO (sigma-Aldrich, <50nm), Fe_2O_3 (sigma-Aldrich, <50nm) and Bi_2O_3 (sigma-Aldrich, <50nm). b) Morphology of Co_3O_4 (sigma-Aldrich) and Fe_3O_4 (sigma-Aldrich, <50nm).

1.5. Systematic Doped Metal Oxides

1.5.1. Doped Perovskite oxides

The perovskite mineral ($CaTiO_3$) was discovered in Russia by Gustav Rose in 1839 and is named after a Russian mineralogist Lev Perovski.[38] Perovskite oxides have a general stoichiometry of ABO_3 where A-site cation can be a lanthanide, alkaline, or alkaline-earth cation while the B-site cation can be metallic elements

from the 3d, 4d or 5d configuration and O being an oxygen anion.[39] Perovskite oxides are mixed oxygen ion and electronic conductors that have wide applications in solid oxide fuel cells (SOFCs),[40] heterogeneous catalysis of hydrocarbon[41] and membranes for oxygen separation[42] due to their high oxygen reactivity. One of the main advantages of the perovskite structure is the possibility of adopting a large number of different A- and B-site cations or through partial substitution a wide range of combinations to adjust the redox properties. Thus perovskite is an ideal candidate for systemic study of oxidizer's properties for ignition. The ideal perovskite oxide is in cubic structure and the space group is Pm3m shown in Figure 1.7.[39]

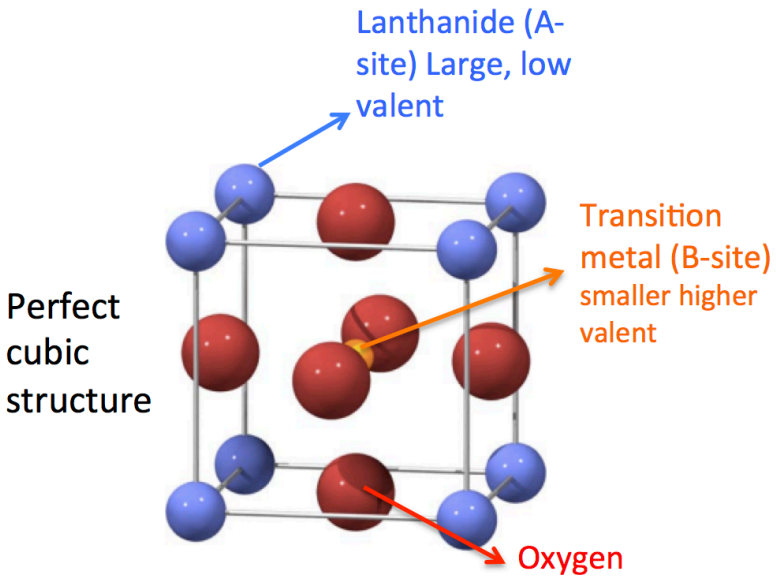

Figure 1.7. Cubic perovskite unit cell.[39]

In cubic perovskite structure, A-cation is 12-fold coordinated with oxygen ions and B-cation is 6-fold coordinated with oxygen ions. Goldschmidt proposed a "tolerance factor" shown as below to evaluate the crystal structure of perovskite:

$$t = \frac{r_A + r_O}{\sqrt{2}(r_{B+}r_O)}$$

where r_A , r_B and r_O are ionic radius of A-site cation, B-site cation and O^{2-} respectively.[43] Cubic structure can only be preserved when 0.9 < t <1. The cubic structure will distort to hexagonal symmetry structure when t > 1, to orthorhombic if 0.75 < t < 0.9 and hexagonal ilmenite structure when t < 0.75.[39]

As mixed electronic-ionic conductors, perovskites have considerable oxygen ion conductivity. In addition, the partial or total substitution of A-site cation by other metal cations with lower valences will lead to elevated number of oxide vacancies.[44] Teraoka et al. reported that A-site substitution of $LaCoFeO_3$, $La_{1-x}A_xCo_{0.4}Fe_{0.6}O_{3-\delta}$ membrane (A= Sr, Ba, Ca) become highly defective at high temperature and reduced oxygen partial pressure and the rate of oxygen permeation increased with the increased substitution, correlating with the oxygen sorptive properties of perovskite oxides resulted from elevated oxygen vacancy concentration.[45] In the study of Teraoka et al, Ba^{2+} substitution perovskite membrane shows a higher rate of oxygen permeation than Sr^{2+} substitution. However, Stevenson et al. obtained a different order that Sr^{2+} substitution showed a higher oxygen permeation flux than Ba^{2+} substitution.[46] The difference could probably result from the difficulties in measuring the oxygen permeation accurately, especially at high temperature. In Chapter 3, I will explore the oxygen ion transport related properties of doped perovskite for nanothermite ignition.

1.5.2. Doped Bi_2O_3

Studies on all of the aforementioned fuels with Bi_2O_3 allude to the importance of oxygen transport since Bi_2O_3 has the highest known oxygen ion conductivity, which one might reasonably expect to be an important parameter, although it has not

heretofore been explored in the thermite reaction. The oxygen ion conductivity is directly related to the temperature dependent internal structure of Bi_2O_3. Pure δ-Bi_2O_3 possesses the highest known oxygen ion conductivity that results from the large number of highly mobile oxygen vacancies, weak Bi-O bond and high polarizability of Bi^{3+} with its lone $6s^2$ electrons. δ-Bi_2O_3 adopts the cubic fluorite structure as shown in Figure 1.8 with ~25% of the oxygen sites vacant.[47]

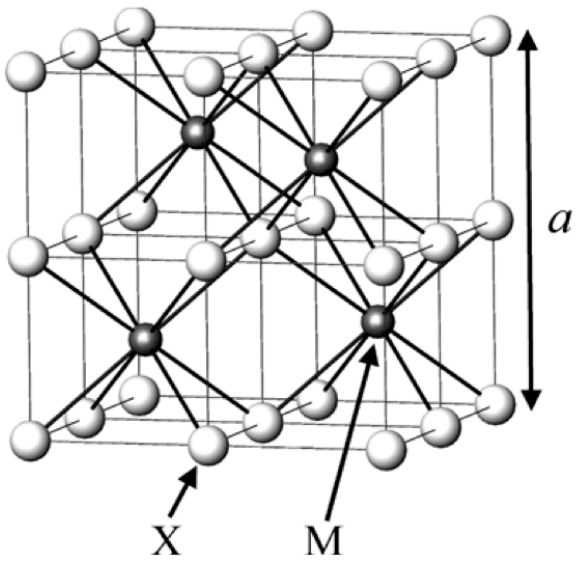

Figure 1.8. Cubic fluorite structure.[47]

The $6s^2$ lone-pair electrons of Bi^{3+} reduce the energy barriers for oxygen ion to diffuse through the lattice in lower symmetry local environments. However, δ-Bi_2O_3 is only thermodynamically stable above 730 °C, up to its melting point at 824 °C.[48] Below 730 °C tetragonal β-Bi_2O_3 (at 650 °C) or the bcc γ-Bi_2O_3 (at 639 °C) is stable, and below about 500 °C the monoclinic α-Bi_2O_3 phase is most stable with reduced oxygen ion conductivity shown in Figure 1.9.[49]

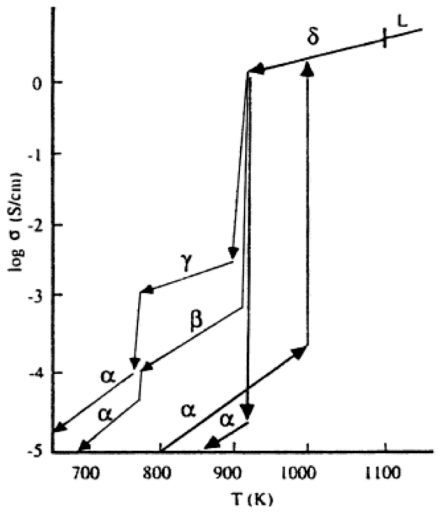

Figure 1.9. Electrical conductivity of Bi_2O_3 as a function of temperature.[49]

But δ-Bi_2O_3 can be stabilized down to room temperature by doping with other oxides.[50] However, due to the mismatch in ionic radii between the host and dopant cations and a related phenomenon, anion ordering, phase stabilization lowers the oxygen ion conductivity.[51] Several studies report that due to the large dopant radii and high polarizability of dysprosium, erbium and yttrium, they are less likely to cause extensive oxygen ion displacement or vacancy ordering, which lead to conductivity decay and thus single dopants of these metal oxides are able to stabilize the fluorite structure of δ-Bi_2O_3.[52-54] Jung et al. found that with two dopants, dysprosium and tungsten stabilized bismuth oxide achieved higher conductivity, again based on their ionic radii and dielectric polarizability.[51] Much research also found small amount of niobium oxide doped bismuth oxides yield a fluorite-type crystal structure based on superlattice ordering of the cubic subcell of δ-Bi_2O_3.[55] In Chapter 4 and 5, I will explore the oxygen ion transport properties of doped Bi_2O_3 for nanothermite ignition/combustion.

1.6. Metal Iodates

Besides conventional common metal oxides based thermites, silver- or halogen-containing thermites gained significant attention due to their potential application for spores neutralization. The bacterial spores' high resistance to heat forms a barrier against the traditional energetic materials and prevents complete neutralization. Traditional energetic materials are also limited by the ability to precisely manipulate the temperature and exposure time. Adding biocidal agents such as iodine into the formulation provided a good way to improve the neutralization efficiency.[58] The metal iodate is employed as an iodine-containing oxidizer. Metal iodates have received a lot of attention recently because of their potential application in dealing with biological weapons from the release of iodine during the thermite reaction shown in the following equation.[56-57]

$$nAl + M(IO_3)_n \rightarrow \frac{n}{2}Al_2O_3 + M + \frac{n}{2}I_2 + \Delta H$$

It was also found that metal iodates are considered as good candidates for spores neutralization due to their low hygroscopicity and light sensitivity. The release of the iodine could also enhance the neutralization of the heat resistant bacterial spores and the function of metal iodate is particle size depandant.[59-60]

Several methods have been used to synthesize the metal iodates. Xu et al. and Huang's group have used the hydrothermal method to synthesize the silver manganese mixed metal iodates $AgMn(IO_3)_3$ and $AgMn(IO_3)_4$ along with monovalent metal gold iodates and their thermal stabilities were studied.[61-62] Wang et al. and Hu et al. have used the wet chemistry co-precipitation method to synthesize the $Bi(IO_3)_3$ particles and found uniformed particles were formed with particle size around 90

nm.[63-64] However, it is still difficult to obtain uniformly distributed nano metal iodates due to the high surface energy.

For this work we employed electrospray, for liquid atomization of the precursor to make size controlled particles. I demonstrate a new approach for the liquid phase co-precipitation reaction. Synthesis of size tunable nano metal iodates by electrospray co-precipitation will be presented in Chapter 8.

1.7. Chemical Looping Combustion

Another oxygen exchange process different from thermite reaction is chemical looping combustion. Chemical looping combustion (CLC) is an approach developed to employ metal oxides as oxygen carriers for fossil fuel oxidation and to subsequently regenerate them by oxidation in air.[65-66] Since there is no net change in the oxygen carrier, thermodynamically this is equivalent to burning the fuel in air. The schematic plot for oxygenation and reduction processes in CLC is shown in Figure 1.10. The direct oxygenation of the fuel by metal oxide raises a central scientific question in choosing from an effective infinite variety of metal oxide combinations is how to choose, and more specifically, what makes for a good oxygen carrier from a microscopy point of view. Some important characters of a good oxygen carrier include its reactivity and stability in both reduction and oxidation cycles, and its ability to completely combust fuels. The latter character is important for the application to achieve maximum fuel combustion efficiency. Different from rapid fuel oxidation in nanothermite occurs in milliseconds, the cycle of chemical looping combustion is usually on the order of minutes with crystal structural revolution in metal oxides. In order to study the detailed in-situ crystal structure revolution during

chemical looping combustion and investigate what microscopic properties of metal oxide affect the reaction initiation and kinetics, an in-operando diffraction technique is needed to collect complete patterns while the combustion is cycling and such a powerful diffraction technique is synchrotron X-ray diffraction. Detailed introduction of this technique is provided in Chapter 2. To minimize variables in metal oxides, doped Bi_2O_3 are employed as oxidizers and the application of doped Bi_2O_3 as oxidizers for CLC will be discussed in Chapter 7.

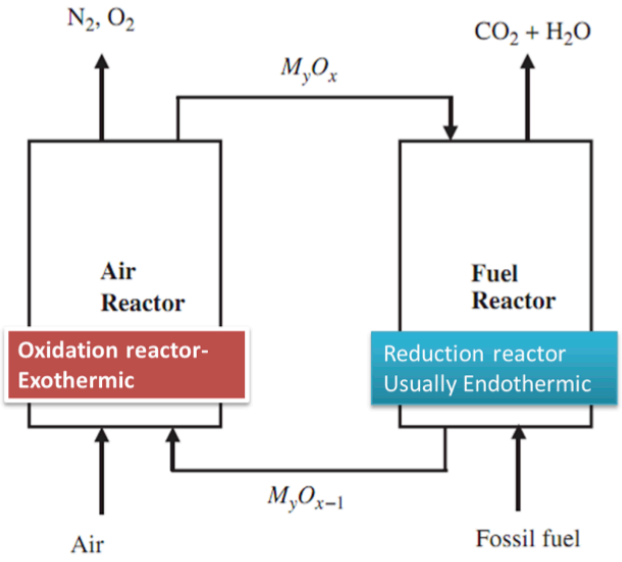

Figure 1.10. Schematic plot of CLC.

1.8. Scope of the Dissertation

As discussed in previous sections, nanoscale solid fuel packed with nanoscale metal oxide allow for the rapid release of large amounts of energy through a redox reaction. The objective of this dissertation is to study the microscopic structure-function relationships of metal oxides for solid fuel oxidation and in chemical looping

combustion. This is enabled by employing systematic doped metal oxides as oxidizers.

The work done in this dissertation will be discussed in nine Chapters. Chapter 1 gives an overview of the relevant literature on nanothermite and unsolved problems. Chapter 2 provides detailed introduction of the ultra-fast heating rate diagnostic tools for nanothermite research. The tools and technique introduced in Chapter 2 are primarily used in this dissertation (Chapter 3 to Chapter 8) to understand the fast reaction of nanothermite regarding the initiation temperature and combustion reactivity. Chapter 3 to Chapter 8 are concerned with the study on the relationship between the microscopic properties of oxidizers and the ignition temperature, combustion reactivity and reaction kinetics. Chapter 3 presents the study on doped perovskite as oxidizer whose crystal structure and morphology can be held constant but oxygen ion transport related parameters are varied by doping. In Chapter 4-5, doped Bi_2O_3 with higher oxygen ion activity compared to perovskites are used as oxidizers mixed with different solid fuels. Chapter 6 summarizes these two systematic doped metal oxides with four different fuels to study the more generic relationship. Chapter 7 presents the application of doped Bi_2O_3 in chemical looping combustion. Chapter 8 introduces new method to synthesize size tunable nano metal iodates. A summary of the works done in this dissertation and recommendations for future work are presented in Chapter 9.

Chapter 2: Experimental Methods

Overview

In order to study what microscopic properties of oxidizer dominate the reaction for solid fuel oxidation, the experimental parameters have to be controlled, e.g., heating rate, experimental configuration, particle size and packing. Studies show that thermite ignition depends on heating rate.[1-2] As discussed in Chapter 1, in particular, ignition is a very different process than steady reaction when the self-heating rate overcomes the inherent heat loss process. To better study thermite ignition, which by its nature is an extremely fast self-heating process, it is necessary to employ heating rates that more closely resemble self-heating rates (>10^5 °C/s). This chapter provides a brief overview of the rapid heating techniques and in situ measurement tools to study the ignition and reaction mechanism of nanothermite, including temperature-jump/time-of-flight mass spectrometer and in-situ high heating rate transmission electron microscope. To explore the condensed phase oxygen ion transport in oxidizer, impedance spectroscopy is employed and descried in this chapter. *In-operando* synchrotron X-ray diffraction and on-line mass spectrometry enable us to monitor both the phase evolution in the solid as well as the production of gaseous products for chemical looping combustion. Other diagnostic tools relevant to nanothemrite research, such as combustion cell are included.

2.1. Temperature-Jump Rapid Heating Diagnostic for Nanothermite Research

2.1.1 Temperature-Jump Techniques

A thermite reaction becomes self-sustaining when the self-heating rate overcomes the inherent heat loss process and thus cannot be evaluated at low heating rates. Our temperature-jump (T-jump) technique can achieve high heating rates up to ~5×10^5 °C/s. This high heating rate is enabled by applying a tunable DC electrical pulse (~2-20 ms) on a thin platinum filament (76 um diameter) t shown in Figure 2.1. The typical length for the platinum wire is about ~10 mm. The temperature of the wire is determined from electric resistance based on the Callendar-Van Dusen equation, through a simultaneously measure of temporal applied voltage and current, which can achieve up to ~1250 °C.[3] Due to the size of nanoparticles compared with the wire and based on our previous results, the temperature of the wire is essentially equal to the temperature of the reactive system.[4] Sample can be deposited on the platinum wire by directly dropper thermite suspension in hexane with a micropipette.

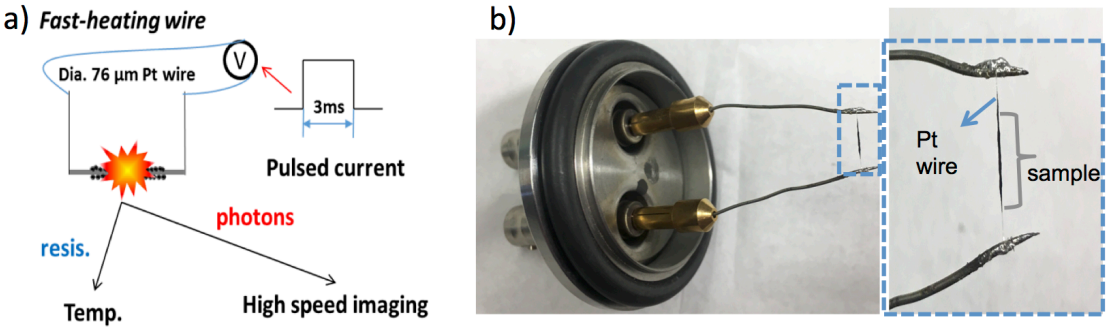

Figure 2.1. a) Schematic design and b) photo of T-jump wire.

2.1.2 Optical Emission and Ignition Studies

In order to analyze nanothermite ignition and combustion that occurs in the magnitudes in microsecond, a high speed camera is used to capture the details of the combustion event. Optical emission is measured using Phantom v12.1 digital camera, which can be set to trigger at the same time as the T-jump heating pulse using a pulse generator (Stanford Research DG 535) so we can directly correlate the optical signal with the temperature profile from the T-jump. Usually the high speed camera is set to a resolution of 256×256 with a framerate of 67066 fps. A homebuilt pressurizable chamber is employed to study the nanothermite ignition/combustion mechanism. The chamber can be pumped down to ~ 1mTorr and desirable gas (e.g., Ar, O_2) can be pumped in. Schematic plot of the pressurizable chamber and a photo of the whole system are shown in Figure 2.2.

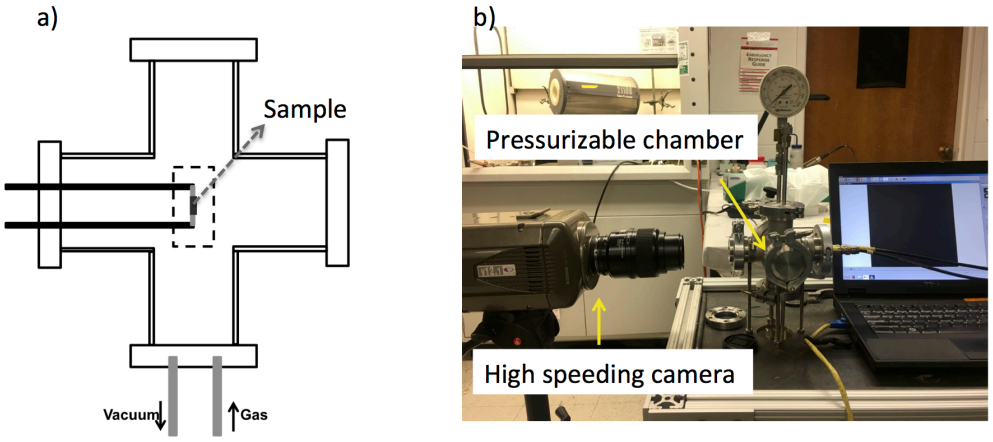

Figure 2.2. a) Schematic plot of the pressurizable chamber b) image of the pressurizable chamber with high speed camera.

An example of snapshots of nano Al/CuO thermite reaction is shown in Figure 2.3a. The most valuable results we can obtain from high speed video is the ignition temperature. Ignition occurs when the self-heating rate overcomes the inherent heat

loss process and is defined when the first flash occurs, shown in the first frame of Figure 2.3a. As was discussed, the camera was triggered at the same time as the T-jump heating pulse, thus we can measure the ignition temperature from the temperature profile shown in Figure 2.3b.

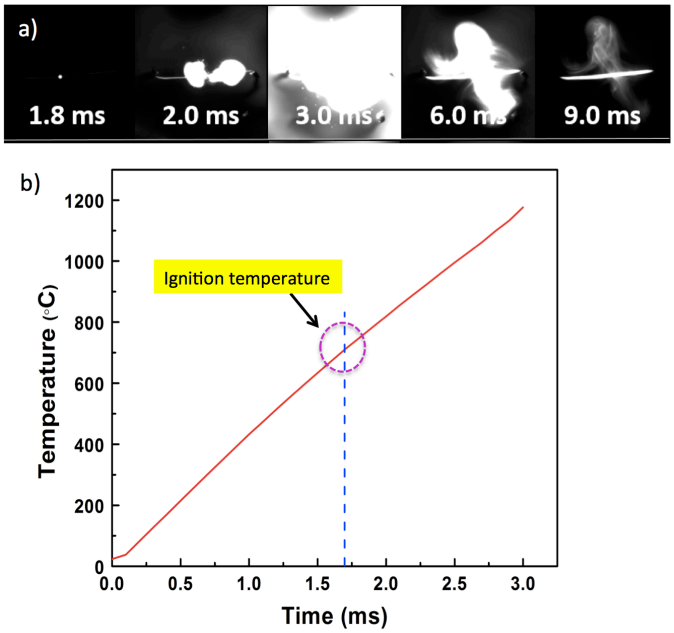

Figure 2.3. a) Selected image for nano Al/CuO thermite reaction recorded by a high speed camera b) temperature profile obtained from T-jump and the identification of ignition temperature.

2.1.3 T-Jump/Time-of-Flight Mass Spectrometer

In addition to the optical emission, thermite combustion usually releases many gaseous species and analyzing these combustion products helps in investigations of the ignition/combustion mechanism. An understanding of decomposition of bare oxidizer, especially the oxygen release temperature from bare oxidizer is important to investigate the thermite reaction mechanism. A home built T-jump/time-of-flight mass spectrometer (T-jump/TOFMS) is used to measure gases evolved in a collision-less environment as schematically shown in pictured in Figure 2.4.

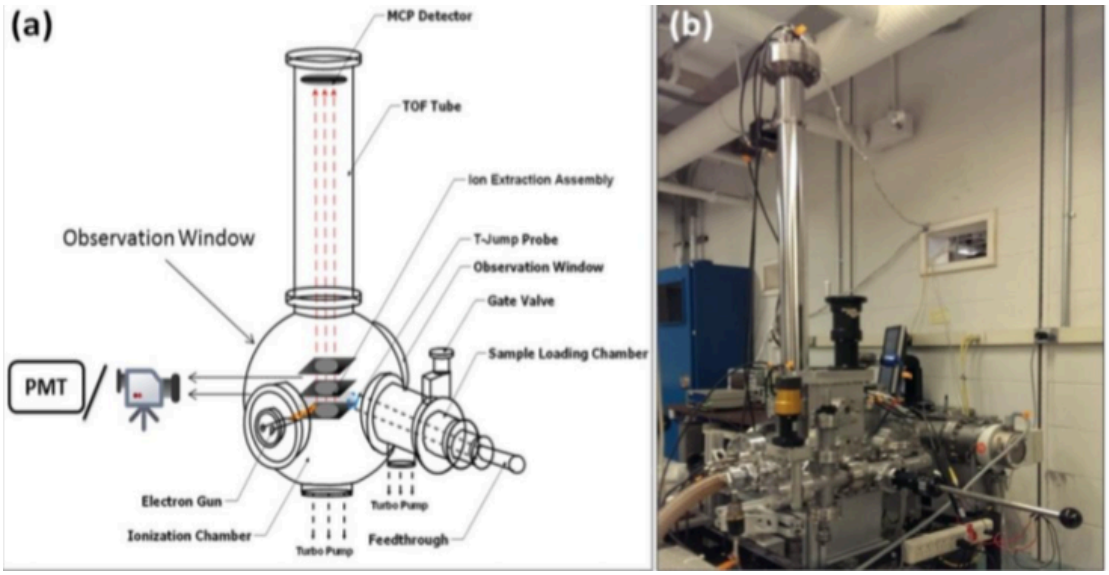

Figure 2.4. a) Schematic and b) image of the T-jump TOFMS.

The TOFMS works by ionizing the gaseous species released from thermite sample coated on the platinum filament s described in 2.1.1. The reaction and ionization occurs under high vacuum (~10^{-7} Torr). After the sample is coated on the T-jump probe at ambient pressure, it is loaded into a sample loading chamber. The loading chamber is separated from the ionization chamber by a gate valve without breaking high vacuum inside the ionization chamber. The electron gun is set for 70 eV and 1 mA. The ionization/extraction region of the TOFMS was pulsed at 10 kHz resulting in a full mass spectrum every 100 μs. A combination of three plates is used to create the electrical field for the ions to accelerate into the TOF tube. Ions are detected and analyzed by a microchannel plate detector (MCP). A 600 MHz digital oscilloscope was used for data acquisition with a sampling rate of 100 mega sample per second. The principle for measuring the time-of-flight to obtain the mass spectrometry is based on the correlation between the ion's time of flight to its mass-to-charge ratio by the following equation:

$$m/z=Kt^2$$

where m/z is the mass-to-charge ratio, K is a proportionality constant related to the instrument settings and t is the measured time-of-flight of the ions. MATLAB scripts allowed for simultaneous data processing on the oscilloscope. An example of the data produced by this instrument is shown in Figure 2.5. Besides, there is an observation window in the ionization chamber and thus the optical signal from the combustion can also be captured by a high speed camera.

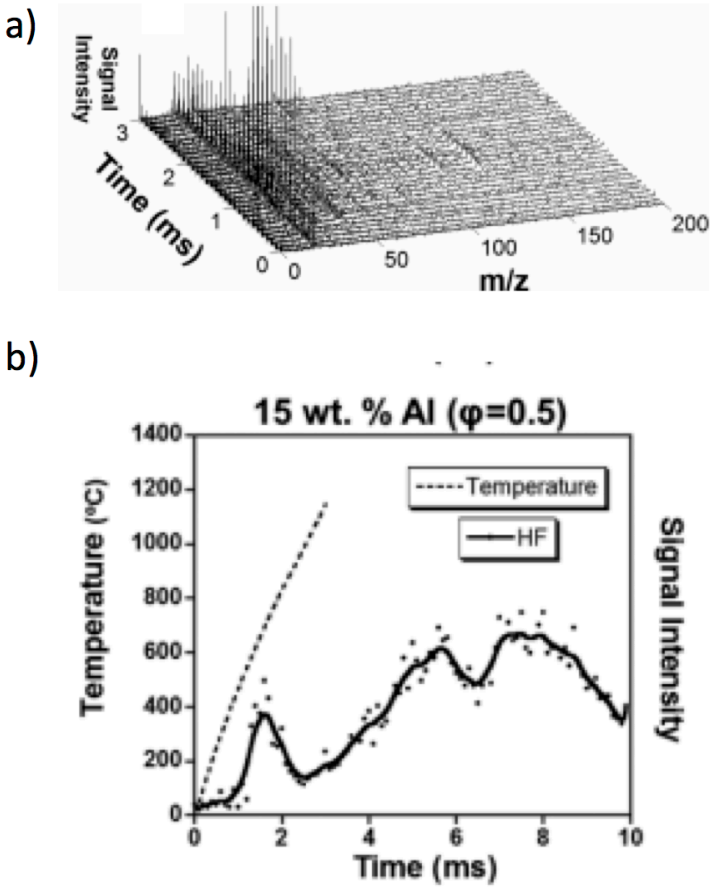

Figure 2.5. a) 3D plot of time-resolved spectra obtained from T-jump TOFMS of Al/PVDF films. b) Temporal wire temperature and HF signal intensity for fuel lean 15% Al containg PVDF films.[5]

The activation energy of ignition or decomposition can also be measured using Flynn–Wall–Ozawa isoconversion method [6-7] from the following equation:

$$\ln \beta = const. - \frac{1.052 E_a}{RT}$$

where β is the heating rate, T is the ignition temperature or decomposition and E_a is the activation energy for ignition or decomposition.

2.1.4 Electrically Heated Microscopy Sample Holder

To evaluate the morphological changes and interface properties of nanoparticles under high heating rate condition we employ a dynamic high heating approach with a Transmission Electron Microscopy (TEM). Protochips Inc. has developed special TEM holders and chips that sample on the chip can be heated from room temperature to a maximum of 1200 °C, with tunable heating rate as high as 10^6 °C/s within or outside the TEM chamber. The Aduro style thermal E-chip and the Protochips TEM sample holder are shown in Figure 2.6. The E-chip contains integrated heating elements that can be joule heated by a DC power supply. More detailed information about this technique can be found on the Protochips Inc.'s website.

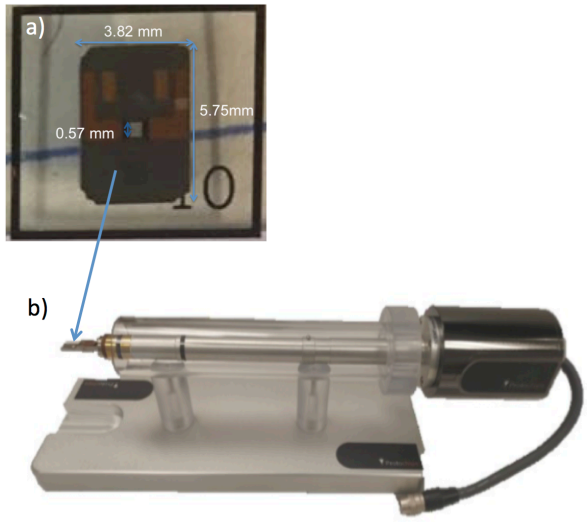

Figure 2.6. a) Protochips Aduro E-chip, b) TEM heating holder

Sullivan et al. used this technique to study the morphology change of nano-Al based thermite at high heating rates and results support the diffusive mechanism that above the melting point of Al, Al diffuses outside of the Al_2O_3 shell.[8] In Chapter 5, this technique will be used to study the reaction mechanism of boron ignition. Silicon nitride based chips were used as they can achieve higher temperature.

2.2. Constant Volume Combustion Cell

To gauge the bulk thermite combustion, a home-built constant volume pressure cell is used to measure the pressure and optical signal.[9-10] Figure 2.7a shows a schematic illustration of the home-built pressure cell. Briefly, a fixed mass of dry and loose thermite particles (25 mg) are placed on a small chip loaded into a fixed volume pressure cell (13 cm^3). A charged nichrome coil is used to ignite thermite by joule heating. Pressure is recorded by an attached piezoelectric pressure sensor, an in-line charge amplifier and signal conditioner. The optical signal is recorded simultaneously by a fiber optical sensor, containing a planoconvex lens (f=50 mm)

and a high-speed photo detector. Peak pressure, pressurization rate and burn time are three important parameters that can be obtained by pressure cell to evaluate the reactivity of thermite composites. Pressurization rate can be calculated based on the pressure profile as the peak pressure divided by the pressure rise time and burn time is defined as the full width of the half maximum (FWHM) of the optical profile shown in Figure 2.7b. By using the pressure cell, product collection is viable since bulk material is loaded compared to the very small amount of sample used in TOFMS.

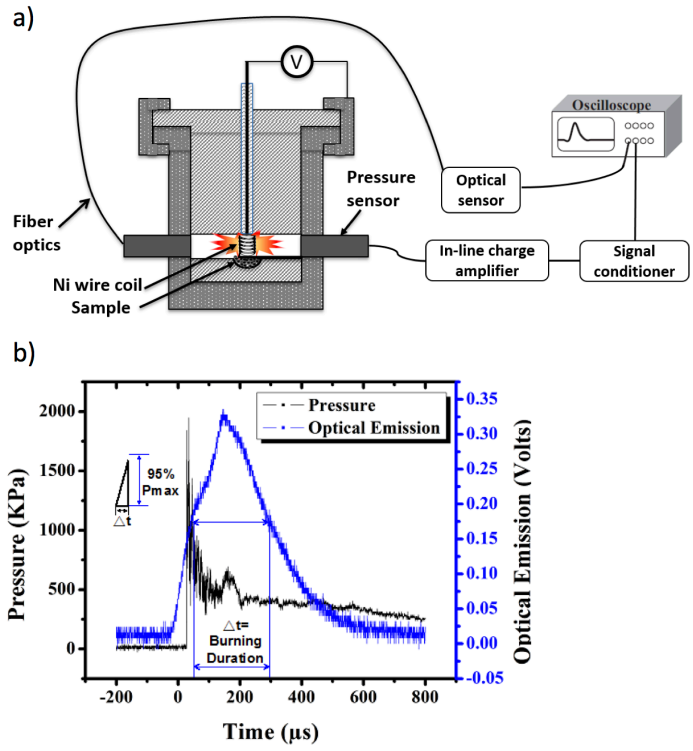

Figure 2.7. a) A schematic of the constant volume pressure cell setup, b) Calculation of pressurization rate and burn time.

A combined assembly of pressure cell and homebuilt pressurizable chamber can help to collect combustion sample in a variety of environments. A schematic illustration is shown in Figure 2.8. The pressure cell is connected with the pressuriable chamber by

a Teflon tube. The chamber and cell can be pumped down to ~ 1mTorr and desirable gas (e.g., Ar, O_2) can be pumped in. The charged nichrome coil is used to ignite thermite by joule heating.

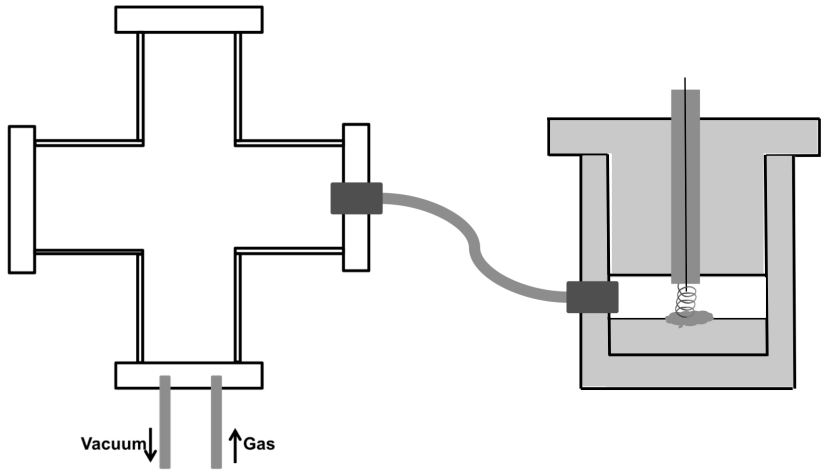

Figure 2.8. Schematic plot of the combined assembly of pressure cell and homebuilt pressurizable chamber.

2.3. Impedance Spectroscopy

As was mentioned in the introduction, the oxygen ion transport might play an important role for condensed phase thermite ignition, although it has not heretofore been explored in the thermite reaction. This suggests that further studies of oxygen ion diffusivity in metal oxides are warranted. Ion-diffusion coefficients can be measured through a determination of mobility or more directly through an electrical measurement of ion conductivity.[11]

Impedance spectroscopy can characterize different regions of ceramic materials over a wide range of frequencies by their electrical relaxation times or time constants. Oxygen ion conductivity is measured from the AC impedance analysis using a Solartron 1260 A, with a symmetric cell by two electrode electrochemical impedance spectroscopy over the frequency range of 1 Hz to 10^6 Hz with perturbation

amplitude of 100 mV. The Solartron 1260 A is interfaced to a computer using the Zplot software for the data analysis. A nulling technique is used to remove any artifacts caused by inductive response of the test leads and the equipment to measure the small impedance at high temperature. The measurements are performed between 200 and 700 °C or 200 and 750 °C in air atmosphere with an interval of 50 °C. Typical impedance spectra for doped Bi_2O_3 at 200 °C and 500 °C over the frequency range of 1 Hz to 10^6 Hz with perturbation amplitude of 100 mV is shown in Figure 2.9.[15] Each arch or semicircle can be associated with particular transport mechanisms (bulk, grain boundary etc.). Impedance measured can be divided into two components: resistance and capacitance. Once resistance and capacitance are measured, the assignment of a controlling mechanism for conductivity can be obtained based on the magnitudes of the measured capacitance as outlined in Table 1. of reference 12.[12] The conductivities can be converted from the bulk resistance and the dimensions of the sample based on $\sigma = {}^{L}/_{RA}$, where σ is the oxygen ion conductivity, R is the bulk resistance, L and A is the thickness and sectional area of the pellets.

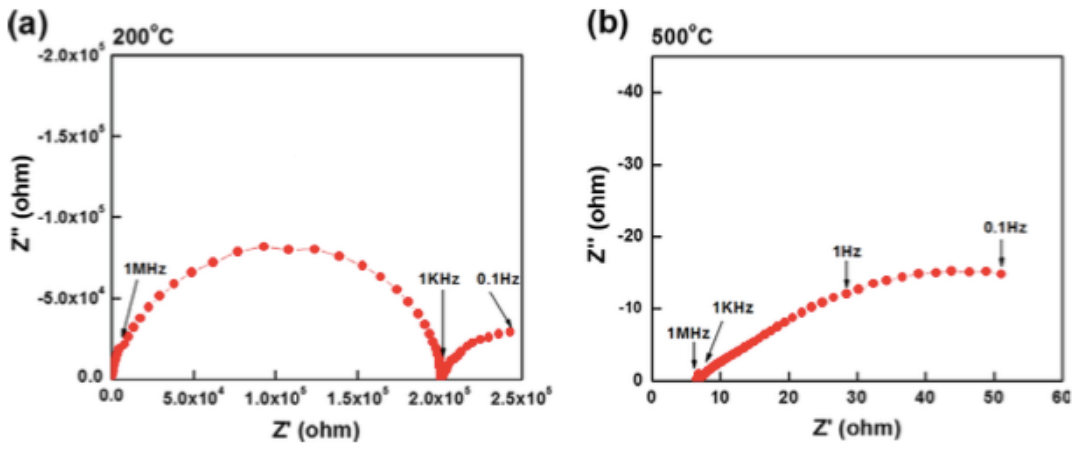

Figure 2.9. Typical impedance spectra of doped Bi_2O_3 in air at: a) 200 °C and b) 500 °C.

2.4. In-Operando Synchrotron X-Ray Diffraction

The cycle of chemical looping combustion is usually on the order of minutes with crystal structural revolution in metal oxides. Traditional diffraction technique completes one pattern on the magnitude of tens of minutes. In order to study the detailed crystal structure revolution during chemical looping combustion and investigate the reaction mechanism, a faster diffraction technique is needed to collect complete patterns while the combustion is cycling and such a powerful diffraction technique is synchrotron X-ray diffraction.

In-operando synchrotron X-ray diffraction (SXRD) experiments were performed in transmission mode on the 17-BM beamline at the Advanced Photon Source (APS) at Argonne National Laboratory. 17BM is dedicated to rapid acquisition of powder diffraction patterns with versatile set-up that can accommodate a wide range of sample environments. A flow-cell/furnace sample holder is used to control sample temperature and atmosphere.[13] Samples can be diluted in fused quartz powder to minimize beam absorption. A schematic plot of the fully assembled flow-cell/furnace, an expanded view of the sample region and a photograph of the flow-cell/furnace are shown in Figure 2.10. Sample is loaded in the center of a 1 mm diameter capillary with a thermocouple placed inside. Two furnace pieces as resistive heaters are placed above and below the capillary respectively.

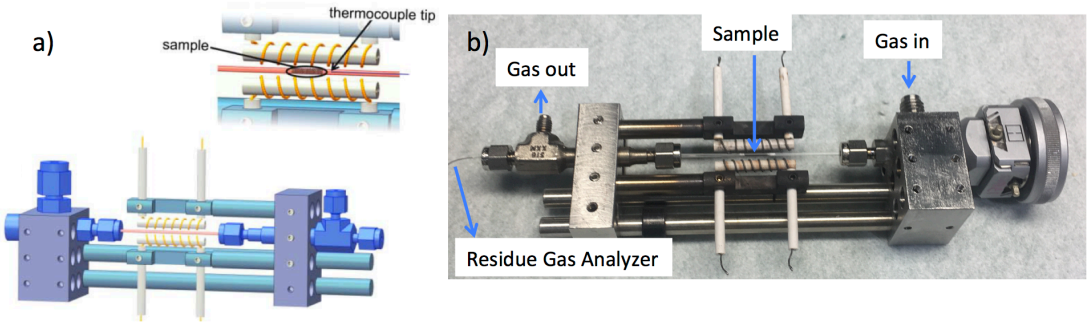

Figure 2.10. a) Schematic plot of the fully assembled flow-cell/furnace, an expanded view of the sample region and b) a photograph of the flow-cell/furnace.

A 2D PerkinElmer a-Si Flat Panel detector is used with an average wavelength of 0.45336 Å and diffraction images are integrated with GSAS-II[14] giving patterns with a Q-range of approximately 0.2 to 6.2 $Å^{-1}$. The beam focused area is 300 μ×300 μ and flux is 6×10^{10} photons/s at 27 keV with a resolution of 1.5×10^{-4} ΔE/E. Complete diffraction patterns are collected every 30 s. An example of the 2D detector captured powder diffraction rings and the integrated Bragg peaks with high statistics is shown in Figure 2.11. The quickness of the synchrotron X-ray diffraction data collection allows us to observe any structural change of oxidizer through chemical looing combustion. Moreover, reaction kinetics can be extracted from the peak intensity which will be discussed in Chapter 8.

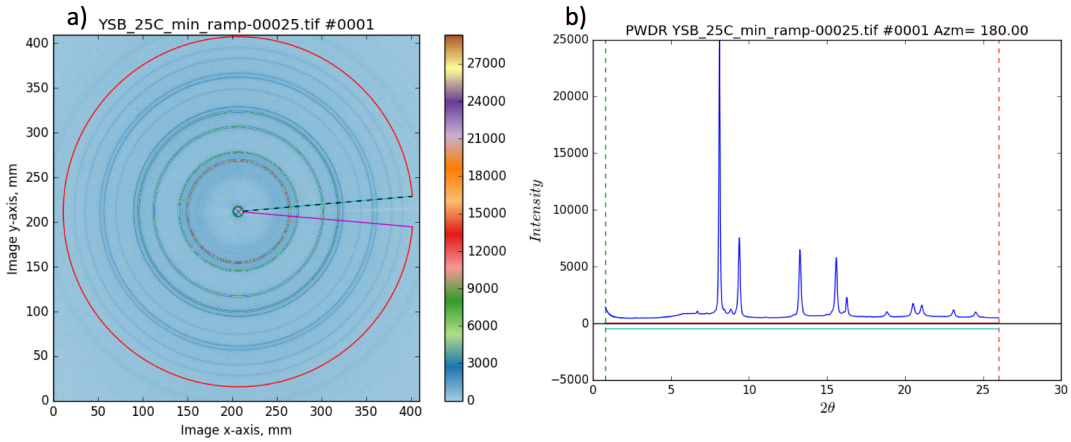

Figure 2.11. a) example of 2D detector captures powder diffraction rings, b) Bragg peaks integrated based on diffraction rings with high statistics.

Chapter 3: Doped Perovskites to Evaluate the Relationship Between Aluminum-Oxidizer Thermite Ignition and Bond Energy, Electronegativity and Oxygen Vacancy*

Summary

Despite our knowledge of the existence of the violent thermite reaction for over 100 years it is still not yet understood how the properties of a metal oxide oxidizer relate to and influence the ignition temperature. To address this shortcoming I prepared a series of perovskite oxidizers that enable a systematic investigation of how materials properties of the oxidizer relate to the ignition temperature. In this chapter, nine lanthanum based perovskites with different Sr^{2+} doping of the A-site, and different B-site transition metals were synthesized. The perovskite O_2 release and ignition temperatures with aluminum were measured by fast heating (> 10^5 K/s) temperature-jump/time-of-flight mass spectrometer coupled with high-speed imaging. These results were then correlated with the average bond energy and overall metal-oxygen electronegativity difference. Remarkably I found a linear relationship between average bond energy and electronegativity with ignition temperature. To my knowledge this is the first demonstration of the connection between metal–oxygen bond energy, electronegativity and ignition temperature.

* The results presented in this chapter have been published in the following journal article: Wang, X. Z.; Wu, T.; Zachariah, M. R., Doped Perovskites To Evaluate the Relationship between Fuel-Oxidizer Thermite Ignition and Bond Energy, Electronegativity, and Oxygen Vacancy. *J Phys Chem C* **2017,** *121* (1), 147-152.

3.1. Introduction

The thermite reaction[1] has been exploited for well over 100 years, and involves the violent reaction between a metallic fuel (e.g. Al, Fe, etc) and a metal oxide oxidizer (e.g. CuO, Bi_2O_3, etc.). More recently with the interest in nanoscale materials, the thermite reaction has generated renewed interest, as the reduced length scale offers the potential to significantly reduce the energy release time (< 1 ms)[2]. By far the most commonly employed fuel is Al due to the high enthalpy of reaction and its ready availability[3]. Despite our knowledge of this seemingly simply oxygen exchange reaction, the rapidity of the reaction has made it difficult to understand it mechanistically.[4]

Substantial effort has been devoted to studying the mechanism and parameters that govern the initiation reaction between nano aluminum and metal oxide. The most direct measure of the onset of runaway violent reaction is the ignition temperature. For metallic fuels, for example aluminum, there is a naturally occurring thin Al_2O_3 shell (~2-5 nm), which prevents direct contact between aluminum and metal oxide and makes the mechanism study difficult[5]. It is generally believed that the prerequisite for ignition is the existence of molten aluminum [6] or the phase change from amorphous alumina to a crystalline polymorph ~500 ˚C. Dean et al. examined the Al-NiO system and found a condensed phase reaction mechnism[8]. Sullivan et al. [9] proposed Al/WO_3 undergoes a reactive sintering mechanism, whereby initiation of the reaction occurs only when condensed-phase reactants have an interfacial contact. In fact the most recent evidence points to metal-metal oxide reactions initiating through a condensed phase reaction[10], even though the bulk of the remaining

chemistry might propagate through gas-solid processes. Jian et al. tried to correlate ignition temperature with gaseous oxygen released from the decomposition of metal oxide [11] but the results showed that there can be large differences in ignition temperatures among different nano thermite formulations involving aluminum and metal oxides. In part the challenge is that ignition is affected by experimental parameters, e.g. heating rate, experimental configuration, particle size and packing. Studies show that thermite ignition depends on heating rate.[12] To better study thermite ignition, which by its nature is an extremely fast self-heating process, it is necessary to employ heating rates that more closely resembles self-heating rates ($>10^5$ °C/s). In particular ignition is a very different process than steady reaction. Ignition becomes self-sustaining when the self-heating rate overcomes the inherent heat loss process and thus cannot be evaluated at low heating rates.

However even for seemingly the same experimental configuration (heating rate, experimental configuration) I have found that the ignition temperatures do not correlate with overall thermite reaction enthalpy as shown in Figure 1.5a for a range of common oxidizers. In summary, when considering the totality of the research into initiation of metal-metal oxide redox reaction to the point of ignition, it is still unclear to say what fundamental properties of the oxidizer determine the ignition point.

In part the problem is due to the large number of variables comprising an oxidizer that might impact ignition including, bond energy, oxygen mobility, crystal structure, reaction interface area, thermal conductivity, heat capacity and thermal contact, etc. In order to deal with this complexity a system is needed in which most of

the dependent variables can be held constant. One such class of material that offers the opportunity for such a study is perovskites.

Perovskite oxides, generally formularized as ABO_3, have been employed in solid oxide fuel and electrolysis cells (SOFC/SOEC)[13], heterogeneous catalysis of hydrocarbon[14], membranes for oxygen separation [15], and chemical looping combustion as oxygen carriers due to their high oxygen reactivity and superior oxygen transport capacities.[16] One of the main advantages of the perovskite structure is the possibility of adopting a large number of different A- and B-site cations or through partial substitution a wide range of combinations to adjust the redox properties. Thus perovskites offer the opportunity to tweeze out from a microscopic prospective structure-function relationship relevant to oxidation of a fuel.

In this chapter, I explored the role of oxygen transport properties, which are related to oxygen vacancy concentration, metal-oxygen bond energy and electronegativity on ignition temperature with nano aluminum. More specifically I evaluated the ignition behavior of a range of perovskites, synthesized by aerosol spray pyrolysis, chosen so as to enable systematic changes to the oxygen vacancy concentrations and bond energy by a) substituting Sr^{2+} and/or b) changing the B-site transition metal. Key to this study was to make these changes while maintaining the same crystal structure, particle morphology and size of the perovskites. The results show a very clear connection, that elevated oxygen vacancy concentration, smaller average bond energy, and smaller electronegativity difference, lowers the ignition temperature.

3.2. Experimental Details

All perovskites were synthesized by aerosol spray pyrolysis[17] from metal nitrate aqueous solutions formulated with the desired metal ratios. $La(NO_3)_3 \bullet 6H_2O$ (≥99.0% pure), $Sr(NO_3)_3$ (≥99.0% pure), $Co(NO_3)_2 \bullet 6H_2O$ (≥98% pure), $Cr(NO_3) \bullet 9H_2O$, and $Fe(NO_3) \bullet 9H_2O$ were obtained from Sigma-Aldrich and pyrolyzed at 1050 °C with a residence time of about 1 s to obtain $LaBO_3$ (B= Cr, Fe, Co), $La_{0.8}Sr_{0.2}BO_{3-\delta}$ (B=Cr, Fe, Co), and $La_{0.6}Sr_{0.4}BO_{3-\delta}$ (B=Cr, Fe, Co). For instance, in order to synthesize $LaCoO_3$, a 0.2mol/L precursor solution, containing stoichiometric $La(NO_3)_3$, $Co(NO_3)_3$ was atomized by a nebulizer to generate nominally 1 μm droplets with compressed air. The atomized droplets flowed through a diffusion dryer, where most of the water was absorbed, leaving solid precursor particles which were then passed to a tubular furnace to produce the desired perovskite particles. The final product was collected on a Millipore member with a pore size of 0.4 micron.

Nano-aluminum particles (~ 50 nm) were purchased from Novacentrix Corporation. To prepare the thermite composite, stoichiometric mixtures of nano-aluminum and perovskite were mixed, and then sonicated in hexane for 30 min. For control of stoichiometry, the Al_2O_3 shell (19% of the mass) content in nano aluminum was accounted for.

The crystal structures of the synthesized perovskites were characterized by X-ray diffraction (XRD) performed on a Bruker D8 diffractometer with Cu Kα radiation. Le Bail refinement of all diffraction patterns was performed with the TOPAS 4.2 software.[18] The morphologies of the perovskites were measured by

scanning electron microscopy (SEM) conducted on a Hitachi SU-70 instrument. Size distributions were obtained by measuring 300 individual nanoparticles statistically from SEM images of each sample, using Nano Measurer 1.2 image analysis software. The morphologies and elemental analysis of thermite powders were measured by SEM equipped with energy dispersive x-ray spectroscopy (EDS).

Oxygen release temperatures (in the absence of fuel) from individual oxidizer, perovskites, were measured with temperature-jump/time-of flight mass spectrometer (T-Jump/TOFMS).[19] A hexane suspension of perovskite powders was droppered onto a 70 um diameter platinum filament, and allowed to air dry. The platinum wire can be joule heated at a rapid rate ~ 4×10^5 °C/s, to ~1300 °C within 3 milliseconds. The filament was directly inserted into the ionization region of a TOFMS, where the gaseous products could be temporally analyzed. The temperature of the wire was determined from electric resistance based on the Callendar-Van Dusen equation, through a simultaneously measure of temporal applied voltage and current. The ionization/extraction region of the TOFMS was pulsed at 10 kHz resulting in a full mass spectrum every 100 μs.

Due to the size of nanoparticles compared with the wire and based on the previous result, the temperature of the wire is essentially equal to the temperature of the oxidizer system.[20] The temperature of the wire corresponding to the initial release of O_2 was regarded as the O_2 release temperature of perovskites.

Ignition temperature was also measured in the T-Jump/TOFMS) using direct optical emission with a high-speed camera (Vision Research Phantom v12.0) operating at 67056 frames/s. The experiment is equivalent to the oxygen release

measurement with the exception of the presence of the fuel. Ignition was determined as the onset of optical emission.

3.3. Results and Discussion

Structure and Morphology

Figure 3.1 shows XRD patterns for each synthesized $LaBO_3$ (B = Cr, Fe, Co), $La_{0.8}Sr_{0.2}BO_{3-\delta}$ (B = Cr, Fe, Co), and $La_{0.6}Sr_{0.4}BO_{3-\delta}$ (B = Cr, Fe, Co). I find that all the synthesized perovskites are pseudocubic, belonging to either cubic (Pm-3m), orthorhombic (Pnma) or rhombohedral (R-3c) space groups. Table S3.1. and Figure S3.1 present the refined results from Le Bail fitting, performed with the TOPAS 4.2 software. Although minor amounts of impurities peaks were found for $La_{0.6}Sr_{0.4}CrO_{3-\delta}$, the perovskite phase dominates. In the BO_6 octahedron the transformation from cubic (Pm-3m) to orthorhombic (Pnma) leads to a symmetry decrease, while the rhombohedral R-3c involves the slight rotation of the BO_6 octahedron with respect to the cubic structure. Compared to the perfect cubic, these distortions of either orthorhombic or rhombohedral structure are slight [21] and the coordinations of oxygen with A-site cation and B-site cation are maintained. Thus it is reasonable to say all perovskites in this study have essentially the same crystal structure, and any slight difference should not have a controlling impact on ignition.

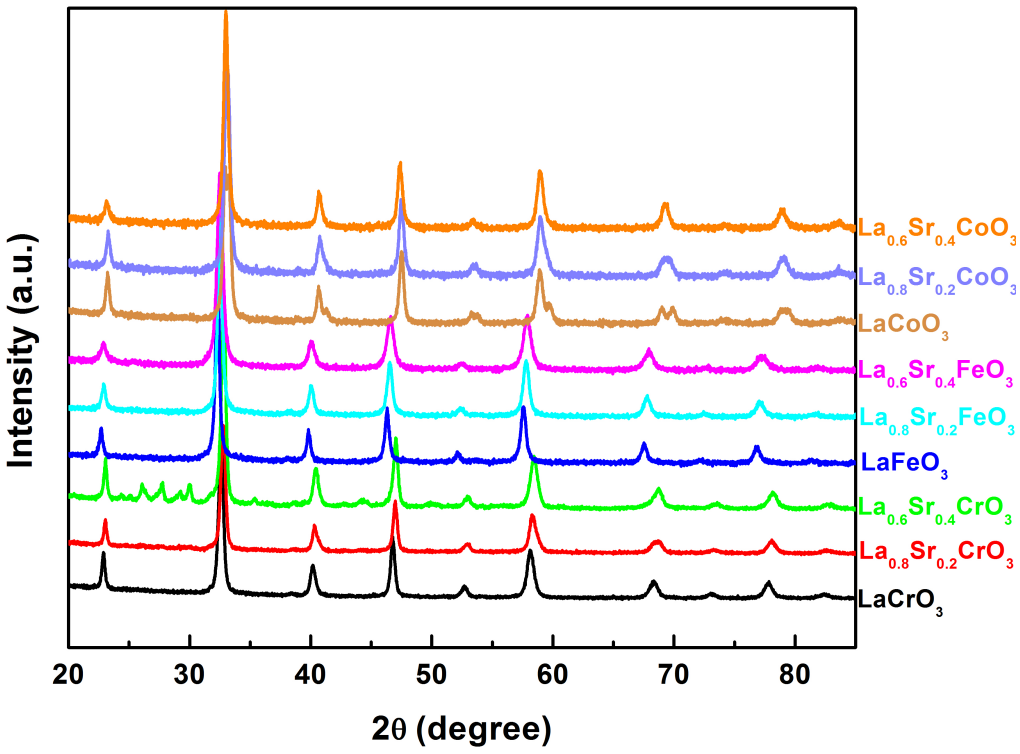

Figure 3.1. X-ray diffraction patterns of aerosol spray synthesized doped perovskite, with their space groups listed in the table

Cubic (Pm-3m)	$La_{0.6}Sr_{0.4}CoO_{3-\delta}$, $La_{0.6}Sr_{0.4}FeO_{3-\delta}$, $La_{0.6}Sr_{0.4}CrO_{3-\delta}$
Orthorhombic (Pnma)	$LaCrO_3$, $LaFeO_3$, $La_{0.8}Sr_{0.2}CrO_{3-\delta}$, $La_{0.8}Sr_{0.2}CoO_{3-\delta}$
Rhombohedral (R-3c)	$LaCoO_3$, $La_{0.8}Sr_{0.2}FeO_{3-\delta}$

Figure 3.2 shows SEM images of (a) $LaFeO_3$, (b) $La_{0.8}Sr_{0.2}FeO_3$ and (c) $LaCrO_3$ (as synthesized) representative powders, indicating essentially the same particle size distribution. The diameter of the particles should be log-normally distributed corresponding to the original spray size distribution. The size distribution of those representative particles measured from SEM images as well as log-normal fit profile are shown in Figure S3.2 and the log-normal fit parameters are listed in table S3.2. All samples have similar narrow log-normal distribution with $\sigma = 0.408 \pm 0.06$, and the average diameter is 115~126 nm. This result is consistent with the previous results that products have the same size distribution when synthesized under the same

condition (precursor concentration, flow rate, etc.).[22] Thus in this study, there are no morphology differences between particles that warrant consideration. Figure S3.3 shows the representative SEM and EDS results for Al/$LaFeO_3$ and Al/$La_{0.6}Sr_{0.2}FeO_3$, indicating that the aluminum and perovskite particles are well mixed with many points of intimate contact between fuel and oxidizer.

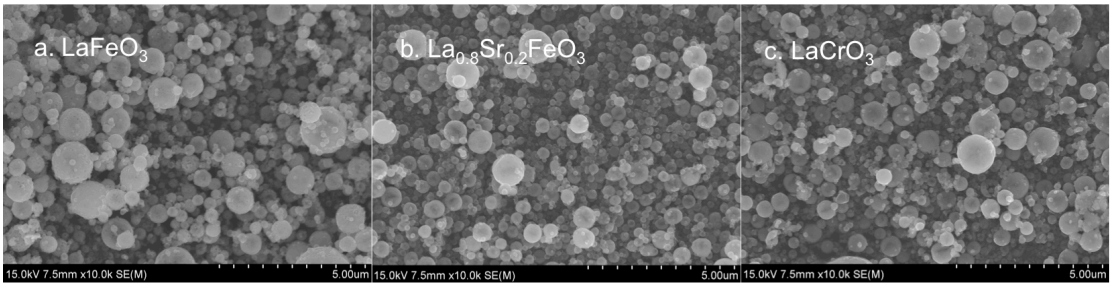

Figure 3.2. SEM image of as synthesized (a) $LaFeO_3$, (b) $La_{0.8}Sr_{0.2}FeO_3$ and (c) $LaCrO_3$ as representative powders

Oxygen Release Temperature and Ignition Temperature

Before I consider fundamental parameters I present two important measurable: the ignition temperature and the gaseous oxygen release temperature of the neat perovskite. The observed oxygen release temperature from the neat oxidizer and the observed ignition temperature of Al/perovskites, measured by T-Jump/TOFMS coupled with a high-speed camera, are shown in Figure 3.3. What this result shows is that all data points lie above the diagonal indicating that ignition occurs before oxygen (O_2) is released into the gas phase by the perovskite. Further for the temperature regime that T-jump/TOFMS could reach (~1350 °C), no O_2 release of $LaCrO_{3-\delta}$ and $LaFeO_{3-\delta}$ and no ignition of $LaCrO_{3-\delta}$ were observed. The time-resolved

mass spectra of neat $LaCoO_3$ and $LaFeO_3$ under T-jump heating are shown in Figure S3.4 as examples.

The results from Figure 3.3 demonstrate that since ignition occurs at a temperature below which oxygen is evolved from the oxidizer, I can conclude the reaction takes place by condensed state redox reaction rather than gas evolution of oxygen leading to subsequent reaction with aluminum.

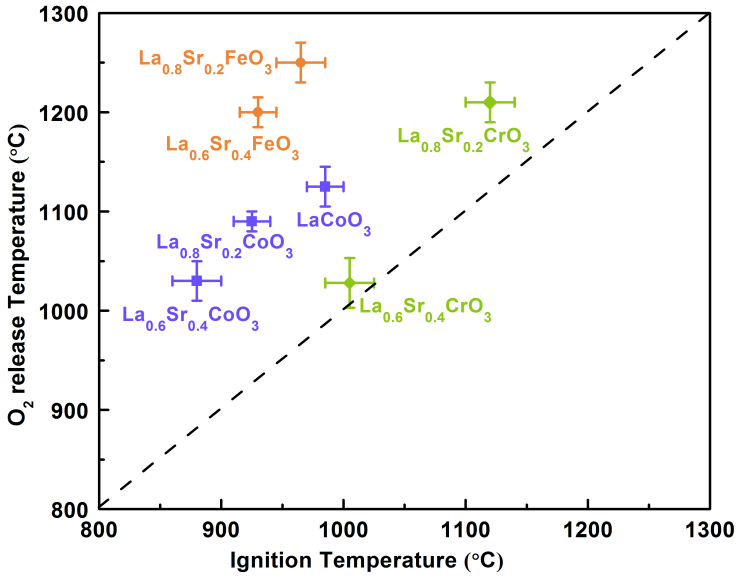

Figure 3.3. Oxygen release temperature from the perovskites vs. ignition temperature for Al/perovskites, indicates that ignition occurs prior to oxygen release (i.e. condensed state reaction).

Bond Energy and Oxygen Vacancy Effects on Ignition

Numerous studies have focused on the defect chemistry and oxygen ion diffusion in perovskite oxides and their impact on redox properties,[23] but has not been attempted for the thermite reaction. Prior work by others and us [24] show a relatively wide range of ignition temperature for the same fuel, implying an oxidizer control mechanism. I thus begin presumptively with the conjecture that oxygen ion transport of these systematic perovskites affects the ignition temperature. Oxygen ion transport,

typically characterized by the ionic conductivity, can be related to the charge of the ion Zq (O^{2-} in this case), the carrier mechanical mobility, μ and the oxygen vacancy concentration, $[V_O^{\cdot\cdot}]$ through equation 1.

$$\sigma = Zq \cdot [V_O^{\cdot\cdot}] \cdot \mu \qquad (1)$$

The use of perovskites is employed to:

a. *Change oxygen vacancy concentration by doping with Sr^{2+}:* Charge balance requires that substitution of Sr^{2+} for La^{3+} in the A-site leads to oxygen vacancies.

b. *Change oxygen ion mobility by doping Sr^{2+} and varying B-site metal ion (Co^{3+}, Fe^{3+}, Cr^{3+}):* Previous research has found that oxygen ion mobility depends on the activation energy for oxygen ion migration,[25] which can be associated with an average bond energy (ABE) in the perovskite lattice.[26] By doping Sr^{2+} and varying the B-site metal, the ABE of the perovskite can be systematically changed. Since for both Pm-3m cubic and R-3c rhombic perovskite, A-site cations are 12-coordinated with oxygen, and B-site cations are 6-coordinated with oxygen, the average bond energy (ABE) of the perovskite can be calculated based on equation 2, where $\Delta H_{A_mO_n}$ and $\Delta H_{B_mO_n}$ are the heats of formation of A_mO_n and B_mO_n oxides at 298 K, respectively, ΔH_A and ΔH_B are the heats of sublimation of A-metal and B-metal at 298 K and D_{O_2} is the dissociation energy of gaseous oxygen.[27] The electron configuration of B-site transition metal cations are fundamentally the same from that of bulk B-site cations proposed by Bockris and Otagawa.[28] (All calculated and experimental results are provided in Table S3.3)

When I consider ignition I refer to the point far from equilibrium, thus the equilibrium vapor pressure of oxygen is not a relevant concept and I can consider that the valency of the transition metal is invariant and oxygen vacancies are at their theoretical maximum values shown in Table S3.

$$ABE = \frac{1}{2}\left(\frac{1}{12m}\left(\Delta H_{A_mO_n} - m\Delta H_A - \frac{n}{2}D_{O_2}\right) + \frac{1}{6m}\left(\Delta H_{B_mO_n} - m\Delta H_B - \frac{n}{2}D_{O_2}\right)\right) \qquad (2)$$

The ABE of perovskites vs. the ignition temperature is shown in Figure 3.4, which clearly indicates that ignition temperature for Al/perovskite increases with ABE. The most important result when looking at the graph is that *the ignition temperature of a thermite reaction is directly correlated to the bond energy of the metal-oxygen bond in the oxidizer. To my knowledge this is the first ever demonstration of this connection.*

Additionally,

a. Holding δ constant, while varying the B-site leads to an ordering of ignition temperature of Cr > Fe > Co, and corresponds to the ordering in the ABE. A higher ABE is consistent with an increase in the activation energy for ion-migration and thus a decrease in oxygen anion mobility.

As discussed previously, Sr^{2+} A-site substitution leads to an elevated oxygen vacancy concentration, δ, resulting from charge balance considerations.

b. Varying δ, through A-site Sr^{2+} substitution, increases vacancies, and thus from equation. 1 increases anion conductivity, but also lowers the ABE due to Sr-O being a weaker bond. Again lower ABE is seen to correspond to lower ignition temperature. This trend holds for all samples corresponding to different Sr levels and B-site element.

c. While ABE dominates ignition temperature according to Figure 3.4; it is also noted that while Sr^{2+} substitution creates oxygen ion vacancies, it is also changing the ABE. $La_{0.8}Sr_{0.2}FeO_3$ has a higher ABE than $LaCoO_3$ but lower ignition temperature, presumably from a higher oxygen vacancy. This is more clearly defined if I pick a condition where the ABE is held constant, but the vacancy concentration is varied. $La_{0.7}Sr_{0.3}FeO_3$, and $LaCoO_3$ have the same nominal ABE, but the former has a slightly lower ignition temperature as seen in Figure 3.4, consistent with a higher vacancy concentration.

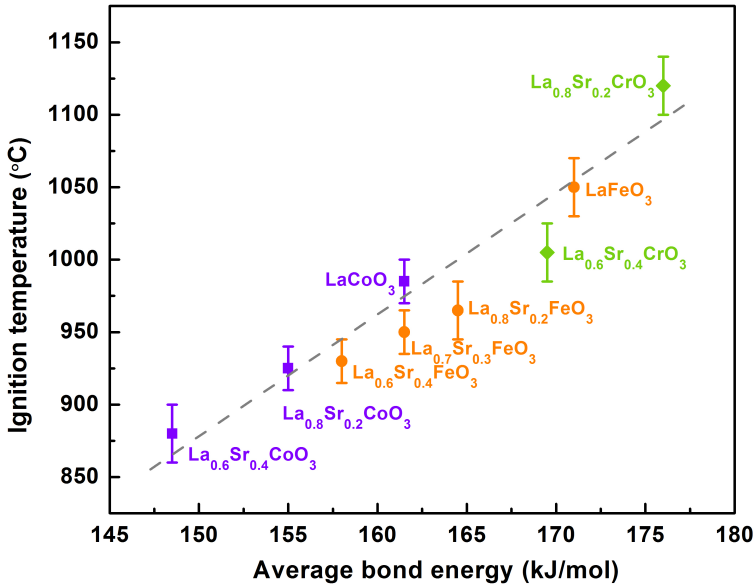

Figure 3.4. Observed relationship between average bond energy (ABE) of perovskites against the ignition temperatures of Al/perovskite.

Electronegativity and Ignition Temperature

Previous research has explored the effect of the e_g occupancy of B-site cation and thus metal-oxygen bond's covalency for catalytic activity in oxygen evolution reactions.[7] Thus electronegativity is another possible metric that could describe the metal-oxygen bond's covalency and energy, and relationship to ignition temperature.

A more ionic character in an M-O bond should yield a more thermally stable perovskite. This nominally should correspond to a metal with a lower electronegativity.[29] Since both A-site substitution and B-site ions affect the ignition temperature, when analyzing the relationship between electronegativity and ignition temperature, it is necessary to consider the electronegativity of both the A and B-site cation. In addition, I also have to consider the oxidation state difference between La (III) and Sr (II). When substituting Sr (II) for La (III)'s, the oxidation state has to be normalized from SrO to Sr_2O_2 as in La_2O_3. That is, in the perovskite crystal, Sr (II) is 8 coordinated with oxygen compared to the original La (III), which is 12 coordinated with oxygen.

The formal calculation of the electronegativity is through equation 3, where χ is the overall electronegativity difference between cation and oxygen and χ_{La-O}, χ_{Sr-O}, and χ_{B-O} are the electronegativity difference between La, Sr and B-site atom and oxygen on the Pauling Scale,[30] a is the mole fraction of Sr and n (=2/3) is a factor used to normalize the oxidation state difference between Sr and La.

$$\chi = (1-a)\chi_{La-O} + n \cdot a\chi_{Sr-O} + \chi_{B-O} \quad (3)$$

The larger the electronegativity difference, χ, the high the ionic character in the perovskite, and the more stable one should expect the perovskite. Figure 3.5. clearly shows there exists a trend that ignition temperature increases with increasing electronegativity difference χ in the perovskite, and that higher ionic character will increase ignition temperature. Electronegativity this offers a potentially simple metric to gauge relative changes in ignition temperature.

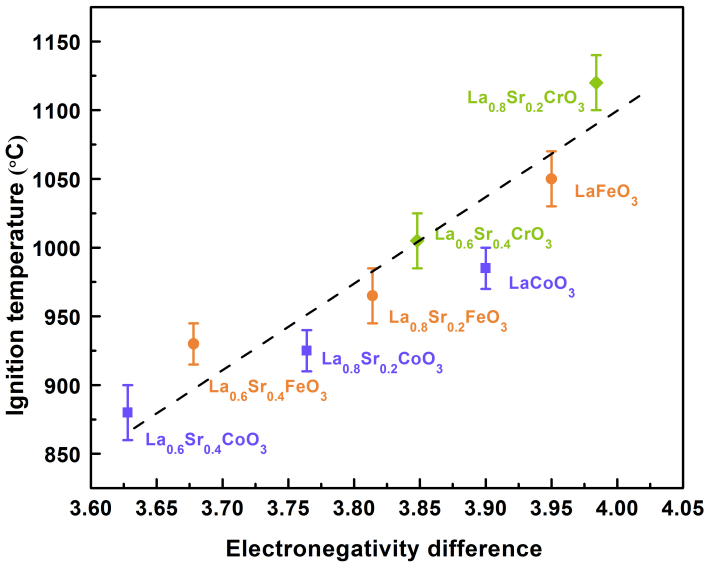

Figure 3.5. Overall electronegativity difference of perovskites versus ignition temperature of Al/perovskite

3.4. Conclusions

In summary, this study reveals for the first time a clear relationship between molecular properties of the oxidizer and ignition temperature in a thermite reaction. This was enabled by employing a perovskite structure whose crystal structure and particle size could be held constant, but whose vacancy concentration and bond energy could be systematically varied. The results clearly demonstrate that smaller bond energy with smaller electronegativity difference and elevated oxygen vacancy concentration lead to a lower ignition temperature. These results provide important insights in manipulating metal oxides' oxidation properties for thermochemical and energetic applications.

3.5. Supplemental Information

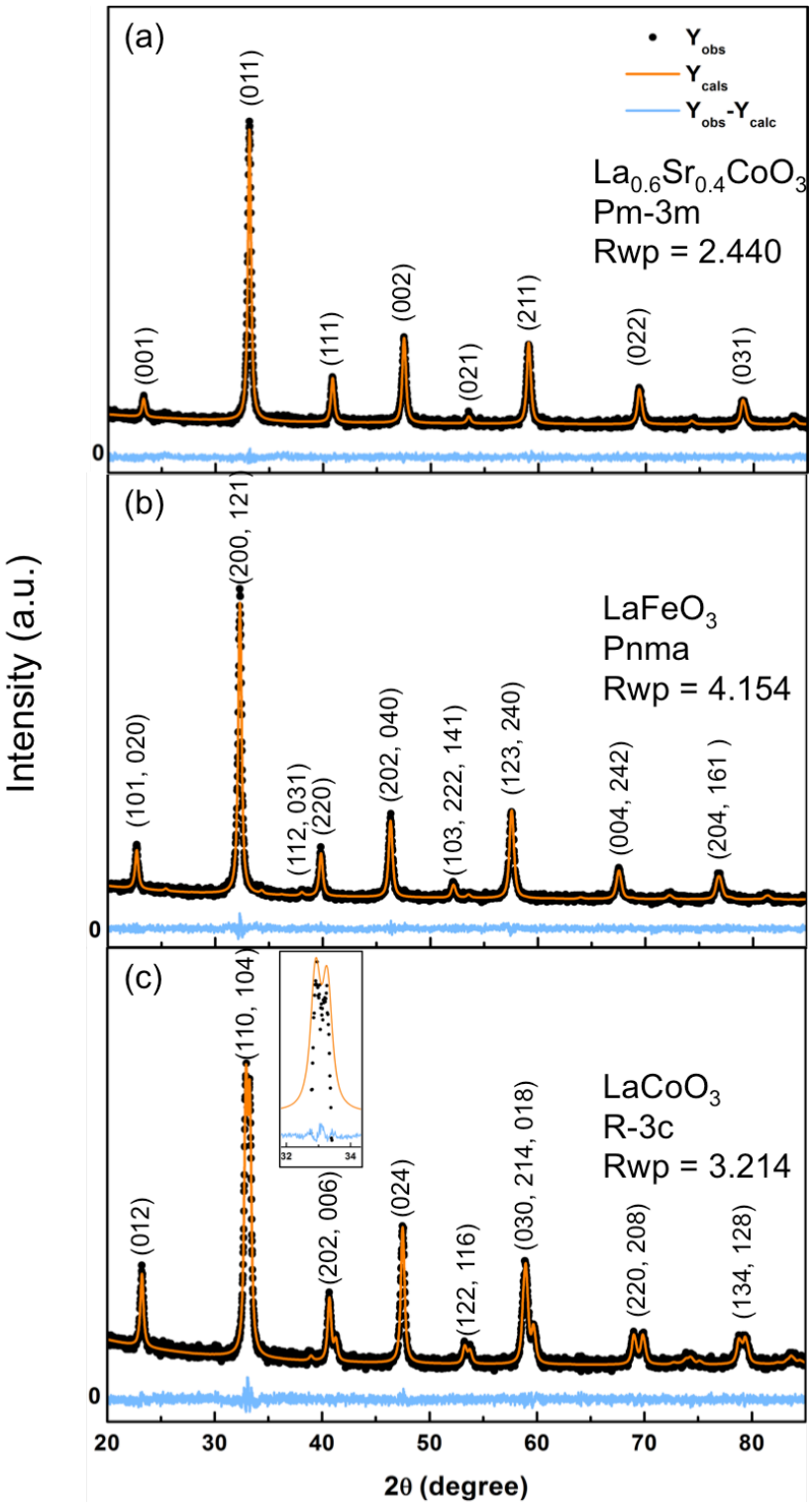

Figure 3S.1. X-ray diffraction patterns with profile fitting based on Le Bail refinements for (a) $La_{0.6}Sr_{0.4}CoO_{3-\delta}$ in Pm-3m, (b) $LaFeO_3$ in Pnma and (c) $LaCoO_3$ in R-3c.

To better figure out which space group specifically each synthesized perovskite belongs, Le Bail refinements were performed for all samples in the cubic (Pm-3m), orthorhombic (Pnma) and rhombohedral (R-3c) space groups, respectively. Refinement with lowest Fitting coefficient, Rwp, was selected as the final result. It is noted from Figure S3.2(a) and 3.2(c) that from cubic (Pm-3m) to rhombehedral (R-3c), peaks split at $2\theta \approx 33°$, 41°, 54°, 59°, 69° and 79°. Satellite peaks at 38° in Figure 3.2(b) is the indication of Pnma space group.

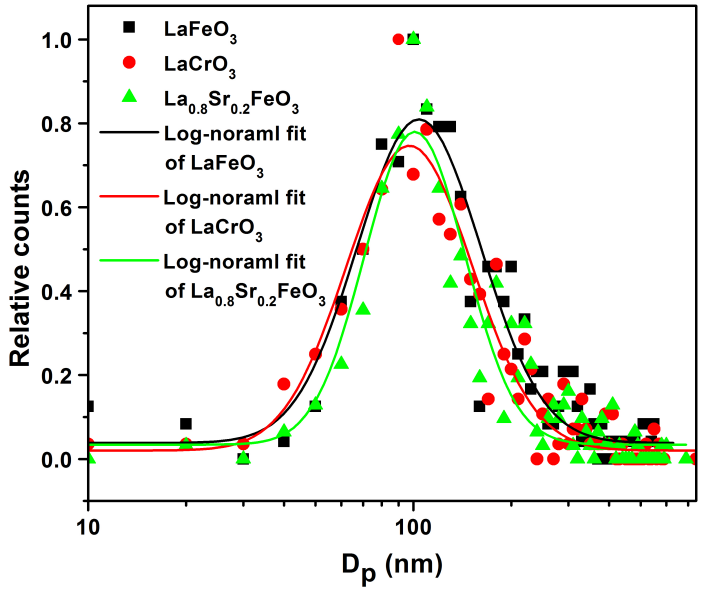

Figure S3.2. Particle size distributions and log-normal fit profiles of representative powers $LaFeO_3$, $La_{0.8}Sr_{0.2}BO_{3-\delta}$, and $LaCrO_3$ measured from SEM images, showing essential the same distribution.

All samples have similar narrow log-normal distribution with $\sigma = 0.408 \pm 0.06$, and the average diameter is 115~126 nm.

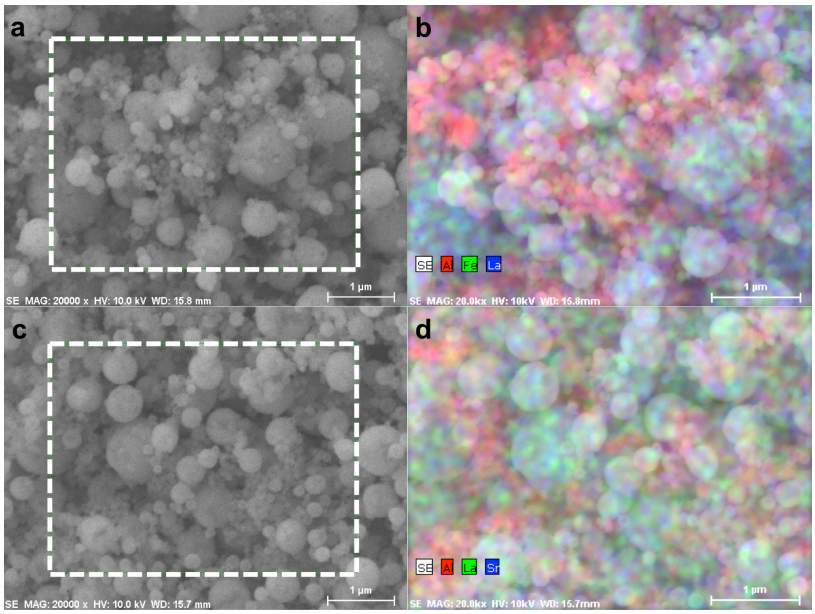

Figure S3.3. SEM images for (a) $LaFeO_3$ and (c) $La_{0.6}Sr_{0.4}FeO_3$ and EDS analysis of the boxed region for (b) $LaFeO_3$ and (d) $La_{0.6}Sr_{0.4}FeO_3$.

The size of the commercial aluminum particle used in this study is ~50 nm while the size distribution in Figure S3.3. tells us the average particle size for perovskite is ~120 nm. Thus it is clearly shown in Figure S3.4 (a) and (c) that the uniform small spherical particles are aluminum while the larger log-normal distributed particles are perovskite oxide. EDS analysis in Figure S3.4 (b) and (d) confirms this.

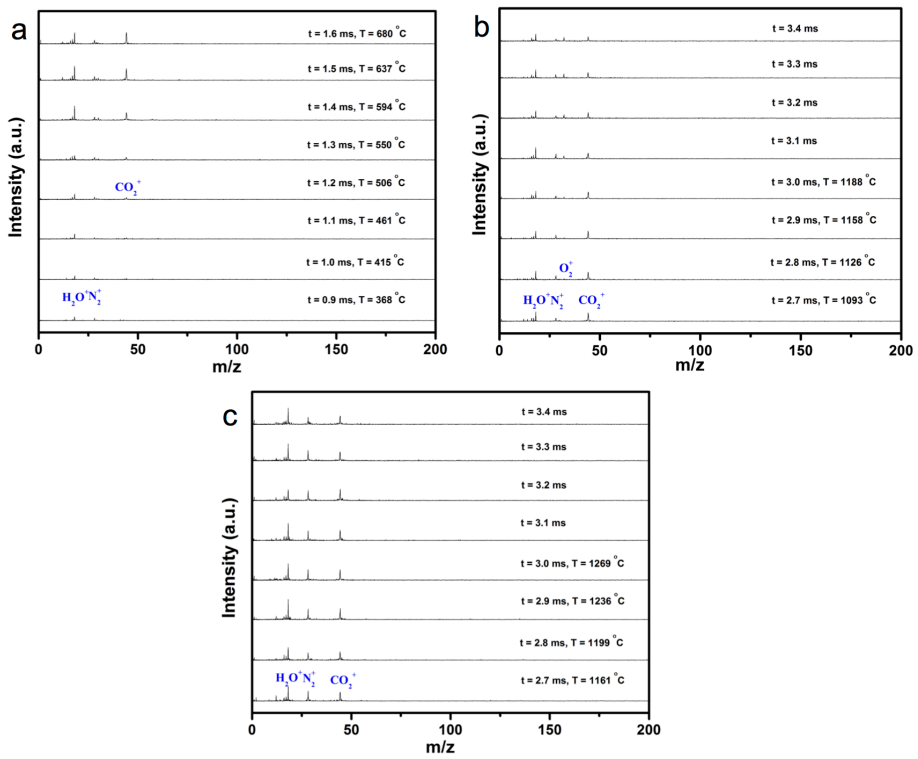

Figure S3.4. TOFMS spectra of (a) $LaCoO_3$ at t=0.9-1.6 ms. (b) $LaCoO_3$ at t=2.7-3.4 ms. (c) $LaFeO_3$ at t=2.7-3.4 ms.

In Figure S3.4 (a), the spectrum at t=0.9 ms represents the background of the T-jump TOFMS with major peaks at m/z=18 (H_2O^+) and m/z=28 (N_2^+). At t=1.2 ms, the carbon contamination from $LaCoO_3$ starts to decompose and results to the formation of CO_2^+ with peaks at m/z=44. It is believed this carbon contamination was mainly from CO_2 in the carrier gas and led to the formation of minor impurities like metal carbonates. In Figure S3.4 (b), peak at m/z=32 started to come out at t=2.8 ms, indicating O_2 released at 1126 °C. Besides O_2, no other gaseous species were detected in the decomposition of $LaCoO_3$. While in Figure S3.4 (c), no peaks at m/z=32 ever showed, indicating no O_2 released during rapid heating.

Table S3.1. Le Bail refinement parameters for perovskites.

			Lattice parameter			
	Phase Symmetry	Crystallite size (nm)[a]	a (Å)	b (Å)	c (Å)	volume (Å^3)
$LaCoO_3$	Rhombohedral (R-3c)	34.0(3)	5.4410(3)		13.118(1)	336.32(5)
$LaCrO_3$	Orthorhombic (Pnma)	37.2(2)	5.4705(4)	7.7625(7)	5.5146(3)	234.18(3)
$LaFeO_3$	Orthorhombic (Pnma)	34.3(2)	5.5467(7)	7.8325(9)	5.5579(5)	241.46(5)
$La_{0.6}Sr_{0.4}CoO_{3-\delta}$	Cubic (Pm-3m)	36.2(2)	3.8347(1)			56.387(6)
$La_{0.6}Sr_{0.4}FeO_{3-\delta}$	Cubic (Pm-3m)	19.8(1)	3.9093(2)			59.74(1)

$La_{0.6}Sr_{0.4}CrO_{3-\delta}$	Cubic (Pm-3m)	28.4(3)	3.8716(3)			58.03(1)
$La_{0.8}Sr_{0.2}FeO_{3-\delta}$	Rhombohedral (R-3c)	27.6(1)	5.5434(4)		13.580(1)	361.40(6)
$La_{0.8}Sr_{0.2}CrO_{3-\delta}$	Orthorhombic (Pnma)	41.2(4)	5.4530(3)	7.7347(9)	5.5004(3)	231.99(3)
$La_{0.8}Sr_{0.2}CoO_{3-\delta}$	Orthorhombic (Pnma)	31.0(2)	5.3942(4)	7.661(1)	5.4447(3)	225.01(3)

[a] determined from Scherrer equation

Table S3.2. Log-normal fit parameters, and R^2 is coefficient of determination.

Equation	$y = y_0 + \frac{A}{\sqrt{2\pi} \cdot \sigma x} \cdot \exp\left(-\frac{(lnx - \mu)^2}{2\sigma^2}\right)$		
		Value	Standard Error
$LaFeO_3$	R^2	0.885	
	y_0	0.03841	0.01529
	μ	125.91989	3.57372
	σ	0.43684	0.02753
	A	96.64812	4.85522
$La_{0.8}Sr_{0.2}FeO_3$	R^2	0.913	
	y_0	0.02023	0.00977
	μ	118.42409	2.73743
	σ	0.44432	0.022
	A	86.81814	3.50334

$LaCrO_3$	R^2	0.877	
	y_0	0.03431	0.01134
	μ	114.63702	2.55421
	σ	0.35535	0.02194
	A	71.49008	3.64684

Table S3.3. Oxygen nonstoichiometry, ABE, oxygen release temperature, and the Al/perovskite thermite ignition temperature.

Perovskite	δ	ABE (kJ/ mol)	O_2 release temperature (°C)	Error (°C)	Ignition temperature (°C)	Error (°C)
$LaCrO_{3-\delta}$	0	183	NA	NA	NA	NA
$La_{0.8}Sr_{0.2}CrO_{3-\delta}$	0.1	176	1210	20	1120	20
$La_{0.6}Sr_{0.4}CrO_{3-\delta}$	0.2	170	1028	25	1005	20
$LaCoO_{3-\delta}$	0	162	1125	20	985	15
$La_{0.8}Sr_{0.2}CoO_{3-\delta}$	0.1	155	1090	10	925	15
$La_{0.6}Sr_{0.4}CoO_{3-\delta}$	0.2	149	1030	20	880	20
$LaFeO_{3-\delta}$	0	171	NA	NA	1050	20
$La_{0.8}Sr_{0.2}FeO_{3-\delta}$	0.1	165	1250	20	965	20
$La_{0.6}Sr_{0.4}FeO_{3-\delta}$	0.2	158	1200	15	930	15
$La_{0.7}Sr_{0.3}FeO_{3-\delta}$	0.15	162	1240	15	950	15

Chapter 4: Doped δ-Bismuth Oxides to Investigate Oxygen Ion Transport as a Metric for Condensed Phase Thermite Ignition [*]

Summary

Nanothermites offer high energy density and high burn rates, but are mechanistically only now being understood. One question of interest is how initiation occurs and how the ignition temperature is related to microscopic controlling parameters. In this study, I explored the potential role of oxygen ion transport in Bi_2O_3 as a controlling mechanism for condensed phase ignition reaction. Seven different doped δ-Bi_2O_3 were synthesized by aerosol spray pyrolysis. The ignition temperatures of Al/doped Bi_2O_3, C/doped Bi_2O_3 and Ta/doped Bi_2O_3 were measured by temperature-jump/time-of-flight mass spectrometer coupled with a high-speed camera respectively. These results were then correlated to the corresponding oxygen ion conductivity (directly proportional to ion diffusivity) for these doped Bi_2O_3 measured by impedance spectroscopy. I find that ignition of thermite with doped Bi_2O_3 as oxidizer occurs at a critical oxygen ion conductivity (~0.06 S/cm) of doped Bi_2O_3 in the condensed-phase so long as the aluminum is in a molten state. These results suggest that oxygen ion transport limits the condensed state Bi_2O_3 oxidized thermite ignition. I also find that the larger oxygen vacancy concentration and the smaller metal-oxide bond energy in doped Bi_2O_3, the lower the ignition temperature.

[*] The results presented in this chapter have been published in the following journal article: Wang, X. Z.; Zhou, W. B.; DeLisio, J. B.; Egan, G. C.; Zachariah, M. R., Doped delta-bismuth oxides to investigate oxygen ion transport as a metric for condensed phase thermite ignition. Phys Chem Chem Phys 2017, 19 (20), 12749-12758.

The latter suggests that I can consider the possibility of manipulating microscopic properties within a crystal, to tune the resultant energetic properties.

4.1. Introduction

The thermite reaction has historically generated interest due to its high specific energy density.[1] Compared to traditional organic based energetic materials such as TNT and RDX, thermites have higher gravimetric and volumetric reaction enthalpies.[2] The kinetics of the reaction are known to be accelerated when the fuel and oxidizer are at the nanoscale, resulting from the increased interfacial contact and reduced characteristic diffusion length scale. Aluminum is by far the most commonly used fuel due to its high oxidation potential, ready availability and low density.[3,4] Nano-aluminum has a native Al_2O_3 shell, which must be breached in order for the fuel and oxidizer to react. Rosenband found melting aluminum leaks through cracks resulting from the expanding outer shell of Al_2O_3.[5] Trunov et al. proposed that ignition occurs when the temperature exceeds the alumina melting point.[6] Sullivan et al. proposed nanothermites undergo a reactive sintering mechanism.[7,8]

On the other hand there are many oxidizers, typically metal oxides, available to complete the redox reaction. It is the properties of the oxidizers on ignition that is very much an open question. More generally, the initiation mechanism of the thermite reaction is being explored by several research groups.[9-12] The basic questions at hand are, what species initiate the reaction, what form are they in, and how is it transported? Answering this question could lead to a better understanding on how best to choose oxidizers. Jian et al.[12] recently investigated whether gas phase oxygen generation from an oxidizer is an essential prerequisite to ignition under rapid heating rate

conditions, and found large differences in ignition temperatures among different nanothermite formulations involving aluminum and metal oxides. For instance, many formulations (e.g., Al-CuO) have ignition temperatures slightly higher than the decomposition temperatures of the oxidizers, suggesting gas-phase oxygen generation may be necessary for the ignition. However, some formulations (e.g., Al-Bi_2O_3) have ignition temperatures lower than the decomposition temperatures of oxidizers, suggesting a condensed phase reaction mechanism that is not governed by the release of gas-phase oxygen. Al-Bi_2O_3 is one of the most interesting formulations for two reasons: The ignition temperature (~630 °C) is much lower than the decomposition temperature of Bi_2O_3 (~1330 °C), which leads to ignition almost certainly through a condensed phase reaction.[13] The other is that Bi_2O_3 has the highest known oxygen ion conductivity,[14] which one might reasonably expect to be an important parameter, although it has not heretofore been explored in the thermite reaction. In Chapter 3, I employed nine lanthanum based perovskites with different Sr^{2+} doping of the A-site, and different B-site transition metals.[15] The perovskites O_2 release and ignition temperatures with aluminum were measured under fast heating (> 10^5 °C/s). The results showed a linear relationship between average bond energy and electronegativity with ignition temperature. This was the first demonstration of the connection between metal–oxygen bond energy, electronegativity and ignition temperature. Furthermore it suggests that further studies of oxygen ion diffusivity in metal oxides are warranted. Ion-diffusion coefficients can be measured through a determination of mobility or more directly through an electrical measurement of ion conductivity.[16] One feature of Bi_2O_3 which makes it particularly attractive for my

purposes is that it is an ionic conductor, which implies that I will have a direct opportunity to measure oxygen-ion conductivity, not readily available in other systems which mostly are mixed ion and electron conductors.[17]

While aluminum is nominally the fuel of choice, for the purposes of tweezing out mechanistic information I will also study both carbon and tantalum as fuels. Based on previous work in our group with carbon black as a fuel,[13] the C/Bi_2O_3 system offers a valuable mechanistic perspective that unlike aluminum, carbon has no oxide shell, thus no barrier for the oxygen species migration that leads to ignition. Additionally, C has high melting point thus not particularly mobile. Therefore, the ignition of C/Bi_2O_3 is expected to be controlled by the transport of bound oxygen from the oxidizer. Tantalum is another candidate as a high energy density fuel due to the high negative enthalpy of formation of tantalum oxide.[18] Similar to aluminum, tantalum also has a surface passivating amorphous oxide shell. However, tantalum has a very high melting temperature (~3000 °C),[19] which lies far above the ignition temperature. Thus I have three different fuels, one (Al) with a low melting point and a passivating oxide, one (Ta) with a high melting point and a passivating oxide and one (C) with a high melting point with no passivating oxide.

Studies on all of the aforementioned fuels with Bi_2O_3 allude to the importance of oxygen transport, which is directly related to the temperature dependent internal structure of Bi_2O_3. Pure cubic δ-Bi_2O_3's high oxygen ion conductivity results from the large number of highly mobile oxygen vacancies, weak Bi-O bond and high polarizability of Bi^{3+} with its lone $6s^2$ electrons. However, δ-Bi_2O_3 is less thermodynamically stable than the monoclinic α-phase below 730°C shown in Figure

1.9,[20] but can be stabilized down to room temperature by doping with other oxides.[21] However, due to the mismatch in ionic radii between the host and dopant cations and a related phenomenon, anion ordering, phase stabilization lowers the oxygen ion conductivity.[14] Several studies report that due to the large dopant radii and high polarizability of dysprosium, erbium and yttrium, they are less likely to cause extensive oxygen ion displacement or vacancy ordering, which lead to conductivity decay and thus single dopants of these metal oxides are able to stabilize the fluorite structure of δ-Bi_2O_3.[22-25] Jung et al. found that with two dopants, dysprosium and tungsten stabilized bismuth oxide achieved higher conductivity.[26] Maria also reports that small amount of niobium oxide doped bismuth oxides yield a fluorite-type crystal structure.[27]

In this study I explored how oxygen-ion conductivity in a metal oxide is related to the ignition temperature, by doping δ-Bi_2O_3 More specifically I evaluated the ignition behavior of seven doped Bi_2O_3 oxidized thermites which were chosen so as to enable systematic changes to their oxygen ion conductivity, without a change in crystal structure and morphology. The results point to a critical oxygen ion conductivity of doped Bi_2O_3 that, when achieved through thermal activation, leads to an ignition condition.

4.2. Experimental Details

Sample preparation

Nano-aluminum particles (~50 nm) were purchased from Novacentrix Corporation, nano-sized carbon black (~50 nm) was obtained from Cabot Corporation and nano-tantalum powders (<50 nm) were purchased from Global Advanced Metals.

$Bi(NO_3)_3 \bullet 5H_2O$ (≥98% pure), $Y(NO_3)_3 \bullet 6H_2O$ (99.8% pure) and $NH_4NbO(C_2O_4)_2 \bullet xH_2O$ were purchased from Sigma-Aldrich. $Dy(NO_3)_3 \bullet 5H_2O$ (99.9% pure) and $(NH_4)_6W_{12}O_{39} \bullet xH_2O$ was purchased from Alfa Aesar. To dissolve $Bi(NO_3)_3 \bullet 5H_2O$, 2 mol/L nitric acid was used.

Seven different compositions with a constant dopant molar concentration of 15 mol% were investigated as listed in Table 4.1:

Table 4.1. Aerosol spray synthesized doped Bi_2O_3.

Doped Bi_2O_3	Abbr.
$(Y_{0.15}Bi_{0.85})_2O_3$	YSB
$(W_{0.15}Bi_{0.85})_2O_{3.45}$	WSB
$(Er_{0.15}Bi_{0.85})_2O_3$	ESB
$(Dy_{0.15}Bi_{0.85})_2O_3$	DSB
$(Dy_{0.1}W_{0.05}Bi_{0.85})_2O_{3.15}$	DWSB10
$(Dy_{0.05}W_{0.1}Bi_{0.85})_2O_{3.3}$	DWSB5
$(Dy_{0.05}Nb_{0.1}Bi_{0.85})_2O_{3.2}$	DNSB

To ensure appropriate comparison, pure Bi_2O_3 is also synthesized. All compositions were prepared by aerosol spray pyrolysis [28] at 750 °C with a constant precursor concentration. Aerosol spray pyrolysis is a single droplet chemistry approach. So long as the temperature is substantially lower than the volatilization temperature of the individual metal components the resulting solid particle will have the same relative concentration as the original solution, insuring accurate stoichiometric fractions.

A 0.2mol/L precursor solution was atomized in a nebulizer into 1 μm droplets by compressed air flow. The atomized droplet flowed through a diffusion dryer, where most of the water was absorbed, and then decomposed into oxides in the furnace. The final product was collected in a Millipore membrane with a pore size of 0.4 micron.

To prepare the thermite composite, stoichiometric mixtures of nano-fuels (aluminum, carbon, or tantalum) and doped Bi_2O_3 were mixed and then sonicated in hexane for 30 min. While calculating the stoichiometry, the Al_2O_3 shell (19% of the mass) and Ta_2O_5 shell (30% of the mass) were considered. For the impedance measurement, each doped Bi_2O_3 sample was pressed into a 13 mm diameter pellet at 30 MPa with a thickness of ~1 mm. The pellets were subsequently sintered in air at 750 °C for 16 h, and Engelhard gold paste was brushed onto both sides of the pellets. Platinum wires were attached to both sides of the painted pellet using gold paste and the cell were sintered at 500 °C for 1 h to burn the organic additives from the paste.

Characterization

Crystal structure and morphology of doped Bi_2O_3

The crystal structures of the synthesized Bi_2O_3 were characterized by X-ray diffraction (XRD) performed on a Bruker D8 diffractometer with Cu Kα radiation. Le Bail refinement of all diffraction patterns was performed with the TOPAS 4.2 software.[29] The morphologies of the particles were measured by scanning electron microscopy (SEM) with a Hitachi SU-70. Size distributions were obtained by measuring 300 individual nanoparticles statistically from SEM images of each sample, using Nano Measurer 1.2 image analysis software.[30]

T-jump ignition test for thermite

Ignition temperature and behavior was measured in a temperature-jump/time-of flight mass spectrometer (T-Jump/TOFMS).[31] The temperature of the wire was calculated from electric resistance based on Callendar-Van Dusen equation, using the

data from simultaneously recorded applied voltage and current. Due to the small dimension of nanoparticles compared with the wire and based on our previous result, the temperature of the wire is essentially equal to the temperature of the thermite system.[32]

Conductivity measurements

Oxygen ion conductivity was measured from the AC impedance analysis using a Solartron 1260 A, with a symmetric cell by two electrode electrochemical impedance spectroscopy over the frequency range of 1 Hz to 10^6 Hz with perturbation amplitude of 100 mV. The Solartron 1260 A was interfaced to a computer using the Zplot software for the data analysis. A nulling technique was used to remove any artifacts caused by inductive response of the test leads and the equipment to measure the small impedance at high temperature. The measurements were performed between 200 and 700 °C or 200 and 750 °C in air atmosphere with an interval of 50 °C. The conductivities were converted from the bulk resistance and the dimensions of the sample based on $\sigma = {}^{L}/_{RA}$, where σ is the oxygen ion conductivity, R is the bulk resistance, L and A is the thickness and sectional area of the pellets.

4.3. Results and Discussion

Structure and morphology

As the oxygen ion conductivity of Bi_2O_3 is highly dependent on crystal structure, it was important to ensure that all doped Bi_2O_3 samples had the same crystal structure. Figure 4.1 shows XRD patterns for all seven doped Bi_2O_3, showing

that all doped Bi_2O_3 prepared were found to be pure fcc structure, indicating they are δ-Bi_2O_3. The XRD pattern of pure Bi_2O_3 is shown in Figure S4.1, showing a tetragonal structure, β-Bi_2O_3. Although α-Bi_2O_3 is the only room-temperature stable structure, it was β-Bi_2O_3 that was obtained via aerosol spray pyrolysis, presumably because of the rapid quench that occurs in aerosol pyrolysis processing that can result in meta-stable phases. The lattice parameters of seven δ-Bi_2O_3 samples at room temperature were determined from the TOPAS program for calculating oxygen vacancy concentrations. Since all doped Bi_2O_3 have the same crystal structure, it is reasonably to assume the crystal structure shouldn't have a controlling impact on ignition.

Figure 4.2 shows the SEM images of DSB and DWSB5 as representative powders, indicating similar particle size distribution. SEM images of DSB at various magnifications can be found in Figure S4.2. The diameter of the particles should be log-normally distributed corresponding to the original spray size distribution. As example the size distribution of DSB and DWSB5 and log-normal fit are shown in Figure S4.3. The log-normal fit parameters are listed in Table S4.1 and show that all particle have a similar narrow log-normal distribution with $\sigma = 0.453 \pm 0.003$, with an average diameter of ~100 nm. Since all particles have a similar size distribution and morphology I can reasonably remove these as variables.

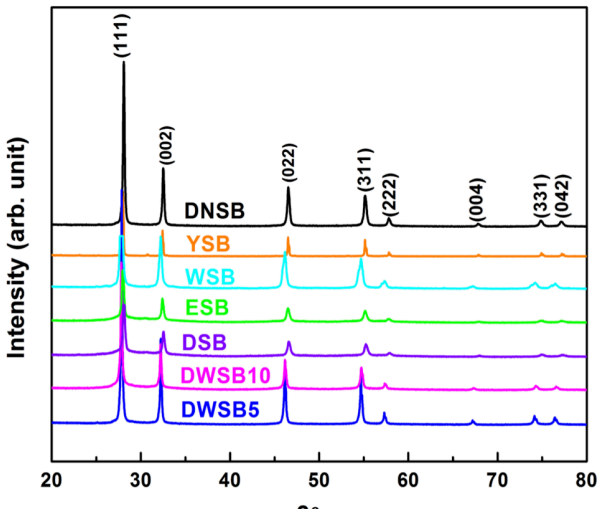

Figure 4.1. X-ray diffraction patterns of aerosol spray synthesized doped Bi_2O_3.

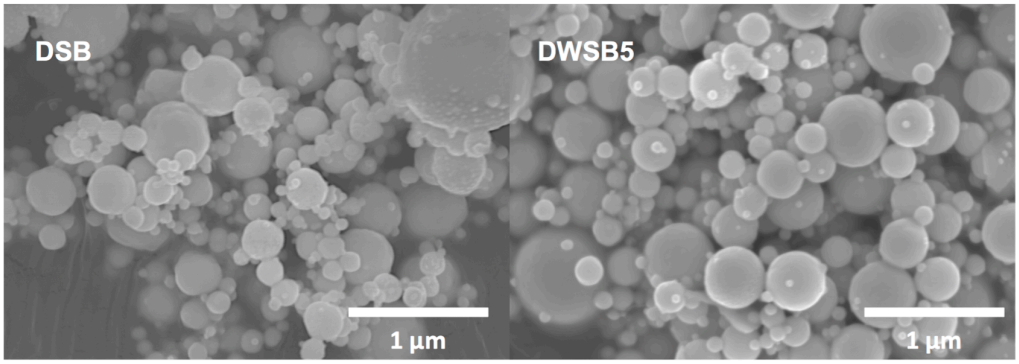

Figure 4.2. SEM images of DSB and DWSB5 particles.

Oxygen Ion Conductivity

Figure 4.3 shows typical impedance spectra obtained for WSB, as an example, at (a) 200 °C and (b) 500 °C. The assignment of a controlling mechanism for conductivity is based on the magnitudes of the measured capacitance as outlined in Table 1. of reference 33.[33] From this I determine that at low temperature (T< 400 °C), as Figure 4.3a shows, the single semicircle at high frequency is attributed to the bulk properties of the sample, and the half semicircle at lower frequency attributed to the electrode impedance. At high temperature (T ≥ 400 °C), as Figure 4.3(b) shows,

the high frequency semicircle corresponding to bulk resistance could no longer be seen, and the resistance was calculated from the intersection with the real axis at high frequency. Impedance spectra in Figure 4.3 fitted in equivalent circuits and fitting parameters are shown in Figure S4.4.

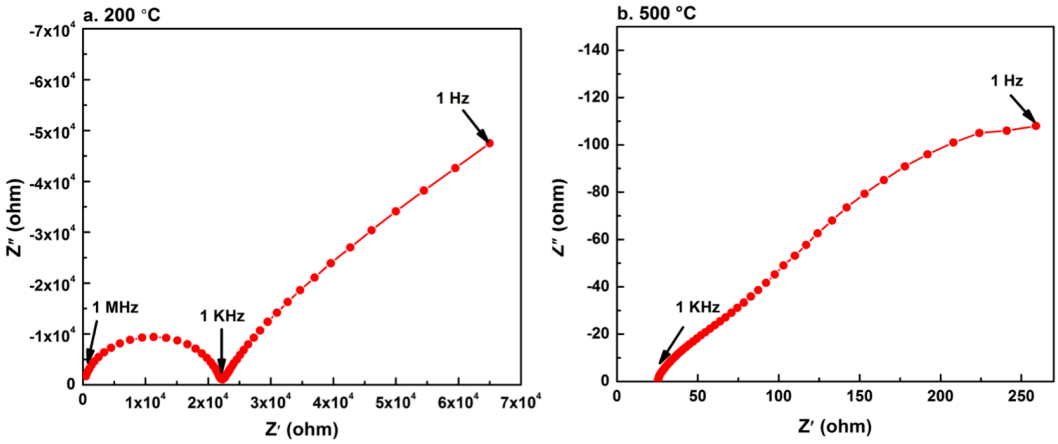

Figure 4.3. Typical impedance spectra (in this case WSB) in air at: (a) 200 °C and (b) 500 °C.

Figure 4.4a shows an Arrhenius plot of the bulk ionic conductivity of doped Bi_2O_3, showing, as expected, an increase in ion-conductivity with temperature. Since oxygen is the only mobile charge carrier in Bi_2O_3, I can reasonably assign the bulk ionic conductivity to oxygen ion conductivity. The conductivities in the region of ignition temperature are shown with more detail in Figure 4.4b. For doped Bi_2O_3, it is found that the slope at high temperature (T ≥ 650 °C) is smaller than at low temperature (T < 650 °C), indicating the activation energy change, due to an order-disorder transition of oxygen lattice in the material.[24,25] Of the δ-Bi_2O_3 samples, ESB and YSB showed the highest oxygen ion conductivity, while WSB shows the lowest, which can be mainly attributed to differences in the oxygen vacancy concentration, $[V_O^{\cdot\cdot}]$ and metal-oxygen bond energy, since other microstructures of doped Bi_2O_3 are

the same. δ-Bi_2O_3 has a defect fluorite-type crystal structure (AX_2) in which 25% of the oxygen sites in the unit cell are vacant.[34] Er^{3+}, Y^{3+} have the same valence as Bi^{3+}, so it is reasonable to assume that ESB and YSB also have ~25% vacant oxygen sites in the unit cell. However, W^{6+} has a higher oxidation state, so WO_3 should correspondingly have ~50% more oxygen than AX_2 in the oxygen sites. Oxygen vacancy concentrations of ESB, WSB, DSB, YSB, DWSB5, DWSB10 and DNSB can thus be estimated based on the percentage of vacant oxygen sites in one unit cell, and the lattice parameter. The calculated oxygen vacancy percentage in one unit cell and $[V_O^{\cdot\cdot}]$ of those doped Bi_2O_3 are shown in Table 4.2. I also notice that the pure β phase Bi_2O_3 has a different conductivity trend compared with δ-Bi_2O_3 samples, with an abrupt conductivity increase between 600 °C to 650 °C, which I attribute to a phase change from β to δ.[35]

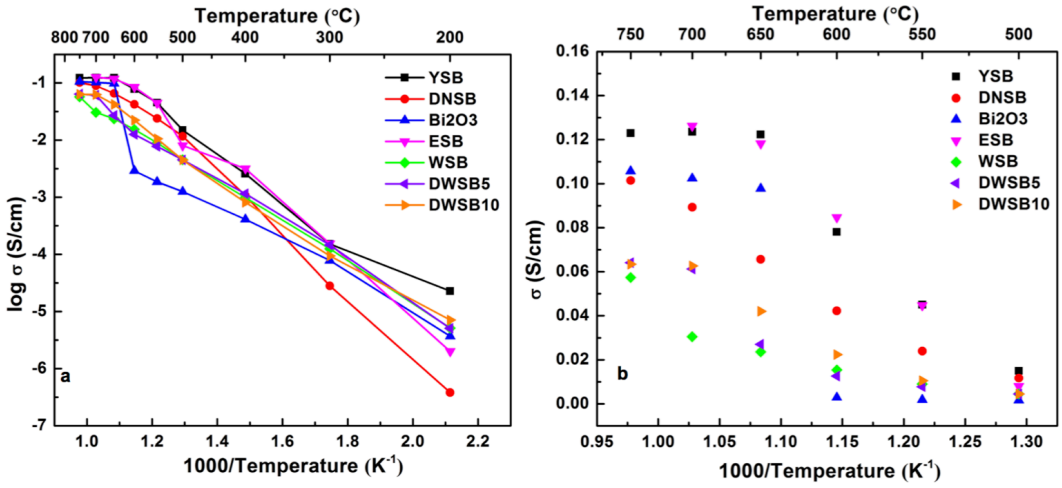

Figure 4.4. (a) Arrhenius plot of measured ion-conductivities for doped Bi_2O_3 and pure Bi_2O_3. (b) Zoomed in measured ion conductivities at 500-750 °C for doped Bi_2O_3 and pure Bi_2O_3.

Table 4.2. Calculated oxygen vacancy percentage in one unit cell and $[V_O^{\cdot\cdot}]$ of doped Bi_2O_3.

Doped Bi_2O_3	Oxygen vacancy %	$[V_O^{\cdot\cdot}]$ (#/cm^3)

ESB	25%	1.2E22
DSB	25%	1.2E22
YSB	25%	1.2E22
DWSB10	21.2%	9.9E21
DNSB	20%	9.6E21
DWSB5	17.5%	8.1E21
WSB	13.7	6.3E21

Ignition and oxygen ion conductivity

The reaction in the Al/Bi_2O_3 formulation is very violent, with an easily discernable visible ignition event. The measurements of ignition temperatures were repeated twice for each formulation and the results are listed in Table S4.2.

Based on the ignition temperature of Al/Bi_2O_3 and the measured conductivities for doped Bi_2O_3, the oxygen ion conductivity at the point of ignition is shown in Figure 4.5a. In Figure 4.5a, I see four data points, corresponding to ESB, DSB, YSB and DNSB, with ignition slightly below the melting temperature of aluminum. These have higher conductivities at the ignition temperature than those that ignite above the melting temperature. The key feature of this plot is that ignition above the aluminum melting point, always occurs at the same oxygen ion conductivity. Noting that ignition temperature is varying, but the oxygen ion conductivity at ignition is constant, even though conductivity is temperature sensitive as seen in Figure 4.4, it may be concluded that there exists a critical oxygen ion conductivity (~0.06 S/cm) that controls the ignition of Al/Bi_2O_3, when other parameters are held constant. WSB has the lowest oxygen ion conductivity, thus it reaches the critical conductivity at a higher temperature, resulting a higher ignition

temperature. Above the melting point, Al is the most mobile species, moving through the alumina shell faster than oxygen transport. Below the melting point it is possible that the reaction interface occurs within the oxide shell as has previously been discussed and requires higher oxygen ion mobility for ignition.

To further investigate the role of molten aluminum core, and the existence of a critical oxygen ion conductivity, I employed carbon as a fuel, which has no surface passivating oxide and no melting phase transition. In contrast to Al/Bi_2O_3, the C/Bi_2O_3 reaction is much less vigorous with no visible emission, thus for determining the point of ignition, temporal CO_2 release was used as shown in Figure 4.6. The onset temperatures of five formulations are listed in Table S4.2. The oxygen ion conductivity as a function of corresponding reaction temperature is shown in Figure 4.5.b. Again I find ignition occurs at an oxygen ion conductivity ~0.065 S/cm, indicating it is dominated by the oxygen ion transport of oxidizer, and the existence of a critical oxygen ion conductivity. It is interesting that C/Bi_2O_3 reaction occurs at a similar temperature as the ignition of Al/Bi_2O_3 as shown in Table S4.2.

Tantalum was also employed as a fuel to further compare with Al/Bi_2O_3 and C/Bi_2O_3. Similar to aluminum, tantalum also has a native oxide shell (Ta_2O_5), but has a very high melting point, with no melting phase transition in the ignition temperature regime. Tantalum is also a high energy density fuel, and the ignition of Ta/Bi_2O_3 was a discernable visible event that was recorded by high-speed camera. Results show that, again, Ta/Bi_2O_3 has similar ignition temperature (Table S4.2) as Al/Bi_2O_3 and a critical oxygen ion conductivity of ~0.065 S/cm shown in Figure 4.5c, indicating ignition is dominated by the oxygen ion transport of the oxidizer.

I note that three different fuels (Al, C and Ta) with very different physical-chemical properties are observed to have essentially equivalent critical oxygen ion conductivity for the ignition of doped Bi_2O_3 oxidized thermites. While this result is surprising, it should be kept in mind that conductivity is a thermally activated process, and thus exponentially dependent on temperature, so that within a range of oxygen ion conductivity ignition occurs. Ignition by its nature is essentially the point where the self-heating by exothermic reaction exceeds heat loss and a non-linear reaction event occurs. Thus the fact that a similar critical condition for initiation is found is perhaps not as surprising upon further reflection. It implies that since the heat loss terms are essentially equivalent for the three different metals that approximately the same flux of oxidizer is need to initiate non-linear heat release regardless of metal type. The different ignition temperatures just reflect when each particular oxidizer can achieve this critical condition.

I also measured the initiation temperatures of Al/β-Bi_2O_3 and C/β-Bi_2O_3. I found again that C/β-Bi_2O_3 reaction starts at a similar temperature as the ignition temperature of Al/β-Bi_2O_3 at ~630 °C, which lies exactly in the regime that oxygen ion conductivity increased abruptly from 0.002S/cm to 0.97S/cm from 600 °C to 650 °C and essentially where the critical conductivity lies.

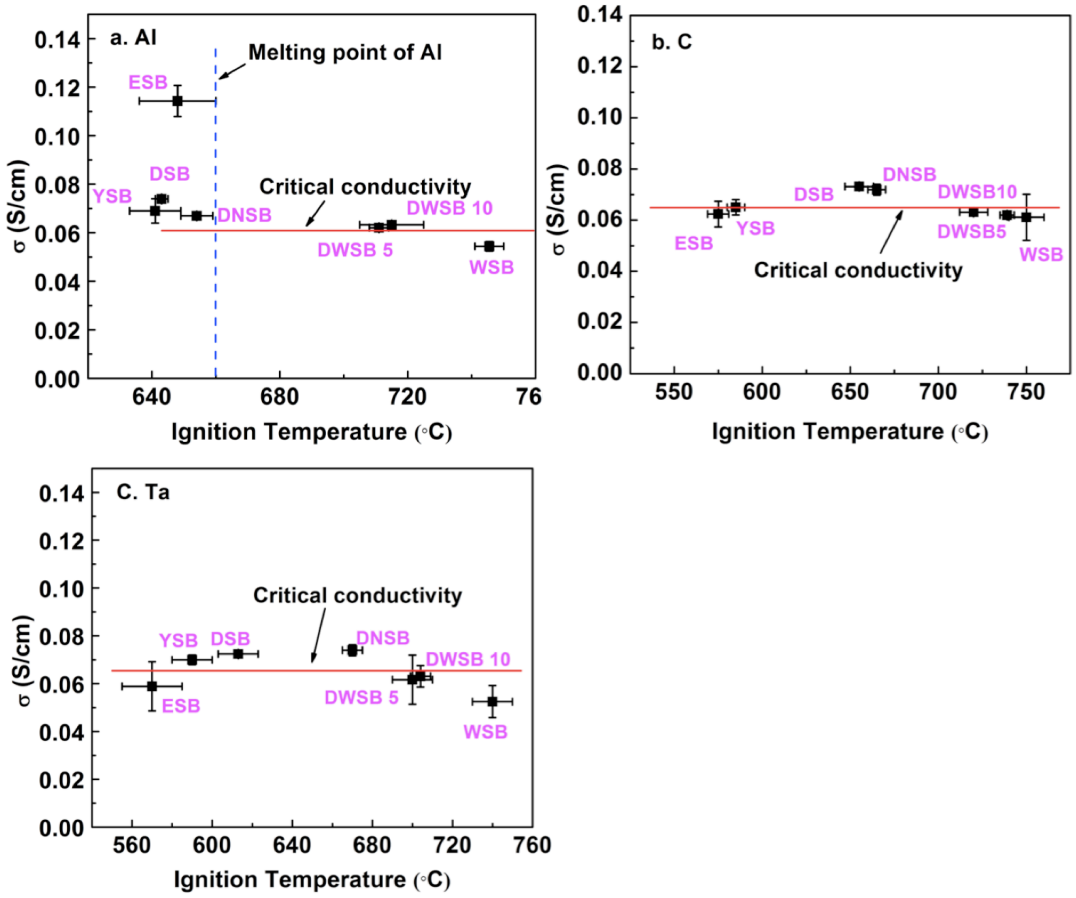

Figure 4.5. Oxygen ion conductivity as a function of corresponding ignition temperature for (a) Al/doped Bi_2O_3, (b) C/doped Bi_2O_3 and (c) Ta/doped Bi_2O_3.

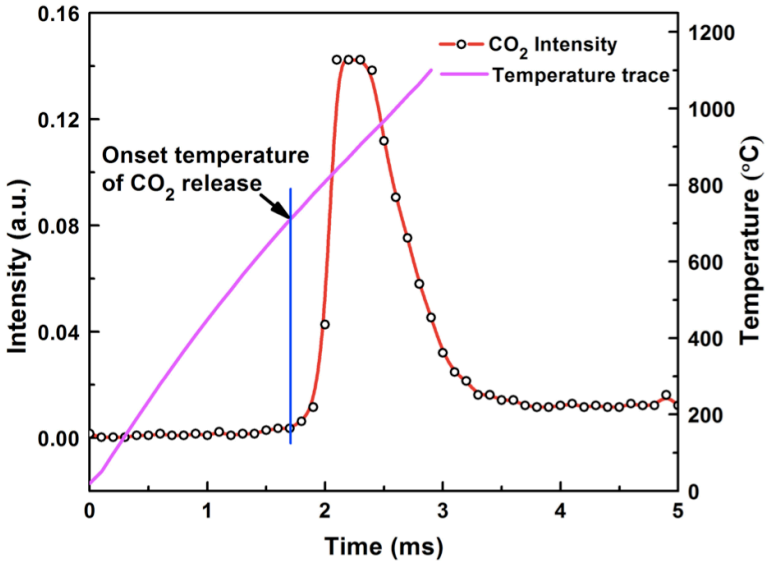

Figure 4.6. Representative T-Jump/TOFMS plot showing the temporal CO_2 release from C/DWSB5.

Effect of oxygen vacancy concentration and bond energy on ignition temperature

Oxygen vacancies and oxygen ion mobility are integral to ion-conductivity based on equation 1, where σ is the conductivity of oxygen ion, Zq is the charge of the ion (O^{2-} in this case), μ is the carrier mechanical mobility, and $[V_O^{\cdot\cdot}]$ is the oxygen vacancy concentration.

$$\sigma = Zq \cdot [V_O^{\cdot\cdot}] \cdot \mu \qquad (1)$$

Previous research has found that μ depends on the activation energy of oxygen ion migration, which can be associated with average metal oxygen bond energy and the critical radius for oxygen ion transportation in the doped Bi_2O_3 lattice.[36] I thus turn my attention to how $[V_O^{\cdot\cdot}]$ and average metal-oxide bond energy affects the ignition temperature as I did in the previous study of perovskites.[15] For fluorite type doped δ-Bi_2O_3 in which that cation is 6-coordinated with oxygen anions, the average metal-oxide bond energy is calculated based on equation 2 where $\Delta H_{A_mO_n}$ is the heat

of formation of A_mO_n at 298 K, ΔH_A is the heat of sublimation of A-metal at 298 K and D_{O_2} is the dissociation energy of gaseous oxygen.[18]

$$\Delta(A-O) = \frac{1}{6m}\left(\Delta H_{A_mO_n} - m\Delta H_A - \frac{n}{2}D_{O_2}\right) \quad (2)$$

Presumably, higher $[V_O^{\cdot\cdot}]$ and lower bond energy should lead to higher oxygen ion conductivity, thus it follows that materials with the high $[V_O^{\cdot\cdot}]$ and low bond energy would have lower ignition temperatures. Figure 4.7 clearly shows that this is indeed the case, as ignition temperature decreases with $[V_O^{\cdot\cdot}]$ (Figure 4.7a) while increasing with bond energy (Figure 4.7b). For instance, in Figure 4.7a, the $[V_O^{\cdot\cdot}]$ of ESB and DSB are the largest, resulting in ESB and DSB having the lowest ignition temperatures. In comparison, W^{6+} has the smallest $[V_O^{\cdot\cdot}]$, resulting in the highest ignition temperature. Boyapati et al [14] found that oxygen ion transport relies on interstitial migration, which is dependent on the occupancy of interstitial sites. W^{6+} has a higher oxidation state, thus WSB has more oxygen ions occupying the interstitial sites, resulting in even lower oxygen ion conductivity. In Figure 4.7b, ESB and DSB have smaller bond energies, resulting in lower temperature. These results imply in a general sense that it may be possible to introduce oxygen vacancies in an oxidizer to achieve high oxygen ion conductivity, and tune ignition behavior.

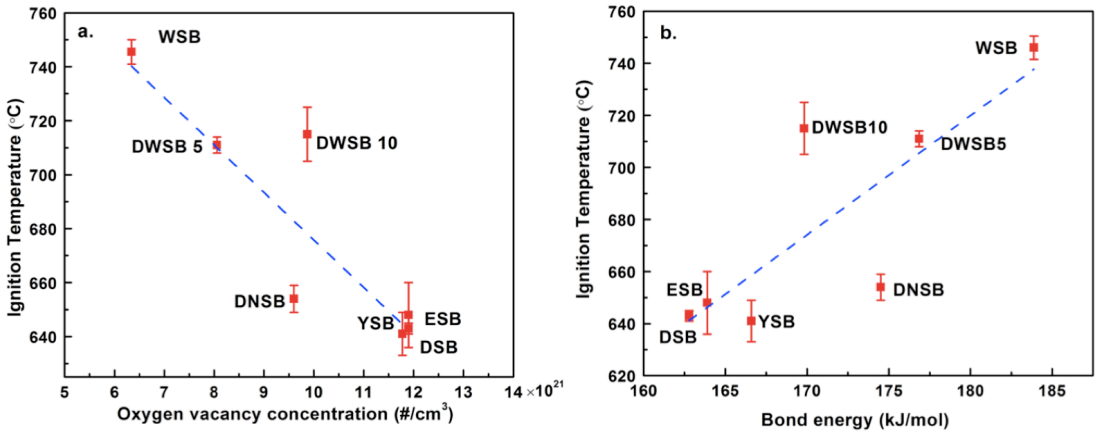

Figure 4.7. The (a) oxygen vacancy concentrations and (b) bond energy vs. their corresponding ignition temperatures of five Al/doped Bi_2O_3 formulations.

Ignition and oxygen ion diffusivity

Oxygen ion's electric mobility is related to mechanical mobility, and in turn through the Nernst-Einstein relation, can be related to diffusivity. Thus from equation 3 the measured conductivity is directly proportional to the diffusivity D, where k is Boltzmann's constant. [37]

$$\sigma = Z^2 q^2 \cdot [V_O^{\cdot\cdot}] \cdot {}^{D}/_{k \cdot T} \qquad (3)$$

I have previously shown the oxygen vacancy concentration in Table 4.2. At the very high heating rates, I can expect that the defect density $[V_O^{\cdot\cdot}]$ is probably relatively constant until the point of ignition. Thus from the measured oxygen ion conductivities at different temperatures shown in Figure 4.4, and known vacancy concentration, I can from equation 3 deduce the oxygen ion diffusivity as a function of temperature, which is presented as an Arrhenius plot in Figure S4.5.

Diffusivity has an exponential temperature dependence nominally expressed by equation 4 [38] where D_0 is temperature-independent pre-exponential, Q_d is the activation energy for diffusion and R is the gas constant.

$$D = D_0 \cdot \exp\left(-\frac{Q_d}{RT}\right) \quad (4)$$

Q_d can be estimated from the slope of the Arrhenius plot of oxygen ion diffusivity (Figure S4.5.) and leads to an activation energy for diffusion between 70~100 kJ/mol. I can also measure the activation energy of ignition using Flynn–Wall–Ozawa isoconversion method [39,40] from equation 5, where β is the heating rate, T is the ignition temperature and E_a is the activation energy for ignition. The ignition temperatures at different heating rates (1.3×10^5 to 5.5×10^5 °C/s) were measured with the T-Jump/TOFMS. Results show that the activation energy for ignition of Al/DWSB 5 is ~ 86±7 kJ/mol (shown in Figure S4.6), which is similar to the activation energy for diffusion, implying that the ignition for condensed phase reaction is consistent with an oxygen ion transport controlled mechanism and consistent with the concept of a critical ion-conductivity for ignition as shown in Figure 4.5.

$$\ln\beta = const. - \frac{1.052E_a}{RT} \quad (5)$$

Based on the ignition temperature, and the Arrhenius plot of diffusivities of doped Bi_2O_3 at different temperature, the diffusivity as a function of corresponding ignition temperature for Al/ Bi_2O_3, C/Bi_2O_3, and Ta/Bi_2O_3 are shown in Figure 4.8.

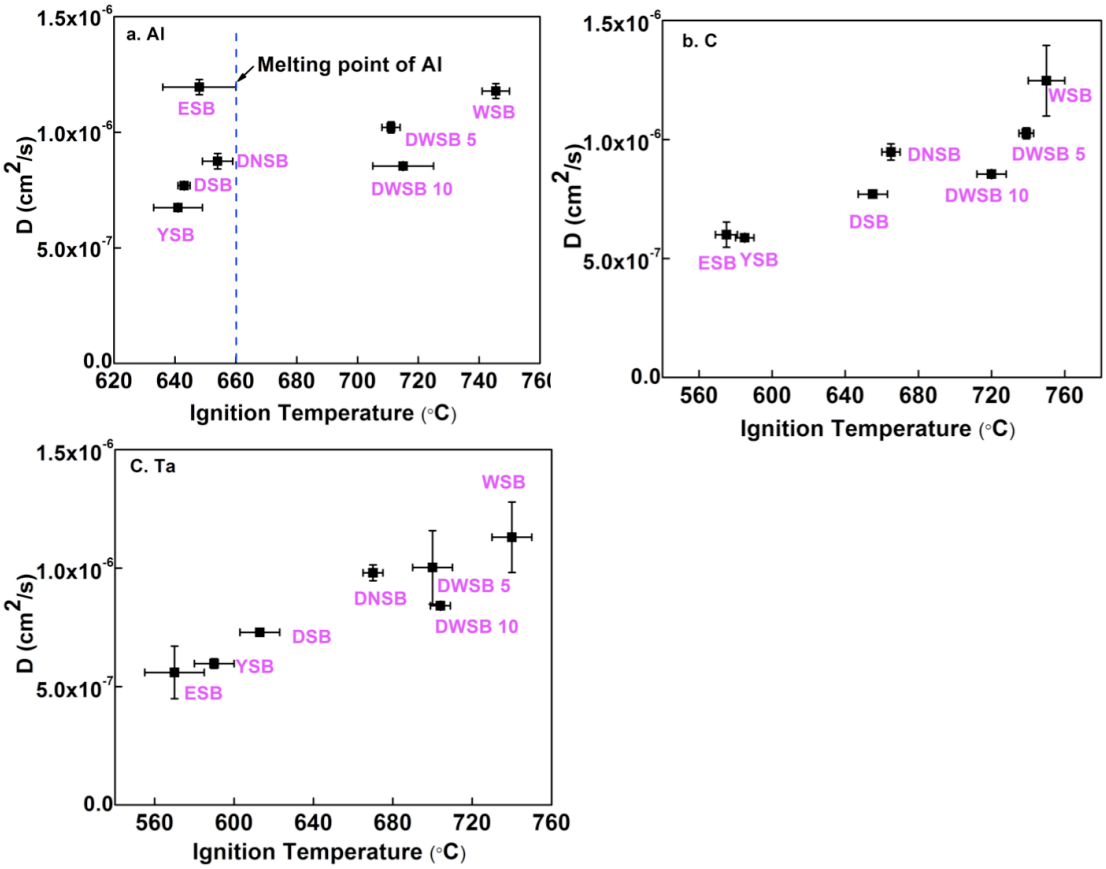

Figure 4.8. Oxygen ion diffusivity as a function of corresponding ignition temperature for (a) Al/doped Bi_2O_3, (b) C/doped Bi_2O_3 and (c) Ta/doped Bi_2O_3.

These results show that there exists a trend that the ignition of doped Bi_2O_3 with aluminum, carbon and tantalum, respectively, increased with oxygen ion diffusivity from ESB to WSB, so long as aluminum is melted. This is mainly a result of decreased $[V_O^{\cdot\cdot}]$ from ESB to WSB shown in Table 4.2. For example, WSB has the lowest $[V_O^{\cdot\cdot}]$, thus in order to reach the critical metric for ignition, the oxygen ion diffusivity of WSB must reach a higher level so as to achieve sufficient oxygen ion flux to initiate ignition.

The characteristic diffusion time, $t = {(0.75r)^2}/{D}$ [38], based on a 100 nm diameter particle and an average diffusivity (~10^{-6} cm^2/s), is ~1.4×10^{-5} s and is quite close to the measured pressure rise time ~1.0×10^{-5} s of Al/Bi_2O_3 obtained in pressure cell measurements (Figure S4.7).[41] This could imply that the initial fast reaction observed in pressure cells is controlled by the diffusion of oxygen from the oxidizer.

We (Zhou et al. [42]) recently reported on a critical reaction rate for Al ignition, which is invariant of ignition temperature and heating rate. Employing a similar method (in supplementary information) to calculate the reaction rate at the ignition point of Al/Bi_2O_3, yields a value of $(1.24\pm0.17)\times10^{-1}$ mol/m^2·s, which is consistent with Zhou et al.'s assumption that reaction rate is roughly constant. The average reaction rate, *R,* of a Bi_2O_3 particle with an Al particle could be estimated based on the burning time, t (~2×10^{-4} s), measured from the optical signal obtained in pressure cell measurements (Figure S4.7) and the dimensions of the Bi_2O_3 particle in equation 6:

$$R = \frac{n_{Bi_2O_3}}{s_{Bi_2O_3} \cdot t} = \frac{\frac{4\pi}{3} r^3 \rho_{Bi_2O_3}}{4\pi r^2 M_{Bi_2O_3} t} \quad (6)$$

Herein, $n_{Bi_2O_3}$ is the number of Bi_2O_3 molecules in a Bi_2O_3 particle, $s_{Bi_2O_3}$ is the surface area of a Bi_2O_3 particle, r is the radius of a Bi_2O_3 particle (~50 nm), $\rho_{Bi_2O_3}$ is the density of Bi_2O_3 (~9.00 g/cm^3), and $M_{Bi_2O_3}$ is the molar mass of Bi_2O_3 (465.96 g/mol). Equation 6 leads to an average reaction rate, *R,* over the whole burning time, of ~ 1.6 mol/m^2·s. This implies that the diffusion controlled ignition rate is about one order of magnitude smaller than the observed average reaction rate, and consistent with a self-accelerating process.

4.4. Conclusion

In this study, I investigated the existence of a correlation between oxygen ion transport in doped Bi_2O_3, and the ignition temperature. By measuring the ionic conductivities as a function of temperature of seven doped Bi_2O_3's with the same crystal structure and morphology, and their corresponding ignition temperatures with three fuels (Al, C, Ta) respectively, I found a critical oxygen ion conductivity exists for Bi_2O_3 oxidized thermite ignition as long as aluminum is molten. The activation energy for ignition of Al/Bi_2O_3 is close to the activation energy of oxygen ion diffusion, which is consistent with an oxygen transport limited rate. Finally I find a correlation between the oxygen vacancy concentration and bond energy vs ignition temperature. The latter suggests that the possibility of manipulating microscopic properties within a crystal can be considered, in order to tune the resultant energetic properties, i.e. in this case ignition temperature.

Acknowledgments

I gratefully acknowledge the support of experimental facility from Dr. Eric Wachsman's group at the University of Maryland's Energy Research Center.

4.5. Supplemental Information

Table S4.1. Log-normal fit parameters of size distribution of DSB and DWSB5, and R^2 is coefficient of determination.

Equation	$y = y_0 + \frac{A}{\sqrt{2\pi}\cdot\sigma x}\cdot \exp\left(-\frac{(lnx-\mu)^2}{2\sigma^2}\right)$		
		Value	Standard Error
DSB	R^2	0.921	
	y_0	0.0265	0.008
	μ	92.8692	2.0649
	σ	0.4491	0.0209
	A	70.7783	2.7297
DWSB5	R^2	0.893	
	y_0	0.0241	0.0083
	μ	98.043	2.566
	σ	0.4563	0.0245
	A	67.4201	3.0005

Table S4.2. Measured T-Jump ignition temperature for Al/Bi_2O_3, C/Bi_2O_3 and Ta/Bi_2O_3.

Metal oxide (MO)	Ignition T for Al/MO (°C)	Ignition for C/MO (°C)	Ignition for Ta/MO (°C)
ESB	648±12	575±6	570±15
DSB	643±2	655±8	613±10
YSB	641±8	585±5	590±10
DWSB10	715±10	720±8	704±5

DWSB5	711±3	739±4	700±10
DNSB	654±5	665±5	670±5
WSB	746±5	750±10	740±10

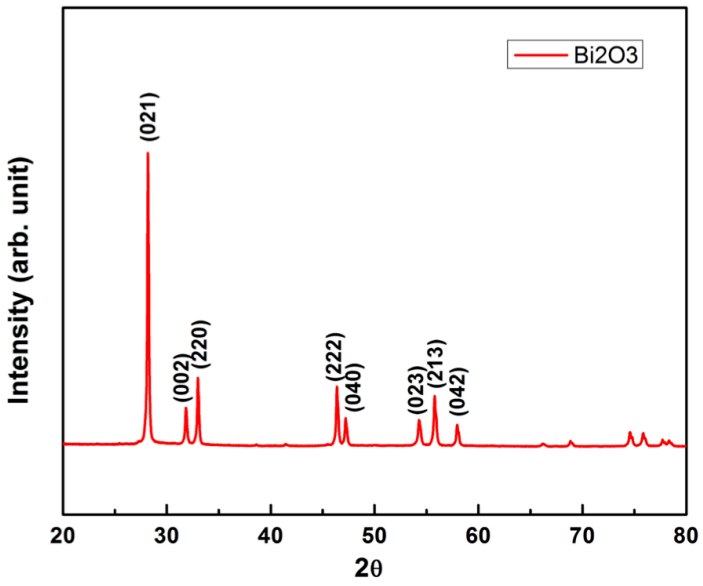

Figure S4.1. XRD pattern of synthesized pure Bi_2O_3

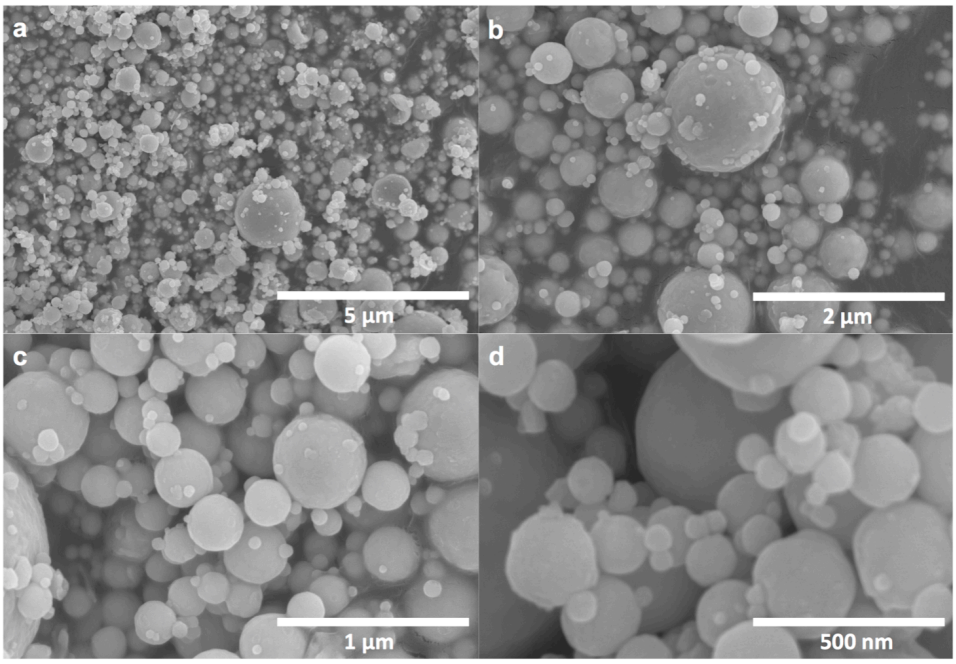

Figure S4.2. SEM images of DSB at various magnitudes: a. 10k, b. 25k, c. 50k, d. 100k.

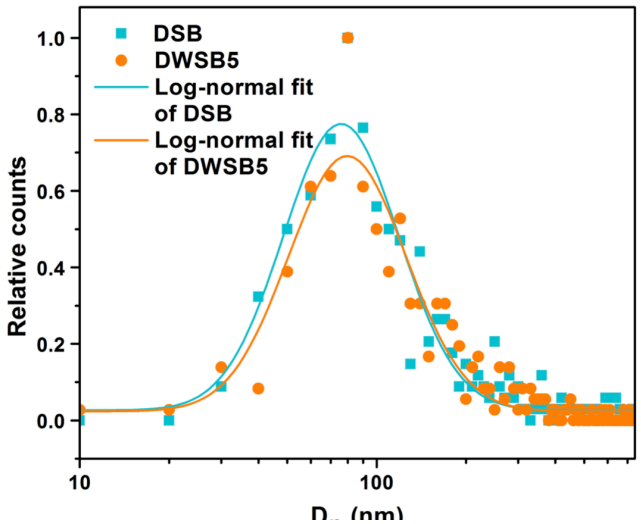

Figure S4.3. Particle size distributions and log-normal fit profiles of representative powers DSB and DWSB5 measured from SEM images, showing essential the same size distribution.

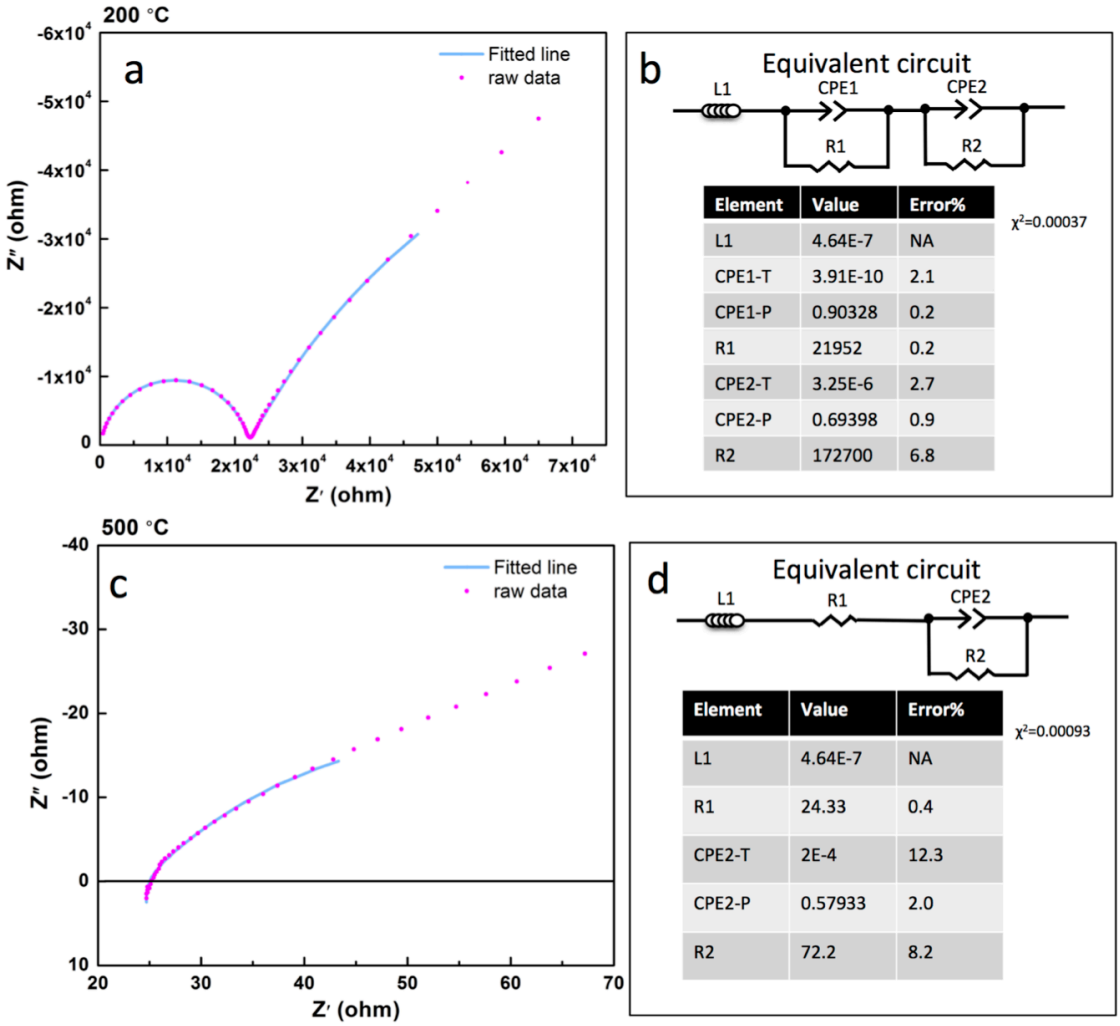

Figure S4.4. (a) Impedance spectra and fitted line for WSB at 200 °C and (b) equivalent circuit and fitting parameters of WSB at 200 °C (c) Impedance spectra and fitted line for WSB at 500 °C and (d) equivalent circuit and fitting parameters of WSB at 500 °C. Fittings were conducted using ZView. In both cases, R1 represents the bulk resistance.

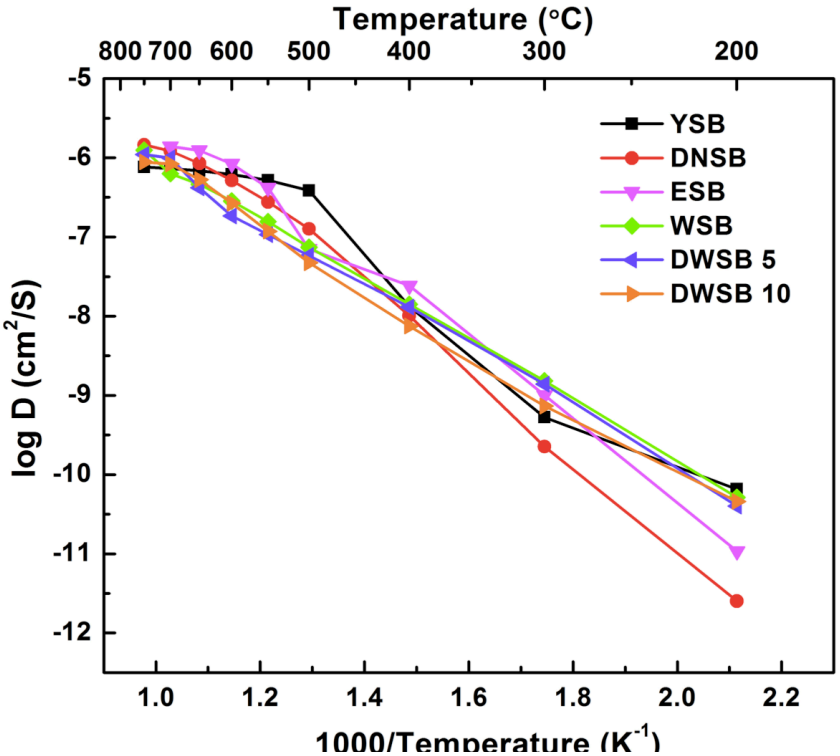

Figure S4.5. Arrhenius plot of diffusivity for doped Bi_2O_3

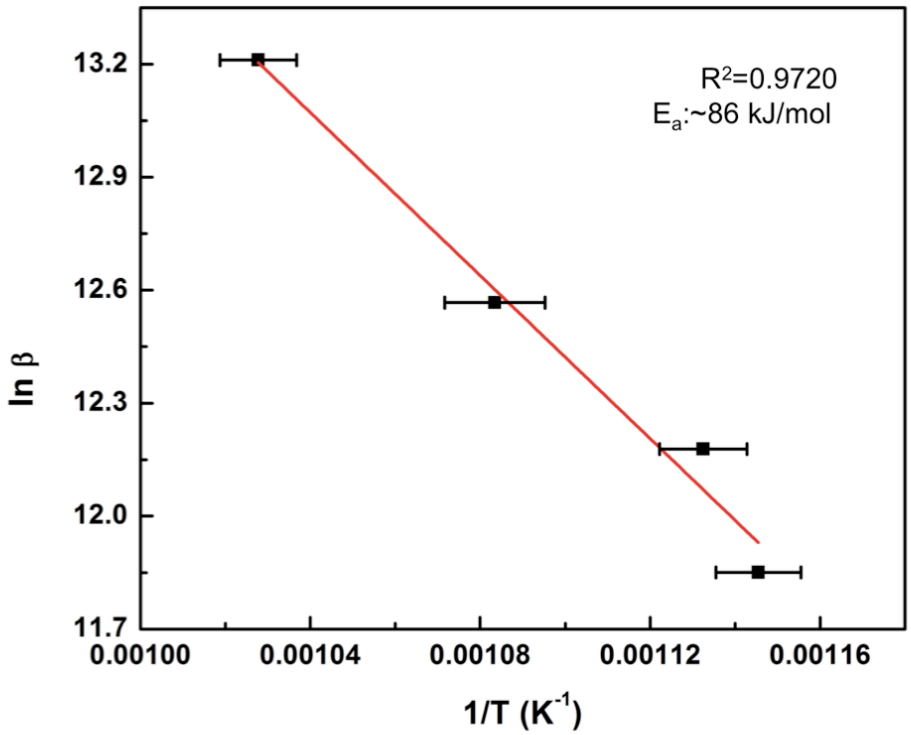

Figure S4.6. Arrhenius plot of heating rate vs ignition temperature of Al/DWSB5.

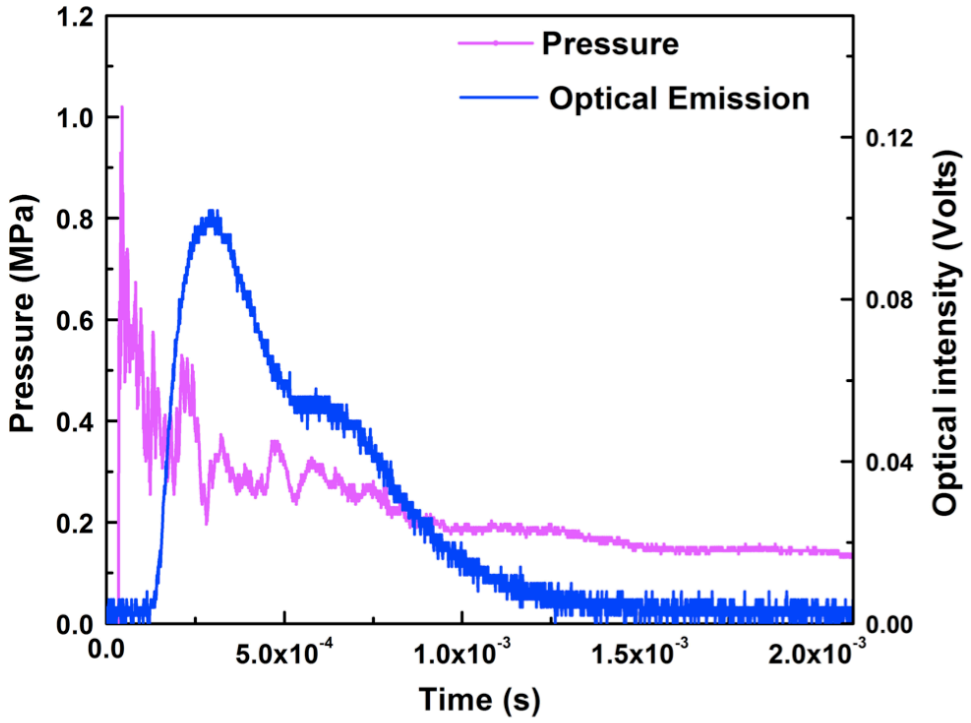

Figure S4.7. Simultaneous optical and Pressure signal for Al/Bi_2O_3.

Calculation of reaction rate[42]

Energy balance equation prior to ignition can be expressed simply as follows:

$$\dot{q}_a\Big|_{T<T_{ig}} = \dot{q}_{gain} + \dot{q}_{c,loss} \quad (1)$$

Herein, $\dot{q}_a$, the accumulated energy of Al coated on wire equals to, $\dot{q}_{c,gain}$, the energy gain from wire by heat conduction subtracted by the heat loss to the surroundings, $\dot{q}_{c,loss}$ At the point of ignition, a rapid excursion in the wire temperature (Figure S4.8) leads to a larger temperature gradient ($\frac{dT}{dt}\Big|_{T>T_{ig}}$). Thus the energy balance when the temperature exceeding the ignition point is:

$$\dot{q}_a\Big|_{T>T_{ig}} = \dot{q}_{gain} + \dot{q}_r + \dot{q}_{c,loss} \quad (2)$$

where $\dot{q}_r$ is the heat generated by thermite reaction. In equation 1 and 2, $\dot{q}_a$ and $\dot{q}_r$ can be expressed as follows:

$$\dot{q}_a = (n_{Al}Cp_{Al} + n_{pt}Cp_{pt})\frac{dT}{dt} \quad (3)$$

$$\dot{q}_r = 4\pi r^2 R\Delta H_r N_{n-Al} \quad (4)$$

Herein, n_{Al} *and* n_{Pt} are the molar amounts of Al and Pt, Cp_{Al} and Cp_{Pt} are the heat capacities of Al and Pt at ignition temperature,[43-44] r is the radius of aluminum particle, N_{n-Al} is the number of nano-Al particles on wire and ΔH_r is the heat of reaction per mole of Al (837.5 kJ/mol)[45]. Since $n_{Al} \ll n_{Pt}$, equation 3 can be simplified as $\dot{q}_a = n_{pt}Cp_{pt}dT/dt$. n_{Pt} can be calculated from the dimension of the platinum wire and the density of platinum (21.45g/cm^3), resulting ~$5.1\times10^{-6}\ mol$. I assume that the sample packing density on the wire is estimated to be 10-20% and the dimension of the sample coated is estimated from SEM[46], thus N_{n-Al} is calculated to be 9.4×10^9.

Ignition is defined where the exothermicity of reaction exceeding the energy dissipation rate. By combining equation 1-4, the reaction rate (R_C) at the ignition temperature can be calculated as a function of the temperature gradient difference prior to and after ignition as follows:

$$R_c = \frac{n_{Pt} Cp_{Pt}}{4\pi r^2 \Delta H_r N_{n-Al}} \left(\left. \frac{dT}{dt} \right|_{T>T_{ig}} - \left. \frac{dT}{dt} \right|_{T<T_{ig}} \right) \quad (5)$$

Considering the uncertainty of temperature-time curve, ignition is defined the point where the extrapolation of the temperature-time curve before ignition deviated by the uncertainty from the temperature-time curve after ignition.

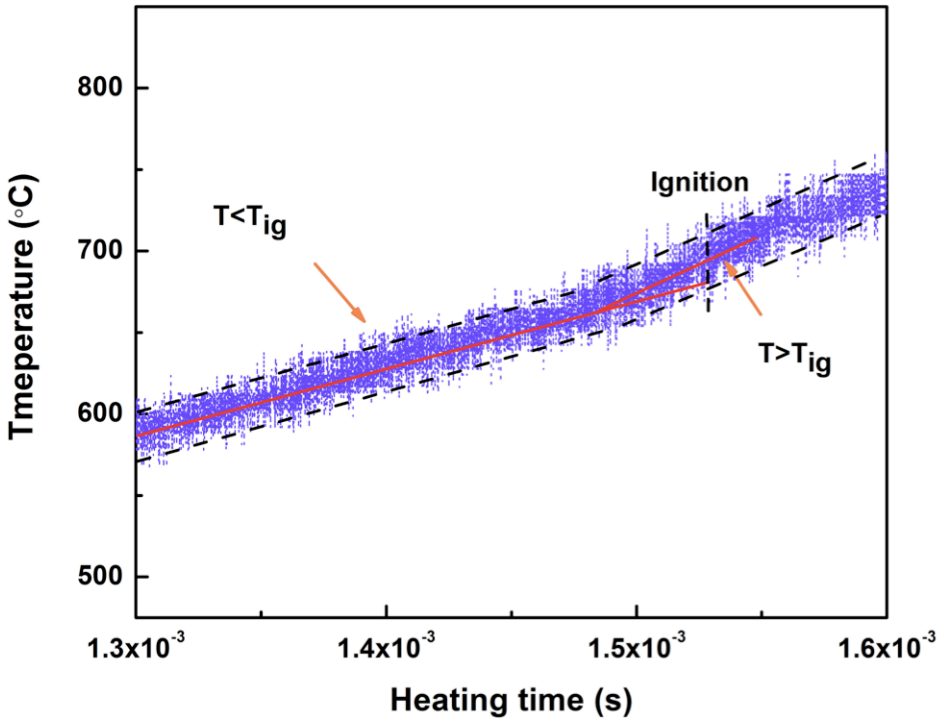

Figure S4.8. Experimental temporal temperature profile for Al/ESB with temperature gradient prior to and after ignition.

Chapter 5: Boron Ignition and Combustion with Doped δ-Bi_2O_3: Bond Energy/Oxygen Vacancy Relationships *

Summary

The purpose of this chapter is to extract a clearer relationship between microscopic properties of the oxidizer, and ignition temperature and combustion kinetics. Pure Bi_2O_3 and a series of Y^{3+} and W^{6+} doped Bi_2O_3 nanoparticles with the same crystal structure and morphology were synthesized via aerosol spray pyrolysis and used as oxidizers in boron-based thermites. This enabled us to vary bond energy and oxygen vacancy concentration systematically. The ignition temperatures and the reactivities of different B/Bi_2O_3 thermites were measured by rapid heating (>10^5 K/s) temperature-jump/time-of-flight mass spectrometer and a confined pressure cell, respectively. With pure Bi_2O_3, the boron could be ignited at a temperature as low as 520 °C. In-situ high heating rate TEM was used to observe the reaction before/after heating. I find very clear relationships that higher oxygen vacancy concentration, and smaller metal-oxygen bond energy lead to lower ignition temperature and higher combustion reactivity.

5.1. Introduction

Significant efforts have been devoted to the understanding and utilization of aluminum-based thermite systems, for pyrotechnics, propellants and explosives applications [1]. However boron is theoretically better due to its higher energy density[1a].

* The results presented in this chapter have been accepted in the following journal article: Wang, X. Z.; Tao, W.; Wang, H.; DeLisio, J. B.; Yang, Y.; Zachariah, M. R., Boron Ignition and Combustion with Doped δ-Bi2O3: Bond Energy/Oxygen Vacancy Relationships. Combust Flame, in press.

Unlike aluminum, which has a low melting point and a high melting point native oxide shell, boron has a high melting point while its oxide, B_2O_3, melts at a low temperature. In particular upon heating, molten B_2O_3 coats the solid boron core and inhibits the further oxidation of boron, which delays ignition and combustion [2], greatly limiting the performance of boron as a fuel. Studies on modifying the surface of boron particles to oxide-free and air-stable boron particles to improve ignition behavior have been investigated.[3] It is generally accepted that the combustion of micron sized boron particles occurs in two stages [4]: the first stage involves removal of the boron oxide shell, followed by a second stage of burning of the boron core.[5] In recent years more efforts have been devoted to the ignition and combustion of nano boron as the reduced length scale offers the potential to significantly reduce the energy release time and enhance the reactivity.[6] Other studies have primarily focused on macroscopic properties, i.e., particles size, crystallization of boron, etc.[7] One issue however that has not been addressed, is what microscopic properties of the solid oxidizer are important to ignition and combustion performance when boron is employed as the fuel.

In a prior work discussed in Chapter 3 using doped perovskites,[8] where crystal structure and morphology were removed as variables, I found a clear correlation between the measured ignition temperature and microscopic properties of the oxidizer, in particular, metal-oxygen bond energy, oxygen vacancy concentration, and electronegativity. However, perovskites have a relatively high metal-oxygen bond energy, which leads to a high ignition temperature and low combustion reactivity.

In Chapter 4, I also found a correlation between oxygen ion conductivity in doped Bi_2O_3 and ignition temperature.[9] The oxygen ion conductivity of Bi_2O_3 is very sensitive to crystal structure, which is also highly temperature dependent: δ-Bi_2O_3 which has the highest conductivity is only stable between 730 °C, up to its melting point at 824 °C. Below 730 °C tetragonal β-Bi_2O_3 (at 650 °C) or the bcc γ-Bi_2O_3 (at 639 °C) is stable, and below about 500 °C the monoclinic α-Bi_2O_3 phase is most stable.[10] Among all the phases, cubic δ-Bi_2O_3 has the highest oxygen ion conductivity.[11] In order to stabilize δ-Bi_2O_3 at room temperature, several studies have reported employing metal ion doping at bismuth sites.[12] In Chapter 4, 15% Er^{3+}, Dy^{3+}, Y^{3+}, W^{6+} and Nb^{5+} were employed to stabilize δ-Bi_2O_3. Since δ-Bi_2O_3 has a defect fluorite-type crystal structure (AX_2), 25% of the oxygen sites in the unit cell are vacant,[13] thus with Y^{3+} substitution which has the same valence as Bi^{3+}, I expect the vacancy concentration to remain unchanged. However, W^{6+} has a higher oxidation state, so its substitution (i.e. WO_3) should correspondingly have ~50% more oxygen than AX_2 in the oxygen sites.

In this study I employ doped Bi_2O_3, synthesized via aerosol spray pyrolysis to enable systematic changes to the metal-oxygen bond energy, and oxygen concentrations. Key to this study is to make these changes while maintaining the same crystal structure, particle morphology and size. The ignition and combustion behavior were measured and analyzed by temperature-jump/time-of-flight mass spectrometer, and a constant-volume pressure cell. In-situ high heating rate transmission electron microscope was used to investigate the B/Bi_2O_3 reaction. The results show that larger oxygen vacancy concentration and smaller metal-oxygen

bond energy leads to lower ignition temperature, higher combustion reactivity with higher peak pressure, larger pressurization rate and shorter burn time.

5.2. Experimental Details

Materials

Boron particles (SB99, ~60 nm) were obtained from the SB Boron Corporation. $Bi(NO_3)_3 \cdot 5H_2O$ (≥98% pure) and $Y(NO_3)_3 \cdot 6H_2O$ (99.8% pure) were purchased from Sigma-Aldrich. $(NH_4)_6W_{12}O_{39} \cdot xH_2O$ was purchased from Alfa Aesar.

Synthesis of pure and doped Bi_2O_3.

Doped Bi_2O_3 listed in Table 5.1. and Pure Bi_2O_3 were synthesized.

Table 5.1. Aerosol spray synthesized doped Bi_2O_3.

Doped Bi2O3 formula	Abbreviation
$(Y_{0.1}Bi_{0.9})_2O_3$	YSB10
$(Y_{0.15}Bi_{0.85})_2O_3$	YSB15
$(Y_{0.3}Bi_{0.7})_2O_3$	YSB30
$(Y_{0.4}Bi_{0.6})_2O_3$	YSB40
$(W_{0.05}Bi_{0.95})_2O_{3.15}$	WSB5
$(W_{0.1}Bi_{0.9})_2O_{3.3}$	WSB10
$(W_{0.15}Bi_{0.85})_2O_{3.45}$	WSB15
$(W_{0.2}Bi_{0.8})_2O_{3.6}$	WSB20

All Bi_2O_3 particles were synthesized via aerosol spray pyrolysis [14] at 750 °C with a residence time of about 1 s from metal nitrate contained aqueous solutions formulated with the desired metal ratios. Nitric acid solution (2 mol/L) was used to dissolve $Bi(NO_3)_3 \cdot 5H_2O$ and deionized water was used to dissolve the other metal nitrates. For example, in order to synthesize $(Y_{0.15}Bi_{0.85})_2O_3$, a 0.2 mol/L precursor

solution, containing stoichiometric $Bi(NO_3)_3$ and $Y(NO_3)_3$ was atomized by a nebulizer to generate nominally 1 μm droplets with compressed air. The atomized droplets passed through a diffusion dryer, where most of the water was evaporated and then passed to a tubular furnace to produce the desired doped Bi_2O_3 particles. The final product was collected on a Millipore membrane with a pore size of 0.4 micron.

Synthesis of B/Bi_2O_3 thermites

Stoichiometric mixtures of SB99 boron particles and Bi_2O_3 were mixed and then sonicated in hexane for 30 min. While calculating the stoichiometry, the B_2O_3 shell (~30% of the mass) was considered. For the pressure cell test, thermites in hexane were dried in a hood overnight for hexane to evaporate.

Materials Characterization

The crystal structures of the synthesized Bi_2O_3 were characterized by X-ray diffraction (XRD) performed on a Bruker D8 diffractometer with Cu Kα radiation. Rietveld refinement of all diffraction patterns was performed with the TOPAS 4.2 software.[15] The morphologies of the Bi_2O_3 were measured by scanning electron microscopy (SEM) conducted on a Hitachi SU-70 instrument. Size distributions were obtained by measuring 300 individual nanoparticles statistically from SEM images of each sample, using Nano Measurer 1.2 image analysis software. The morphology of boron nano particles was measured by transmission electron microscope (TEM) with a JEM 2100 instrument and the elemental composition was measured by TEM equipped electron energy loss spectroscopy (EELS).

In-situ high heating rate TEM

The morphology changes of B/Bi_2O_3 were explored using Protochips rapid heating stages (Protochips, Inc) within a TEM with a JEM 2100 instrument.[16] This stage provides rapid heating of the sample within the TEM, from room temperature to a maximum of 1200 °C, with tunable heating rate as high as 10^6 °C/s. B/Bi_2O_3 sample was first heated to 480 °C at a rate of 4×10^5 °C/s and then hold at constant temperature for 10 ms. TEM images were taken prior to and after rapid heating. The same procedures were repeated to heat the sample to 500, 520 and up to 825 °C in steps of ~ 20 °C and images were taken after each heating step. Elemental composition was measured by TEM equipped with energy dispersive x-ray spectroscopy (EDS).

Ignition temperature measurement of thermites

Ignition temperature was measured in a temperature-jump/time-of-flight mass spectrometer (T-Jump/TOFMS) using direct optical emission with a high-speed camera (Vision Research Phantom v12.0) operating at 67056 frames/s.[17] A hexane suspension of sample was coated onto a 70 μm diameter platinum filament, and allowed to air dry. The platinum wire can be joule heated at a rapid rate ~ 4×10^5 °C/s, to ~1200 °C within 3 milliseconds. The filament was directly inserted into the ionization region of a TOFMS, where the gaseous products could be temporally analyzed. The temperature of the wire was determined from electric resistance based on the Callendar-Van Dusen equation, through a simultaneously measure of temporal applied voltage and current. Due to the size of nanoparticles compared with the wire,

and based on the previous result, the temperature of the wire is essentially equal to the temperature of the oxidizer system.[18] The ionization/extraction region of the TOFMS was pulsed at 10 kHz resulting in a full mass spectrum every 100 μs. A 600 MHz digital oscilloscope was used for data acquisition with a sampling rate of 100 megasamples/second.

Pressure cell measurement.

Pressure and optical signal from thermite combustion were measured by a home-built pressure cell.[19] Briefly, a fixed mass of dry and loose thermite particles (25 mg) were placed on a small chip loaded into a fixed volume pressure cell (13 cm^3). A charged nichrome coil was used to ignite thermite by joule heating. Pressure was recorded by an attached piezoelectric pressure sensor, an in-line charge amplifier and signal conditioner. The optical signal was recorded simultaneously by a fiber optical sensor, containing a planoconvex lens (f=50 mm) and a high-speed photo detector.

5.3. Results and Discussion

Structure and morphology

Figure 5.1 shows XRD patterns for YSB and WSB. Based on Rietveld refinements, all the synthesized doped Bi_2O_3 were δ-Bi_2O_3 with a single cubic phase in Fm-3m space group and the lattice parameters are listed in Table S1.This is important as I want to eliminate crystal structure as a potentially confounding variable in ignition and combustion behavior. Figure S4.1 shows the XRD pattern of synthesized pure Bi_2O_3, as β-Bi_2O_3 with a tetragonal structure.

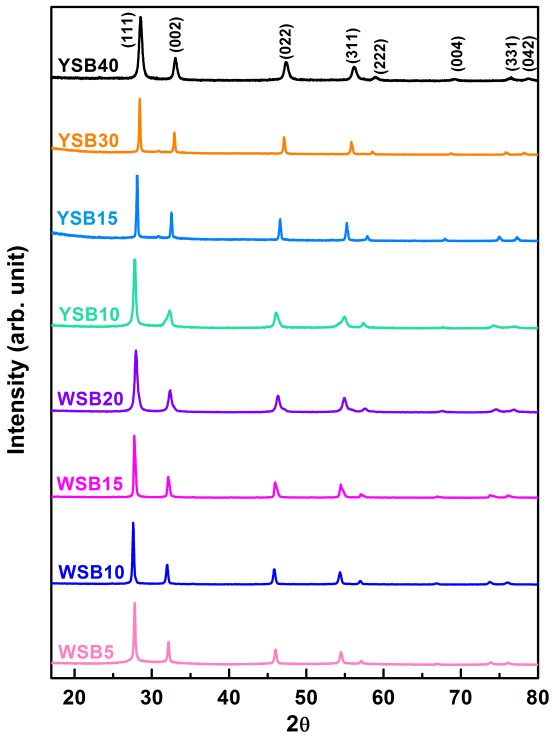

Figure 5.1. X-ray diffraction patterns of aerosol spray synthesized doped Bi_2O_3 showing that all doped Bi_2O_3 have the same cubic phase in Fm-3m space group.

Figure 5.2a and 5.2b shows SEM images of YSB30 and WSB20 as representative powders, indicating similar particle morphology and size distribution, consistent with the previous results.[8-9] Particle size distributions should be log-normally distributed corresponding to the original spray size distribution. Particle size distributions should be log-normally distributed corresponding to the original spray size distribution and are shown in Figure 5.2c along with the log-normal fits of representative powders. The log-normal fit parameters are listed in Table S5.2, and indicate the synthesized doped Bi_2O_3 have similar narrow size distribution with $\sigma = 0.283 \pm 0.013$, and an average diameter of 90~100 nm. The key point is that I can eliminate particle size and morphology as variables in ignition and combustion.

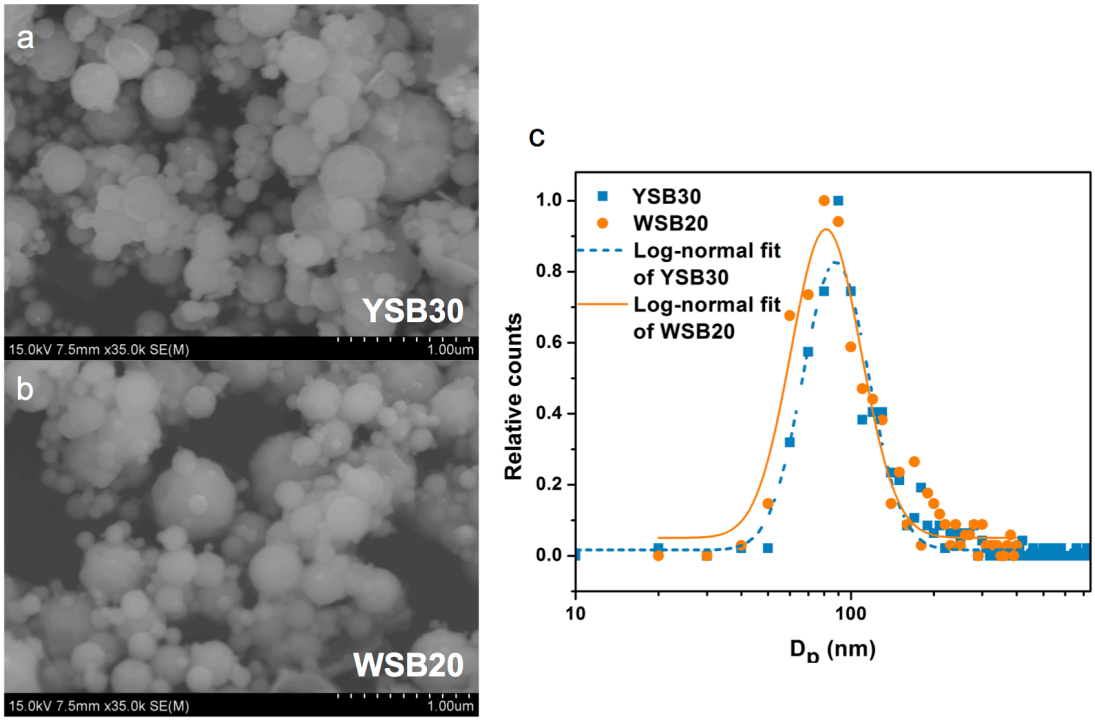

Figure 5.2. SEM images of a. YSB30 and b. WSB20 particles; c, particle size distributions and log-normal fit profiles of YSB30 and WSB20 with $\sigma = 0.283 \pm 0.013$.

Ignition properties of B/undoped Bi_2O_3

T-Jump/TOFMS

T-Jump/TOFMS measurements were employed to study boron based thermite ignition at a heating rate of ~ 4×10^5 °C/s. Figure 5.3a shows the mass spectra of decomposition products of pure Bi_2O_3, decomposed at ~ 870 °C (2.2 ms) with major peaks at m/z 209 (Bi^+), 104.5 (Bi^{2+}) and 32 (O_2^+). The peak at m/z 30 probably belongs to NO^+, due to the incompletely decomposed nitrogen-containing impurities from the precursor and was common to all samples. When mixed stoichiometrically with boron, a violent reaction was initiated as seen in the frames from a high-speed camera as shown in Figure 5.4. Based on the video, the ignition occurred at ~520 °C (0.892 ms) and the combustion event is short, ~ 0.3 ms (from 0.892 ms to 1.190 ms).

Figure 5.3b shows the corresponding B/Bi_2O_3 mass spectra whose major products include m/z 43 (BO_2^+), 44 ($HOBO^+$), 70 ($B_2O_3^+$), 104.5 (Bi^{2+}) and 209 (Bi^+), minor products of 11(B^+), 27 (BO^+), and again NO^+ impurities. B^+ and BO^+ and BO_2^+ may be occurring from electron impact fragmentation of $B_2O_3^+$. To rule out the possibility that $B_2O_3^+$ was coming from the evaporation of the B_2O_3 shell, mass spectra of pure B are shown in Figure S5.1 with no existence of any B-containing products listed above, indicating BO^+, BO_2^+, $HOBO^+$ and $B_2O_3^+$ are the products of reaction between B and Bi_2O_3. From T-Jump/TOFMS I found no gaseous oxygen released prior to ignition, and thus conclude that the ignition of B/Bi_2O_3 is a condensed phase reaction. Yeh and Kuo[7b] reported the main ignition product of boron particles in gaseous oxygen include HOBO and BO_2, while Ao et al [20] reported the primary combustion product of boron contained propellant is B_2O_3. These contradictions revealed that the combustion products were affected by many factors such as the ambient temperature, pressure, reaction atmosphere, and the physical and chemical properties of boron particles. The results from T-Jump/TOFMS show that the main species released from B/Bi_2O_3 were HOBO, B_2O_3, BO_2 and BO, shown in Figure 5.3.

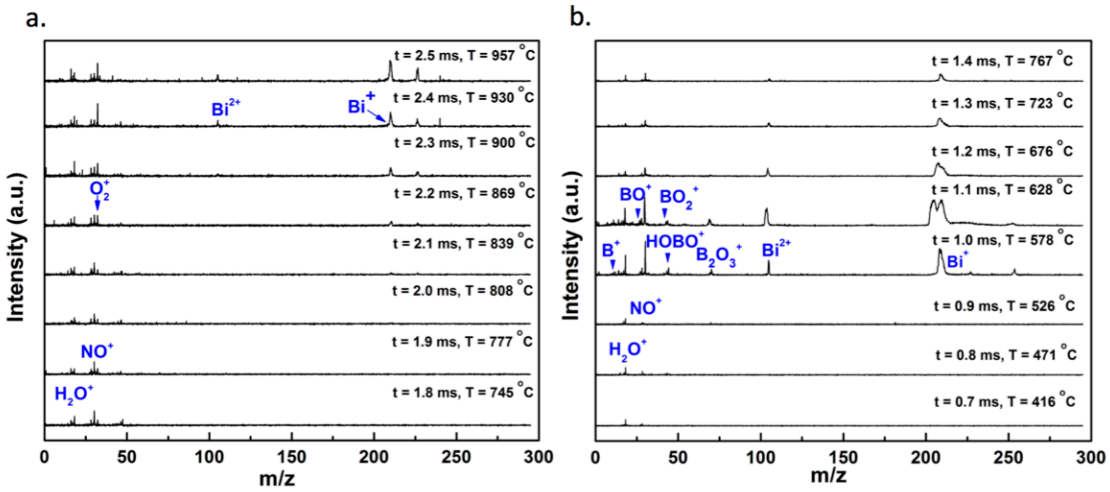

Figure 5.3. Mass spectra for (a) Bi_2O_3 and (b) B/Bi_2O_3. Each spectrum is separated in time by 100 μs.

Figure 5.5 shows the HOBO, B_2O_3, BO and BO_2 release from B/Bi_2O_3, occurred within ~ 0.3 ms (from ~ 0.9 ms to 1.2 ms) and peaked between 1.0 and 1.1 ms and is consistent with the visual optical event time from the high speed camera (0.3 ms) with the maximum brightness at ~ 1.05 ms shown in Figure 5.4.

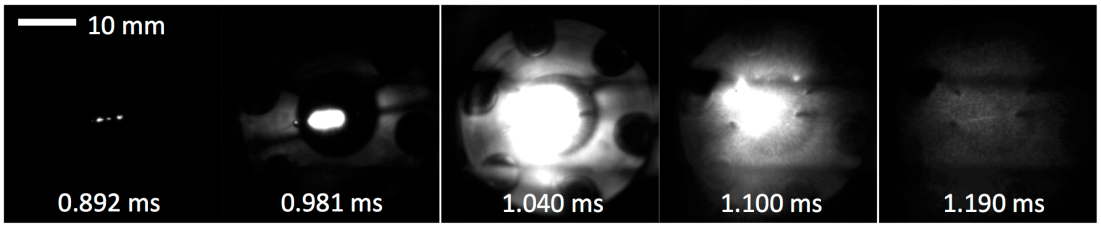

Figure 5.4. High speed images of B/Bi_2O_3 during heating in T-Jump/TOFMS (scale bar applies for all images).

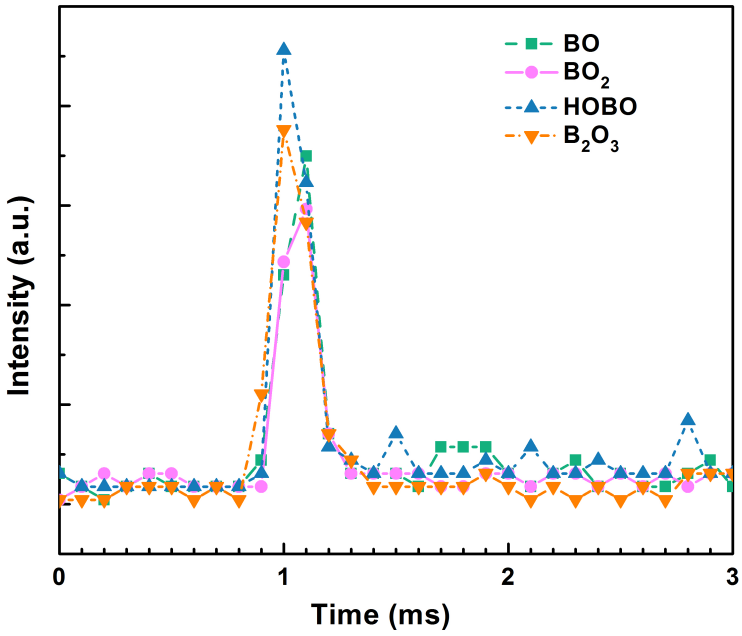

Figure 5.5. BO, HOBO and B_2O_3 intensity released from B/Bi_2O_3 T-Jump/MS.

It was surprising of the low ignition temperature of B/Bi_2O_3 (~520 °C), compared with the reported ignition temperatures of boron particles varying in the range of 1100-1700 °C [21] and the ignition temperature of Al/Bi_2O_3 (~630 °C by Piekiel et al.[22]). TEM and EELS analysis of boron particles show that the boron nanoparticle has a B_2O_3 shell with a thickness of ~ 2 nm (Figure S5.2). As stated above, although boron has a high melting point core (~ 2076 °C), its oxide, B_2O_3 shell, melts at a low temperature (~ 450 °C). In addition, Bi_2O_3 also has a relatively low melting point (~ 817 °C) compared with other common metal oxides. I have already justified that the ignition of B/Bi_2O_3 is a condensed phase reaction, dominated by solid-state diffusion.[9] Since the ignition temperature of B/Bi_2O_3 is above the melting point of the B_2O_3 shell, suggests the possibility that molten B_2O_3 wetting Bi_2O_3 may play a role in ignition. To understand why B/Bi_2O_3 ignites at such a low temperature, *in-situ* high heating rate TEM was employed to explore the morphology change of B/Bi_2O_3 thermites.

In-situ TEM Rapid Heating

Figure 5.6a and 5.6b show before and after heating images, and EDS for the thermite heated at 4×10^5 °C/s to 825 °C/s and held for 10 ms. Prior to heating, Fig. 6a, shows (from EDS) that the dark spherical particles are Bi_2O_3 while the light aggregates are boron. After rapid *in-situ* heating, I see in Figure 5.6b, that a large oval Bi particle was formed (indicated by the arrow). This is confirmed by the EDS line scan analysis across this particle which showed increased Bi but not O. With the boron core having a high melting temperature, the boron oxidation reaction must be strongly dependent on the diffusion of oxygen through the B_2O_3 shell. This can be seen by comparing the dotted circled region in the inserts of Figure 5.6a, b. In Figure 5.6a, I observe that the interface between B and Bi_2O_3 is sharp. However, in the same area, after rapid heating, shown in the inset in Figure 6b, the region becomes highly diffuse without any discernable particle boundaries. I attribute this to the low melting points of B_2O_3 shell and Bi_2O_3. The Tammann temperature ($T_{Tammann} = 0.5T_{melting}$) describes the temperature, referenced to the melting point, at which atoms from the bulk exhibit appreciable mobility.[23] Given that the melting temperature of B_2O_3 is above the Tammann temperature of Bi_2O_3, I propose that molten B_2O_3 wets Bi_2O_3 creating an interface so that high mobility condensed phase oxygen ions can diffuse through the liquid B_2O_3 shell. Comparing Figure 5.6a and 5.6b, I find reaction between B and Bi_2O_3 occurs only where they are physically in contact since there is no changes observed for separated B or Bi_2O_3 particles. To better learn how the

reaction was initiated, I stepwise increased the temperature in step of 10 or 20 °C from 480 °C to 825 °C to capture morphology changes.

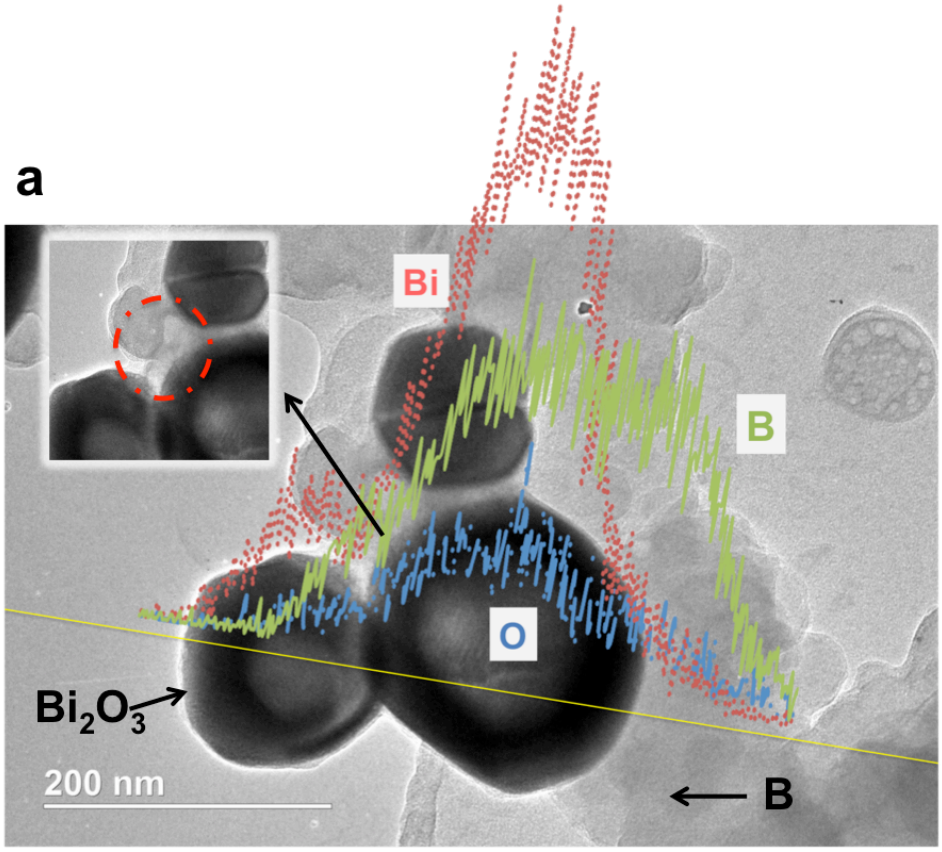
a
Bi
B
O
Bi_2O_3
200 nm
B

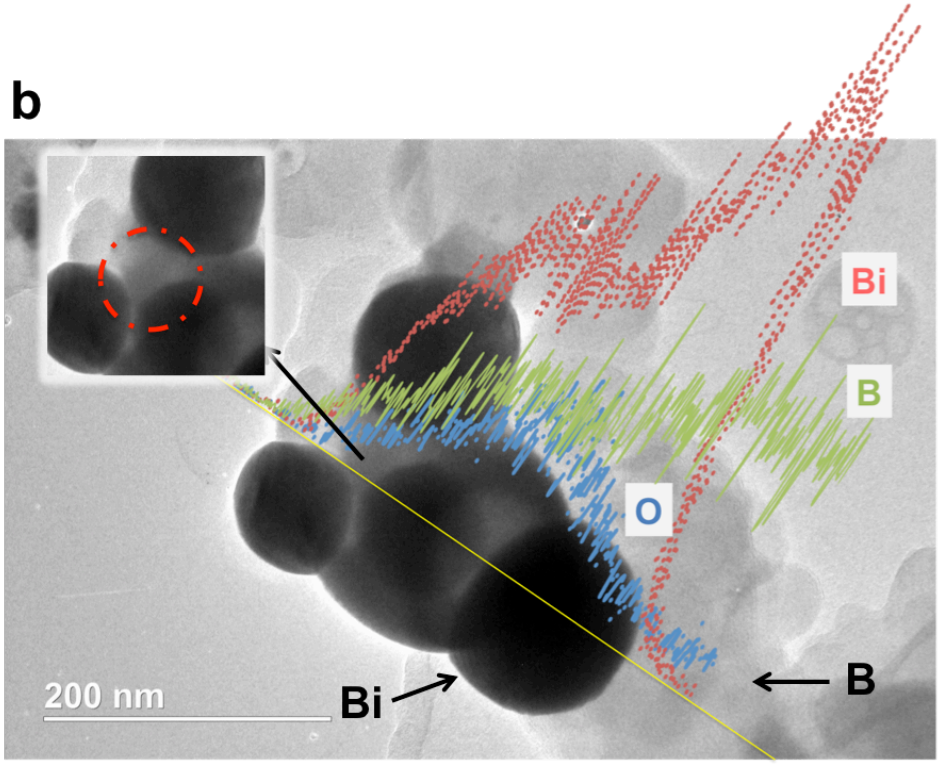
b
Bi
B
O
200 nm
Bi
B

Figure 5.6. TEM images and elemental line scan of (a) B/Bi_2O_3 particles prior to *in-situ* heating. (b) Product of B/Bi_2O_3 particles in panel after *in-situ* heating at 4×10^5 °C/s to 825 °C/s for 10 ms (dot lines represent Bi, solid lines represent B and dash dot lines represent oxygen).

Continuous TEM images after each heating step of the thermite reaction can be found in Figure S5.3. It is obvious that throughout the whole heating process, boron particles were inert, without any obvious morphology changes due to its high melting point. With the limitation of resolution, I was not able to see the B_2O_3 shell. The volume of Bi_2O_3 particles increased as the temperature approached melting point (~ 817 °C) and eventually as seen in the last frame (825 °C), burst. Nevertheless reaction only occurred in the area where B and Bi_2O_3 were in contact. After heating to above 530 °C, some areas where B and Bi_2O_3 are in contact had obvious morphology changes and reaction is believed to occur with the formation of new particles (labeled in video). It is likely then that the low ignition temperature can be attributed to molten B_2O_3 wetting Bi_2O_3 creating access where high mobility solid-state oxygen can diffuse through the liquid B_2O_3 shell. This is in contrast to aluminum, where aluminum ions diffuse through a solid oxide shell, and thus requires that the core be somewhat mobile, which is why for almost all systems, the low temperature limit to aluminum ignition is near its melting point.[24]

Ignition temperature: bond energy & oxygen vacancy considerations

Previous studies on aluminum-based thermites employed a series of doped perovskites, and doped Bi_2O_3 with the aim of systematically varying metal-oxygen bond energy, and oxygen vacancy concentration. In those works I was able to see that the oxygen ion transport is a metric for thermite ignition and there exists a linear

relationship, that lower metal-oxygen bond energies and larger oxygen vacancy concentrations lead to lower ignition temperature.

To see if the same behavior could be observed in another fuel, boron with seven doped bismuth oxides, which share the same crystal structure and particle morphology and size distribution, were mixed. Based on the lattice parameter and the fluorite structure of δ-Bi_2O_3, the estimated oxygen vacancy ratio in the unit cell and oxygen vacancy concentrations are listed in Table 2. As discussed in the previous work, I calculated the metal-oxygen (M-O) bond energy of these synthesized doped Bi_2O_3 based on equation 1, where A stands for Bi, A' is the dopant metal and a is the dopant molar ratio. $\Delta(A-O)$ is calculated by equation 2, where $\Delta H_{A_mO_n}$ is the heat of formation of A_mO_n at 298 K, ΔH_A is the heat of sublimation of A-metal at 298 K and D_{O_2} is the dissociation energy of gaseous oxygen and the calculated results are listed in Table 2. [25]

Thus doping with Y^{3+} or W^{6+} should increase bond energy. The higher the dopant ratio, the higher the metal-oxygen bond energy, and the more difficult should be oxygen ion migration.

$$\text{M}-\text{O bond energy} = (1-a)\cdot\Delta(A-O) + a\cdot\Delta(A'-O) \quad (1)$$

$$\Delta(A-O) = \frac{1}{6m}\left(\Delta H_{A_mO_n} - m\Delta H_A - \frac{n}{2}D_{O_2}\right) \quad (2)$$

Figure 5.7 shows the relationship between the calculated metal-oxygen bond energy of doped Bi_2O_3, and the measured ignition temperature of B/doped Bi_2O_3. There is a clear trend that M-O bond energy is proportional to the resultant ignition temperature. This is a gratifying result in that it is a second fuel confirming a result I previously observed with aluminum, and confirms that the likelihood that this is a

general result. Additionally, while bond energy dominates ignition temperature, exceptions were found, for example, YSB10 has higher metal-oxygen bond energy than WSB5, but has a lower ignition temperature. Presumably this is reflective of the importance of higher oxygen vacancy concentration. Thus I observe that smaller metal–oxygen bond energy and higher vacancy concentration lead to lower ignition temperature.

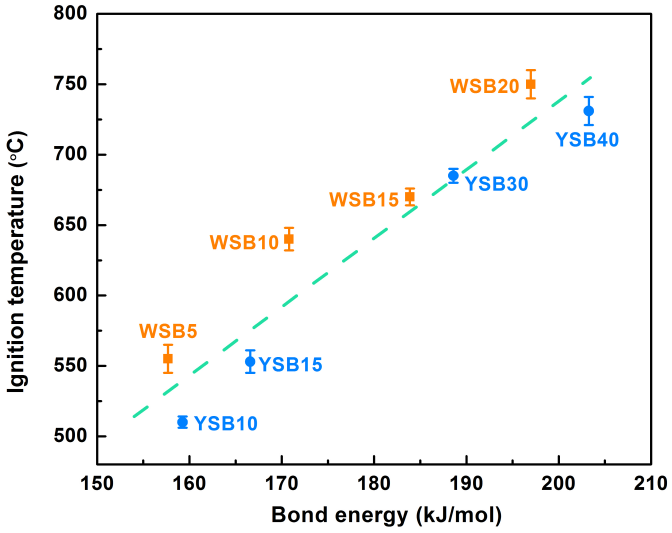

Figure 5.7. Observed relationship between metal-oxygen bond energy of doped Bi_2O_3 versus the ignition temperatures of B/ Bi_2O_3.

Combustion: bond energy and oxygen vacancy effects

It can be divided the synthesized doped Bi_2O_3 into two groups: YSB with constant 25% oxygen vacancy in the lattice, and WSB with varying oxygen vacancy ratio. Pressure cell measurements of those two groups of doped Bi_2O_3 with boron were taken so as to study the effects of oxidizers' bond energy and oxygen vacancy for boron based thermite combustion properties. According to previous studies, the optical intensity generally correlates with the flame temperature in the pressure

cell.[19a] Peak pressure, pressurization rate obtained from the pressure signal and burn time obtained by measuring the peak's full width at half maximum are three parameters that I use to evaluate the combustion performance of thermites. Pressure histories of B with doped Bi_2O_3 can be found in Figure S5.4. Figure 5.8a shows the pressurization rate for B/doped Bi_2O_3 thermite verses the metal-oxygen bond energy of oxidizer. I find that the pressurization rate and peak pressure of thermite reaction decreased significantly with increased metal-oxygen bond energy of oxidizer. Pressurization rate dropped one order of magnitude from WSB5 to WSB20 and three orders from YSB15 to YSB40. It is generally acknowledged that gaseous products contribute to the pressure rise,[26] in which low-boiling point Bi (1564 °C) makes it an important gaseous species that increases pressure in the thermite reaction since both Y (3338 °C) and W (5555 °C) have high boiling point. Thus with more W^{6+} or Y^{3+} doped in Bi_2O_3, less gaseous Bi is produced and thus peak pressure is further lowered. It is also noted that although YSB10 and YSB15 have higher bond energy and lower Bi molar ratio than WSB5, they showed significantly higher pressurization rates than B/WSB5, which is probably due to the higher oxygen vacancy concentrations. Thus both metal-oxygen bond energy and oxygen vacancy concentration in oxidizer affect the combustion performance of B/doped Bi_2O_3 thermites. Since the pressurization rate can be correlated with the flame propagation velocities, or reactivity, one would assume that a system with a larger pressurization rate would show a shorter burn time. Thus the burn time is expected to show a reversed trend as pressurization rate with the bond energy of oxidizer. Figure 5.8b shows the burn time for B/doped Bi_2O_3

thermite verses the metal-oxygen bond energy of oxidizer and indicate that burn time generally increased with the metal-oxygen bond energy of doped Bi_2O_3 as expected.

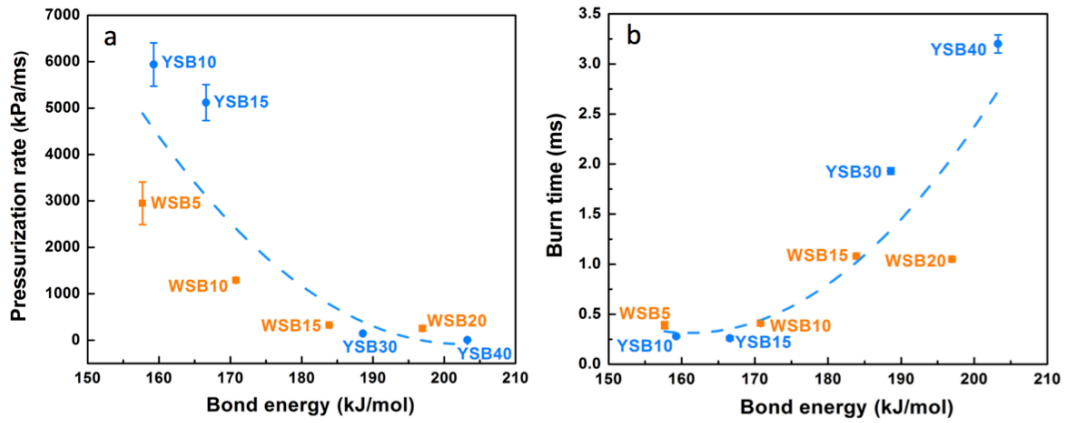

Figure 5.8. Pressurization rate (a) and burn time (b) of B/doped Bi_2O_3 thermite vs. metal-oxygen bond energy of doped Bi_2O_3.

Table 5.2. Metal-oxygen bond energy of doped Bi_2O_3 and calculated oxygen vacancy percentage in one unit cell and oxygen vacancy concentration, $V_O^{\cdot\cdot}$ of doped Bi_2O_3.

Thermite	M-O bond energy of oxidizer (kJ/mol)	Oxygen vacancy % of oxidizer	$[V_O^{\cdot\cdot}]$ of oxidizer (#/cm^3)
B+WSB5	158	21.3	9.7E21
B+WSB10	171	17.5	8.0E21
B+WSB15	184	13.8	6.4E21
B+WSB20	197	10	4.7E21
B+YSB10	159	25	1.2E22
B+YSB15	167	25	1.2E22

B+YSB30	189	25	1.2E22
B+YSB40	203	25	1.2E22

Ignition and combustion: crystallite size effects

The effect of different crystallite size on ignition/combustion is still unknown. In order to investigate the effect of crystallite size on ignition temperature and combustion reactivity, YSB15 synthesized at different temperature with different crystallite size are employed as oxidizer. YSB15 are synthesized at 650 to 900 °C with a 50 °C interval. The crystal structures of YSB15 synthesized are shown in Figure 5.9.

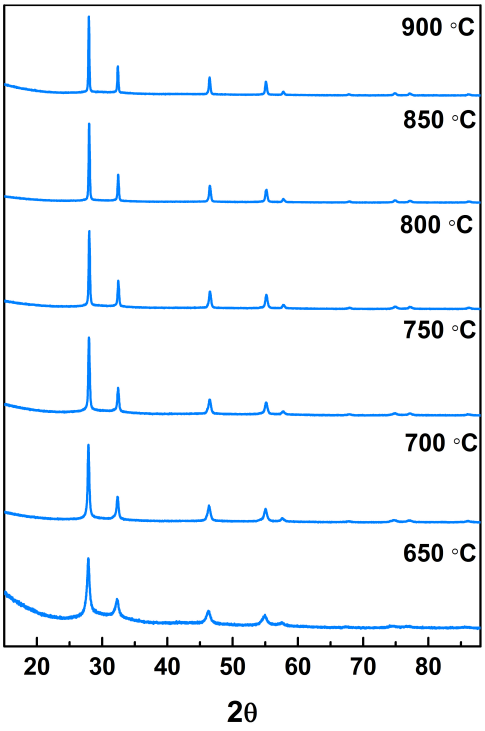

Figure 5.9. Crystal structure of YSB15 synthesized at 650, 700, 750, 800, 850, and 900 °C.

The crystallite size increases with synthesis temperature. The crystallite size for YSB15 ranges from 12nm (650 °C) to 90 nm (900 °C). I picked up the YSB15 with smallest and largest crystallite size: 12nm (650 °C) and 90 nm (900 °C) and measured their ignition temperatures with nano boron. The ignition temperatures are found to be very close: ~550 °C. The combustion reactivities are also measured by pressure cell and the pressure profile are found to be close as well shown in Figure 5.10. I thus conclude that in the crystallite size range of below 100 nm, the ignition temperature and combustion reactivity will not be affected by the crystallite size.

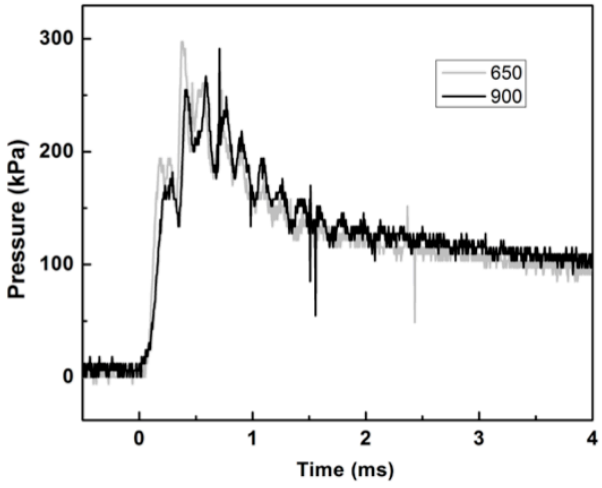

Figure 5.10. Pressure profile of YSB15 synthesized at 650 and 900 °C.

5.4. Conclusion

In summary, this study reveals a clear relationship between molecular properties of the oxidizer and ignition temperature as well as combustion performance (pressure peak, pressurization rate and burn time) of boron based nano-thermites. This was enabled by employing a systematically doped Bi_2O_3, whose crystal structure and particle size and morphology are maintained the same, but

whose oxygen vacancy concentration and bond energy are varied. I found a clear relationship that larger oxygen vacancy concentration and smaller metal-oxygen bond energy lead to lower ignition temperature and higher combustion reactivity with higher peak pressure, pressurization rate and shorter burn time of boron based thermites. In addition, in-situ high heating rate TEM was used to explore the morphology change, both prior to and after the initiation of B/Bi_2O_3. I proposed that B/Bi_2O_3 ignites (~520 °C) at lower temperature than Al/Bi_2O_3 (~630 °C) because, and in part based on TEM images, the molten B_2O_3 wets Bi_2O_3 creating an interface so that high mobility solid-state oxygen can diffuse through the liquid B_2O_3 shell.

Acknowledgments

Special thanks to Dr. Sz-Chian Liou and Dr. Wen-An Chiou for technical assistance.

5.5. Supplemental Information

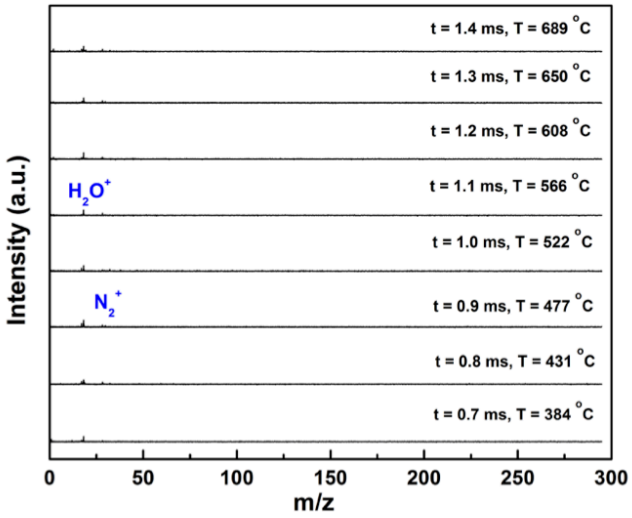

Figure S5.11. Mass spectra for boron in T-jump TOFMS. Each spectrum is separated in time by 100 μs.

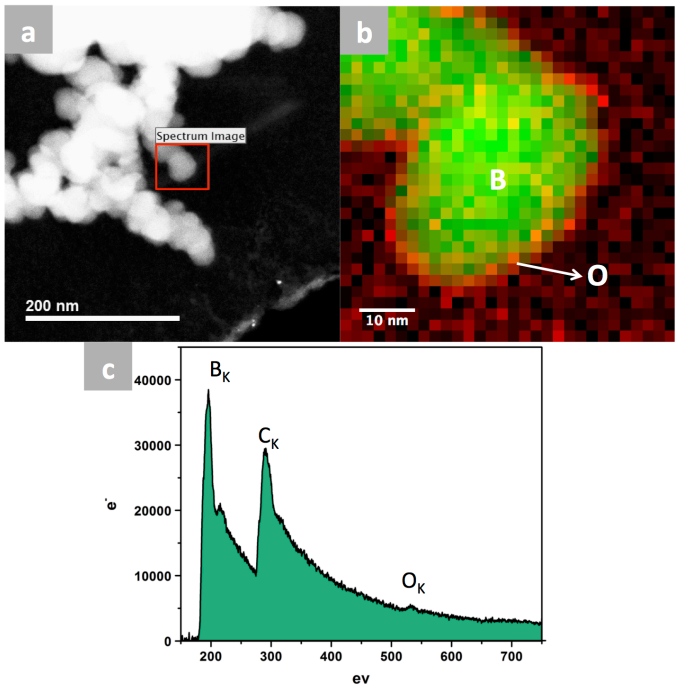

Figure S5.12. a. TEM image of boron particles. b. EELS analysis of boxed region in Figure S3a, with green pixels representing boron, bright red pixels representing oxygen, and B_2O_3 shell is estimated to

be 2nm thick. c. EELS spectrum of boron particles showing the peaks of B, C and O, indicating the existence of B_2O_3 shell.

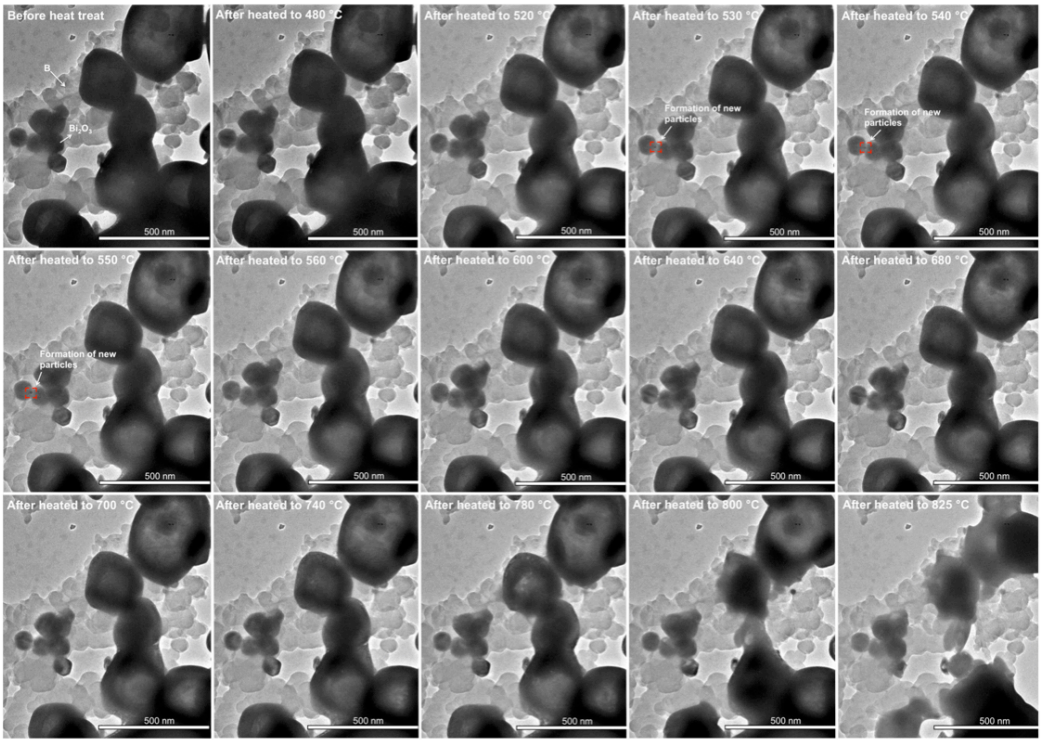

Figure S5.13. Contineous TEM images after each heating step.

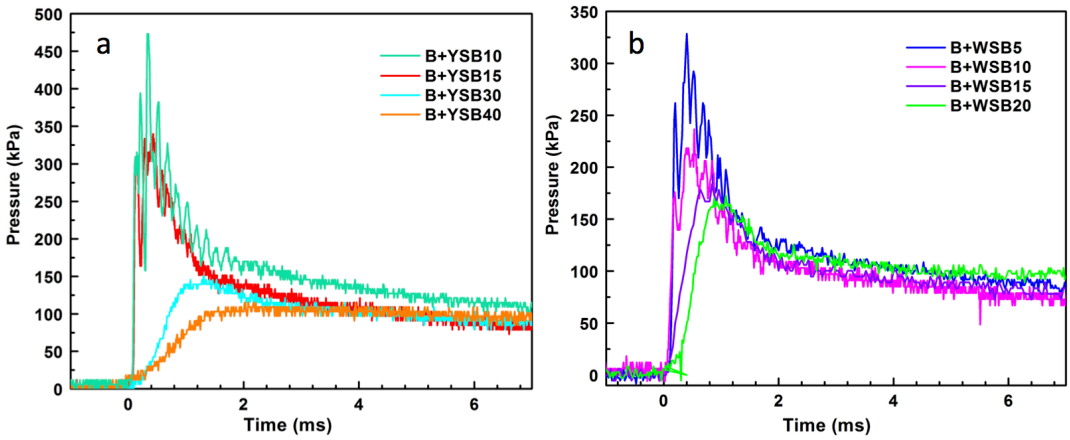

Figure S5.14. Pressure emission profiles for a. B/YSB and b. B/WSB

Table S5.1. Lattice parameters of doped Bi_2O_3

Doped Bi_2O_3	Lattice parameters, a (Å)
WSB5	5.5985(3)
WSB10	5.5945(2)
WSB15	5.5915(4)
WSB20	5.5565(5)
YSB10	5.5289(5)
YSB15	5.5230(3)
YSB30	5.4895(8)
YSB40	5.462(1)

Table S5.2. Log-normal fit parameters of size distribution of YSB30 and WSB20, and R^2 is coefficient of determination.

Equation	$y = y_0 + \frac{A}{\sqrt{2\pi}\cdot\sigma x}\cdot \exp\left(-\frac{(lnx-\mu)^2}{2\sigma^2}\right)$		
		Value	Standard Error
YSB30	R^2	0.938	
	y_0	0.0164	0.0053
	μ	95.0487	1.0148
	σ	0.2741	0.0105
	A	51.0239	1.6653
WSB20	R^2	0.926	
	y_0	0.0506	0.0145

	μ	88.4523	1.5729
	σ	0.2926	0.0181
	A	54.0702	2.7468

Chapter 6: Is the Relationship between Microscopic Properties of Metal Oxides and Reaction Threshold Generic to Different Fuels and Oxidizers?*

Summary

The redox reaction between fuel (metal, metalloid, etc.) and metal oxide is ubiquitous. On the other hand simple thermodynamic considerations do not seem to yield much insight into what makes for a vigorous oxidizer. In previous chapters, the ignition temperature is found to be correlated with the microscopic properties of oxidizers for Al/doped Bi_2O_3, B/Bi_2O_3 and Al/perovskite. In this chapter, if the correlation is generic to different fuels and oxidizers is studied: two different systematically doped metal oxide systems: perovskites (9 compounds) and δ-Bi_2O_3 (12 compounds) were synthesized in a manner such that for each system the crystal structure and morphology were maintained. Four fuels (Al, B, Ta, C) with different physical properties, covering almost all fuel types, were included in this study. The initiation temperature and oxygen release temperature was measured by fast heating (> 10^5 K/s) temperature-jump/time-of-flight mass spectrometer coupled with high-speed imaging. These results were then correlated with the average metal-oxygen bond energy in the oxidizer, and overall metal-oxygen electronegativity. In general, within each systematic metal oxide, I found linear relationships between average bond energy and electronegativity of the metal oxides with initiation temperature for

* The results presented in this chapter are in the process of under review to the Physical Chemistry and Chemical Physics under the title "What Atomic Properties of Metal Oxide Control the Reaction Threshold of Solid Elemental Fuels" with authors Wang, X.; Zachariah, M. R.,

all four fuels, despite their very different physical/chemical properties. These results indicate that intrinsic microscopic properties of metal oxide control fuel-metal oxide reaction initiation.

6.1. Introduction

Metal (Al, Mg, Ti), metalloid (B, Be) or nonmetals (C) are commonly employed as high energy density fuels. Very often the oxidant is an oxygen donor that can be intimately packed together with the fuel. Typically this is a metal oxide, which can under appropriate condition lead to very rapid redox reactions. Nominally with the appropriate fuel-oxidizer pair based on the overall thermodynamics, the reaction once initiated, releases sufficient thermal energy to enable a self-sustainable reaction during this seemingly simple oxygen exchange process. Mass diffusion typically controls the overall reaction rate of these separate entities of solid-state fuel and metal oxide. More recently with the interest in nanoscale materials, the reduced length scale offers the potential to significantly reduce the energy release time. [1] Observationally the initiation temperature is an important easy metric and is the onset temperature of vigorous self-sustaining redox reaction between fuel and metal oxide. The initiation temperature results from a complex interplay of many variables, most obviously the nature of reactants, but also experimental parameters, e.g. heating rate, experimental configuration and packing. However even for seemingly the same experimental configurations, I and others have found that there can be large differences in initiation temperatures among different fuel-metal oxide formulations.[2]

As discussed, one reason is that there are a large number of variables that might affect the initiation temperature, including crystal structure, reaction interface area, morphology, particles size, thermal conductivity, heat capacity, etc. In order to deal with this level of complexity, I have recently focused on a doping strategy to manipulate the properties of specific metal oxide system in a subtle, but systematic manner. The basic concept is to keep as many of the other variables constant (e.g. particle size, crystal structure, density).

In Chapter 3-5, I synthesized two classes of systematically doped metal oxides (doped perovskites and doped δ-Bi_2O_3) in which many of the dependent variables can be held constant.[3] Perovskite oxides, generally, ABO_3, have been employed in solid oxide fuel and electrolysis cells (SOFC/SOEC),[4] heterogeneous catalysis of hydrocarbon,[5] membranes for oxygen separation,[6] and chemical looping combustion as oxygen carriers.[7] Perovskites are useful for my study, as it is possible to adjust redox properties by adopting a large number of different A- and B- site cations. δ-Bi_2O_3 has also been explored by us because of its intrinsic high oxygen ion conductivity, partly due to the ~25% oxygen vacancy, which is why it is often used as an electrolyte in SOFC.[8] Pure δ-Bi_2O_3 is not room temperature stable and oxygen ion conductivity is thus reduced.[9] By doping with other oxides, the cubic structure δ-Bi_2O_3 can be stabilized down to room temperature. In prior work I showed that the initiation of Al/doped perovskite and Al/doped δ-Bi_2O_3 could be correlated with the microscopic properties of the metal oxide, e.g. metal-oxygen bond energy, oxygen vacancy concentration, and electronegativity so long as aluminum is molten in each system. However, it is unknown if the correlation is generic.

In this study, four different fuels with different physical properties were studied: Al with a low melting point core (Al: 660 °C) and a high melting point passivating shell (Al_2O_3: 2072 °C), B with a high melting point core (B: 2076 °C) and a low melting point passivating oxide (B_2O_3: 450 °C), Ta with a high melting point core (Ta: 3020 °C) and a high melting point passivating oxide (Ta_2O_5: 1872 °C) and C with a high melting point core (C: 3827 °C) but no passivating oxide.[10] Doped perovskites and doped δ-Bi_2O_3 were employed as oxygen carriers. The initiation temperatures were measured by temperature-jump/time-of-flight mass spectrometer (T-Jump/TOFMS) and a high-speed camera. These results were then correlated with the average bond energy and overall metal-oxygen electronegativity difference of doped metal oxide. In general, I found linear relationships between average bond energy and electronegativity with initiation temperature for all four fuels despite their wide range of physical/chemical properties.

6.2. Experimental Details

Synthesis of Doped Metal Oxides.

In this study, 9 doped perovskites and 12 doped Bi_2O_3 listed in Table 6.1 were synthesized. All doped metal oxides were prepared by aerosol spray pyrolysis whereby precursors of metal salts aqueous solutions are continuously atomized into droplets and thermally decomposed to metal oxide particles (for details see the supplementary information).[11] Briefly, 0.2 M precursor solution, containing stoichiometric nitrates was atomized by a nebulizer to generate nominally 1 μm droplets with compressed air. The atomized droplets flowed through a diffusion

dryer, where most of the water was absorbed, leaving solid precursor particles which were then passed to a tubular furnace, set at 1050 °C for doped perovskites and 750 °C for doped Bi_2O_3 to produce the desired doped metal oxide particles.

Table 6.1. Aerosol spray synthesized doped perovskites and Bi_2O_3 with abbreviation.

Doped Perovskite	*Doped Bi_2O_3*	Abbr.
$LaCrO_3$	$(Y_{0.15}Bi_{0.85})_2O_3$	YSB15
$La_{0.8}Sr_{0.2}CrO_{3-\delta}$	$(Y_{0.3}Bi_{0.7})_2O_3$	YSB30
$La_{0.6}Sr_{0.4}CrO_{3-\delta}$	$(Y_{0.4}Bi_{0.6})_2O_3$	YSB40
$LaFeO_3$	$(W_{0.05}Bi_{0.95})_2O_{3.15}$	WSB5
$La_{0.8}Sr_{0.2}FeO_{3-\delta}$	$(W_{0.1}Bi_{0.9})_2O_{3.3}$	WSB10
$La_{0.6}Sr_{0.4}FeO_{3-\delta}$	$(W_{0.15}Bi_{0.85})_2O_{3.45}$	WSB15
$LaCoO_3$	$(W_{0.2}Bi_{0.8})_2O_{3.6}$	WSB20
$La_{0.8}Sr_{0.2}CoO_{3-\delta}$	$(Er_{0.15}Bi_{0.85})_2O_3$	ESB15
$La_{0.6}Sr_{0.4}CoO_{3-\delta}$	$(Dy_{0.15}Bi_{0.85})_2O_3$	DSB15
	$(Dy_{0.1}W_{0.05}Bi_{0.85})_2O_{3.15}$	DWSB10
	$(Dy_{0.05}W_{0.1}Bi_{0.85})_2O_{3.3}$	DWSB5
	$(Dy_{0.05}Nb_{0.1}Bi_{0.85})_2O_{3.2}$	DNSB

Fuel/Doped Metal Oxide Compositions.

Nano aluminum particles (~50 nm, 81 wt% active) were purchased from Novacentrix Corporation, nano-sized carbon black (~50 nm) was obtained from Cabot Corporation, Boron particles (SB99, ~60 nm, 70 wt% active) were obtained from the SB Boron Corporation and nano tantalum powders (<50 nm, 70 wt% active) were purchased from Global Advanced Metals. Stoichiometric mixtures of fuel (Al, B, Ta, C) and doped metal oxides were mixed respectively and then sonicated in hexane for 30 min. For control of stoichiometry, the Al_2O_3 shell (19% of the mass), B_2O_3 shell (30% of the mass) and Ta_2O_5 shell (30% of the mass) content were accounted for.

Characterization.

The crystal structures and morphology of the as-synthesized metal oxides were characterized by X-ray diffraction (XRD) performed on a Bruker D8 diffractometer with Cu Kα radiation and scanning electron microscopy (SEM) conducted on a Hitachi SU-70 instrument respectively. Le Bail refinement of all diffraction patterns was performed with the TOPAS 4.2 software.[12] Size distributions were obtained by measuring 300 individual nanoparticles statistically from SEM images of each sample, using Nano Measurer 1.2 image analysis software.

Temperature-Jump Measurement.

Initiation temperature of fuel/metal oxide and oxygen release temperature (in the absence of fuel) from individual oxidizer, were measured with T-Jump/TOFMS [13] coupled with high-speed camera (Vision Research Phantom v12.0) operating at 67056 frames/s, using direct optical emission. A hexane suspension of samples was droppered onto a 70 um diameter platinum filament, which was heated at a rapid rate ~ 4×10^5 °C/s, to ~1200 °C within 3 milliseconds. The filament was directly inserted into the vacuum ionization region of a TOFMS, where the gaseous products could be temporally analyzed. The temperature of the wire was determined from electric resistance based on the Callendar-Van Dusen equation, through a simultaneously measure of temporal applied voltage and current. The ionization/extraction region of the TOFMS was pulsed at 10 kHz resulting in a full mass spectrum every 100 μs. A 600 MHz digital oscilloscope was used for data acquisition with a sampling rate of 100 mega sample per second.

Due to the size of nanoparticles compared with the wire and based on my previous result, the temperature of the wire is essentially equal to the temperature of the oxidizer system.[14]

6.3. Results and Discussion

Structure and morphology

As example XRD patterns for the as-synthesized doped Bi_2O_3 are shown in Figure 6.1. Based on Le Bail refinements, all the synthesized doped Bi_2O_3 were in the δ-phase with a single cubic Fm-3m space group, and the lattice parameters are listed in Table S6.1. The XRD patterns for all synthesized perovskites and refined results are shown in Figure 3.1 and S3.1 with all perovskites in pseudocubic structures. Thus it is reasonable to argue that within each system type, the doped metal oxides have essentially the same crystal structure, and I can eliminate crystal structure as a controlling impact on initiation temperature of redox reaction with fuel.

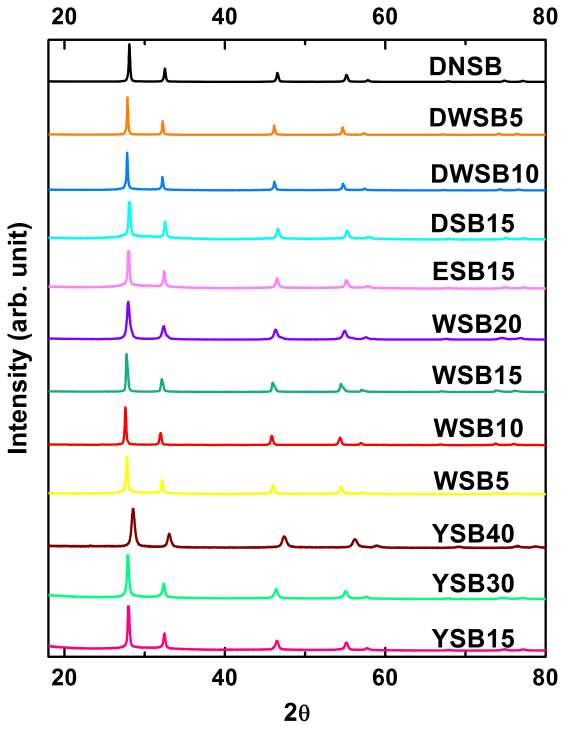

Figure 6.1. X-ray diffraction patterns of aerosol spray synthesized doped Bi_2O_3.

The SEM images of (a) $LaFeO_3$, (b) $La_{0.8}Sr_{0.2}FeO_3$ and (c) $LaCrO_3$ as representative powders can be found in Figure 3.2 and the particle size distributions are shown in Figure S3.2, indicating essentially the same morphology and particle size distribution, consistent with my previous results.[15] Similar results were found for doped Bi_2O_3 shown in Figure 5.2. Thus in this study I am able to ensure that all oxides have the same morphology and particle size distribution, eliminating these factors as variables impacting initiation temperature.

.

Reaction mechanism

Two important measurables relevant to understanding reactivity, are the reaction threshold itself, and if and when oxygen gas is released from the oxidizer. Oxygen release temperatures of synthesized doped metal oxides were measured with T-jump/TOFMS. Metallic fuel (Ta, Al) or metalloid fuel (B) reacted with metal oxides vigorously with an easily discernable visible initiation event. Initiation was determined as the onset of optical emission. In contrast to Al, Ta and B, the C/metal oxide reaction is much less vigorous with no visible emission, and thus I employed the temporal CO_2 release to define the reaction threshold (For more details see the supplementary information).

The observed oxygen release temperature from the neat metal oxides and the observed initiation temperature of Al, B, C, Ta/perovskites are shown in Figure 6.2. What this result shows is that almost all data points lie above the diagonal, indicating that reaction initiation occurs before oxygen (O_2) is released into the gas phase by the perovskite. Further for the temperature regime that T-jump/TOFMS could reach (~1350 °C), no O_2 release of $LaCrO_3$ and $LaFeO_3$ and no initiation of fuel/$LaCrO_3$ were observed. The results from Figure 6.2 demonstrate that since initiation occurs at a temperature below which oxygen is evolved from the oxidizer, one must conclude the reaction takes place by condensed state redox reaction rather than gas evolution of oxygen leading to subsequent reaction. For doped Bi_2O_3, I have previously justified that initiations are in the condensed phase.[3b]

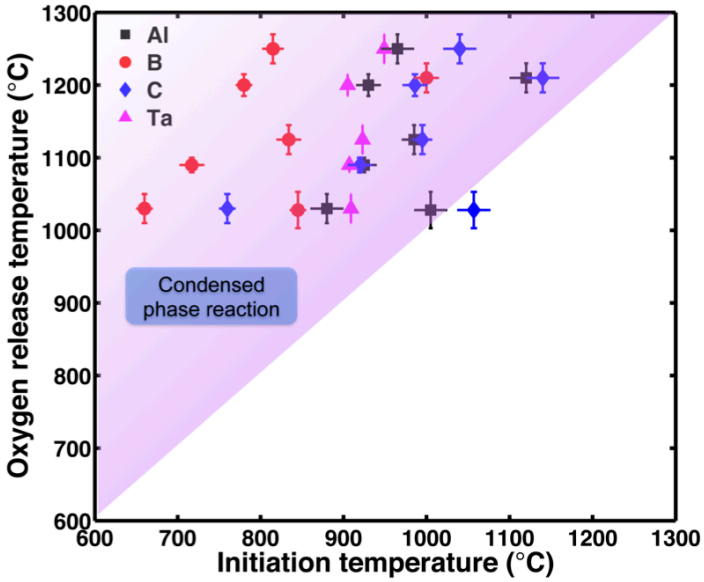

Figure 6.2. Oxygen release temperature from the perovskites vs. initiation temperature for Al/perovskite, B/perovskite, C/perovskite and Ta/perovskite, indicates that redox initiation occurs prior to oxygen release (i.e. condensed state reaction).

Bond energy and $[V_O^{\cdot\cdot}]$ vs. initiation temperature

In the previous work, I have justified that for Al/Bi_2O_3 and Al/perovskite composites, oxygen ion transport limits the condensed phase initiation. I also find that smaller metal-oxygen bond energy and larger oxygen vacancy concentration in doped perovskite or Bi_2O_3, lower the initiation temperature. In this study, for the purposes of tweezing out mechanistic information I expand the fuels to include B, Ta and C. Thus I have four different fuels (Al, B, Ta, C) with completely different physical properties.

The metal-oxygen bond energy for doped metal oxide can be estimated based on its stoichiometry, coordination numbers and thermodynamic data. Since for *Pm-3m* cubic, *Pnma* orthorhombic or *R3c* rhombic perovskite, A-site cations are 12-coordinated with oxygen, and B-site cations are 6-coordinated with oxygen, the

average bond energy (ABE) of the perovskite can be estimated based on equation 1, where $\Delta H_{A_mO_n}$ and $\Delta H_{B_mO_n}$ are the heats of formation of A_mO_n and B_mO_n oxides at 298 K, respectively, ΔH_A and ΔH_B are the heats of sublimation of A-metal and B-metal at 298 K and D_{O_2} is the dissociation energy of gaseous oxygen.[16] For fluorite type doped δ-Bi_2O_3 in which that cation is 6-coordinated with oxygen anions, the average metal-oxygen bond energy is estimated based on equation 2 and 3, where a is the dopant molar ratio. Since δ-Bi_2O_3 has a defect fluorite-type crystal structure (AX_2) in which 25% of the oxygen sites in the unit cell are vacant,[17] oxygen vacancy concentration, $[V_O^{\cdot\cdot}]$ of doped δ-Bi_2O_3 can thus be estimated based on the percentage of vacant oxygen sites in one unit cell, and the lattice parameter as reported in the previous literature. The calculated ABE of both doped perovskites and δ-Bi_2O_3 and $[V_O^{\cdot\cdot}]$ of doped δ-Bi_2O_3 are listed in Table S6.2.

$$ABE_{perovskite} = \frac{1}{2}\left(\frac{1}{12m}\left(\Delta H_{A_mO_n} - m\Delta H_A - \frac{n}{2}D_{O_2}\right) + \frac{1}{6m}\left(\Delta H_{B_mO_n} - m\Delta H_B - \frac{n}{2}D_{O_2}\right)\right) \quad (1)$$

$$ABE_{doped\ Bi_2O_3} = (1-a)\cdot\Delta(A-O) + a\cdot\Delta(A'-O) \quad (2)$$

$$\Delta(A-O) = \frac{1}{6m}\left(\Delta H_{A_mO_n} - m\Delta H_A - \frac{n}{2}D_{O_2}\right) \quad (3)$$

The calculated ABE of doped perovskite and Bi_2O_3, and the corresponding measured initiation temperature with different fuels is shown in Figure 6.3. It is apparent that in each system, the initiation temperature increases with average M-O bond energy in the oxidizer, indicating that the redox initiation was dominated by oxygen transport of metal oxide, rather than the properties of the fuel. I was surprised by these results. Four fuels with very different physical properties show similar trends with two very different oxidizer families. Within each oxidizer family all fuels appear to behave similarly, but each oxidizer family shows distinctive behavior. This result

implies that the initiation of a fuel/metal oxide redox reaction relies mainly on the microscopic property of metal oxide. Within each system, the heat loss terms are essentially equivalent for the four different fuels such that approximately the same flux of oxygen is needed to initiate a non-linear heat release regardless of fuel type. *One may conclude, there is a general trend that suggests an oxidizer control mechanism, regardless of fuel type.*

Obviously of course, if the fuel has no role, then the data points for all fuels would be overlaid. But clearly the differences between fuels are larger than the experimental uncertainties. Boron clearly has the lowest initiation temperature, and is also more sensitive to the ABE. Tantalum by contrast appears to be less sensitive to the ABE of oxidizer, indicating the initiation of Ta/metal oxide is more fuel sensitive. It is reported that metal oxides react with Ta, when cracks appeared in the Ta_2O_5 shell due to its amorphous to crystalline phase change. These cracks serve as channels for oxygen ion diffuse to the tantalum core.[18] Not surprising then that Ta is less sensitive to the oxidizer, although the general bond energy trends still tend to hold. Thus there are physical aspects to the fuel that moderate the trends on oxide character. This is also the case for aluminum where the reaction threshold for all doped metal oxide was above ~660 °C (melting point of Al), to enable molten aluminum to diffuse through the oxide shell. All doped metal oxides reacted with boron above ~520 °C (higher than the melting point of B_2O_3 shell, 450 °C), so molten B_2O_3 wets oxidizer possibly creating an interface where solid-state oxygen can diffuse through the liquid B_2O_3 shell.

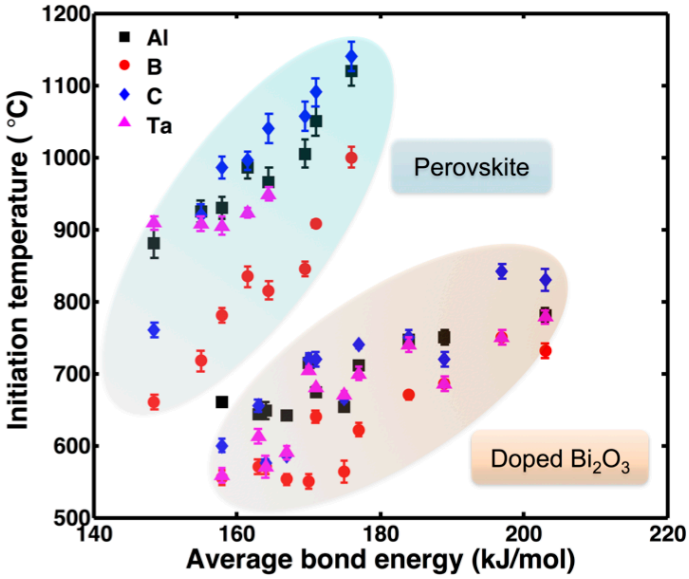

Figure 6.3. Observed relationship between average bond energy (ABE) of all doped metal oxides against the initiation temperatures of four fuels Al-B-C-Ta.

The fact that the two systematic oxidizers do not overlay implies other parameters come into play besides that average bond energy. Presumably this would include oxygen vacancy concentration, $[V_O^{\cdot\cdot}]$, which impacts the oxygen ion transport of metal oxides and thus metal oxide's oxidation capability. The $[V_O^{\cdot\cdot}]$ of all aliovalent dopant doped δ-Bi_2O_3 vs. the initiation temperature of these doped δ-Bi_2O_3 with different fuels is shown in Figure 6.4. Apparently initiation temperature decreases with $[V_O^{\cdot\cdot}]$. Thus both metal-oxygen bond energy and $[V_O^{\cdot\cdot}]$ affect the initiation temperature. The $[V_O^{\cdot\cdot}]$ of perovskites is reported to be significantly lower than that of doped δ-Bi_2O_3.[19] This difference in $[V_O^{\cdot\cdot}]$ probably leads to the discontinuity of initiation temperature vs. bond energy trend switching from doped perovskites to δ-Bi_2O_3.

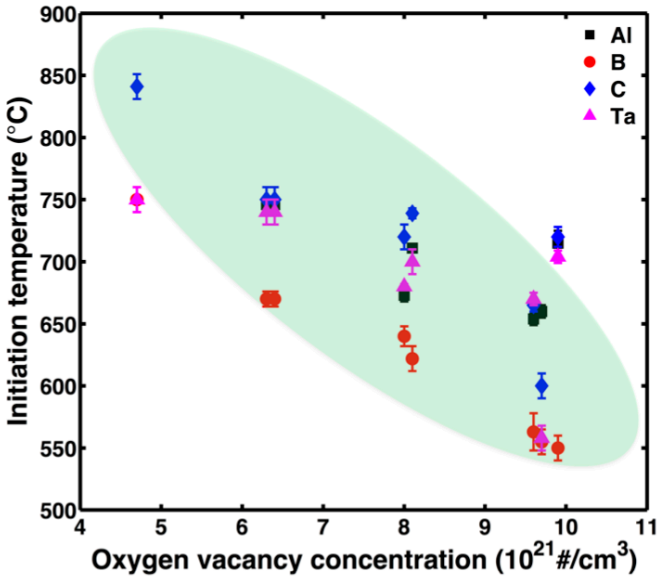

Figure 6.4. Observed relationship between oxygen vacancy concentration of aliovalent doped δ-Bi_2O_3 vs. the initiation temperatures of four fuels Al-B-C-Ta.

Crystal structure comparison

The differences in crystal structure between the different oxide classes could possibly be another reason impacting initiation temperature in addition to bond energy and $[V_O^{\cdot\cdot}]$. It is known that "free volume" and "critical radius" are important crystallographic parameters in oxygen ion transport.[20] The critical radius refers to the limit radius that mobile oxygen can pass, and the free volume is obtained by subtracting the volume of all constituent ions from the overall unit cell volume. It would be reasonable to expect that a larger critical radii and free volume results in faster oxygen ion transport and thus a lower initiation temperature. With doped perovskites in Pm-3m, Pnma, or R-3c space groups and doped Bi_2O_3 in Fm-3m space group, the oxygen ion experiences different degrees of openness in the lattice.

Consider the cubic $La_{0.6}Sr_{0.4}CoO_3$ (space group: Pm-3m) and $(Y_{0.15}Bi_{0.85})_2O_3$ (space group: Fm-3m) as representative for perovskite and the doped Bi_2O_3 respectively. As both systems under consideration are high symmetry cubic structures, we can compare the ion arrangements on (111) lattice planes in Figure 6.5. It is quite clear that oxygen ions are more tightly packed in $La_{0.6}Sr_{0.4}CoO_3$ than in $(Y_{0.15}Bi_{0.85})_2O_3$, which should manifest itself with a higher ion-mobility for the bismuth oxide. This can be seen more quantitatively by calculating the critical radius and free volume per oxygen ion in Table 6.2. One sees that doped Bi_2O_3 has much larger free volume and a larger critical radius than doped perovskite, consistent with its elevated oxygen ion mobility. This may be partially responsible for the lower redox initiation temperature for the same ABE for the doped Bi_2O_3 relative to the perovskites.

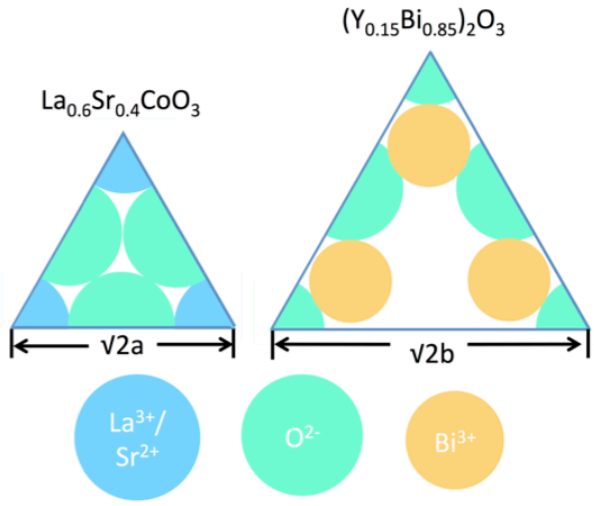

Figure 6.5. Schematic view of the (111) lattice plane of a cubic unit cell $La_{0.6}Sr_{0.4}CoO_3$ and $(Y_{0.15}Bi_{0.85})_2O_3$ (same length scale), a and b are the lattice parameters for $La_{0.6}Sr_{0.4}CoO_3$ and $(Y_{0.15}Bi_{0.85})_2O_3$ respectively.

Table 6.2. The critical radius and free volume per oxygen ion in $(Y_{0.15}Bi_{0.85})_2O_3$ and $La_{0.6}Sr_{0.4}CoO_3$.

	Critical radius (Å)	Free volume/oxygen ion ($Å^3$)
$La_{0.6}Sr_{0.4}CoO_3$	0.87	3.2
$(Y_{0.15}Bi_{0.85})_2O_3$	1.02	14.4

Electronegativity vs. initiation temperature

Finally I have previously explored electronegativity as a potentially even simpler metric. A larger electronegativity difference between metal and oxygen should yield a more ionic bond, and thus a more stable structure, because the degree of hybridization between metal and oxygen depends on the electronegativity difference, and electronegativity is the average of the ionization potential and the electron affinity. Figure 6.6 shows a clear trend that initiation temperature increases with increasing electronegativity difference χ, in the metal oxide, calculated on the Pauling Scale,[21]and that higher ionic character increases initiation temperature. Thus electronegativity appears to be a very effective simple metric determining the initiation temperature.

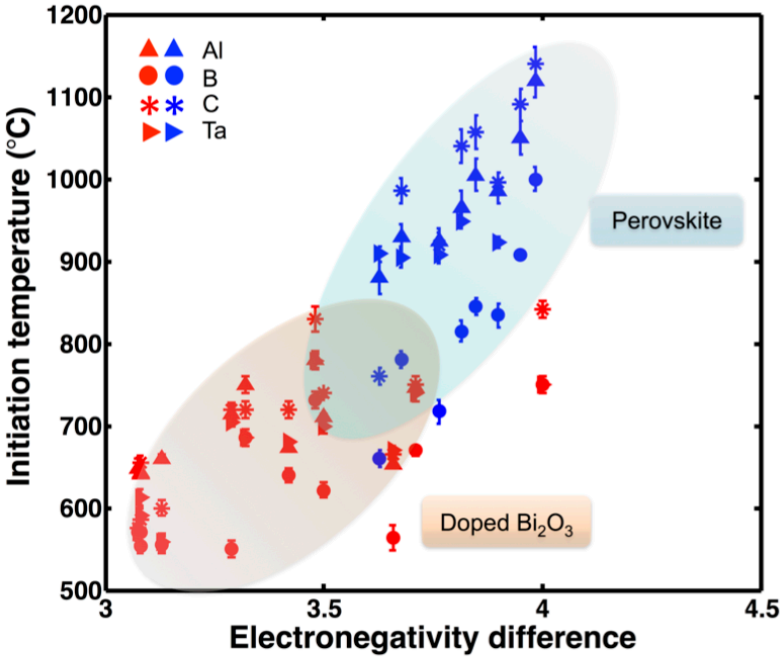

Figure 6.6. Overall electronegativity difference of doped metal oxide versus initiation temperature of Al/B/C/Ta with doped metal oxides.

6.4. Conclusion

The goal of this chapter was to explore if the correlation between the microscopic properties of an oxidizer and the reactivity with solid elemental fuels is generic applying to different fuels and oxidizers. This was evaluated using two systematic doped metal oxides: perovskites and δ-Bi_2O_3, sharing the same crystal structure and morphology within each system, as oxidants with four fuels (Al, B, C, Ta) with very different physical and chemical properties. I found that, within each oxidizer family, initiation temperature increases with M-O bond energy of the oxidizer, seemingly independent of fuel type. The absolute value for initiation of perovskites and δ-Bi_2O_3 doesn't overlap, which I attribute to differences in oxygen

vacancy concentration and crystal structure in these two groups of metal oxides. I also found that initiation temperature increased with the electronegativity difference of oxidizer for all four fuels, indicating electronegativity might be a simpler metric than metal-oxygen bond energy to evaluate the reaction threshold.

6.5. Supplemental Information

Table S6.1. Lattice parameters of doped Bi_2O_3.

Doped Bi_2O_3	Lattice parameters, a (Å)
YSB15	5.5230(3)
YSB30	5.4895(8)
YSB40	5.462(1)
WSB5	5.5985(3)
WSB10	5.5945(2)
WSB15	5.5915(4)
WSB20	5.5565(5)
ESB15	5.522(1)
DSB15	5.5236(7)
DWSB10	5.5642(3)
DWSB5	5.581(2)
DNSB	5.5364(2)

Initiation Temperature Measurement of C/metal oxides.

In contrast to Al, Ta, and B, the C/metal oxide reaction is much less vigorous with no visible emission, thus I employed the temporal CO_2 release to define the reaction threshold. CO_2 release temperatures form C/perovskite were also measured from T-Jump/TOFMS. It is noted here that the perovskite synthesized via aerosol spray pyrolysis naturally has carbon-containing contamination, which will bring trouble for us to determine the CO_2 release from the redox reaction of C/perovskite. To solve this problem, I preheat the sample to burn C-containing impurities: a hexane suspension of C/perovskite was droppered onto a 70 um diameter platinum filament, and allowed to air dry. After the platinum filament with C/perovskite sample was inserted into the vacuum chamber, the platinum wire was in-situ joule heated at a rapid rate ~ 2×10^5 °C/s, to ~650 °C within 3 milliseconds to burn the carbon contamination impurities. Then platinum wire was again joule heated at a rapid rate ~ 4×10^5 °C/s, to ~1200 °C within 3 milliseconds to initiate the reaction of C/perovskite. CO_2 release for C/$La_{0.6}Sr_{0.4}CoO_3$ w/o and with in-situ pre heat treat is shown in Figure S6.1. It is seen that after in-situ pre heat treat, the CO_2 release from C/$La_{0.6}Sr_{0.4}CoO_3$ was clearer and the initiation temperature (onset temperature of CO_2) of C/$La_{0.6}Sr_{0.4}CoO_3$ is measurable. The temperature of the wire corresponding to the initial release of CO_2 after twice heat-treat was regarded as the CO_2 release temperature of C/perovskite. CO_2 releases for other C/$La_{1-x}Sr_xBO_{3-\delta}$ composites with in-situ pre heat treat are shown in Figure S6.2.

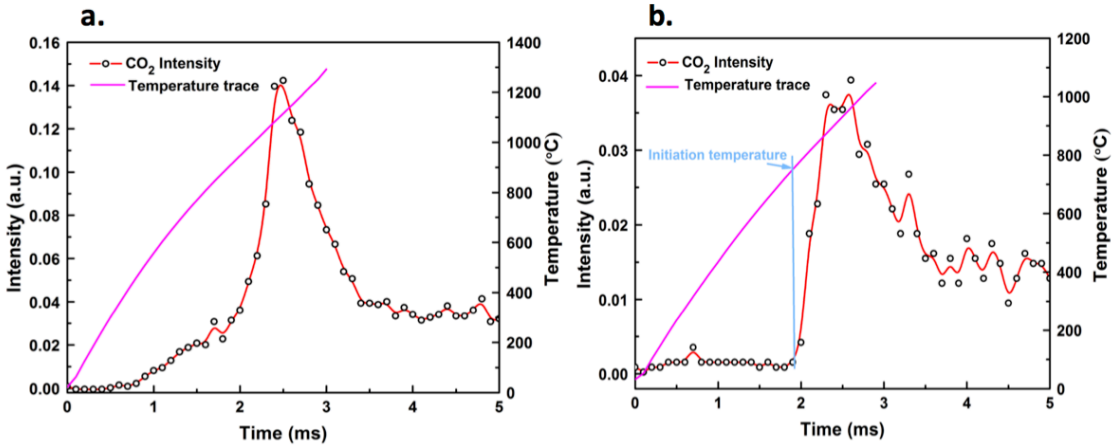

Figure S6.1. Temporal CO_2 release for $C/La_{0.6}Sr_{0.4}CoO_3$ w/o and with in-situ pre heat treat.

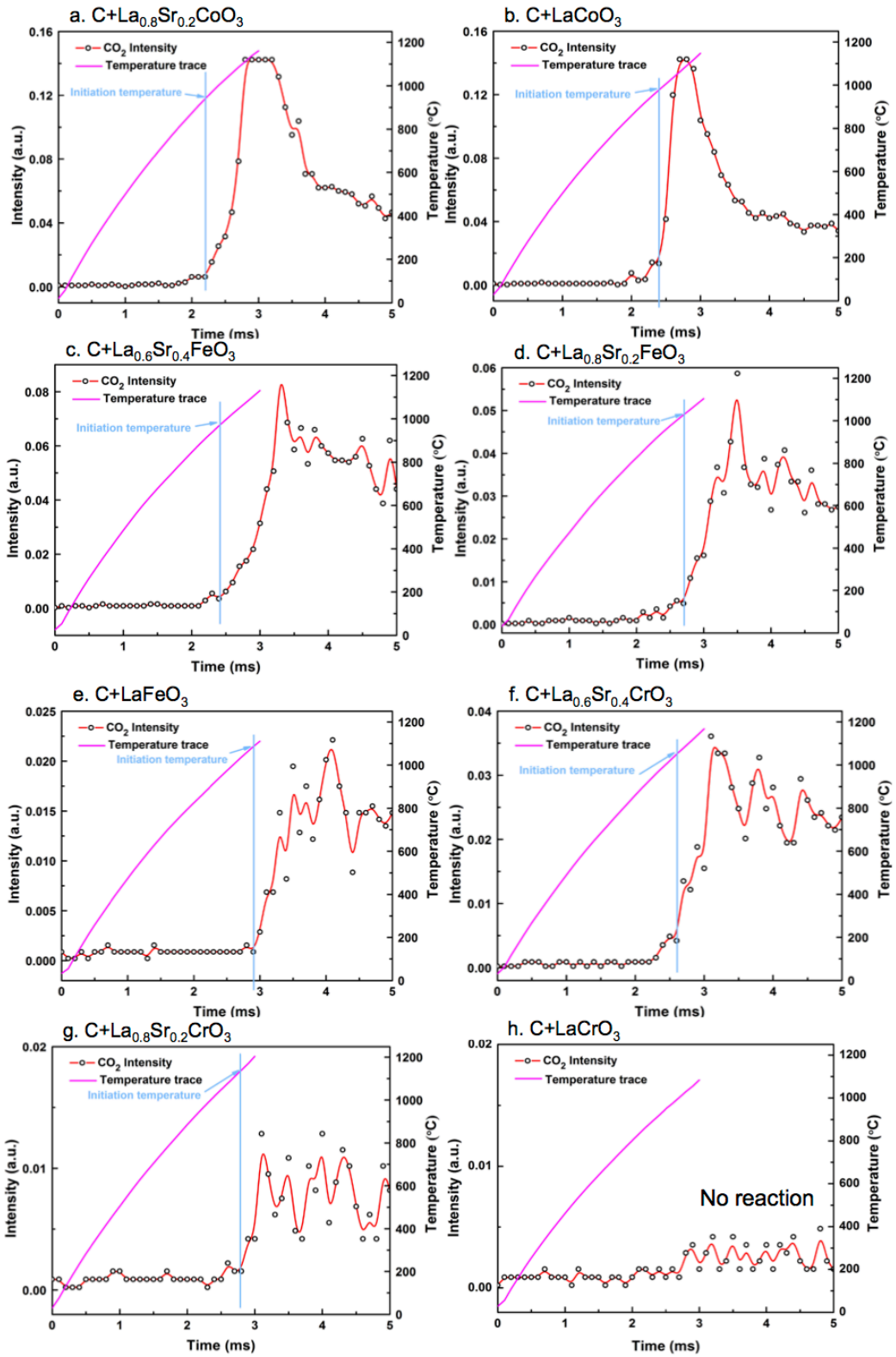

Figure S6.2. Temporal CO_2 release for $C/La_{1-x}Sr_xBO_{3-\delta}$ with in-situ pre heat treat

Table S6.2. Calculated ABE of both doped perovskites and δ-Bi_2O_3 and Vo" of doped δ-Bi_2O_3.

Doped metal oxide	ABE (kJ/mol)	$[V_O^{\cdot\cdot}]$ (#/cm^3)
$LaCrO_{3-\delta}$	183	
$La_{0.8}Sr_{0.2}CrO_{3-\delta}$	176	
$La_{0.6}Sr_{0.4}CrO_{3-\delta}$	170	
$LaCoO_{3-\delta}$	162	
$La_{0.8}Sr_{0.2}CoO_{3-\delta}$	155	
$La_{0.6}Sr_{0.4}CoO_{3-\delta}$	149	
$LaFeO_{3-\delta}$	171	
$La_{0.8}Sr_{0.2}FeO_{3-\delta}$	165	
$La_{0.6}Sr_{0.4}FeO_{3-\delta}$	158	
YSB15	167	1.2E22
YSB30	189	1.2E22
YSB40	203	1.2E22
WSB5	158	9.7E21
WSB10	171	8.0E21
WSB15	184	6.4E21
WSB20	197	4.7E21
ESB15	164	1.2E22
DSB15	163	1.2E22
DWSB10	170	9.9E21
DWSB5	177	8.1E21
DNSB	175	9.6E21

Chapter 7: Study of C/Doped δ-Bi_2O_3 Redox Reactions by In-Operando Synchrotron X-ray Diffraction: Bond Energy/Oxygen Vacancy and Reaction Kinetics Relationship*

Summary

One major technical and economic hurdle on sequestration of CO_2, is its separation from nitrogen when fossil fuels are burned in air. An alternative, thermodynamically equivalent approach is to use a metal oxide as an oxygen carrier (oxidizer), and then recycle the carrier following its reduction by exothermic re-oxidation in air. This process termed chemical looping combustion (CLC), which places many requirements on the oxygen carrier. Here we explore, how to evaluate the relationship between the microscopic properties of an oxygen carrier and its performance in CLC. In this chapter, systematically doped Bi_2O_3 were synthesized as oxygen carriers for the oxidation of carbon. *In-operando* synchrotron X-ray diffraction and on-line mass spectrometry enable us to monitor both the phase evolution in the solid as well as the production of gaseous products. Initiation temperature and reaction kinetics were deduced based on the X-ray diffraction peak intensity change. Results show that lower metal-oxygen bond energy and higher oxygen vacancy concentration of doped Bi_2O_3 led to lower onset temperature, faster reaction rate and smaller activation energy for carbon oxidation. These results provide important insights into manipulating oxygen carrier's microscopic properties for CLC applications.

* The results presented in this chapter have been published in the following journal article: Wang, X. Z.; Jayathilake, R.; Taylor, D. D.; Rodriguez, E. E.; Zachariah, M. R., Study of C/Doped delta-Bi2O3 Redox Reactions by in Operando Synchrotron X-ray Diffraction: Bond Energy/Oxygen Vacancy and Reaction Kinetics Relationships. *J Phys Chem C* **2018,** *122* (16), 8796-8803.

7.1.Introduction

The most convenient method to implement combustion is to use the oxygen in air, which nominally carries a thermal penalty of nitrogen. If one now considers sequestering CO_2, nitrogen poses an additional penalty during any subsequent separation process. One option is to use pure oxygen, i.e., oxy-fuel combustion, which requires a pre-separation process from air.[1-3]

Another approach that would mitigate the need for a nitrogen separation step is to employ an alternative source of oxygen. Not with standing water, which is the most abundant oxygen source but thermodynamically inaccessible as an oxidizer, metal oxides are ubiquitous oxygen carriers and through judicious choice can be used as oxidants to hydrocarbons or solid carbon. Naturally such an approach only makes sense if the reduced oxide can be recycled and if thermodynamically there is little or no loss of overall energy efficiency per mass of fuel.

Chemical looping combustion (CLC) is an approach developed to employ metal oxides as oxygen carriers and to subsequently regenerate them by oxidation in air.[4,5] Since there is no net change in the oxygen carrier, thermodynamically this is equivalent to burning the fuel in air. The scientific challenge then becomes the exact choice of oxygen carrier and involves thermodynamic, kinetic and materials considerations as well as economics. Some important characters of a good oxygen carrier include its reactivity and stability in both reduction and oxidation cycles, and its ability to completely combust fuels. The latter character is important for the application to achieve maximum fuel combustion efficiency.

The central scientific question in choosing from an effective infinite variety of metal oxide combinations is how to choose, and more specifically, what makes for a good oxygen carrier from a microscopy point of view. For obvious reasons transition metal oxides have been the most widely studied, and most focusing on exploring the reaction rate and cycling stability.[6,7] In studies where fuel is gaseous, the most studied simple oxygen carriers by now are Ni-based, Cu-based and Fe-based transition oxides.[8,9] Some other studies focused on direct oxygenation of carbon by those metal oxides. Siriwardane et al.[10] investigated coal CLC over CuO, Fe_2O_3, Co_3O_4, NiO and Mn_2O_3 using TGA and found CuO showed the best reduction/oxidation performance. However, there are large number of variables existing in those metal oxides that might impact CLC performance including, bond energy, oxygen mobility, crystal structure, reaction interface area, thermal conductivity, heat capacity and thermal contact, etc. In order to deal with this complexity a system is needed in which most of the dependent variables can be held constant. To improve the performance of condensed phase CLC between carbon and metal oxide further, more must be known about the mechanism of the reaction.

A mixture of carbon and metal oxide is very similar to a thermite system with essentially the same type of redox reaction. Studies within our group have explored the reaction mechanism of C/CuO reaction by employing temperature-jump time-of-flight mass spectrometer (T-jump/TOFMS) and T-jump TOFMS measurements on C/CuO and bare CuO revealed the evidence of condensed phase initiation of carbon oxidation by CuO.[11] In Chapter 3 and 6, I employed a series of doped perovskites,[12] where crystal structure and morphology were removed as variables, for which I found

a clear correlation between the measured initiation temperature and microscopic properties of the oxidizer, such as metal-oxygen bond energy, oxygen vacancy concentration, and electronegativity. Another group of perovskites was selected as oxygen carriers for methane oxidation in CLC reactions and the oxygen storage capacities of the perovskties were found to be dependent on the electronegativity of the transition metal on the B-site.[13] Another systematic metal oxides I studied were doped δ-Bi_2O_3, where I probed the oxygen-ion conductivity and found that I could correlate this to a threshold condition for reaction with solid fuel (Al, C, Ta) in Chapter 4.[14] Compared with perovskites, doped δ-Bi_2O_3 has higher oxygen mobility with ~25% of the oxygen sites vacant in its fluorite structure, and is a reason why it is commonly employed as an electrolyte in solid-oxide fuel cells.[15,16] The high conductivity δ-phase Bi_2O_3 is only high temperature (730-824 °C) stable but can be stabilized down to room temperature by doping other metal ions.[17-19] Thus in this study, I employ doped δ-Bi_2O_3 as oxygen carriers to study the structure-function relationship of oxygen carrier properties on carbon oxidation for CLC. I employ *in-operando* synchrotron X-ray diffraction (SXRD) to study the trajectory of the reaction of carbon with yttrium and tungsten doped Bi_2O_3, synthesized by aerosol spray pyrolysis. Heating rates were varied to determine the activation energy for the carbon/doped Bi_2O_3 reaction. The results show a very clear connection between oxygen vacancy concentration, average bond energy of oxygen carrier and the initiation temperature, reaction rate and activation energy of carbon/doped Bi_2O_3 redox reaction.

7.2. Experimental Details

Experimental

Nano-sized carbon black (~50 nm) was obtained from Cabot Corporation. $Bi(NO_3)_3 \cdot 5H_2O$ (≥98% pure) and $Y(NO_3)_3 \cdot 6H_2O$ (99.8% pure) were purchased from Sigma-Aldrich. $(NH_4)_6W_{12}O_{39} \cdot xH_2O$ was purchased from Alfa Aesar.

Synthesis of doped Bi_2O_3.

Seven doped Bi_2O_3 listed in Table 7.1 were synthesized by aerosol spray pyrolysis[20-22] at 750 °C with a residence time of about 1 s from metal nitrate contained aqueous solutions formulated with the desired metal ratios.

Table 7.1. Aerosol spray synthesized doped Bi_2O_3.

Doped Bi2O3 formula	Abbreviation
$(Y_{0.15}Bi_{0.85})_2O_3$	YSB15
$(Y_{0.3}Bi_{0.7})_2O_3$	YSB30
$(Y_{0.4}Bi_{0.6})_2O_3$	YSB40
$(W_{0.05}Bi_{0.95})_2O_{3.15}$	WSB5
$(W_{0.1}Bi_{0.9})_2O_{3.3}$	WSB10
$(W_{0.15}Bi_{0.85})_2O_{3.45}$	WSB15
$(W_{0.2}Bi_{0.8})_2O_{3.6}$	WSB20

To dissolve $Bi(NO_3)_3 \cdot 5H_2O$, 2 mol/L nitric acid was used. For example, in order to synthesize $(Y_{0.15}Bi_{0.85})_2O_3$, a 0.2 mol/L precursor solution, containing stoichiometric $Bi(NO_3)_3$ and $Y(NO_3)_3$ was atomized by a nebulizer to generate

nominally 1 μm droplets with compressed air. The atomized droplets flowed through a diffusion dryer, where most of the water was absorbed and then the flow passed to a tubular furnace to produce the desired doped Bi_2O_3 particles. The final product was collected on a Millipore membrane with a pore size of 0.4 micron.

C/Bi_2O_3 composites.

Stoichiometric mixtures of carbon black particles and Bi_2O_3 were mixed and then sonicated in hexane for 30 min and dried in the hood overnight.

Materials characterization.

The crystal structures of the as-synthesized Bi_2O_3 were characterized by X-ray diffraction (XRD) using a Bruker D8 diffractometer with Cu Kα radiation with an average wavelength of 1.54178 Å. Rietveld refinement of all diffraction patterns was performed with the TOPAS 4.2 software[23]. The morphologies of the Bi_2O_3 were measured by scanning electron microscopy (SEM) with a Hitachi SU-70. Size distributions were obtained by measuring 300 individual nanoparticles statistically from SEM images of each sample, using the Nano Measurer 1.2 image analysis software.

***In-operando* synchrotron X-ray powder diffraction**

In-operando synchrotron powder X-ray diffraction (SXRD) experiments were performed in transmission mode on the 17-BM beamline at the Advanced Photon

Source (APS) at Argonne National Laboratory. A 2D PerkinElmer a-Si Flat Panel detector was used with an average wavelength of 0.45336 Å and diffraction images were integrated with GSAS-II[24] giving patterns with a Q-range of approximately 0.2 to 6.2 $Å^{-1}$. A flow-cell/furnace sample holder[25] was used to control sample temperature and atmosphere and the measurement was under a gas flow of 100% He at 15 mL/min. Samples were diluted in fused quartz powder to minimize beam absorption.

To evaluate the redox reaction of C/doped Bi_2O_3, all the samples were heated to 750 °C at 25 °C/min with diffraction patterns collected every 30 s. For C/YSB, the samples were directly cooled down to room temperature after ramping with a cooling rate of ~ 100 °C/min. For C/WSB, after ramping the samples were held at 750 °C for several minutes with diffraction patterns collected every 20 s and then cool down to room temperature with diffraction patterns collected every 30 s. Peak refinement of all diffraction patterns were performed with sequential refinement mode of GSAS-II and TOPAS 4.2.

7.3. Results and Discussion

All of the as-prepared doped Bi_2O_3 were synthesized by aerosol spray pyrolysis and their XRD patterns and representative SEM images results are shown in Figure 5.1-5.2 and Table 5.2. Based on Rietveld refinements on the XRD patterns, all the doped Bi_2O_3 have a single cubic phase in Fm-3m space group with the lattice parameters listed in Table 7.2. Previous published study about aerosol sprayed doped

Bi_2O_3 revealed that synthesized under the same conditions (precursor concentration, follow rate, pyrolysis temperature, etc.) all samples share the same crystal structure and morphology and size distribution.[14] All doped Bi_2O_3 in this study have an average particle size of about 90-100 nm with similar size distribution. With all the doped Bi_2O_3 having the similar crystal structure, particle size and morphology those factors can be considered eliminated as variables in carbon redox reaction. In the previous study, I estimated the metal-oxygen bond energy and oxygen vacancy concentration, $[V_O^{\cdot\cdot}]$, based on the stoichiometry and thermodynamic parameters of doped Bi_2O_3.[14] I estimated the oxygen vacancy concentration, $[V_O^{\cdot\cdot}]$, based on the crystal structure of doped δ-Bi_2O_3. δ-Bi_2O_3 has a defect fluorite-type crystal structure (AX_2) in which 25% of the oxygen sites in the unit cell are vacant.[15] Y^{3+} has the same valence as Bi^{3+}, so it is reasonable to assume that YSB also has ~25% vacant oxygen sites in the unit cell. I will show that Y^{3+} and W^{6+} substitutes for Bi^{3+} at the same lattice site. However, W^{6+} has a higher oxidation state, so WO_3 should correspondingly have ~50% more oxygen than AX_2 in the oxygen sites. The percentage of vacant oxygen sites in one unit cell for each doped Bi_2O_3 is shown in Table 7.2. In one unit cell 8 oxygen ion sites exist. Oxygen vacancy concentrations of YSB and WSB can thus be estimated based on the percentage of vacant oxygen sites in one unit cell and the lattice parameter. The calculated oxygen vacancy percentages in one unit cell and $[V_O^{\cdot\cdot}]$ of those doped Bi_2O_3 are shown in Table 7.2.

The metal-oxygen bond energy of these synthesized doped Bi_2O_3 were estimated based on equation 1, where A stands for Bi, A' is the dopant metal and x is the dopant molar ratio. $\Delta(A-O)$ ($\Delta(A'-O)$) represents the bond energy between A

(A') cation and oxygen and is calculated by equation 2, where $\Delta H_{A_mO_n}$ is the heat of formation of A_mO_n at 298 K, ΔH_A is the heat of sublimation of A-metal at 298 K and D_{O_2} is the dissociation energy of gaseous oxygen (498 kJ/mol).[26] The reader should recognize that equation 1 neglects any enthalpy of mixing of metal oxides. However since I am interested in relative comparisons, I expect this to be a secondary effect. The calculated metal-oxygen bond energy of all doped Bi_2O_3 are listed in Table 7.2. The calculated bond energy increases with the dopant ratio of Y^{3+} and W^{6+}, because the bond energies of Y-O (~291 kJ/mol) and W-O (~406 kJ/mol) are larger than that of Bi-O (~145 kJ/mol).

$$\text{M} - \text{O bond energy} = (1-x)\cdot\Delta(A-O) + x\cdot\Delta(A'-O) \quad (1)$$

$$\Delta(A-O) = \frac{1}{6m}\left(\Delta H_{A_mO_n} - m\Delta H_A - \frac{n}{2}D_{O_2}\right) \quad (2)$$

Table 7.2. Lattice parameter, percentage of vacant oxygen sites in one unit cell, oxygen vacancy concentration and metal-oxygen (M-O) bond energy of doped Bi_2O_3.

Doped Bi_2O_3	Lattice parameters, a (Å)	Percentage of vacant oxygen sites in one unit cell, r (%)	Oxygen vacancy concentration, $[V_O^{\cdot\cdot}]$ (#/cm^3)	M-O bond energy (kJ/mol)
WSB5	5.5985(3)	21.3	9.7E21	158
WSB10	5.5945(2)	17.5	8.0E21	171
WSB15	5.5915(4)	13.8	6.3E21	184
WSB20	5.5565(5)	10	4.7E21	197
YSB15	5.5230(3)	25	1.2E22	167

YSB30	5.4895(8)	25	1.2E22	189
YSB40	5.462(1)	25	1.2E22	203

***In-operando* reaction of carbon with yttrium doped Bi_2O_3**

Figure 7.1a shows a contour plot of SXRD patterns (74 scans) of C/YSB15 at all recorded temperatures at a heating rate of 25 °C/min, with the blue and orange boxes representing heating and cooling respectively. Figure 7.1b shows the temporal temperature profile, indicating a ramping process with a constant heating rate and a rapid cooling process. Figure 7.1c shows representative SXRD patterns of C/YSB15 (selected 8 scans) at selected temperatures, with the blue and orange curves representing heating and cooling respectively. In the SXRD patterns, the δ-phase of Bi_2O_3 dominates the diffraction pattern since carbon black is amorphous. Crystallizing in a cubic structure with space group *Fm*-3*m*, δ-Bi_2O_3 has an anion-deficient fluorite-type structure where the oxide vacancies are disordered.[27] Representative Rietveld refinements for cubic YSB15 is shown in Figure S7.1a with structure information listed in Table S7.1. These results confirmed that Y^{3+} and Bi^{3+} share the same positions in the lattice and that only a single phase exists. As the temperature increased, the peak intensity of C/YSB15 decreased and was almost gone by ~ 650 °C. I regarded the peak intensity decay as the indication of consumption of YSB15 and thus the completion of the oxidation reaction. The redox reaction of C/YSB15 occurs on the order of minutes, necessitating diagnostics such as SXRD, which can collect complete diffraction patterns every 30 s during the reaction. Since

Bi would be molten at these high temperatures, not until the reactor was cooled below ~ 200 °C did I observe the crystallization of elemental Bi. Representative refinement for Bi in rhombohedral *R-3m* is shown in Figure S7.1b.

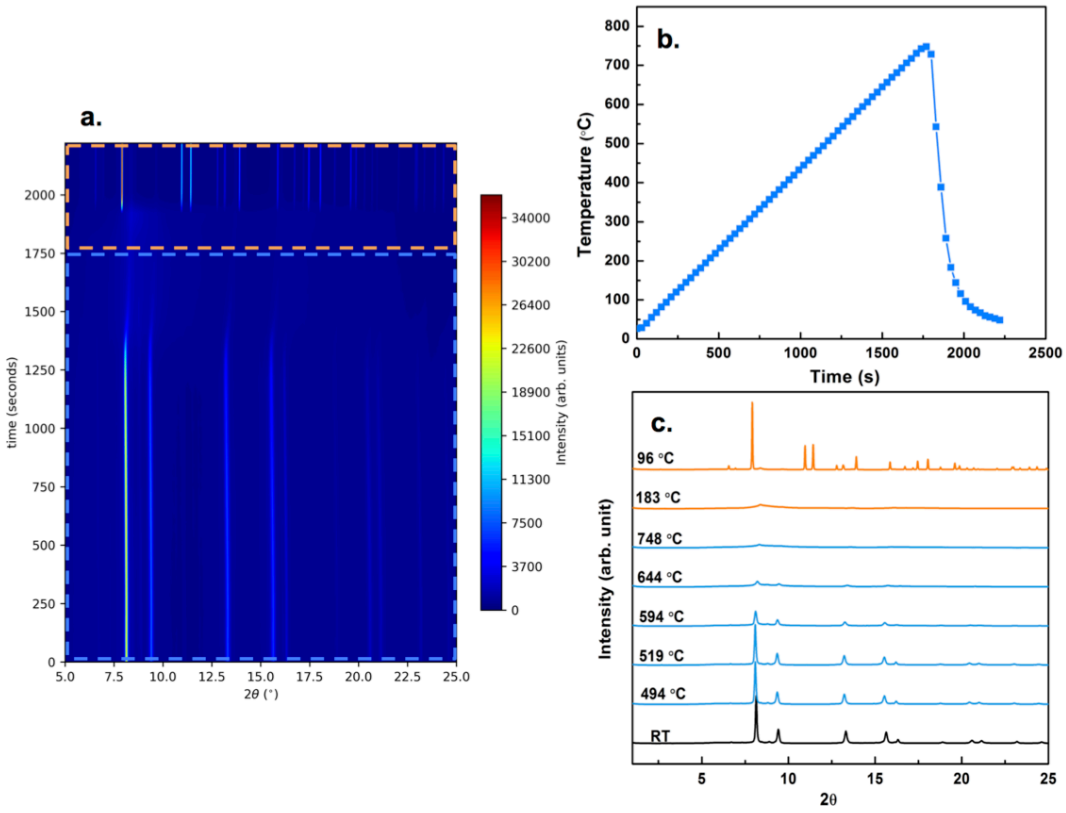

Figure 7.1. *In-operando* SXRD (λ = 0.45336 Å) a. contour plot b. Temperature vs. time and c. Selected patterns for C/YSB15 at a heating rate of 25 °C/min, with the blue and orange boxes/curves representing heating and cooling respectively.

Reaction Energetics

In the previous study of thermite composites of doped Bi_2O_3 with aluminum at high heating rate, I found that ignition temperature (reaction threshold) increased with the metal-oxygen bond energy of doped Bi_2O_3 (oxidizer).[14] A mixture of carbon and

doped Bi_2O_3 is physically similar to a mixture of aluminum and doped Bi_2O_3 and may share reaction energetic properties. YSB15, 30 and 40, with the same $[V_O^{\cdot\cdot}]$, was used as the oxygen carrier to explore the effect of metal-oxygen bond energy on carbon redox initiation temperature. As stated above, the decay of SXRD peaks were regarded as the occurrence of redox reaction. In order to determine the initiation temperature, single peak fits to the (022) Bragg reflection located at $2\theta \approx 13°$ were performed using the sequential refinement mode of GSAS-II. Fractional normalized peak intensity vs. temperature for YSB15, 30 and 40 at a heating rate of 15 °C/min is shown is Figure 7.2a. I found that the peak intensity stayed near constant in time and then had a sharp drop off that was linear. I thus make a tangent to the linear drop-off region and extrapolate till it intersects the near horizontal peak intensity initially seen. This intersection is the onset of reaction. An illustration of initiation temperature determination is shown is Figure S7.2. These initiation temperatures show a clear increase with higher M-O bond energy in Figure 7.2b. The reaction rate can be evaluated by mapping the temperature (x-axis) to time, through the heating rate, and then taking the instantaneous slope of Figure S7.3. The calculated instantaneous reaction rate vs. temperature is shown in Figure 7.2c. C/YSB15 had the highest peak reaction rate and initiates at a lower temperature while C/YSB40 had the lowest peak reaction rate, which occurred at a higher temperature. This is also consistent with a simple observation of Figure 7.2a, the extent of reaction at 750 °C, shows a faster overall rate in the order YSB15> YSB30>YSB40. Plotting the peak reaction rate seen in Figure 7.2c with respect to M-O bond energy also shows that the peak

reaction rate observed scales with bond energy (Figure 7.2d). Lower M-O bond energy leads to earlier and faster reaction.

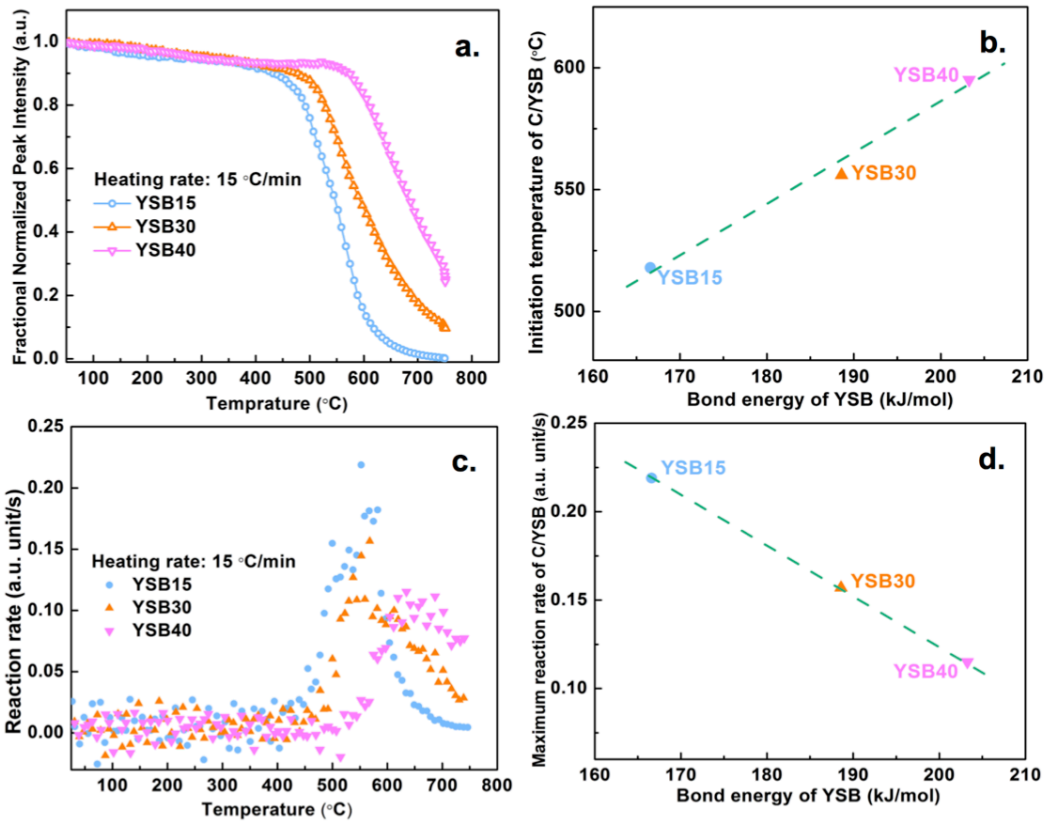

Figure 7.2. a. Fractional normalized peak intensity for the (022) Bragg reflection ($2\theta \approx 13°$) and c. Instantaneous reaction rate for C with YSB15, 30 and 40 at a heating rate of 15 °C/min vs. temperature. b. Initiation temperature and d. Maximum reaction rate of C/YSB at heating rate of 15 °C/min vs. bond energy of YSB.

Activation energy vs. bond energy

A variable heating rate (5, 15, 25 and 50 °C/min) experiment was also performed to determine the apparent activation energy for the initiation reaction of C/YSB. Fractional normalized peak intensity vs. temperature for carbon with YSB at

a heating rate of 25 °C/min is shown is Figure S7.4. Figure 7.3a shows the representative fractional normalized peak intensity vs. temperature for C/YSB30 at different heating rates.

In this study, I employ the Flynn-Wall-Ozawa isoconversion method[28-31] to calculate the apparent activation energy for the reaction initiation. This isoconversion method is based on the principle that the reaction rate at constant extent of conversion is a function only of temperature, which allows for model-free estimates of the activation energy. No assumption on reaction order is needed. I have already studied in chapter 4 that the reaction between solid carbon and solid doped Bi_2O_3 is condensed phase reaction without the revolution of O_2 since doped Bi_2O_3 is stable without decomposition when heated up to its melting point.[14] The Osawa method [29,31] employs equation 4, where β is the heating rate, T is the initiation temperature and E_a is the activation energy for the initiation reaction to determine the apparent activation energy. The results are shown in Figure 7.3b with activation energy determined from the slope of the Arrhenius plot.

$$\ln \beta = const. - \frac{1.052E_a}{RT} \quad (4)$$

The calculated activation energies for initiation of C/YSB15, 30 and 40 are 109, 144 and 238 kJ/mol respectively, which are also plotted in Figure 7.3c showing again a correlation that high M-O bond energy increases the activation energy for reaction. While not a one-for-one comparison the magnitudes of the bond energy and activation energies are remarkably similar and are reminiscent of what one observes for simple bond fission processes.

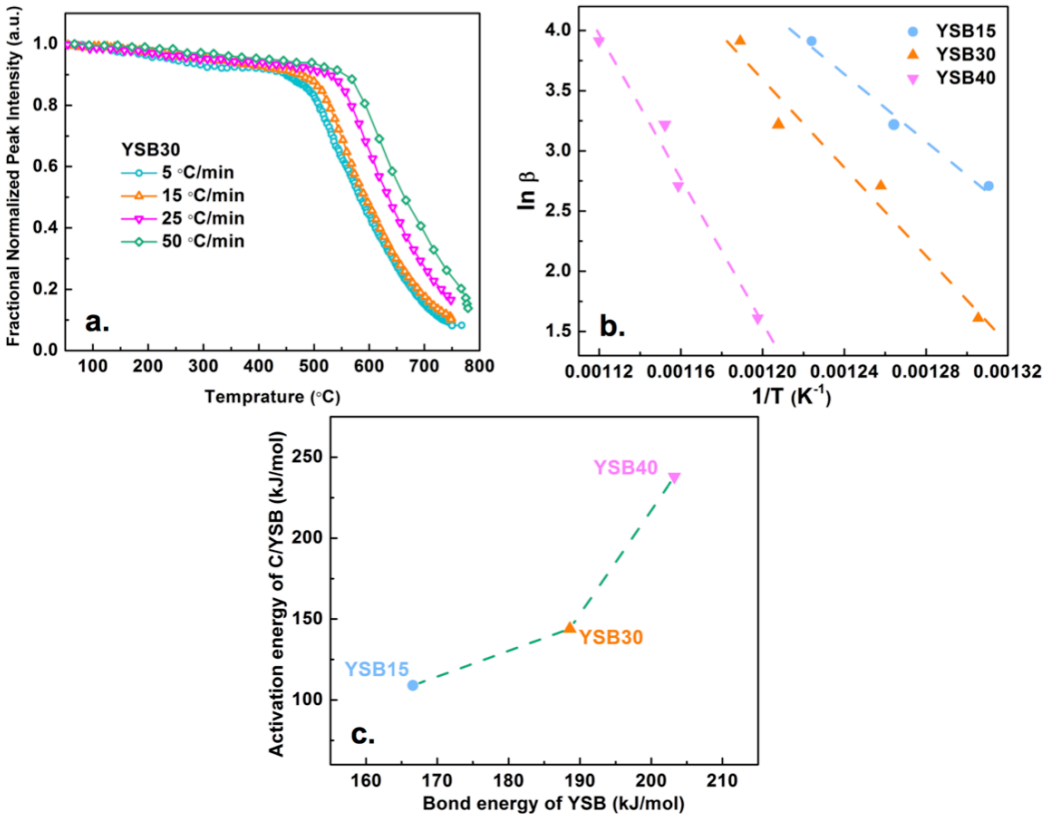

Figure 7.3. a. Fractional normalized peak intensity for the (022) Bragg reflection (2θ ≈ 13°) of YSB30 mixed with carbon at variable heating rate: 5, 15, 25, 50 °C/min vs. temperature b. Arrhenius plots for the Ozawa isoconversion method. c. Activation energy of C/YSB vs. bond energy of YSB.

CO_2 release from the redox reaction

CO_2 was reported to be the main product specie of carbon combustion.[Ref] The release of gaseous product, CO_2 and CO, was in-situ analyzed by a residual gas analyzer (RGA) coupled with the SXRD. Figure 7.4 shows the temporal CO_2 and CO concentration for C/YSB30 at a heating rate of 50 °C/min along with the temperature profile. The appearance of CO_2 at ~570 °C, closely coincides with the initiation temperature determined from the SXRD peak decay. CO on the other hand is only

slightly above background indicating that the combustion was complete with little likely coke formation.

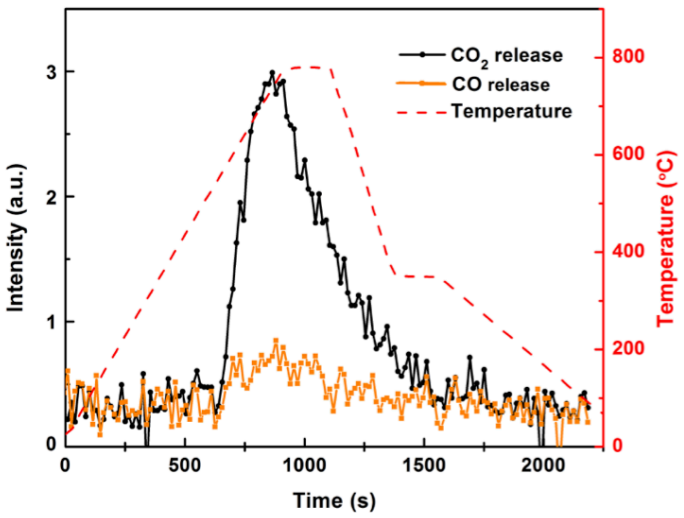

Figure 7.4. Temporal temperature and CO_2 and CO/N_2 release from C/YSB30 at a heating rate of 50 °C/min.

Carbon with tungsten doped Bi_2O_3

Compared with C/YSB composites, I found that the reaction in the C/WSB system to be more complex. Although WSB synthesized in this study was stable at room temperature in the cubic δ-Bi_2O_3 form, it was unstable upon heating. Figure 7.5a shows a contour plot of the SXRD patterns of C/WSB20 at a heating rate of 25 °C /min. Figure 7.5b shows the temporal temperature profile, indicating a ramping up process, a steady-state region, followed by a cooling process. Figure 7.5c shows eight representative SXRD patterns at selected temperatures. Compared with C/YSB, C/WSB20 displays a more complex change during heating. As the temperature

increased I see a shift to higher angle, indicating a decrease in unit cell volume. This transition occurs between 570-610 °C and is highlighted for the reader by the green box denoting the boundaries. After the peak shift, no change in peak intensity is observed until ~ 680 °C, indicting peak shift resulting from thermal effects, and not reaction with carbon. Reaction commences at ~ 680 °C, and the XRD effectively showed little crystal structure by 750 °C. The small peaks at 750 °C were analyzed by peak match shown in Figure S7.5. A broad bump was found between 2θ range of 5~12, which I think belongs to unreacted amorphous carbon and amorphous/liquid bismuth. The other peaks could possibly be assigned to WO_2, WO_3 and Bi_4O_7, indicating partial activity of W^{6+} with carbon. Similar to the case in C/YSB, When cooled, Bragg reflections corresponding to Bi do not appear until the temperature was cooled down below ~ 200 °C as seen in the SXRD patterns in the orange box/curves shown in Figure 7.5a and 7.5c.

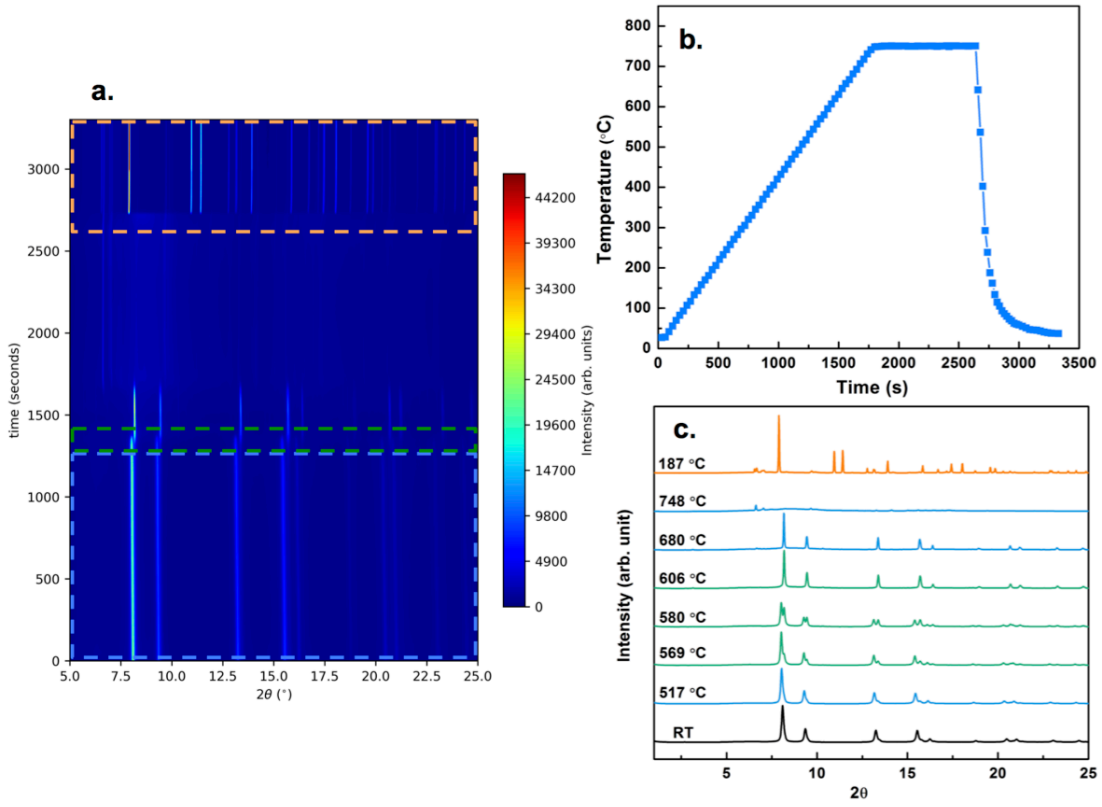

Figure 7.5. *In-operando* SXRD (λ=0.45336 Å) a. Contour plot b. Temperature vs. time and c. Selected patterns for C/WSB20 at a heating rate of 25 °C/min. with the blue box/curves of WSB20 in cubic structure, green showing peak shifts within cubic structure and orange in cooling process.

Contour plots of SXRD patterns and representative SXRD patterns of C/WSB5, C/WSB10, C/WSB15 at selected temperatures are shown in Figure S7.6-S7.8. Similar observations of peak movements from lower angle to higher angle within cubic structure were found for all WSB samples when heated above ~580 (±20) °C. However, for C/WSB5 I also observed a phase change from cubic to monoclinic when heated to ~400 °C and a phase change back to cubic from monoclinic when heated above ~580 °C. A more detailed analysis can be found in the Supplemental Information. In situ XRD of WSB5 (Figure S7.10) shows that even in

the absence of carbon I observe the phase change from cubic to monoclinic but not monoclinic back to cubic. Thus I can conclude that phase change from cubic to monoclinic is due to thermal effects, while phase change from monoclinic back to cubic is due to the interaction with carbon.

Initiation temperature relationship to bond energy and oxygen vacancy concentration

For C/YSB, initiation temperatures were determined based on the peak intensity profile. However, different from C/YSB, whose peak intensity decay was only due to the consumption of YSB, the peak intensity change of C/WSB was more complex. The phase changes between cubic and monoclinic, and peak moves to higher angle might also lead to peak intensity changes. Because the $2\theta \approx 8°$ (single peak (111) for cubic and (132) for monoclinic) sustained a single peak over the whole reaction for C/WSB, I focused on it as the signature for subsequent refinement using TOPAS 4.2. For all samples, in the peak shift range, peak intensities of peaks that are very close at $2\theta \approx 8.0°$ and 8.2 occurred at higher temperature (T>600 °C) were added together. Fractional normalized peak intensity vs. temperature for carbon with WSB5, 10, 15 and 20 at a heating rate of 25 °C/min is shown in Figure S7.11. Initiation temperatures are defined based on the peak intensity change with temperature, and listed in Table S4 with detailed description shown in the Supplemental Information.

The correlation of initiation temperature of C/doped Bi_2O_3 with metal-oxygen energy of doped Bi_2O_3 at a heating rate of 25 °C /min is shown in Figure 7.6. It is apparent that, similar to the C/YSB results, the initiation temperature of C/WSB

increased with metal-oxygen bond energy of doped Bi_2O_3. The initiation temperature of C/WSB5 didn't follow the C/WSB trend, which is probably due to reduced oxygen ion mobility of WSB5 resulting from the phase change from the vacancy abundant cubic to vacancy lean monoclinic structure.[32] It is also noted that C/WSB and C/YSB have different trends of initiation temperature vs. bond energy. This is also likely due to the reduced oxygen vacancy concentration of WSB compared with YSB. For example, WSB15 has similar metal-oxygen bond energy as YSB30, but C/WSB15 reacted at a higher temperature than C/YSB30, which may be due to YSB30 having a larger oxygen vacancy concentration. Thus I conclude that oxygen vacancy also affects the initiation temperature, similar to the previous observation of the oxidation on metals.[12,14]

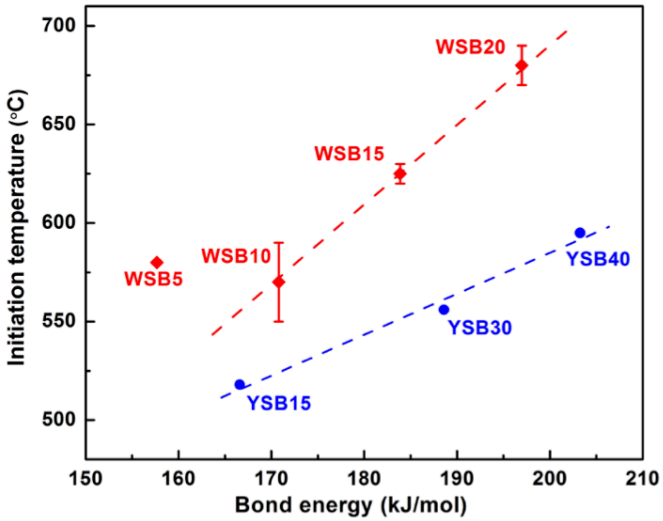

Figure 7.6. Initiation temperature of C/doped Bi_2O_3 vs. bond energy of doped Bi_2O_3.

7.4. Conclusion

In this chapter, systematically doped Bi_2O_3 were employed to better understand how the properties of an oxygen carrier influence the oxidation of carbon for CLC applications. *In-operando* synchrotron X-ray diffraction and on-line mass spectrometry was used to monitor both the phase evolution in the solid as well as the production of gaseous products. Initiation temperature and reaction kinetics were extracted to show that lower metal-oxygen bond energy and higher oxygen vacancy concentration of doped Bi_2O_3 led to lower onset temperature, faster reaction rate and smaller activation energy for carbon oxidation. These results provide important insights into manipulating oxygen carrier's microscopic properties for CLC applications.

Acknowledgments

This work was performed ion collaboration with Dr. Efrain Rodriguez and his graduate student Rishvi Jayathilake and Daniel D. Taylor.

7.5. Supplemental Information

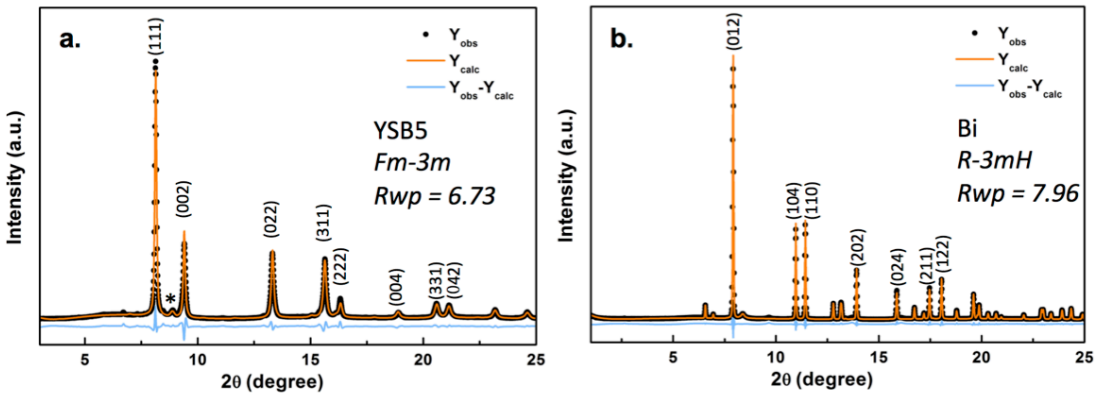

Figure S7.1. Synchrotron X-ray diffraction patterns (λ = 0.45336 Å) with profile fitting based on Rietveld refinements for (a) YSB15 in Fm-3m, asterisk indicates the existence of ~2% Y_2BiO_2 impurity (b) Bismuth in R-3m.

Table S7.1. Rietveld refinement results (structure information with site information, fractional coordinates and thermal parameters) for YSB15 in Fm-3m (Figure 7.3a), indicating Bi and Y share the same position in the lattice.

Atom	Site	x	y	z	Occupancy
Bi1	4	0	0	0	0.59(8)
Y	4	0	0	0	0.41(8)
O1	8	0.25	0.25	0.25	0.284
O2	32	0.302	0.302	0.302	0.094
O3	48	0.5	0.179	0.179	0.015

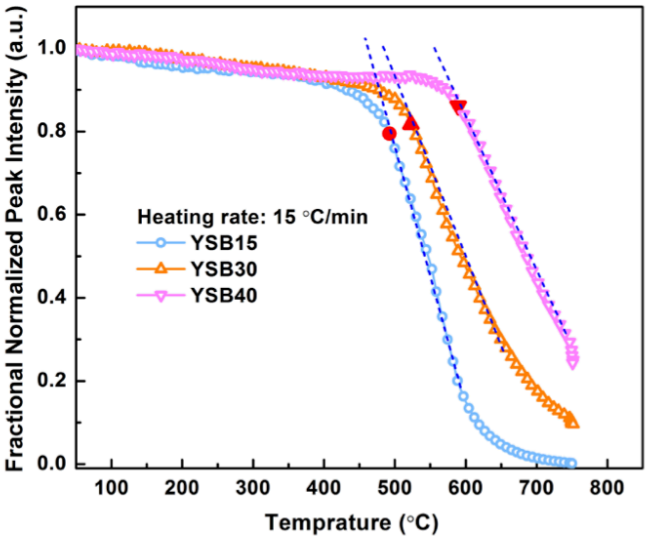

Figure S7.2. Illustration of reaction temperature determination for C with YSB15, 30 and 40 at a heating rate of 15 °C/min.

I found that the peak intensity stayed near constant in time and then had a sharp drop off that was linear. I thus make a tangent to the linear drop-off region and extrapolate till it intersects the near horizontal peak intensity initially seen. This intersection is the onset of reaction. Solid red symbol represents the reaction temperature.

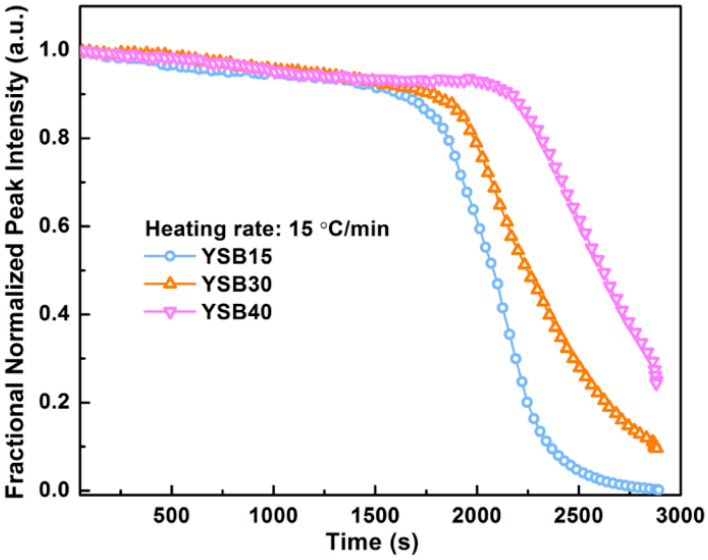

Figure S7.3. Fractional normalized peak intensity at $2\theta \approx 13°$ vs. time for C with YSB15, 30 and 40 at a heating rate of 15 °C/min.

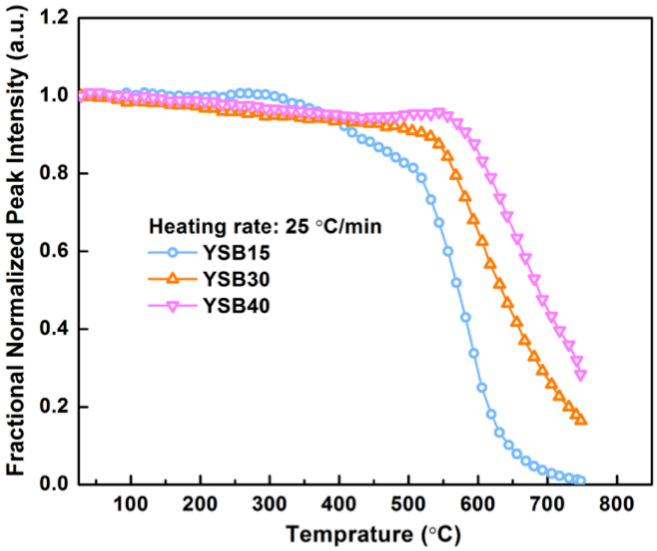

Figure S7.4. Fractional normalized peak intensity of C with YSB15, 30 and 40 at a heating rate of 25 °C/min.

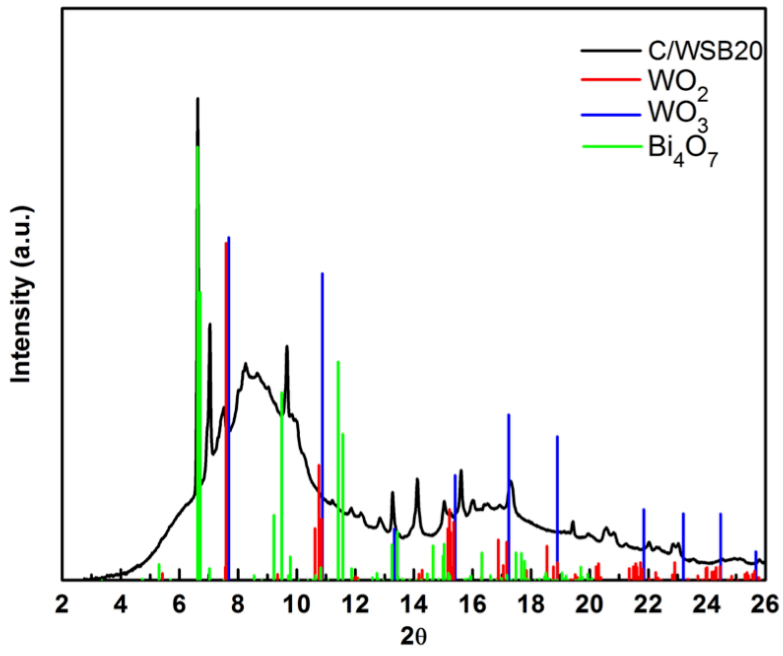

Figure S7.5. Peak match for C/WSB20 at 750 °C.

A broad bump was found between 2θ range of 5~12, which I think belongs to unreacted amorphous carbon and amorphous/liquid bismuth. The other peaks could possibly be assigned to WO_2, WO_3 and Bi_4O_7, indicating partial activity of W^{6+} with carbon.

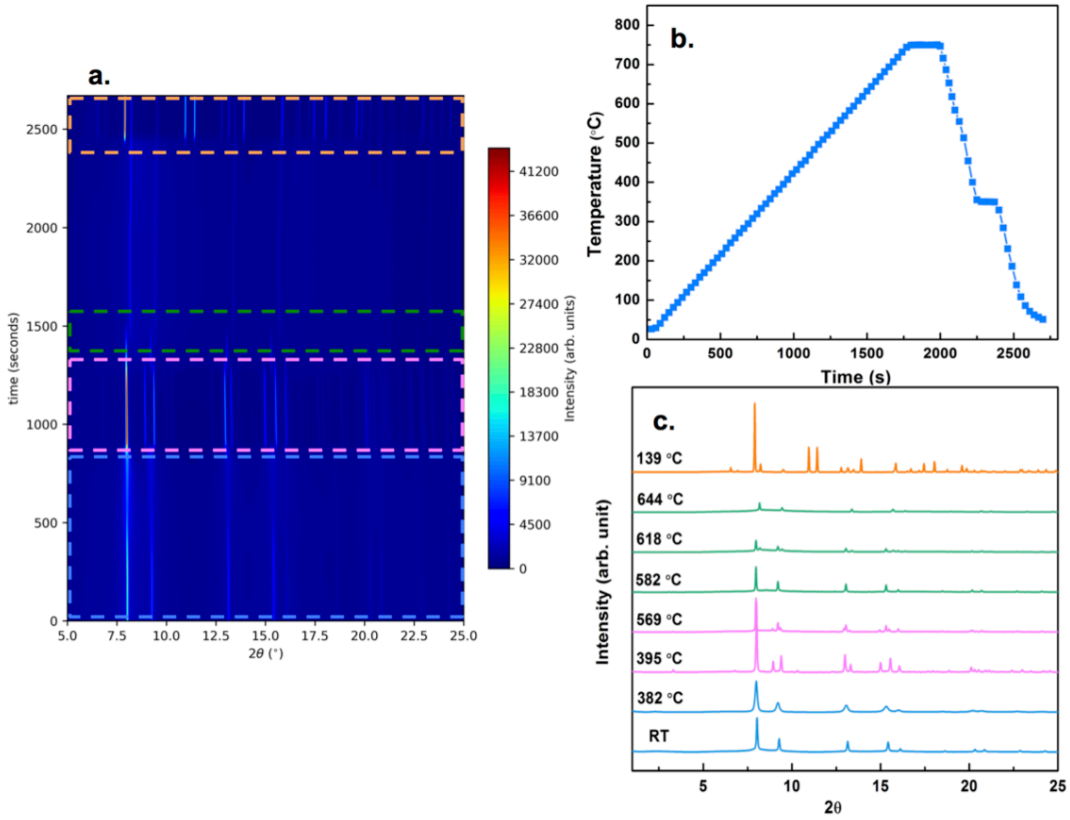

Figure S7.6. *In-operando* SXRD (λ=0.45336 Å) a. Contour plot b. Temperature vs. time and c. Selected patterns for C/WSB5 at a heating rate of 25 °C/min. with the blue box/curves of WSB5 in cubic structure, magenta in monoclinic structure, green showing peak shifts within cubic structure and orange in cooling process.

Representative Rietveld refinements for cubic WSB5 at room temperature is shown in Figure S7.9a with structure information listed in Table S7.2. Starting from the cubic δ-phase, the peak width broadened and intensity weakened upon heating (blue boxed region), which indicated a decrease in crystallinity and possibly

amorphization. When heated above ~400 °C (magenta boxed region), the cubic δ-phase WSB5 transformed to monoclinic structure,[33] with narrower peaks and enhanced peak intensities. A representative refinement with the SXRD data for the monoclinic structure is shown in Figure S7.9b. I thus conclude that upon heating, the cubic structure overcame the kinetic barrier and transformed to the more stable monoclinic phase. As the temperature was further increased above ~580 °C, the monoclinic structure transformed back to cubic structure. In order to know if phase change between cubic to monoclinic of C/WSB5 is due to heat or the interaction with carbon, in situ XRD of bare WSB5 was measured. XRD of neat WSB5 (Figure S7.10) shows that even in the absence of carbon I observe the phase change from cubic to monoclinic at 400~500 °C but no transfer back to cubic when heated above 500 °C. Thus I can safely conclude that phase change from cubic to monoclinic is due to heat and phase change from monoclinic back to cubic is due to the interaction with carbon.

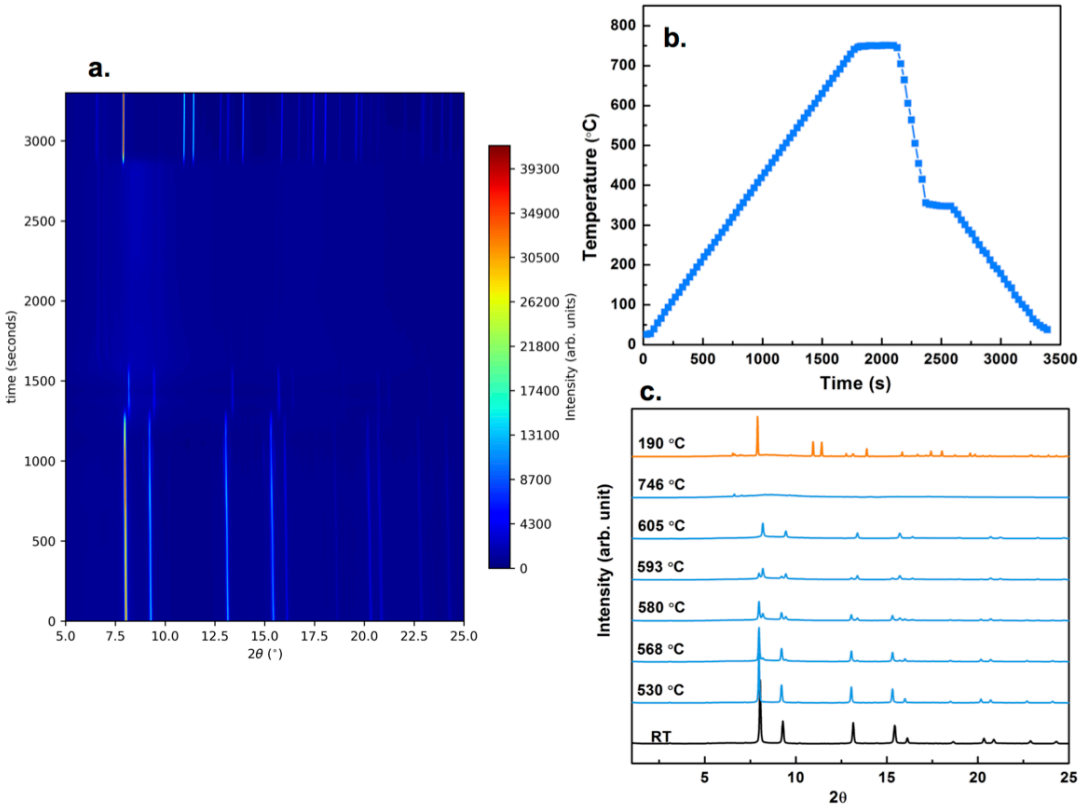

Figure S7.7. *In-operando* SXRD (λ = 0.45336 Å) a. Contour plot and b. Temperature vs. time and c. Selected patterns for C/WSB10 at a heating rate of 25 °C/min, with the blue box/curves of WSB10 upon heating, and orange of Bi upon cooling.

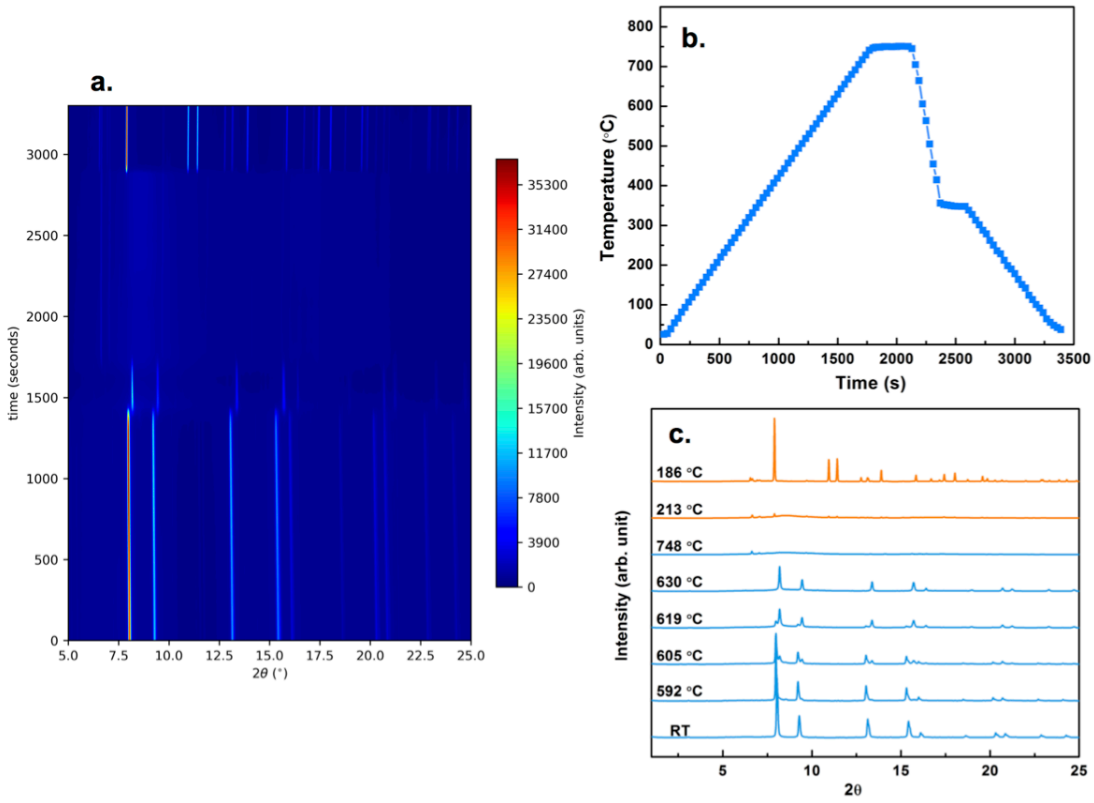

Figure S7.8. *In-operando* SXRD (λ = 0.45336 Å) a. Contour plot and b. Temperature vs. time and c. Selected patterns for C/WSB15 at a heating rate of 25 °C/min, with the blue box/curves of WSB15 upon heating, and orange of Bi upon cooling.

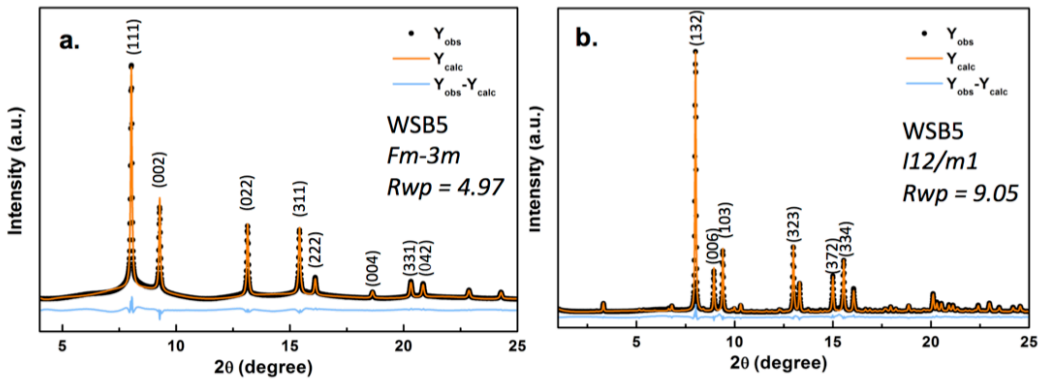

Figure S7.9. Synchrotron X-ray diffraction patterns (λ = 0.45336 Å) with profile fitting based on Rietveld refinements for (a) WSB5 at room temperature in Fm-3m and (b) WSB5 at 395 °C in I12/m1.

Table S7.2. Rietveld refinement results (structure information with site information, fractional coordinates and thermal parameters) for WSB5 in Fm-3m (Figure S7.9a), indicating Bi and W share the same position in the lattice.

Atom	Site	x	y	z	Occupancy
Bi1	4	0	0	0	0.8(2)
W	4	0	0	0	0.2(2)
O1	8	0.25	0.25	0.25	0.43
O2	32	0.354	0.354	0.354	0.08

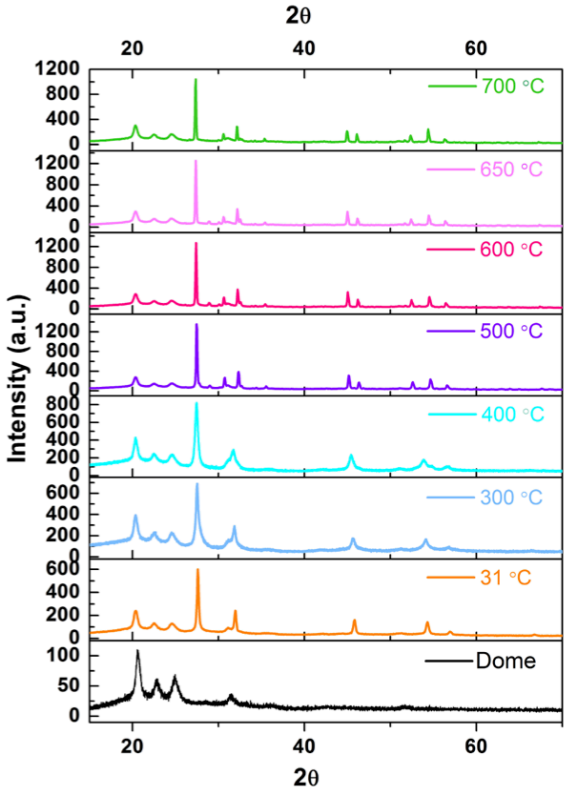

Figure S7.10. In situ XRD for bare WSB5 at different temperature.

All diffraction patterns contains diffraction of protecting plastic dome, which was used to provide enough mechanical stability at high temperature[34] and powder patterns from the plastic dome is provided as reference.

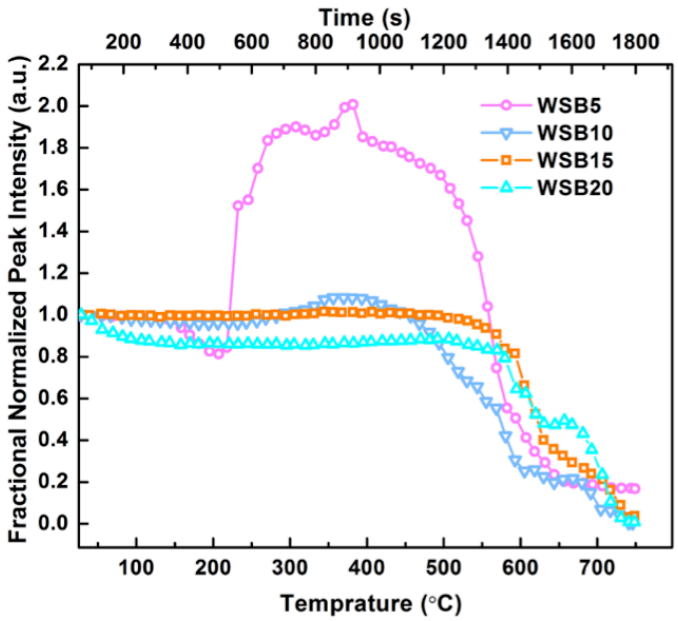

Figure S7.11. Fractional normalized peak intensity of carbon with WSB5, 10, 15 and 20 at a heating rate of 15 °C/min.

For C/WSB20, when temperature was increased above 570 °C up to 610 °C, the peak intensity decreased about 30%, due to peak movements from lower angle to high angle. After the peak movements accomplished at ~ 610 °C, there was no change in peak intensity until ~ 680 °C, indicating no interaction with carbon occurred below 680 °C. When the temperature was further increased above 680 °C, the peak intensity started to decrease dramatically, indicating the occurrence of redox reaction between carbon and WSB20. Thus I regard the initiation temperature of C/WSB20 to be 680 °C.

For C/WSB15, when temperature was further increased above 590 °C to 630 °C, the peak intensity decreased about 40%, which is I believe due to both the

peak shifts and the redox reaction of C/WSB15 since there was not a peak intensity plateau occurred like C/WSB20. So reaction of C/WSB15 definitely occurred before 630 °C. If I assume the peak shifts would lead to ~30% peak intensity decrease for all the WSB samples, as C/WSB20, I can conclude that the reaction of C/WSB15 initiated within the temperature range of 620 to 630 °C.

For C/WSB5, phase change from cubic δ-phase to monoclinic lead to the intensity increase and intensity peaked at ~ 380 °C. As temperature is further increased, the peak intensity dropped rapidly, which are, I believe, due to the phase transfer from monoclinic back to δ-phase, peak shifts and redox reaction between carbon and WSB5. Since I already know that the phase transfer from monoclinic back to cubic was due to the reaction with carbon, I can identify reaction temperature of C/WSB5 to be 580 °C.

C/WSB10 also showed slight trace of phase transfer from cubic δ-phase to monoclinic, which led to slight peak intensity increase (250 °C < T < 450 °C). Using the same analysis method as C/WSB15, the initiation temperature of C/WSB10 can be assigned in the range of 550 to 590 °C. Based on the above discussion, the initiation temperature of C/WSB is listed in Table S7.3.

Table S7.3. Initiation temperature of C/WSB.

Composite	Initiation temperature (°C)
C/WSB5	~580
C/WSB10	~550-590
C/WSB15	~620-630
C/WSB20	~680

Chapter 8: Synthesizing Size Tunable Nanoscale Metal Iodates via Electrospray Co-Precipitation Method*

Summary

Metal iodate, which is an iodine-containing oxidizer, has wide applications in thermite reactions. The large amount of heat as well as iodine generated in the reaction can kill the spores of virulent bacterial. Electrospray technique has been applied in nanoparticles synthesis but it has never been used coupled with liquid-phase reaction. In this chapter, the electrospray co-precipitation method was used to successfully synthesize various nano metal iodates with different morphologies including $Cr(IO_3)_3$, $Mn(IO_3)_2$, $Fe(IO_3)_3$, $Ni(IO_3)_2$, $Zn(IO_3)_2$, and $Bi(IO_3)_3$ for the first time, to the author's knowledge. The $Bi(IO_3)_3$ system was chosen to investigate the effect of experimental parameters such as concentration of precursor on nanoparticle's morphology and particle size. The composition, morphology and size of the nanoparticles were investigated by XRD, TGA, SEM and TEM adequately. The results showed that by using the electrospray co-precipitation method, the morphology and particles size could be tuned from around 10 nm to hundreds of nanometers by varying certain experimental parameters.

8.1. Introduction

Metal iodate, is an iodine-containing oxidizer, has received a lot of attention recently because of its potential application in dealing with biological weapons

* I would like to thank my collaborators for this study, Mei Wang (contribute equally), Dr. Haiyang Wang, Yong Yang, Tao Wu, Dr. Xinliang Mei and Dr. Chengbo Ru for all their hard work and input that made this chapter possible.

through the release of iodine during the thermite reaction shown in the following equation.[1]

$$nAl + M(IO_3)_n \rightarrow \frac{n}{2}Al_2O_3 + M + \frac{n}{2}I_2 + \Delta H$$

The spores' high resistance to heat forms a barrier against the traditional energetic materials and prevents complete neutralization. Adding biocidal agents such as iodine provided a good way to bypass this problem.[2] It was found that adding iodine thermites not only accelerated its ignition and burn time, the releasing of the iodine could also enhance the neutralization of the heat resistant bacterial spores.[3] Several methods have been used to synthesize the metal iodates. Xu et al. and Huang's group have used the hydrothermal method to synthesize the silver manganese mixed metal iodates $AgMn(IO_3)_3$ and $AgMn(IO_3)_4$ along with monovalent metal gold iodates and their thermal stabilities were studied.[4] Phanon et al. employed the method of evaporating the nitric acid solution containing metal salts mixed with $LiIO_3$ solution to synthesize $Zn(IO_3)_2$, $Mn(IO_3)_2$, $Co(IO_3)_2$, $Mg(IO_3)_2$ and β-$Ni(IO_3)_2$ and studied their structures, decomposition temperature.[5] Wang et al. and Hu et al. have used the wet chemistry co-precipitation method to synthesize the $Bi(IO_3)_3$ particles and found uniformed particles were formed with particle size around 90 nm.[6]

Electrospray is used for liquid atomization by applying electrical force. The idea of the electrospray was first introduced in 1882 when Lord Rayleigh indicated that there is a limit on the amount of charge that a liquid droplet could carry.[7] It is a method that liquid atomizes into small droplets by means of electrical forces. In the electrospray process, a liquid containing the precursor of binders, sorbents and functional particles, flows out through a small nozzle connected to a high voltage. In

electrospray, the liquid is dispersed into small, charged monodisperse droplets due to that charges build up on the surface, which create a columbic driven hydrodynamic instability that overcomes the surface tension of the solution.[8] Based on the cone-jet mode theory, the size of charged droplets can be controlled by tuning the applied voltage, flow rate, and electric conductivity of the liquid. Compared with other liquid atomization methods, electrospray has several advantages. The fine droplets formed by electrospray can be very small, which could go down to microns or nanometers. The size distribution of droplets generated by electrospray is usually narrow which allows production of particles of nearly uniform size. In addition, due to their mutual repulsion the charged droplets are self-dispersing in the space and therefore would not coalesce together.[9] Because of these advantages, electrospray has been widely used in nanotechnology. Due to high surface energy of nano particles, they agglomerate easily and result in particles of non-uniform size distribution. The electrospray method serves a good way to solve the problem and has also been widely used for nano particles production. However, no work has been reported so far to use the electrospray method for the liquid phase co-precipitation reaction. In this chapter, the electrospray co-precipitation method was used to synthesize various nano metal iodates with different morphologies including $Cr(IO_3)_3$, $Mn(IO_3)_2$, $Fe(IO_3)_3$, $Ni(IO_3)_2$, $Zn(IO_3)_2$, $Bi(IO_3)_3$ successfully. The $Bi(IO_3)_3$ system was chosen to investigate the effect of the experimental parameters such as concentration of precursor and precipitant on nanoparticle's morphology and particle size for its near spherical morphology and superior combustion performance. The composition, morphology, and size of the nanoparticles were investigated by X-ray diffraction (XRD),

thermogravimetry analysis (TGA), scanning electron microscopy (SEM) and transition electron microscopy (TEM). The characterization results showed that by using the electrospray co-precipitation method, the particles size of bismuth iodate can be tuned from around 10 nm to hundreds of nanometers. These particles not only had a uniform size distribution, but also had a spherical-shaped morphology.

8.2. Experimental

Chemicals.

Bismuth (III) nitrate pentahydarate (98.0%), chromium (III) nitrate nonahydrate (99.0%), manganese (II) acetate tetrahydrate (99.99%), iron(III) nitrate nonahydrate (98.0%), nickel(II) acetate tetrahydrate (99.0%) were purchased from Sigma-Aldrich, zinc (II) chloride (99.0%) and nitric acid (69.5%) were purchased from Fisher Chemicals and iodic acid (99.5%) was purchased from Alfa Aesar. All reagents used in the experiments were of analytical grade purity and were used without any further purification. To dissolve bismuth (III) nitrate pentahydarate, 2 M nitric acid was used.

Electrospray Set-up and Synthesis of Metal Iodates.

All metal iodates were synthesized by the home-built electrospray co-precipitation system, as shown in the Figure 8.1. A pump connected to a syringe was used to generate continuous flow at a desired speed in the electrospray system. The syringe contained metal salts precursor (solution A) while the top of the syringe was a connected to a nozzle which is a stainless capillary with the inner diameter of 150 microns. The capillary was maintained at a positive voltage which can be tuned with

a range of 0-5000V. A copper ring was grounded at the position a few millimeters below the capillary. The voltage difference between the capillary and the copper ring was tuned to generate the stable Taylor cone electrospray. A glass beaker containing iodic acid (solution B) maintained with negative 2000 volts, was used to accelerate the charged droplets as well as being the reactor for the co-precipitation reaction. In this study, $Cr(IO_3)_3$, $Mn(IO_3)_2$, $Fe(IO_3)_3$, $Ni(IO_3)_2$, $Zn(IO_3)_2$, $Bi(IO_3)_3$ were synthesized and shown in Table 8.1. The flowrate of solution A to be sprayed out was set at 4 mL/h. The reaction duration was set for 2 h with strong stirring to obtain the precipitates. The precipitates were washed by deionized water for 6 times and then dried in the oven at 75 °C for 12 h.

Table 8.1. Synthesis of various metal iodates.

Metal iodates	Solution A/concentration	Solution B/concentration
$Cr(IO_3)_3$	$Cr(NO_3)_3$/ 0.5 M	HIO_3/ 2.5 M
$Mn(IO_3)_2$	$Mn(AC)_2$ /0.5 M	HIO_3/ 2.5 M
$Fe(IO_3)_3$	$Fe(NO_3)_3$ /0.5 M	HIO_3/ 2.5 M
$Ni(IO_3)_2$	$Ni(AC)_2$ /0.5 M	HIO_3/ 2.5 M
$Zn(IO_3)_2$	$ZnCl_2$ /0.5 M	HIO_3/ 2.5 M
$Bi(IO_3)_3$	$Bi(NO_3)_3$/0.5 M + HIO_3 /2M	HIO_3/ 2.5 M

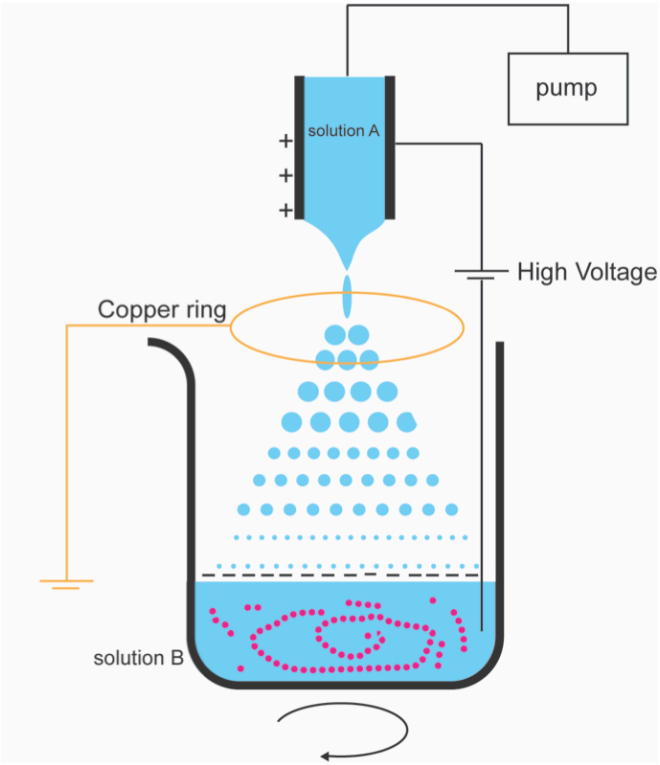

Figure 8.1. Schematic of electrospray co-precipitation set-up.

Crystal structure, morphology and structure stability of metal iodate

The crystal structures of the synthesized metal iodate were characterized by X-ray diffraction (XRD) performed on a Bruker D8 diffractometer with Cu Kα radiation. The morphologies of the particles were measured by scanning electron microscopy (SEM) with a Hitachi SU-70 and transition electron microscopy (TEM) with a JEM 2100. Size distributions were obtained by measuring 50 individual nanoparticles statistically from SEM images of each sample, using Nano Measurer 1.2 image analysis software. Thermogravimetry analysis (TGA) and differential scanning calorimetry (DSC) measurements were obtained by a TA Instrument Q600,

ramping at 10 °C/min from room temperature to 1000 °C under 100 ml/min of argon flow.

8.3. Results and Discussion

Figure 8.2 showed the SEM images of the synthesized samples showed that various metal iodates with different morphologies were successfully prepared via the electrospray co-precipitation method. The results indicated that $Mn(IO_3)_2$ and $Zn(IO_3)_2$ have similar needle-like shape structure. This result collaborates with previous reports that $Zn(IO_3)_2$, $Mn(IO_3)_2$, $Mg(IO_3)_2$ and $Co(IO_3)_2$ are isostructural.[10] According to the images, $Mn(IO_3)_2$ has the diameter of around 150 nm in width and the length size range of 500 nm~1100 nm. Similarly, $Zn(IO_3)_2$ have the diameter of around 200 nm in width and the length size range of 500 nm~2400 nm. $Cr(IO_3)_3$, $Bi(IO_3)_3$, $Fe(IO_3)_3$, and $Ni(IO_3)_2$ are of similar structures and morphology. They are of the irregular shape from oval to sphere. The average diameters of $Cr(IO_3)_3$, $Bi(IO_3)_2$, $Fe(IO_3)_3$, $Ni(IO_3)_2$ are around 50 nm, 100 nm, 110 nm and 200 nm respectively.

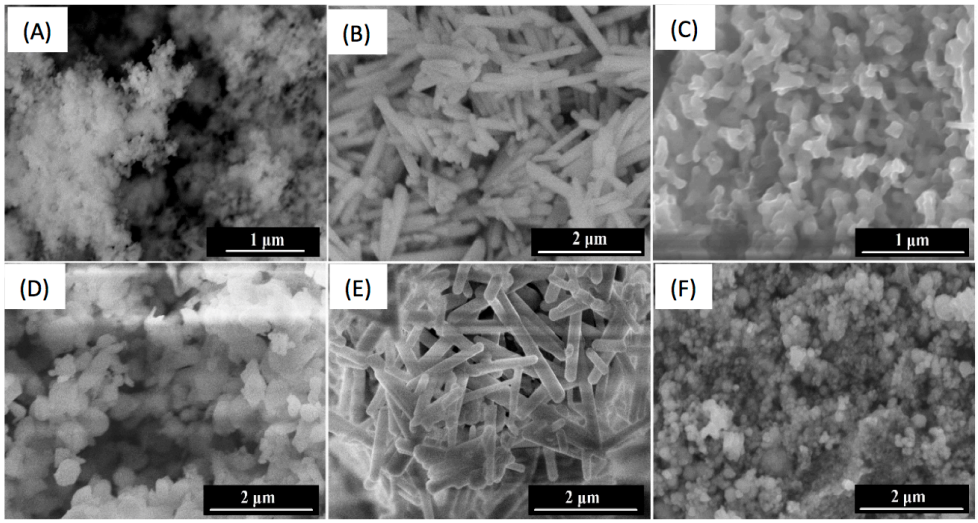

Figure 8.2. SEM images of various metal iodates synthesized by electrospray co-precipitation method A) $Cr(IO_3)_3$, B) $Mn(IO_3)_2$, C) $Fe(IO_3)_3$, D) $Ni(IO_3)_2$, E) $Zn(IO_3)_2$, F) $Bi(IO_3)_3$.

Crystal structure

The composition of the synthesized sample was characterized by the X-Ray Diffraction and its spectra of as prepared $Bi(IO_3)_3$ was shown in Figure 8.3. According to the XRD results, the $Bi(IO_3)_3$ sample obtained directly from the electrospray co-precipitation method (shown in red line) was amorphous because it was synthesized at the room temperature, which is consistent with previous findings.[11] In order to further confirm the composition of as-prepared sample, the sample was sintered at 375 °C for 10 min to crystalize and its XRD pattern was obtained (blue line). For comparison, the XRD pattern of the pure $Bi(IO_3)_3$ (PDF 01-073-5236) was also shown in Figure 8.3 (black line). It is obvious that the sintered sample contains $Bi(IO_3)_3$ with diffraction peaks referred to the characteristic refraction plane of (-1 1 2), (0 1 3) (2 1 0) (1 1 3), (-2 -1 2), (-1 0 5), (3 0 1). This

shows that after sintering, the $Bi(IO_3)_3$ sample has the monoclinic structure and it belongs to the $P2_{1/n}$(N 14) group with the unit cell dimension of a=8.88 Å, b = 5.94 Å and c = 15.24 Å.[12] The XRD result suggests that pure $Bi(IO_3)_3$ was successfully prepared by the electrospray co-precipitation method.

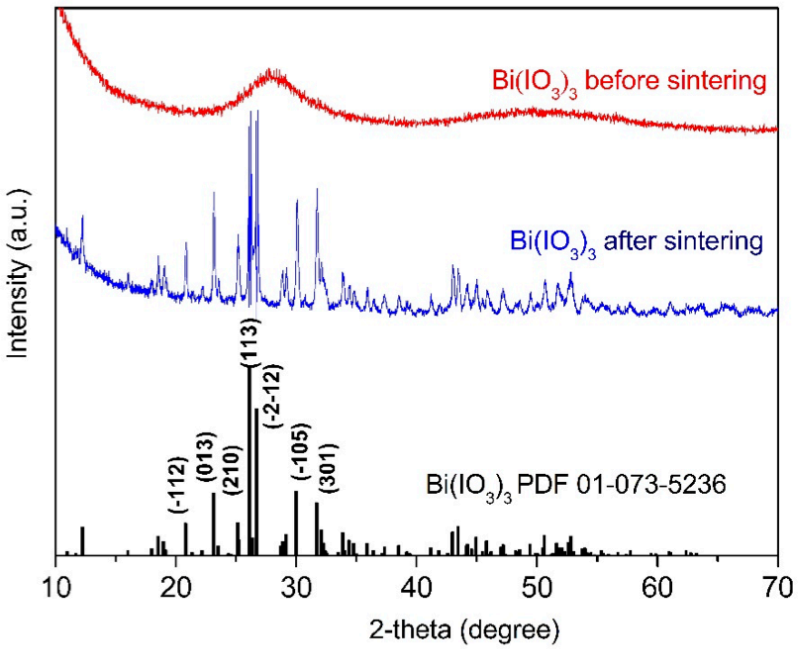

Figure 8.3. XRD spectra of prepared sample before and after annealing.

TGA and DSC Analysis

In order to further confirm the composition of $Bi(IO_3)_3$, TGA analysis was performed and the result of the as-prepared $Bi(IO_3)_3$ was shown in Figure 8.4. The weight loss during 30 °C to around 200 °C is due to the loss of free water and bond water. The DSC curve indicated that there are two exothermic steps at the 275°C and

350 °C while without weight loss in TAG. These may be corresponding with the amorphous $Bi(IO_3)_3$ transition to crystalline and the transition between the crystalline phases. The mass loss beginning from the 425 °C is because of the decomposition of the $Bi(IO_3)_3$. The final weight remaining is 31.83%. Based on the decomposition of $Bi(IO_3)_3$, the theoretical weight left will be 31.75%, which is almost the same as the experimental result.

$$2Bi(IO_3)_3 \rightarrow Bi_2O_3 + 3I_2 + 3O_2 \qquad (2)$$

The TGA and DSC result further confirmed that by using the electrospray co-precipitation method, $Bi(IO_3)_3$ could be synthesized with almost no impurities.

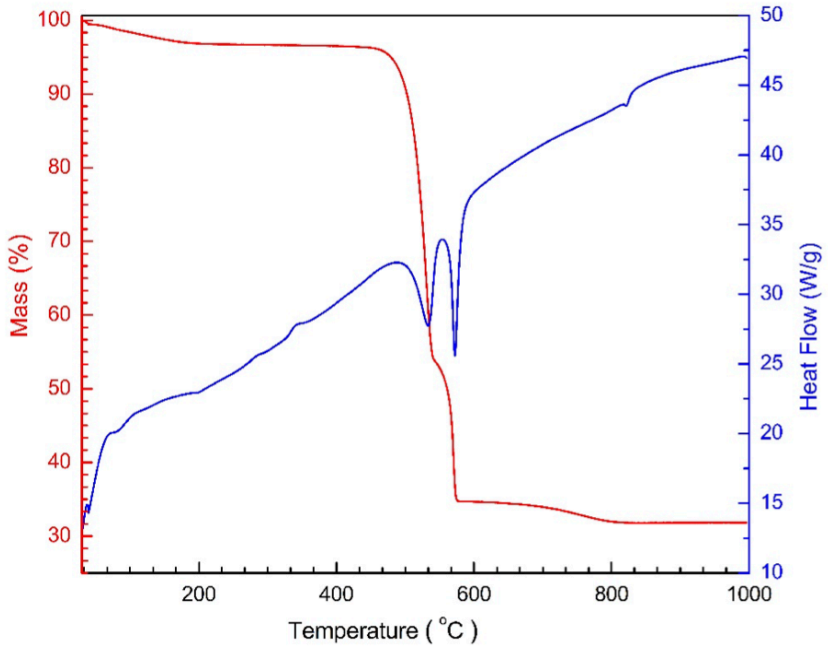

Figure 8.4. TGA and DSC results of $Bi(IO_3)_3$

Morphology and microstructure of $Bi(IO_3)_3$

To investigate how to synthesize size tunable metal iodate by varying the experimental parameters in the electrospray co-precipitation method, I pick $Bi(IO_3)_3$ as a representative since $Bi(IO_3)_3$ is a highly reactive oxidizer. Previous research shows that there is a correlation between the mass loading of sprayed precursors and average particle diameter.[13] This suggests it is possible that varying the concentration of $Bi(NO_3)_3$ could lead to particles with different sizes. In this study, the concentration of $Bi(NO_3)_3$ precursor in the syringe was varied from 0.1M to 2.0M. The beaker contains 2 ml of 5 M HIO_3 solution which is of a large excess compared to the concentration of the solution in the syringe. The concentration of HIO_3 was specifically chosen: a. since the concentration of bismuth nitrate sprayed out remains constant during the reaction period, the large excess of iodic acid enables its concentration as well as the supersaturation of the system to be regarded as almost constant, making more uniform size distribution particles; b, high concentration of HIO_3 could also guarantee the acidity of the system and avoid the formation of oxynitrates as well as the purity of $Bi(IO_3)_3$ product.[14]

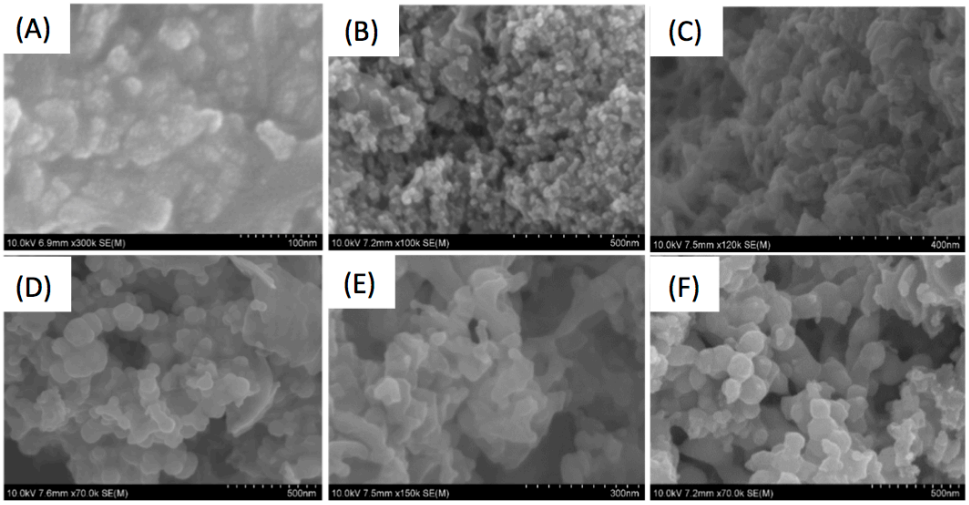

Figure 8.5. SEM images of $Bi(IO_3)_3$ with different concentration of $Bi(NO_3)_3$ precursor solution (A)0.1M, (B)0.5 M, (c)0.6M, (D)1.0M, (E)1.5M, (F)2.0M.

Figure 8.5 shows the SEM images of the as-prepared sample with different concentration of the $Bi(NO_3)_3$ precursor solution. The SEM results further confirmed that the morphology of the prepared $Bi(IO_3)_3$ samples were irregular shaped from oval to sphere and the particles were closely packed together. However, when the concentration of bismuth nitrate is 0.1M, the morphology and size distribution of the prepared $Bi(IO_3)_3$ cannot be seen clearly from SEM. In order to further confirm the size and morphology of the $Bi(IO_3)_3$ particles as well as rule out the interference of the gold particles to make the samples conductive, the TEM characterization of the particles was performed and shown as Figure 8.6.

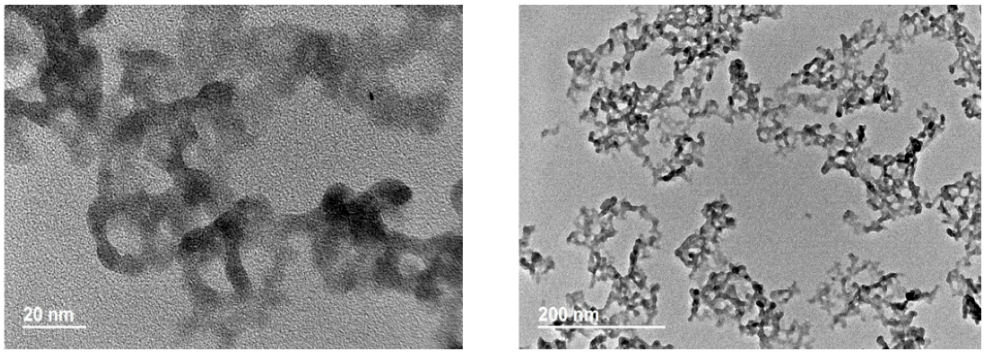

Figure 8.6. TEM images of $Bi(IO_3)_3$ with concentration of $Bi(NO_3)_3$ precursor solution 0.1M.

The TEM results indicated that the average size diameter of the $Bi(IO_3)_3$ is around 11nm. The particles were monodispersed and the size distribution was very uniform. Figure 8.7 shows the average size of $Bi(IO_3)_3$ particles vs. the concentration of $Bi(NO_3)_3$ solutions and I found a direct correlation between them: $Bi(IO_3)_3$ particle size increases with the concentration of $Bi(NO_3)_3$. The concentrations of the $Bi(NO_3)_3$ were 0.1M, 0.5M, 0.6M, 1.0M, 1.5M and 2.0M and the corresponding average size diameters of $Bi(IO_3)_3$ were 11 nm, 25 nm, 31 nm, 65 nm, 37nm and 72 nm respectively.

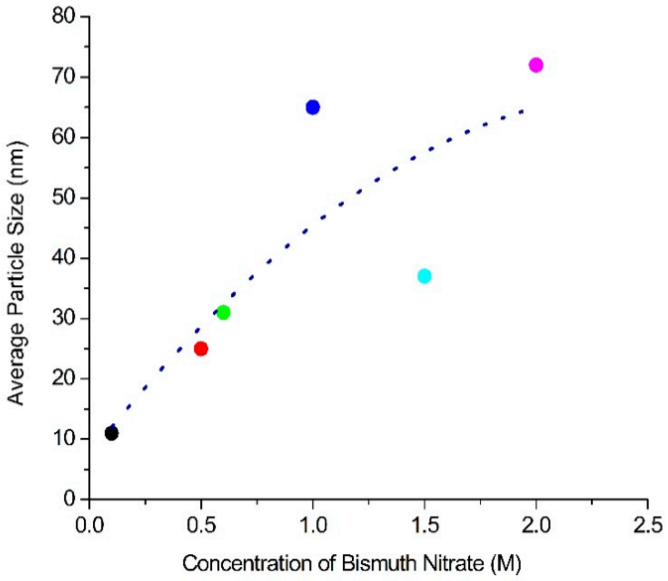

Figure 8.7. Average $Bi(IO_3)_3$ particles size with different concentration of $Bi(NO_3)_3$ precursor solution.

In order to investigate the mechanism of the reaction and why the particle size of $Bi(IO_3)_3$ increases with the concentration of $Bi(NO_3)_3$, it is important to compare the droplets size sprayed out in the electrospray system. I sprayed the $Bi(NO_3)_3$ precursor solution directly to an aluminum foil substrate. The distance between the substrate and the nozzle was the same as that between the nozzle and surface of the HIO_3 solution and the same flow rate and voltage were also applied as the synthesis process.[15] The SEM results were shown in Figure 8.8.

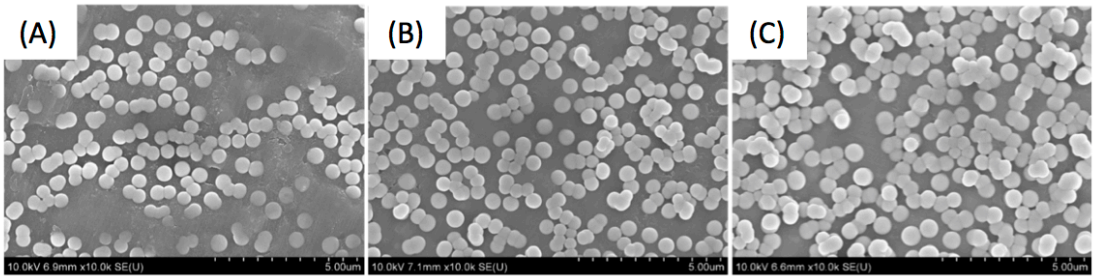

Figure 8.8. SEM images of $Bi(NO_3)_3$ precursor solution (A) 0.2M, (B) 0.5 M and (C) 1.0 M.

During the experiments, it was observed that when the droplets reached the substrate, they were not dried yet. The particles shown in the picture were $Bi(NO_3)_3$ dry particles indicating the projection of the droplet size reaching the surface of the HIO_3 solution. Based on the results, the corresponding average droplet size are 500 nm, 505 nm and 524 nm corresponding to the $Bi(NO_3)_3$ precursor solution of 0.2 M, 0.5 M, 1.0 M respectively, which indicated that the droplets reaching the beaker are almost the same even though I vary the precursor concentration. Based on the scaling law, the droplet size sprayed out is a function of the liquid conductivity, surface tension, flowrate and liquid viscosity.[16] Since $Bi(NO_3)_3$ is dissolved in HNO_3 solution, its concentration would not change those parameters greatly. From the SEM results, I can also know that the size distribution of the droplets is very narrow, which also confirmed that using the electrospray atomization method, droplets of very narrow size distribution could be created. The mechanism for smaller $Bi(NO_3)_3$ concentration can form smaller particles might be explained by classical nucleation and growth theory, illustrated in Figure 8.9.

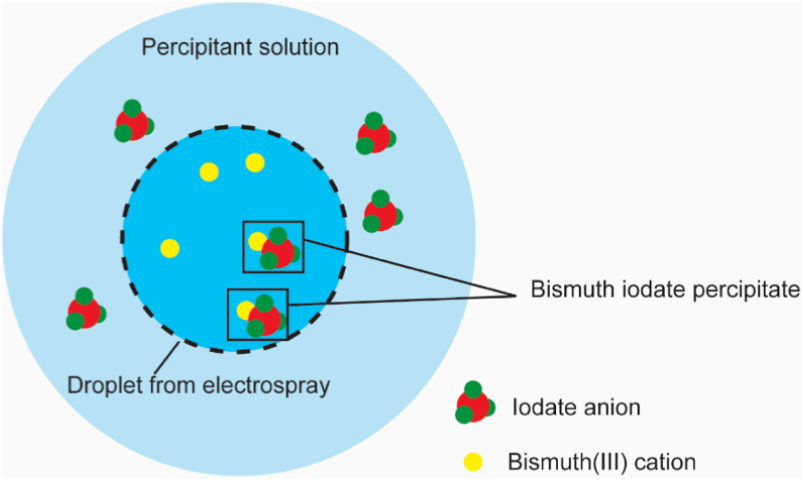

Figure 8.9. Proposed reaction process.

When the droplets entered the beaker, the reaction rate was very fast and the Bi^{3+} will react with IO_3^- before it diffused in HIO_3 solution. Since the droplets entering the beaker are of the same sizes, but of different concentrations, each droplet can be regarded as a micro-reactor, in which the precipitation reaction occurred. The micro-reactor enabled the nucleation and growth steps to happen in a controlled more reproducible manner.[17] The larger concentration of $Bi(NO_3)_3$ droplets contained more reactant in one droplet, thus more $Bi(IO_3)_3$ monomers will form in one droplet. It is also known that the particle growth rate is proportional to solute concentration and a higher monomer concentration leads to a larger growth rate resulting a growth into a bigger particles.[18] Similar result was found in previous report that the increased metal salts concentration leads to larger particles with wider size distribution.[19]

I further reverse the solution in the spray to that with the beaker to check whether a similar trend exists as well as confirm the proposed mechanism. Different concentration of HIO_3 droplets were sprayed out from the syringe with the beaker

containing a constant 5M concentration of $Bi(NO_3)_3$, which is large excess of the concentration of HIO_3 in order to maintain high reaction rate. The corresponding particle sizes are shown in Figure 8.10.

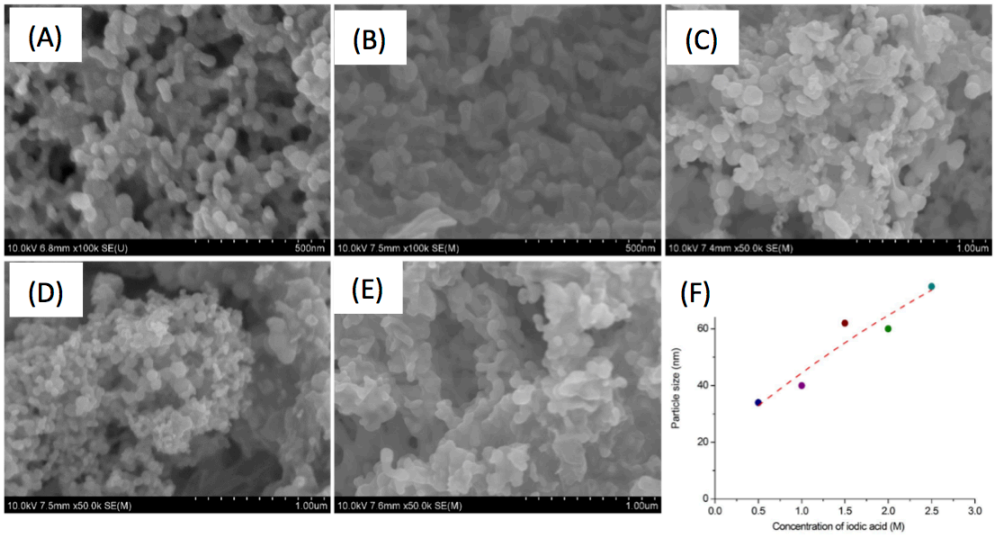

Figure 8.10. SEM images of $Bi(IO_3)_3$ with different concentration of HIO_3 solution (A)0.5M, (B)1.0 M, (c)1.5M, (D)2.0M, (E)2.5M, (F) Correlation of average $Bi(IO_3)_3$ particles size with different concentration of HIO_3 solution.

The SEM results showed that the average particles size of $Bi(IO_3)_3$ are 34 nm, 40 nm, 62 nm, 60 nm and 75 nm respectively with the concentration of HIO_3 to be 0.5M, 1.0M, 1.5M, 2.0M and 2.5 M. Similar as the spraying out $Bi(NO_3)_3$ solution, the average particle sizes of $Bi(IO_3)_3$ increased with the increasing concentration of the HIO_3 which is consistent with the above mechanism. According to the images, I can also know that the lower concentration of HIO_3 gives more uniform size distribution of $Bi(IO_3)_3$ particles. The stoichiometry reaction coefficients of Bi^{3+} and IO_3^- are 1:3. The lower concentration of HIO_3 consumed less Bi^{3+} allowing Bi^{3+} as well as supersaturation of the system to remain constant. Because the nucleation rate

and growth rate are constant in the system during the reaction, the particles are more uniform.

In above experiments, the limiting reagent is the solution in the syringe. I wanted to see how the experiment conditions will affect the morphology and particle size of the $Bi(IO_3)_3$ if the limiting reagent is the solution in the beaker. I was able to study this by spraying 2 M $Bi(NO_3)_3$ in the syringe into 2ml 0.05M HIO_3 solution in the beaker contained. The SEM results are shown in Figure 11. The results showed that the average of the $Bi(IO_3)_3$ size was around 210 nm, which could further expand the average size range of as-prepared $Bi(IO_3)_3$ from around 75 nm to 200 nm to better make this method to produce size tunable metal iodate. The reason for the bigger particle size can be explained. The reaction rate was relatively low compared with the previous case, leading to the Bi^{3+} diffusing into the HIO_3 solution, making the instant supersaturation ratio in the system very low, which decreased the nucleation rate and thus made fewer nuclei, resulting in the bigger particles. However, the supersaturation ratio of the system changed continuously with the depletion of the HIO_3 in the beaker, leading to non-monodispersed particles.

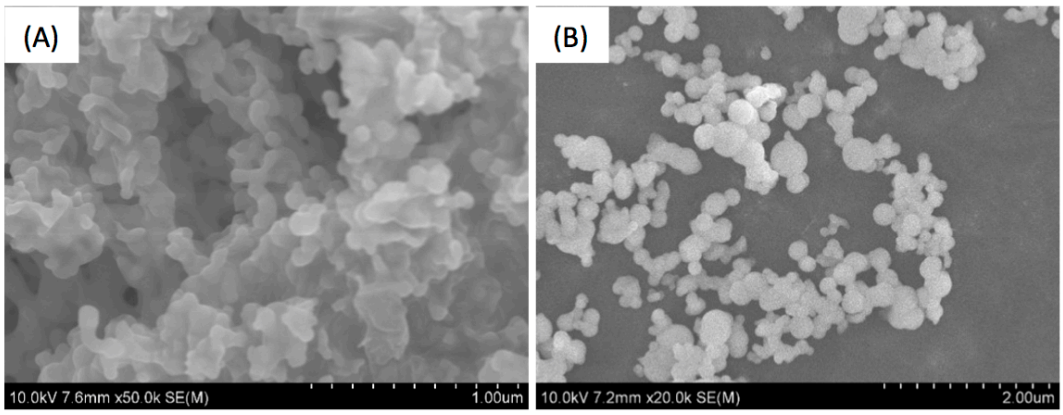

Figure 8.11. SEM image of Bi(IO3)3 of 2M Bi(NO3)3 reacting with 5M HIO3 (A) and 0.05M HIO3 (B).

8.4. Conclusion

In conclusion, I was able to synthesize different metal iodates by using the electrospray co-precipitation method successfully and they were characterized with SEM to justify the size-tunable. Among these metal iodates, $Mn(IO_3)_2$ and $Zn(IO_3)_2$ have the needle-like structure while $Cr(IO_3)_3$, $Bi(IO_3)_2$, $Fe(IO_3)_3$, $Ni(IO_3)_2$ have the irregular spherical shaped morphology. The $Bi(IO_3)_3$ system was chosen to investigate the effects of the experimental conditions on the morphologies and size of the nanoparticles. $Bi(IO_3)_3$ nanoparticles were characterized with XRD, TGA-DSC, SEM and TEM respectively. The XRD and TGA showed amorphous $Bi(IO_3)_3$ with no impurities was synthesized by the electrospray co-precipitation method. The SEM and TEM confirmed the as-prepared $Bi(IO_3)_3$ had irregular shape from oval to sphere and its size increased with the increasing concentration of precursor solution. By tuning the experimental conditions, $Bi(IO_3)_3$ nanoparticles of size around 10nm-200nm could be successfully prepared.

Chapter 9: Summary

9.1. Conclusions

The goal of this dissertation was to provide a better understanding of how fundamental microscopic properties of metal oxide affect the function of them for solid fuel oxidation that might affect their application towards energetic materials. This was enabled primarily by using systematic doped metal oxides that share the same crystal structure and morphology to minimize variables existed in metal oxides. Four different fuels with completely different physical/chemical properties were used to obtain a more generic and comprehensive understanding of thermite reaction mechanism.

In Chapter 1, I give an introduction of energetic materials in nanoscale and nanothermite that is a composition of solid fuel and metal oxide. However for the seemingly simple oxygen exchange reaction, there can be large differences in the function for fuel oxidation among different metal oxide. The large number of variables among metal oxides has limited our understanding of what properties of metal oxide control the initiation and reaction kinetics.

Chapter 2 presented the experimental techniques and tools to study the rapid initiation and propagation of nanothermite particularly temperature-jump system and constant volume combustion cell. The oxygen ion transport was studied by impedance spectroscopy and the crystal structure revolution of metal oxide during chemical looping combustion was analyzed by *in-operando* synchrotron X-ray diffraction.

In Chapter 3, systematic perovskite oxides whose crystal structure and particle size could be held constant, but whose vacancy concentration and bond energy could be systematically tuned was employed as oxidizers mixed with aluminum as fuel. The ignition temperature was measured by temperature-jump/time-of-flight mass spectrometer (T-jump/TOFMS). The bond energy and oxygen vacancy were estimated based on the stoichiometry and the thermodynamic parameters of doped perovskites. For the first time I found a clear relationship between molecular properties of the oxidizer, e.g., bond energy and oxygen vacancy concentration, and ignition temperature in a thermite reaction.

In Chapter 4-5, another systematic doped metal oxide: doped δ-Bi_2O_3 with higher oxygen activity was mixed with Al and B as fuels, respectively. Similar trend between bond energy, oxygen vacancy concentration and ignition temperature as Al/doped perovskite was found for Al/doped δ-Bi_2O_3 and B/doped δ-Bi_2O_3. Besides ignition temperature, the combustion reactivity of B/doped δ-Bi_2O_3 can also be correlated with the bond energy and oxygen vacancy concentration. This suggests that the possibility of manipulating microscopic properties within a crystal can be considered, in order to tune the resultant energetic properties. In addition, in-situ high heating rate TEM was used to explore the morphology change, both prior to and after the initiation of B/Bi_2O_3. It was proposed that B/Bi_2O_3 ignites at low temperature because the molten B_2O_3 wets Bi_2O_3 creating an interface so that high mobility solid-state oxygen can diffuse through the liquid B_2O_3 shell.

Chapter 6 summarized two systematic doped metal oxide covered in Chapter 3-5 as oxidizer with four fuels that have different melting points for core/passivation

layers (Al, B, Ta) and carbon that with no shell passivation. Within each oxidizer family, initiation temperature can be correlated with metal-oxygen bond energy of the oxidizer, seemingly independent of fuel type. The absolute value for initiation of perovskites and δ- Bi_2O_3 doesn't overlap, which can be attributed to their differences in oxygen vacancy concentration and crystal structure.

Chapter 7 employed the doped δ-Bi_2O_3 as oxidizer for solid carbon oxidation in the application of chemical looping combustion. *In-operando* synchrotron X-ray diffraction and on-line mass spectrometry was used to monitor both the phase evolution in the solid as well as the production of gaseous products. Reaction kinetics and initiation temperatures were extracted from the diffraction peak intensity changes. Results show that lower metal-oxygen bond energy and higher oxygen vacancy concentration of doped Bi_2O_3 led to lower onset temperature, faster reaction rate and smaller activation energy for carbon oxidation. These results provide important insights into manipulating oxygen carrier's microscopic properties for CLC applications.

In Chapter 8, size-tunable metal iodates were synthesized by electrospray co-precipitation method. Nano $Mn(IO_3)_2$, $Zn(IO_3)_2$, $Cr(IO_3)_3$, $Bi(IO_3)_2$, $Fe(IO_3)_3$, and $Ni(IO_3)_2$ were synthesized successfully. In addition, by tuning the experimental conditions in electrospray co-precipitation, $Bi(IO_3)_3$ nanoparticles of size ranges 10 nm to 200 nm could be successfully prepared.

9.2. Recommendations for Future Work

9.2.1. Assemble Systematic Doped Metal Oxides in Energetic Fibers or Films

In my dissertation, powdered doped metal oxides are intimately mixed with fuels. However for the application in propellants, such as solid rocket motors used in the Space Shuttle, polymer composites containing energetic materials are extremely important. Very often this is energetic fiber or energetic film. Previous studies in the fabrication of fibers and films focused on improving their mechanical stability, particle loading and reactivity by tuning mass loading, polymer and fabrication method. However, there has been no study on how the fundamental microscopic properties of oxidizer affect the reactivity of energetic fibers or films. It was reported that Yan et al. fabricated NC-Al/Bi_2O_3 fibers by electrospinning shown in Figure 9.1.[1] Systematic doped Bi_2O_3 might replace Bi_2O_3 to produce systematic NC-Al/doped Bi_2O_3 fibers and combustion reactivity can be measured. The relationship between the propagation rate of fiber combustion and the microscopic properties of oxidizer can be studied.

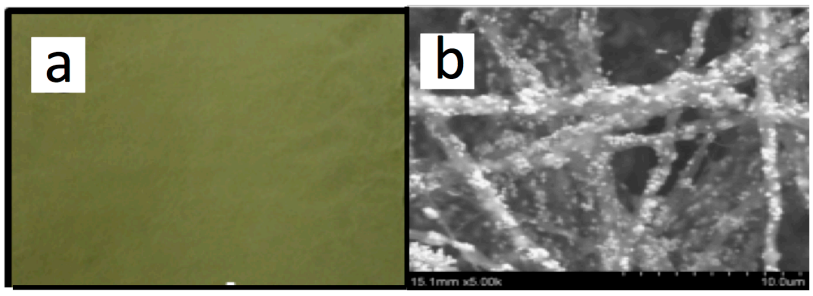

Figure 9.1. a. Photograph and b. SEM of NC-Al/Bi_2O_3 fibers synthesized by electrospinning.

9.2.2. Explore Simpler Systematic Metal Oxides

Doped perovskite or doped Bi_2O_3 covered in this dissertation are relatively complex mixed oxides that direct thermodynamic parameters are not readily available. It is ideal if simpler systematic metal oxides can be found and employed as oxidizers to simplify variables in the thermite system. Spinel oxides have the general formula of AB_2O_4 where the A and B are metal ions that from almost all the main group metals and transition metals and O being an oxygen anion. The structures of spinels were little known until Bragg and Nishikawa confirmed that spinels generally have a cubic structure formed of A-O tetrahedrons and B-O octahedrons.[2] An example of spinel oxide structured, Co_3O_4 is shown in Figure 9.2.[3] Spinels have revealed fascinating prospective as catalyst due to their controllable composition, structure, valence and morphology.[4] The manifold compositions also make spinel oxides good candidates as systematic oxides to study the ignition mechanism especially when A and B are the same metal, e.g., Co_3O_4 ($CoCo_2O_4$), Fe_3O_4 ($FeFe_2O_4$) and Mn_3O_4 ($MnMn_2O_4$). With some basic thermodynamic parameters readily available, the relationship between those thermodynamic parameters (e.g., enthalpy of reaction, formation energy of metal oxide) and their function as oxidizer can be studied.

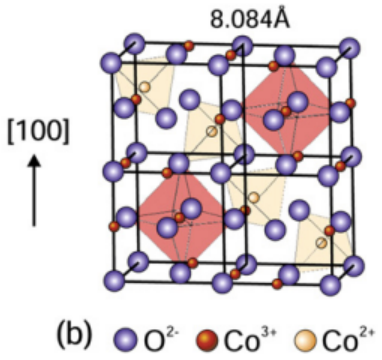

Figure 9.2. Spinel structure of Co_3O_4.

9.2.3. Explore Doped Perovskites for CLC by In-Operando Synchrotron X-Ray

Simple metal oxides suffer from poor cycling stability due to their tendency of sintering under chemical looping combustion operation temperature (700 – 900 °C). The perovskite oxides, as mixed ionic and electronic conductor, are reported to be good oxidizer candidates for chemical looping combustion due to their high thermal stability and oxygen reactivity. It has been discussed in Chapter 7 that *in-operando* synchrotron X-ray diffraction is powerful to study the phase evolution in the solid and analyze reaction kinetics when doped Bi_2O_3 was used as oxidizer. It is promising that the employment of aerosol spray pyrolysised doped perovskite in chemical looping combustion can also be studied for better understanding on how the microscopic structure of oxidizer affect the cycling in oxidation and reduction reactions. A preliminary measurement of in situ synchrotron X-ray diffraction $La_{0.8}Sr_{0.2}CoO_3$ for five cycles under the atmosphere in air, helium and methane at a constant temperature ~700 °C is shown in Figure 9.3. The crystal structure changed from perovskite structure (orthorhombic) to brownmillerite when $La_{0.8}Sr_{0.2}CoO_3$ is reduced to $La_{0.8}Sr_{0.2}CoO_{3-\delta}$ in methane and regenerated back to perovskite structure in air.

Similar as C/doped Bi_2O_3, the reaction kinetics and cycling are supposed to be analyzed and the morphology change after cycling can be analyzed as well.

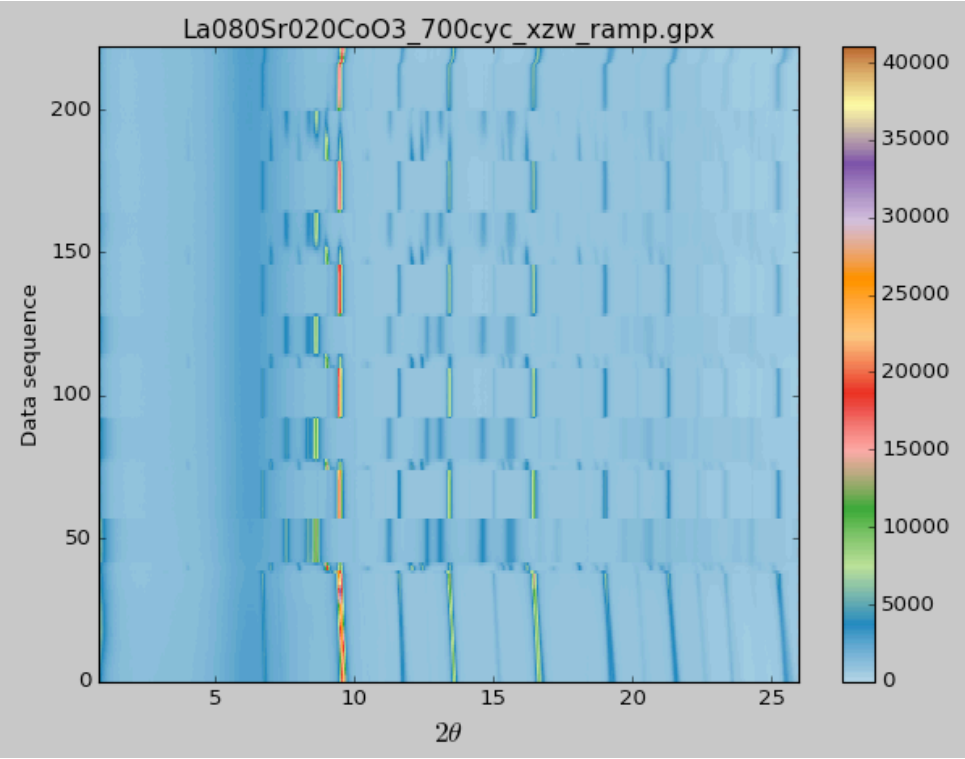

Figure 9.3. Contour plot of in situ synchrotron X-ray diffraction for $La_{0.8}Sr_{0.2}CoO_3$ for five cycles under the atmosphere cycling between air, helium and methane at a constant temperature ~700 °C.

Bibliography

Chapter 1:

1. Akhavan, J., *The chemistry of explosives, 2nd ed*. Royal Society of Chemistry: Cambridge, UK, **2004**.

2. Tillotson, T. M.; Gash, A. E.; Simpson, R. L.; Hrubesh, L. W.; Satcher, J. H.; Poco, J. F., Nanostructured energetic materials using sol-gel methodologies. *J Non-Cryst Solids* **2001,** *285* (1-3), 338-345.

3. Sundaram, D.; Yang, V.; Yetter, R. A., Metal-based nanoenergetic materials: Synthesis, properties, and applications. *Prog Energ Combust* **2017,** *61*, 293-365.

4. Yen, N. H.; Wang, L. Y., Reactive Metals in Explosives. *Propell Explos Pyrot* **2012,** *37* (2), 143-155.

5. Dreizin, E. L., Metal-based reactive nanomaterials. *Prog Energ Combust* **2009,** *35* (2), 141-167.

6. Kim, S. H.; Zachariah, M. R., Enhancing the rate of energy release from nanoenergetic materials by electrostatically enhanced assembly. *Adv Mater* **2004,** *16* (20), 1821.

7. Shende, R.; Subramanian, S.; Hasan, S.; Apperson, S.; Thiruvengadathan, R.; Gangopadhyay, K.; Gangopadhyay, S.; Redner, P.; Kapoor, D.; Nicolich, S.; Balas, W., Nanoenergetic composites of CuO nanorods, nanowires, and Al-nanoparticles. *Propell Explos Pyrot* **2008,** *33* (2), 122-130.

8. Zhou, X.; Torabi, M.; Lu, J.; Shen, R. Q.; Zhang, K. L., Nanostructured Energetic Composites: Synthesis, Ignition/Combustion Modeling, and Applications. *Acs Appl Mater Inter* **2014,** *6* (5), 3058-3074.

9. Yetter, R. A.; Risha, G. A.; Son, S. F., Metal particle combustion and nanotechnology. *P Combust Inst* **2009,** *32*, 1819-1838.

10. Aumann, C. E.; Skofronick, G. L.; Martin, J. A., Oxidation Behavior of Aluminum Nanopowders. *J Vac Sci Technol B* **1995,** *13* (3), 1178-1183.

11. Young, G.; Sullivan, K.; Zachariah, M. R.; Yu, K., Combustion characteristics of boron nanoparticles. *Combust Flame* **2009,** *156* (2), 322-333.

12. Huang, Y.; Risha, G. A.; Yang, V.; Yetter, R. A., Effect of particle size on combustion of aluminum particle dust in air. *Combust Flame* **2009,** *156* (1), 5-13.

13. Rossi, C., *Al-Based Energetic Nano Materials: Design, Manufacturing, Properties and Applications*. John Wiley & Sons, Inc: Hoboken, NJ, USA, 2015.

14. Foley, T. J.; Johnson, C. E.; Higa, K. T., Inhibition of oxide formation on aluminum nanoparticles by transition metal coating. *Chem Mater* **2005,** *17* (16), 4086-4091.

15. Trunov, M. A.; Schoenitz, M.; Dreizin, E. L., Effect of polymorphic phase transformations in alumina layer on ignition of aluminium particles. *Combust Theor Model* **2006,** *10* (4), 603-623.

16. Granier, J. J.; Pantoya, M. L., Laser ignition of nanocomposite thermites. *Combust Flame* **2004,** *138* (4), 373-383.

17. Rosenband, V., Thermo-mechanical aspects of the heterogeneous ignition of metals. *Combust Flame* **2004,** *137* (3), 366-375.

18. Stamatis, D.; Dreizin, E. L.; Higa, K., Thermal Initiation of Al-MoO_3 Nanocomposite Materials Prepared by Different Methods. *J Propul Power* **2011,** *27* (5), 1079-1087.

19. Sullivan, K. T.; Chiou, W. A.; Fiore, R.; Zachariah, M. R., In situ microscopy of rapidly heated nano-Al and nano-Al/WO_3 thermites. *Appl Phys Lett* **2010,** *97* (13).

20. Van Devener, B.; Perez, J. P. L.; Jankovich, J.; Anderson, S. L., Oxide-Free, Catalyst-Coated, Fuel-Soluble, Air-Stable Boron Nanopowder as Combined Combustion Catalyst and High Energy Density Fuel. *Energ Fuel* **2009,** *23* (12), 6111-6120.

21. Sullivan, K.; Young, G.; Zachariah, M. R., Enhanced reactivity of nano-B/Al/CuO MIC's. *Combust Flame* **2009,** *156* (2), 302-309.

22. Chintersingh, K. L.; Schoenitz, M.; Dreizin, E. L., Oxidation kinetics and combustion of boron particles with modified surface. *Combust Flame* **2016,** *173*, 288-295.

23. J. F. Xi, J. Z. L., H. P. Li, Y. Wang, Y. W. Zhang, J. H. Zhou, K. F. Cen, Progress in methods of promoting the ignition and combustion of boron particles. *Hanneng Cailiao/Chin. J. Energ. Mater* **2013,** *21*, 533-538.

24. A, M., J. M. K. Semple, Combustion of boron particles at atmospheric pressure. *Combust. Sci. Technol* **1969,** *1*, 191-191.

25. Ulas, A.; Kuo, K. K.; Gotzmer, C., Ignition and combustion of boron particles in fluorine-containing environments. *Combust Flame* **2001,** *127* (1-2), 1935-1957.

26. Dreizin, E. L.; Keil, D. G.; Felder, W.; Vicenzi, E. P., Phase changes in boron ignition and combustion. *Combust Flame* **1999,** *119* (3), 272-290.

27. Yeh, C. L.; Kuo, K. K., Ignition and combustion of boron particles. *Prog Energ Combust* **1996,** *22* (6), 511-541.

28. Mohan, G.; Williams, F. A., Ignition and Combustion of Boron in O_2-Inert Atmospheres. *Aiaa J* **1972,** *10* (6), 776-&.

29. Piekiel, N. W.; Zhou, L.; Sullivan, K. T.; Chowdhury, S.; Egan, G. C.; Zachariah, M. R., Initiation and Reaction in Al/Bi_2O_3 Nanothermite: Evidence for the Predominance of Condensed Phase Chemistry. *Combust Sci Technol* **2014,** *186* (9), 1209-1224.

30. Haynes, W. M., *CRC handbook of Chemistry and Physics*. 2007; Vol. 5.

31. Langmuir, L. M. a. D. B., Resistance, Emissivities and Melting Point of Tantalum. *Phys. Rev* **1939,** *55* (8), 743.

32. DeLisio, J. B.; Wang, X. Z.; Wu, T.; Egan, G. C.; Jacob, R. J.; Zachariah, M. R., Investigating the oxidation mechanism of tantalum nanoparticles at high heating rates. *J Appl Phys* **2017,** *122* (24).

33. Zhou, W. B.; DeLisio, J. B.; Li, X. Y.; Liu, L.; Zachariah, M. R., Persulfate salt as an oxidizer for biocidal energetic nano-thermites. *J Mater Chem A* **2015,** *3* (22), 11838-11846.

34. Zhou, W. B.; DeLisio, J. B.; Wang, X. Z.; Zachariah, M. R., Reaction mechanisms of potassium oxysalts based energetic composites. *Combust Flame* **2017,** *177*, 1-9.

35. Bazyn, T.; Glumac, N.; Krier, H.; Ward, T. S.; Schoenitz, M.; Dreizin, E. L., Reflected shock ignition and combustion of aluminum and nanocomposite thermite powders. *Combust Sci Technol* **2007,** *179* (3), 457-476.

36. Schoenitz, M.; Umbrajkar, S.; Dreizin, E. L., Kinetic analysis of thermite reactions in Al-MoO_3 nanocomposites. *J Propul Power* **2007,** *23* (4), 683-687.

37. Jian, G. Q.; Chowdhury, S.; Sullivan, K.; Zachariah, M. R., Nanothermite reactions: Is gas phase oxygen generation from the oxygen carrier an essential prerequisite to ignition? *Combust Flame* **2013,** *160* (2), 432-437.

38. http://webmineral.com/data/Perovskite.shtml#.WwQ4M5PwZ24.

39. Levy, M. Crystal structure and defect properties in ceramic materials. Imperial College London, London, 2005.

40. Huang, Y. H.; Dass, R. I.; Xing, Z. L.; Goodenough, J. B., Double perovskites as anode materials for solid-oxide fuel cells. *Science* **2006,** *312* (5771), 254-257.

41. Royer, S.; Duprez, D.; Can, F.; Courtois, X.; Batiot-Dupeyrat, C.; Laassiri, S.; Alamdari, H., Perovskites as Substitutes of Noble Metals for Heterogeneous Catalysis: Dream or Reality. *Chem Rev* **2014,** *114* (20), 10292-10368.

42. Schiestel, T.; Kilgus, M.; Peter, S.; Caspary, K. J.; Wang, H.; Caro, J., Hollow fibre perovskite membranes for oxygen separation. *J Membrane Sci* **2005,** *258* (1-2), 1-4.

43. Pena, M. A.; Fierro, J. L. G., Chemical structures and performance of perovskite oxides. *Chem Rev* **2001,** *101* (7), 1981-2017.

44. Ishihara, T.; Matsuda, H.; Takita, Y., Doped $LaGaO_3$ Perovskite-Type Oxide as a New Oxide Ionic Conductor. *J Am Chem Soc* **1994,** *116* (9), 3801-3803.

45. Teraoka, Y.; Nobunaga, T.; Yamazoe, N., Effect of Cation Substitution on the Oxygen Semipermeability of Perovskite-Type Oxides. *Chem Lett* **1988,** (3), 503-506.

46. Stevenson, J. W.; Armstrong, T. R.; Carneim, R. D.; Pederson, L. R.; Weber, W. J., Electrochemical properties of mixed conducting perovskites La(1-x)M(x)Co(1-y)Fe(y)O(3-delta) (M=Sr,Ba,Ca). *J Electrochem Soc* **1996,** *143* (9), 2722-2729.

47. Hull, S.; Norberg, S. T.; Tucker, M. G.; Eriksson, S. G.; Mohn, C. E.; Stolen, S., Neutron total scattering study of the delta and beta phases of Bi_2O_3. *Dalton T* **2009,** (40), 8737-8745.

48. Jung, D. W.; Lee, K. T.; Wachsman, E. D., Dysprosium and Gadolinium Double Doped Bismuth Oxide Electrolytes for Low Temperature Solid Oxide Fuel Cells. *J Electrochem Soc* **2016,** *163* (5), F411-F415.

49. Sammes, N. M.; Tompsett, G. A.; Nafe, H.; Aldinger, F., Bismuth based oxide electrolytes - Structure and ionic conductivity. *J Eur Ceram Soc* **1999,** *19* (10), 1801-1826.

50. T. Takahashi, H. I., and Y. Nagai, High oxide ion conduction in sintered Bi2O3 containing SrO, CaO or La_2O_3. *J. Appl. Electrochem* **1972,** *2* (2), 97-104.

51. Jung, D. W.; Duncan, K. L.; Wachsman, E. D., Effect of total dopant concentration and dopant ratio on conductivity of $(DyO_{1.5})_x$-$(WO_3)_y$-$(BiO_{1.5})_{1-x-y}$. *Acta Mater* **2010,** *58* (2), 355-363.

52. Wachsman, E. D.; Boyapati, S.; Jiang, N. X., Effect of Dopant Polarizability on Oxygen Sublattice Order in Phase-Stabilized Cubic Bismuth Oxides. *Ionics* **2001,** *7* (1-2), 1-6.

53. Takahashi T, I. H., High oxide ion conduction in sintered oxides of the system Bi_2O_3-WO_3. *Journal of Applied Electrochemistry* **1973,** *3* (1), 65-72.

54. Verkerk, M. J.; Burggraaf, A. J., High Oxygen Ion Conduction in Sintered Oxides of the Bi2o3-Dy2o3 System. *J Electrochem Soc* **1981,** *128* (1), 75-82.

55. M, T. Synthesis and characterisation of d-Bi2O3 related materials stabilised by substitutions of Ca, Ga, Nb and Re. University of Birmingham, 2010.

56. Feng, J. Y.; Jian, G. Q.; Liu, Q.; Zachariah, M. R., Passivated Iodine Pentoxide Oxidizer for Potential Biocidal Nanoenergetic Applications. *Acs Appl Mater Inter* **2013,** *5* (18), 8875-8880.

57. Sullivan, K. T. P., N. W.; Chowdhury, S.; Wu, C.; Zachariah, M. R.; Johnson, C. E. , Ignition and Combustion Characteristics of Nanoscale Al/$AgIO_3$: A Potential Energetic Biocidal System. . *Combust. Sci. Technol* **2010,** *183*, 285-302.

58. Setlow, P., Spores of Bacillus subtilis: their resistance to and killing by radiation, heat and chemicals. *J Appl Microbiol* **2006,** *101* (3), 514-525.

59. Zhang, S. S.; Schoenitz, M.; Dreizin, E. L., Iodine Release, Oxidation, and Ignition of Mechanically Alloyed Al-I Composites. *J Phys Chem C* **2010,** *114* (46), 19653-19659.

60. Grinshpun, S. A.; Adhikari, A.; Yermakov, M.; Reponen, T.; Dreizin, E.; Schoenitz, M.; Hoffmann, V.; Zhang, S. S., Inactivation of Aerosolized Bacillus atrophaeus (BG) Endospores and MS2 Viruses by Combustion of Reactive Materials. *Environ Sci Technol* **2012,** *46* (13), 7334-7341.

61. Xu, X.; Hu, C. L.; Yang, B. P.; Mao, J. G., Syntheses, crystal structures and magnetic properties of three new silver manganese(II) or manganese(III) mixed metal iodates. *Crystengcomm* **2013,** *15* (38), 7776-7782.

62. Huang, C.; Hu, C. L.; Xu, X.; Yang, B. P.; Mao, J. G., Explorations of a Series of Second Order Nonlinear Optical Materials Based on Monovalent Metal Gold(III) Iodates. *Inorg Chem* **2013,** *52* (19), 11551-11562.

63. Wang, H. Y.; DeLisio, J. B.; Jian, G. Q.; Zhou, W. B.; Zachariah, M. R., Electrospray formation and combustion characteristics of iodine-containing Al/CuO nanothermite microparticles. *Combust Flame* **2015,** *162* (7), 2823-2829.

64. Hu, X. L.; DeLisio, J. B.; Li, X. Y.; Zhou, W. B.; Zachariah, M. R., Direct Deposit of Highly Reactive Bi(IO3)(3)- Polyvinylidene Fluoride Biocidal Energetic Composite and its Reactive Properties. *Adv Eng Mater* **2017,** *19* (1).

65. Richter, H. J.; Knoche, K. F., Reversibility of Combustion Processes. *Acs Sym Ser* **1983,** *235*, 71-85.

66. Garcia-Labiano, F.; de Diego, L. F.; Adanez, J.; Abad, A.; Gayan, P., Reduction and oxidation kinetics of a copper-based oxygen carrier prepared by impregnation for chemical-looping combustion. *Ind Eng Chem Res* **2004,** *43* (26), 8168-8177.

Chapter 2:

1. Levitas, V. I.; Asay, B. W.; Son, S. F.; Pantoya, M., Melt dispersion mechanism for fast reaction of nanothermites. Appl Phys Lett 2006, 89 (7).

2. Trunov, M. A.; Schoenitz, M.; Zhu, X. Y.; Dreizin, E. L., Effect of polymorphic phase transformations in Al2O3 film on oxidation kinetics of aluminum powders. Combust Flame 2005, 140 (4), 310-318.

3. Zhou, L.; Piekiel, N.; Chowdhury, S.; Zachariah, M. R., T-Jump/time-of-flight mass spectrometry for time-resolved analysis of energetic materials. Rapid Commun

Mass Sp 2009, 23 (1), 194-202.

4. Chowdhury, S.; Sullivan, K.; Piekiel, N.; Zhou, L.; Zachariah, M. R., Diffusive vs Explosive Reaction at the Nanoscale. J Phys Chem C 2010, 114 (20), 9191-9195.

5. DeLisio, J. B.; Hu, X. L.; Wu, T.; Egan, G. C.; Young, G.; Zachariah, M. R., Probing the Reaction Mechanism of Aluminum/Poly(vinylidene fluoride) Composites. J Phys Chem B 2016, 120 (24), 5534-5542.

6. Wall, J. H. F. a. L. A., General Treatment of the Thermogravimetry of Polymers. J. Res. Natl. Bur. Stand. 1966, 70 (6), 487-523.

7. Jian, G. Q.; Zhou, L.; Piekiel, N. W.; Zachariah, M. R., Low Effective Activation Energies for Oxygen Release from Metal Oxides: Evidence for Mass-Transfer Limits at High Heating Rates. Chemphyschem 2014, 15 (8), 1666-1672.

8. Sullivan, K. T.; Chiou, W. A.; Fiore, R.; Zachariah, M. R., In situ microscopy of rapidly heated nano-Al and nano-Al/WO3 thermites. Appl Phys Lett 2010, 97 (13).

9. Sullivan, K.; Zachariah, M. R., Simultaneous Pressure and Optical Measurements of Nanoaluminum Thermites: Investigating the Reaction Mechanism. J Propul Power 2010, 26 (3), 467-472.

10. Wang, H.; Jian, G.; Zhou, W.; DeLisio, J. B.; Lee, V. T.; Zachariah, M. R., Metal Iodate-Based Energetic Composites and Their Combustion and Biocidal Performance. Acs Appl Mater Inter 2015, 7 (31), 17363-17370.

11. Barsoum M, B. M. W., Fundamentals of ceramics. CRC press: 2002.

12. Irvine J T S, S. D. C., West A R., Electroceramics: characterization by impedance spectroscopy. Adv Mater 1990, 2 (3), 132-138.

13. Chupas, P. J.; Chapman, K. W.; Kurtz, C.; Hanson, J. C.; Lee, P. L.; Grey, C. P., A versatile sample-environment cell for non-ambient X-ray scattering experiments. J Appl Crystallogr 2008, 41, 822-824.

14. Toby, B. H.; Von Dreele, R. B., GSAS-II: the genesis of a modern open-source all purpose crystallography software package. J Appl Crystallogr 2013, 46, 544-549.

15. D. W. Jung, K. L. Duncan and E. D. Wachsman, Effect of Total Dopant Concentration and Dopant Ratio on Conductivity of $(DyO_{1.5})_x$-$(WO_3)_y$-$(BiO_{1.5})_{1-x-y}$. *Acta Mater.*, 2010, **58**(2), 355-363.

Chapter 3:

1. Goldschmidt, H. V., T., Reduction of Oxides with Aluminum. J. Soc. Chem. Ind. 1898, 19.

2. (a) Apperson, S.; Shende, R. V.; Subramanian, S.; Tappmeyer, D.; Gangopadhyay, S.; Chen, Z.; Gangopadhyay, K.; Redner, P.; Nicholich, S.; Kapoor, D., Generation of fast propagating combustion and shock waves with copper oxide/aluminum nanothermite composites. Appl Phys Lett 2007, 91 (24); (b) Dreizin, E. L., Metal-based reactive nanomaterials. Prog Energ Combust 2009, 35 (2), 141-167; (c) Zhou, X.; Torabi, M.; Lu, J.; Shen, R. Q.; Zhang, K. L., Nanostructured Energetic Composites: Synthesis, Ignition/Combustion Modeling, and Applications.

Acs Appl Mater Inter 2014, 6 (5), 3058-3074.

3. (a) Yen, N. H.; Wang, L. Y., Reactive Metals in Explosives. Propell Explos Pyrot 2012, 37 (2), 143-155; (b) Rossi, C., Al-Based Energetic Nano Materials: Design, Manufacturing, Properties and Applications. John Wiley & Sons, Inc: Hoboken, NJ, USA, 2015.

4. Zarko, V. E. G., A. A., Energetic Nanomaterials: Synthesis, Characterization, and Application. Elsevier: Amsterdam, Netherlands, 2016.

5. (a) Foley, T. J.; Johnson, C. E.; Higa, K. T., Inhibition of oxide formation on aluminum nanoparticles by transition metal coating. Chem Mater 2005, 17 (16), 4086-4091; (b) Trunov, M. A.; Schoenitz, M.; Dreizin, E. L., Effect of polymorphic phase transformations in alumina layer on ignition of aluminium particles. Combust Theor Model 2006, 10 (4), 603-623.

6. (a) Granier, J. J.; Pantoya, M. L., Laser ignition of nanocomposite thermites. Combust Flame 2004, 138 (4), 373-383; (b) Rosenband, V., Thermo-mechanical aspects of the heterogeneous ignition of metals. Combust Flame 2004, 137 (3), 366-375.

7. Stamatis, D.; Dreizin, E. L.; Higa, K., Thermal Initiation of Al-MoO3 Nanocomposite Materials Prepared by Different Methods. J Propul Power 2011, 27 (5), 1079-1087.

8. Dean, S. W.; Pantoya, M. L.; Gash, A. E.; Stacy, S. C.; Hope-Weeks, L. J., Enhanced Convective Heat Transfer in Nongas Generating Nanoparticle Thermites. J Heat Trans-T Asme 2010, 132 (11).

9. Sullivan, K. T.; Chiou, W. A.; Fiore, R.; Zachariah, M. R., In situ microscopy

of rapidly heated nano-Al and nano-Al/WO3 thermites. Appl Phys Lett 2010, 97 (13).

10. (a) Piekiel, N. W.; Egan, G. C.; Sullivan, K. T.; Zachariah, M. R., Evidence for the Predominance of Condensed Phase Reaction in Chemical Looping Reactions between Carbon and Oxygen Carriers. J Phys Chem C 2012, 116 (46), 24496-24502; (b) Wen, J. Z.; Ringuette, S.; Bohlouli-Zanjani, G.; Hu, A. M.; Nguyen, N. H.; Persic, J.; Petre, C. F.; Zhou, Y. N., Characterization of thermochemical properties of Al nanoparticle and NiO nanowire composites. Nanoscale Res Lett 2013, 8; (c) Piekiel, N. W.; Zhou, L.; Sullivan, K. T.; Chowdhury, S.; Egan, G. C.; Zachariah, M. R., Initiation and Reaction in Al/Bi2O3 Nanothermite: Evidence for the Predominance of Condensed Phase Chemistry. Combust Sci Technol 2014, 186 (9), 1209-1224; (d) Zhou, W. B.; DeLisio, J. B.; Wang, X. Z.; Egan, G. C.; Zachariah, M. R., Evaluating free vs bound oxygen on ignition of nano-aluminum based energetics leads to a critical reaction rate criterion. J Appl Phys 2015, 118 (11).

11. Jian, G. Q.; Chowdhury, S.; Sullivan, K.; Zachariah, M. R., Nanothermite reactions: Is gas phase oxygen generation from the oxygen carrier an essential prerequisite to ignition? Combust Flame 2013, 160 (2), 432-437.

12. (a) Trunov, M. A.; Schoenitz, M.; Zhu, X. Y.; Dreizin, E. L., Effect of polymorphic phase transformations in Al2O3 film on oxidation kinetics of aluminum powders. Combust Flame 2005, 140 (4), 310-318; (b) Levitas, V. I.; Asay, B. W.; Son, S. F.; Pantoya, M., Melt dispersion mechanism for fast reaction of nanothermites. Appl Phys Lett 2006, 89 (7).

13. (a) Huang, Y. H.; Dass, R. I.; Xing, Z. L.; Goodenough, J. B., Double perovskites as anode materials for solid-oxide fuel cells. Science 2006, 312 (5771),

254-257; (b) Laguna-Bercero, M. A. K., J. A.; Skinner, S. J. , Performance and Characterization of (La, Sr)MnO3/YSZ and La0.6Sr0.4Co0.2Fe0.8O3 Electrodes for Solid Oxide Electrolysis Cells. Chem. Mater. 2009, 22, 1134-1141.

14. Dai, X. P.; Wu, Q.; Li, R. J.; Yu, C. C.; Hao, Z. P., Hydrogen production from a combination of the water-gas shift and redox cycle process of methane partial oxidation via lattice oxygen over LaFeO3 perovskite catalyst. J Phys Chem B 2006, 110 (51), 25856-25862.

15. Schiestel, T.; Kilgus, M.; Peter, S.; Caspary, K. J.; Wang, H.; Caro, J., Hollow fibre perovskite membranes for oxygen separation. J Membrane Sci 2005, 258 (1-2), 1-4.

16. (a) Hallberg, P.; Jing, D. Z.; Ryden, M.; Mattisson, T.; Lyngfelt, A., Chemical Looping Combustion and Chemical Looping with Oxygen Uncoupling Experiments in a Batch Reactor Using Spray-Dried CaMn1-xMxO3-delta (M = Ti, Fe, Mg) Particles as Oxygen Carriers. Energ Fuel 2013, 27 (3), 1473-1481; (b) Liu, L.; Taylor, D. D.; Rodriguez, E. E.; Zachariah, M. R., Influence of transition metal electronegativity on the oxygen storage capacity of perovskite oxides. Chem Commun 2016, 52 (68), 10369-10372.

17. Jian, G. Q.; Liu, L.; Zachariah, M. R., Facile Aerosol Route to Hollow CuO Spheres and its Superior Performance as an Oxidizer in Nanoenergetic Gas Generators. Adv Funct Mater 2013, 23 (10), 1341-1346.

18. Cheary, R. W.; Coelho, A., A Fundamental Parameters Approach to X-Ray Line-Profile Fitting. J Appl Crystallogr 1992, 25, 109-121.

19. Zhou, L.; Piekiel, N.; Chowdhury, S.; Zachariah, M. R., T-Jump/time-of-flight

mass spectrometry for time-resolved analysis of energetic materials. Rapid Commun Mass Sp 2009, 23 (1), 194-202.

20. Chowdhury, S.; Sullivan, K.; Piekiel, N.; Zhou, L.; Zachariah, M. R., Diffusive vs Explosive Reaction at the Nanoscale. J Phys Chem C 2010, 114 (20), 9191-9195.

21. Muller, O. R., R., The Major Ternary Structural Families. Springer: Berlin, Heidelberg, Germany, 1974.

22. Liu, L.; Zachariah, M. R.; Stoliarov, S. I.; Li, J., Enhanced thermal decomposition kinetics of poly(lactic acid) sacrificial polymer catalyzed by metal oxide nanoparticles. Rsc Adv 2015, 5 (123), 101745-101750.

23. (a) Cherry, M.; Islam, M. S.; Catlow, C. R. A., Oxygen-Ion Migration in Perovskite-Type Oxides. J Solid State Chem 1995, 118 (1), 125-132; (b) Ishihara, T.; Matsuda, H.; Takita, Y., Doped Lagao3 Perovskite-Type Oxide as a New Oxide Ionic Conductor. J Am Chem Soc 1994, 116 (9), 3801-3803; (c) Teraoka, Y.; Nobunaga, T.; Yamazoe, N., Effect of Cation Substitution on the Oxygen Semipermeability of Perovskite-Type Oxides. Chem Lett 1988, (3), 503-506; (d) Stevenson, J. W.; Armstrong, T. R.; Carneim, R. D.; Pederson, L. R.; Weber, W. J., Electrochemical properties of mixed conducting perovskites La(1-x)M(x)Co(1-y)Fe(y)O(3-delta) (M=Sr,Ba,Ca). J Electrochem Soc 1996, 143 (9), 2722-2729; (e) Nemudry, A.; Weiss, P.; Gainutdinov, I.; Boldyrev, V.; Schollhorn, R., Room temperature electrochemical redox reactions of the defect perovskite SrFeO2.5+x. Chem Mater 1998, 10 (9), 2403-2411.

24. (a) Puszynski, J. A.; Bulian, C. J.; Swiatkiewicz, J. J., Processing and ignition

characteristics of aluminum-bismuth trioxide nanothermite system. J Propul Power 2007, 23 (4), 698-706; (b) Piercey, D. G.; Klapooke, T. M., Nanoscale Aluminum-Metal Oxide (Thermite) Reactions for Application in Energetic Materials. Cent Eur J Energ Mat 2010, 7 (2), 115-129.

25. Zhao, H. L.; Xu, N. S.; Cheng, Y. F.; Wei, W. J.; Chen, N.; Ding, W. Z.; Lu, X. G.; Li, F. S., Investigation of Mixed Conductor BaCo0.7Fe0.3-xYxO3-delta with High Oxygen Permeability. J Phys Chem C 2010, 114 (41), 17975-17981.

26. (a) Cook, R. L.; Sammells, A. F., On the Systematic Selection of Perovskite Solid Electrolytes for Intermediate Temperature Fuel-Cells. Solid State Ionics 1991, 45 (3-4), 311-321; (b) Sammells, A. F.; Cook, R. L.; White, J. H.; Osborne, J. J.; Macduff, R. C., Rational Selection of Advanced Solid Electrolytes for Intermediate Temperature Fuel-Cells. Solid State Ionics 1992, 52 (1-3), 111-123.

27. (a) Li, S. G.; Jin, W. Q.; Huang, P.; Xu, N. P.; Shi, J.; Lin, Y. S.; Hu, M. Z. C.; Payzant, E. A., Comparison of oxygen permeability and stability of perovskite type La0.2A0.8Co0.2Fe0.8O3-δ (A = Sr, Ba, Ca) membranes. Ind Eng Chem Res 1999, 38 (8), 2963-2972; (b) Haynes, W. M., CRC handbook of Chemistry and Physics. 2007; Vol. 5.

28. Bockris, J. O.; Otagawa, T., The Electrocatalysis of Oxygen Evolution on Perovskites. J Electrochem Soc 1984, 131 (2), 290-302.

29. Ramam, K.; Chandramouli, K., Dielectric and Piezoelectric Properties of Combinatory Effect of a-Site Isovalent and B-Site Acceptor Doped Plzt Ceramics. Ceram-Silikaty 2009, 53 (3), 189-194.

30. Pauling, L., The Nature of the Chemical Bond. IV. The Energy of Single

Bonds and the Relative Electronegativity of Atoms. J. Am. Chem. Soc. 1932, 54, 3570-3582.

Chapter 4:

1. S. H. Fischer and M. C. Grubelich, Theoretical Energy Release of Thermites, Intermetallics, and Combustible Metals, 24th International Pyrotechnics Seminar, Monterey, Ca, July, 1998.

2. E. L. Dreizin, Metal-Based Reactive Nanomaterials, *Prog. Energy Combust. Sci.*, 2009, **35**(2), 141-167.

3. N. H. Yen and L.Y. Wang, Reactive Metals in Explosives, *Properllants Explots. Pyrotech.,* 2012, **37**, 143-145.

4. F. Noor, H. Zhang, T. Korakianitis T and D. Wen, Oxidation and Ignition of Aluminum Nanomaterials, *Phys. Chem. Chem. Phys*., 2013, **15**(46), 20176-20188.

5. V. Rosenband, Thermo-Mechanical Aspects of the Heterogeneous Ignition of Metals, *Combust. Flame*, 2004, **137**(3), 366-375.

6. M. A. Trunov, M, Schoenitz and E. L. Dreizin, Effect of Polymorphic Phase Transformations in Alumina Layer on Ignition of Aluminium Particles, *Combust. Theory Modell.*, 2006, **10**(4), 603-623.

7. K. T. Sullivan, W. A. Chiou, R. Fiore and M. R. Zachariah, In Situ Microscopy of Rapidly Heated Nano-Al and Nano-Al/WO_3 Thermites, *Appl. Phys. Lett.,* 2010, **97**(13), 133104–133106.

8. K. T. Sullivan, N. W. Piekiel, C. Wu, S. T. Chowdhury, S. T. Kelly, T. C. Hufnagel, K. Fezzaa and M. R. Zachariah, Reactive Sintering: An Important Component in the Combustion of Nanocomposite Thermites, *Combust. Flame*, 2012, **159**(1), 2-15.

9. W. Zhou, J. B. DeLisio, X. Wang and M. R. Zachariah, Reaction Mechanisms of Potassium Oxysalts Based Energetic Composites, *Combust. Flame*, 2017, **177**, 1-9.

10. M. Schoenitz, S. M. Umbrajkar and E. L. Dreizin, Kinetic Analysis of Thermite Reactions in Al-MoO_3 Nanocomposites, *J. Propul. Power*, 2007, **23**(4), 683-687.

11. T. Bazyn, N. Glumac, H. Krier, T. S. Ward, M. Schoenitz and E. L. Dreizin, Reflected Shock Ignition and Combustion of Aluminum and Nanocomposite Thermite Powders, *Combust. Sci. Technol.*, 2007, **179**(3), 457-476.

12. G. Jian, S. Chowdhury, K. Sullivan and M. R. Zachariah, Nanothermite Reactions: Is Gas Phase Oxygen Generation From the Oxygen Carrier an Essential Prerequisite to Ignition?, *Combust. Flame,* 2013, **160**(2), 432-437.

13. N. W. Piekiel, L. Zhou, K. T. Sullivan, S. Chowdhury, G. C. Egan and M. R. Zachariah, Initiation and Reaction in Al/B_2O_3 Nanothermites: Evidence for the Predominance of Condensed Phase Chemistry, *Combust. Sci. Technol.,* 2014, **186**(9), 1209-1224.

14. S. Boyapati, E. D. Wachsman and N. Jiang, Effect of Oxygen Sublattice Ordering on Interstitial Transport Mechanism and Conductivity Activation Energies in Phase-Stabilized Cubic Bismuth Oxides, *Solid State Ionics*, 2001, **140**(1), 149-160.

15. X. Wang, T. Wu and M. R. Zachariah, Doped Perovskites to Evaluate the Relationship Between Fuel-Oxidizer Thermite Ignition and Bond Energy, Electronegativity and Oxygen Vacancy, *J. Phys. Chem. C*, 2017, **121**, 147-152.

16. M. Barsoum, *Fundamentals of Ceramics,* McGraw-Hill Companies, Inc, USA, 1997.

17. F. S. Baumann, J. Fleig, H. U. Habermeier and J. Maier, $Ba_{0.5}Sr_{0.5}Co_{0.8}Fe_{0.2}O_{3-\delta}$ Thin Film Microelectrodes Investigated by Impedance Spectroscopy, *Solid State Ionics*, 2006, **177**(35), 3187-3191.

18. D. R. Lide, Standard Thermodynamic Properties of Chemical Substances, *CRC handbook of Chemistry and Physics*, 2007, **5**.

19. L. Malter and D. B. Langmuir, Resistance, Emissivities and Melting Point of Tantalum, *Phys. Rev.*, 1939, **55**(8), 743.

20. D. W. Jung, K. Duncan and E. D. Wachsman, Doubly Doped Bi_2O_3 Electrolytes with Higher Conductivity, *ECS Trans*, 2006, **1**(7), 63-71.

21. T. Takahashi, H. Iwahara and Y. Nagai, High Oxide Ion Conduction in Sintered Bi_2O_3 Containing SrO, CaO or La_2O_3, *J. Appl. Electrochem.*, 1972, **2**(2), 97-104.

22. E. D. Wachsman, S. Boyapati and N, Jiang, Effect of Dopant Polarizability on Oxygen Sublattice Order in Phase-Stabilized Cubic Bismuth Oxides, *Ionics*, 2001, **7**(1-2), 1-6.

23. T, Takahashi and H. Iwahara, High Oxide Ion Conduction in Sintered Oxides of the System Bi_2O_3-WO_3, *J. Appl. Electrochem.*, 1973, **3**(1), 65-72.

24. M. J. Verkerk and A. J. Burggraaf, High Oxygen Ion Conduction in Sintered Oxides of the Bi_2O_3- Dy_2O_3 System, *J. Appl. Electrochem.*, 1981, **128**(1), 75-82.

25. E. D. Wachsman and K. T. Lee, Lowering the Temperature of Solid Oxide Fuel Cells, *Science*, 2011, **334**(6058), 935-939.

26. D. W. Jung, K. L. Duncan and E. D. Wachsman, Effect of Total Dopant Concentration and Dopant Ratio on Conductivity of $(DyO_{1.5})_x$-$(WO_3)_y$-$(BiO_{1.5})_{1-x-y}$. *Acta Mater.*, 2010, **58**(2), 355-363.

27. M. Thompson, Synthesis and Characterisation of δ-Bi_2O_3 Related Materials Stabilised by Substitutions of Ca, Ga, Nb and Re, University of Birmingham, June, 2010.

28. T. Wu, A. SyBing, X. Wang X, M. R. Zachariah, Aerosol Synthesis of Phase Pure Iodine/Iodic Biocide Microparticles, *J. Mater. Res*, 2017, **32**(4), 890-896.

29. R. W. Cheary and A. A. Coelho, Fundamental Parameters Approach to X-Ray Line-Profile Fitting, *J. Appl. Crystallogr*., 1992, **25**, 109-121.

30. Y. He, F. Wu, X. Sun, R. Li, Y. Guo, C. Li, L. Zhang, F. Xing, W. Wang and J. Gao, Factors That Affect Pickering Emulsions Stabilized by Graphene Oxide, *ACS Appl. Mater. Interfaces*, 2013, **5**(11), 4843-4855.

31. L. Zhou, N. Piekiel, S. Chowdhury and M. R. Zachariah, T-Jump/Time-of-Flight Mass Spectrometry for Time-Resolved Analysis of Energetic Materials, *Rapid Commun. Mass Spectrom.,* 2009, **23**, 194–202.

32. C. Snehaunshu, K, Sullivan, N, Piekiel, L. Zhou and M. R. Zachariah, Diffusive vs Explosive Reaction at the Nanoscale, *J. Phys. Chem. C*, 2010, **114**(20), 9191-9195.

33 J. T. Irvine, D. C. Sinclair and A. R. West, Electroceramics: Characterization by Impedance Spectroscopy, *Adv. Mater.*, 1990, **2**(3), 132-138.

34. H. A. Harwig, On the Structure of Bismuthsesquioxide: The α, β, γ, and δ-Phase, *Zeitschrift für anorganische und allgemeine Chemie*, 1978, **444**(1), 151-166.

35. N. M. Sammes, G. A. Tompsett, H. Näfe and H, F. Aldinger, Bismuth Based Oxide Electrolytes-Structure and Ionic Conductivity, *J. Eur. Ceram. Soc.*, 1999, **19**(10), 1801-1826.

36. H. Zhao, N. Xu, Y. Cheng, W. Wei, N. Chen, W. Ding, X. Lu and F. Li, Investigation of Mixed Conductor $BaCo_{0.7}Fe_{0.3-x}Y_xO_{3-\delta}$ with High Oxygen Permeability, *J. Phys. Chem. C*, 2010, **114**(41), 17975-17981.

37. H. Rickert, *Electrochemistry of solids*, Springer Verlag, Berlin, 1982.

38. W. D. Kingery, H. K. Bowen and D. R. Uhlmann, *Introduction to ceramics,* John Willey & Sons, New York**,** 1976.

39. J. H. Flynn and L. A. Wall, General Treatment of the Thermogravimetry of Polymers, *J. Res. Natl. Bur. Stand.*, 1966, **70**(6), 487-523.

40. G. Jian, L. Zhou, N. W. Piekiel and M. R. Zachariah, Low Effective Activation Energies for Oxygen Release from Metal Oxides: Evidence for Mass-Transfer Limits at High Heating Rates, *ChemPhysChem*, 2014, **15**(8), 1666-1672.

41. H. Wang, G. Jian, W. Zhou, J. B. DeLisio, V. Lee and M. R. Zachariah, Metal Iodate-Based Energetic Composites and Their Combustion and Biocidal Performance, *ACS Appl. Mater Interfaces*, 2015, **7**(31), 17363-17370.

42. W. Zhou, J. B. DeLisio, X. Wang, G. C. Egan and M. R. Zachariah, Evaluating Free Vs Bound Oxygen On Ignition Of Nano-Aluminum Based Energetics Leads to A Critical Reaction Rate Criterion, *J. Appl. Phys,* 2015, **118**(11), 114303.

43. N. Cabrera, a. N. F. M., Theory of the Oxidation of Metals. *The Physical Society Reports on Progress in Physics* **1949,** *12*.

44. 69, N. S. R. D., NIST Chemistry WebBook. America, 2008.

45. A. Rai, K. P., L. Zhou and M. R. Zachariah, Understanding the Mechanism of Aluminum Nanoparticle Oxidation. *Combust. Theory Modell.* **2006,** *10* (5), 843-859.

46. Zhou, L.; Piekiel, N.; Chowdhury, S.; Zachariah, M. R., Time-Resolved Mass Spectrometry of the Exothermic Reaction between Nanoaluminum and Metal Oxides: The Role of Oxygen Release. *J Phys Chem C* **2010,** *114* (33), 14269-14275.

Chapter 5:

1. (a) Dreizin, E. L., Metal-based reactive nanomaterials. *Prog Energ Combust* **2009,** *35* (2), 141-167; (b) Zhou, W. B.; DeLisio, J. B.; Wang, X. Z.; Zachariah, M. R., Reaction mechanisms of potassium oxysalts based energetic composites. *Combust Flame* **2017,** *177*, 1-9; (c) Granier, J. J.; Pantoya, M. L., Laser ignition of nanocomposite thermites. *Combust Flame* **2004,** *138* (4), 373-383; (d) Zhou, W. B.; DeLisio, J. B.; Wang, X. Z.; Egan, G. C.; Zachariah, M. R., Evaluating free vs bound oxygen on ignition of nano-aluminum based energetics leads to a critical reaction rate criterion. *J Appl Phys* **2015,** *118* (11); (e) Wang, H. Y.; Jacob, R. J.; DeLisio, J. B.;

Zachariah, M. R., Assembly and encapsulation of aluminum NP's within AP/NC matrix and their reactive properties. *Combust Flame* **2017,** *180*, 175-183; (f) Eisenreich, N.; Fietzek, H.; Juez-Lorenzo, M. D.; Kolarik, V.; Koleczko, A.; Weiser, V., On the mechanism of low temperature oxidation for aluminum particles down to the nano-scale. *Propell Explos Pyrot* **2004,** *29* (3), 137-145.

2. (a) Van Devener, B.; Perez, J. P. L.; Jankovich, J.; Anderson, S. L., Oxide-Free, Catalyst-Coated, Fuel-Soluble, Air-Stable Boron Nanopowder as Combined Combustion Catalyst and High Energy Density Fuel. *Energ Fuel* **2009,** *23* (12), 6111-6120; (b) Sullivan, K.; Young, G.; Zachariah, M. R., Enhanced reactivity of nano-B/Al/CuO MIC's. *Combust Flame* **2009,** *156* (2), 302-309.

3. (a) Chintersingh, K. L.; Schoenitz, M.; Dreizin, E. L., Oxidation kinetics and combustion of boron particles with modified surface. *Combust Flame* **2016,** *173*, 288-295; (b) J. F. Xi, J. Z. L., H. P. Li, Y. Wang, Y. W. Zhang, J. H. Zhou, K. F. Cen, Progress in methods of promoting the ignition and combustion of boron particles. *Hanneng Cailiao/Chin. J. Energ. Mater* **2013,** *21*, 533-538.

4. (a) A, M., J. M. K. Semple, Combustion of boron particles at atmospheric pressure. *Combust. Sci. Technol* **1969,** *1*, 191-191; (b) Ulas, A.; Kuo, K. K.; Gotzmer, C., Ignition and combustion of boron particles in fluorine-containing environments. *Combust Flame* **2001,** *127* (1-2), 1935-1957; (c) Il'in, A. P.; Yablunovskii, G. V.; Gromov, A. A.; Popenko, E. M.; Bychin, N. V., Combustion of mixtures of ultrafine powders of aluminum and boron in air. *Combust Explo Shock+* **1999,** *35* (6), 656-659.

5. Dreizin, E. L.; Keil, D. G.; Felder, W.; Vicenzi, E. P., Phase changes in boron ignition and combustion. *Combust Flame* **1999,** *119* (3), 272-290.

6. Young, G.; Sullivan, K.; Zachariah, M. R.; Yu, K., Combustion characteristics of boron nanoparticles. *Combust Flame* **2009,** *156* (2), 322-333.

7. (a) Mohan, G.; Williams, F. A., Ignition and Combustion of Boron in O2-Inert Atmospheres. *Aiaa J* **1972,** *10* (6), 776-&; (b) Yeh, C. L.; Kuo, K. K., Ignition and combustion of boron particles. *Prog Energ Combust* **1996,** *22* (6), 511-541.

8. Wang, X. Z.; Wu, T.; Zachariah, M. R., Doped Perovskites To Evaluate the Relationship between Fuel-Oxidizer Thermite Ignition and Bond Energy, Electronegativity, and Oxygen Vacancy. *J Phys Chem C* **2017,** *121* (1), 147-152.

9. Wang, X. Z.; Zhou, W. B.; DeLisio, J. B.; Egan, G. C.; Zachariah, M. R., Doped delta-bismuth oxides to investigate oxygen ion transport as a metric for condensed phase thermite ignition. *Phys Chem Chem Phys* **2017,** *19* (20), 12749-12758.

10. (a) Harwig, H. A., On the Structure of Bismuthsesquioxide: The α, β, γ, and δ-Phase. *Z Anorg Allg Chem* **1978,** *444* (1), 151-166; (b) Jung, D. W.; Duncan, K. L.; Wachsman, E. D., Effect of total dopant concentration and dopant ratio on conductivity of $(DyO_{1.5})_x$-$(WO_3)_y$-$(BiO_{1.5})_{1-x-y}$. *Acta Mater* **2010,** *58* (2), 355-363.

11. Takahashi T, I. H., High oxide ion conduction in sintered oxides of the system Bi2O3-WO3. *Journal of Applied Electrochemistry* **1973,** *3* (1), 65-72.

12. (a) Wachsman, E. D.; Boyapati, S.; Jiang, N. X., Effect of Dopant Polarizability on Oxygen Sublattice Order in Phase-Stabilized Cubic Bismuth Oxides. *Ionics* **2001,** *7* (1-2), 1-6; (b) Verkerk, M. J.; Burggraaf, A. J., High Oxygen Ion

Conduction in Sintered Oxides of the Bi2o3-Dy2o3 System. *J Electrochem Soc* **1981,** *128* (1), 75-82.

13. (a) Wang, X. Z.; Jayathilake, R.; Taylor, D. D.; Rodriguez, E. E.; Zachariah, M. R., Study of C/Doped delta-Bi2O3 Redox Reactions by in Operando Synchrotron X-ray Diffraction: Bond Energy/Oxygen Vacancy and Reaction Kinetics Relationships. *J Phys Chem C* **2018,** *122* (16), 8796-8803; (b) Fung, K. Z.; Baek, H. D.; Virkar, A. V., Thermodynamic and Kinetic Considerations for Bi2o3-Based Electrolytes. *Solid State Ionics* **1992,** *52* (1-3), 199-211.

14. (a) Wu, T.; SyBing, A.; Wang, X. Z.; Zachariah, M. R., Aerosol synthesis of phase pure iodine/iodic biocide microparticles. *J Mater Res* **2017,** *32* (4), 890-896; (b) Jian, G. Q.; Liu, L.; Zachariah, M. R., Facile Aerosol Route to Hollow CuO Spheres and its Superior Performance as an Oxidizer in Nanoenergetic Gas Generators. *Adv Funct Mater* **2013,** *23* (10), 1341-1346.

15. Cheary, R. W.; Coelho, A., A Fundamental Parameters Approach to X-Ray Line-Profile Fitting. *J Appl Crystallogr* **1992,** *25*, 109-121.

16. DeLisio, J. B.; Wang, X. Z.; Wu, T.; Egan, G. C.; Jacob, R. J.; Zachariah, M. R., Investigating the oxidation mechanism of tantalum nanoparticles at high heating rates. *J Appl Phys* **2017,** *122* (24).

17. Zhou, L.; Piekiel, N.; Chowdhury, S.; Zachariah, M. R., T-Jump/time-of-flight mass spectrometry for time-resolved analysis of energetic materials. *Rapid Commun Mass Sp* **2009,** *23* (1), 194-202.

18. Chowdhury, S.; Sullivan, K.; Piekiel, N.; Zhou, L.; Zachariah, M. R., Diffusive vs Explosive Reaction at the Nanoscale. *J Phys Chem C* **2010,** *114* (20), 9191-9195.

19. (a) Sullivan, K.; Zachariah, M. R., Simultaneous Pressure and Optical Measurements of Nanoaluminum Thermites: Investigating the Reaction Mechanism. *J Propul Power* **2010,** *26* (3), 467-472; (b) Wang, H.; Jian, G.; Zhou, W.; DeLisio, J. B.; Lee, V. T.; Zachariah, M. R., Metal Iodate-Based Energetic Composites and Their Combustion and Biocidal Performance. *Acs Appl Mater Inter* **2015,** *7* (31), 17363-17370.

20. Ao, W.; Wang, Y.; Wu, S. X., Ignition kinetics of boron in primary combustion products of propellant based on its unique characteristics. *Acta Astronaut* **2017,** *136*, 450-458.

21. Sundaram, D.; Yang, V.; Yetter, R. A., Metal-based nanoenergetic materials: Synthesis, properties, and applications. *Prog Energ Combust* **2017,** *61*, 293-365.

22. Piekiel, N. W.; Zhou, L.; Sullivan, K. T.; Chowdhury, S.; Egan, G. C.; Zachariah, M. R., Initiation and Reaction in Al/Bi_2O_3 Nanothermite: Evidence for the Predominance of Condensed Phase Chemistry. *Combust Sci Technol* **2014,** *186* (9), 1209-1224.

23. Moulijn, J. A.; van Diepen, A. E.; Kapteijn, F., Catalyst deactivation: is it predictable? What to do? *Appl Catal a-Gen* **2001,** *212* (1-2), 3-16.

24. Wu, T.; Wang, X. Z.; Zavalij, P. Y.; DeLisio, J. B.; Wang, H. Y.; Zachariah, M. R., Performance of iodine oxides/iodic acids as oxidizers in thermite systems. *Combust Flame* **2018,** *191*, 335-342.

25. Haynes, W. M., *CRC handbook of Chemistry and Physics*. 2007; Vol. 5.

26. Jian, G. Q.; Feng, J. Y.; Jacob, R. J.; Egan, G. C.; Zachariah, M. R., Super-reactive Nanoenergetic Gas Generators Based on Periodate Salts. *Angew Chem Int Edit* **2013,** *52* (37), 9743-9746.

Chapter 6:

1. (a) Dreizin, E. L., Metal-based reactive nanomaterials. *Prog Energ Combust* **2009,** *35* (2), 141-167; (b) Zhou, W. B.; DeLisio, J. B.; Wang, X. Z.; Zachariah, M. R., Reaction mechanisms of potassium oxysalts based energetic composites. *Combust Flame* **2017,** *177*, 1-9; (c) Apperson, S.; Shende, R. V.; Subramanian, S.; Tappmeyer, D.; Gangopadhyay, S.; Chen, Z.; Gangopadhyay, K.; Redner, P.; Nicholich, S.; Kapoor, D., Generation of fast propagating combustion and shock waves with copper oxide/aluminum nanothermite composites. *Appl Phys Lett* **2007,** *91* (24).

2. (a) Jian, G. Q.; Chowdhury, S.; Sullivan, K.; Zachariah, M. R., Nanothermite reactions: Is gas phase oxygen generation from the oxygen carrier an essential prerequisite to ignition? *Combust Flame* **2013,** *160* (2), 432-437; (b) Dreizin, E. L., Experimental study of stages in aluminum particle combustion in air. *Combust Flame* **1996,** *105* (4), 541-556; (c) Sundaram, D.; Yang, V.; Yetter, R. A., Metal-based nanoenergetic materials: Synthesis, properties, and applications. *Prog Energ Combust* **2017,** *61*, 293-365.

3. (a) Wang, X. Z.; Wu, T.; Zachariah, M. R., Doped Perovskites To Evaluate the Relationship between Fuel-Oxidizer Thermite Ignition and Bond Energy,

Electronegativity, and Oxygen Vacancy. *J Phys Chem C* **2017,** *121* (1), 147-152; (b) Wang, X. Z.; Zhou, W. B.; DeLisio, J. B.; Egan, G. C.; Zachariah, M. R., Doped delta-bismuth oxides to investigate oxygen ion transport as a metric for condensed phase thermite ignition. *Phys Chem Chem Phys* **2017,** *19* (20), 12749-12758.

4. (a) Huang, Y. H.; Dass, R. I.; Xing, Z. L.; Goodenough, J. B., Double perovskites as anode materials for solid-oxide fuel cells. *Science* **2006,** *312* (5771), 254-257; (b) Kan, W. H.; Samson, A. J.; Thangadurai, V., Trends in electrode development for next generation solid oxide fuel cells. *J Mater Chem A* **2016,** *4* (46), 17913-17932.

5. (a) Zhu, J. J.; Li, H. L.; Zhong, L. Y.; Xiao, P.; Xu, X. L.; Yang, X. G.; Zhao, Z.; Li, J. L., Perovskite Oxides: Preparation, Characterizations, and Applications in Heterogeneous Catalysis. *Acs Catal* **2014,** *4* (9), 2917-2940; (b) Xiao, Y. H.; Zhu, W. L.; Cai, G. H.; Chen, M. L.; Zheng, Y.; Zhong, F. L.; Jiang, L. L., Effects of A-site non-stoichiometry in YxInO3+delta on the catalytic performance during methane combustion. *Phys Chem Chem Phys* **2017,** *19* (45), 30418-30428.

6. Wu, X. Y.; Chang, L.; Uddi, M.; Kirchen, P.; Ghoniem, A. F., Toward enhanced hydrogen generation from water using oxygen permeating LCF membranes. *Phys Chem Chem Phys* **2015,** *17* (15), 10093-10107.

7. (a) Sarshar, Z.; Kleitz, F.; Kaliaguine, S., Novel oxygen carriers for chemical looping combustion: La1-xCexBO3 (B = Co, Mn) perovskites synthesized by reactive grinding and nanocasting. *Energ Environ Sci* **2011,** *4* (10), 4258-4269; (b) Liu, L.; Taylor, D. D.; Rodriguez, E. E.; Zachariah, M. R., Influence of transition metal

electronegativity on the oxygen storage capacity of perovskite oxides. *Chem Commun* **2016,** *52* (68), 10369-10372.

8. Hull, S.; Norberg, S. T.; Tucker, M. G.; Eriksson, S. G.; Mohn, C. E.; Stolen, S., Neutron total scattering study of the delta and beta phases of Bi2O3. *Dalton T* **2009,** (40), 8737-8745.

9. T. Takahashi, H. I., and Y. Nagai, High oxide ion conduction in sintered Bi2O3 containing SrO, CaO or La2 O3. *J. Appl. Electrochem* **1972,** *2* (2), 97-104.

10. Wu, T.; Wang, X. Z.; DeLisio, J. B.; Holdren, S.; Zachariah, M. R., Carbon addition lowers initiation and iodine release temperatures from iodine oxide-based biocidal energetic materials. *Carbon* **2018,** *130*, 410-415.

11. (a) Wu, T.; SyBing, A.; Wang, X. Z.; Zachariah, M. R., Aerosol synthesis of phase pure iodine/iodic biocide microparticles. *J Mater Res* **2017,** *32* (4), 890-896; (b) Jian, G. Q.; Feng, J. Y.; Jacob, R. J.; Egan, G. C.; Zachariah, M. R., Super-reactive Nanoenergetic Gas Generators Based on Periodate Salts. *Angew Chem Int Edit* **2013,** *52* (37), 9743-9746.

12. Cheary, R. W.; Coelho, A., A Fundamental Parameters Approach to X-Ray Line-Profile Fitting. *J Appl Crystallogr* **1992,** *25*, 109-121.

13. (a) Zhou, L.; Piekiel, N.; Chowdhury, S.; Zachariah, M. R., T-Jump/time-of-flight mass spectrometry for time-resolved analysis of energetic materials. *Rapid Commun Mass Sp* **2009,** *23* (1), 194-202; (b) Jian, G.; Piekiel, N. W.; Zachariah, M. R., Time-Resolved Mass Spectrometry of Nano-Al and Nano-Al/CuO Thermite under Rapid Heating: A Mechanistic Study. *J Phys Chem C* **2012,** *116* (51), 26881-26887.

14. Chowdhury, S.; Sullivan, K.; Piekiel, N.; Zhou, L.; Zachariah, M. R., Diffusive vs Explosive Reaction at the Nanoscale. *J Phys Chem C* **2010,** *114* (20), 9191-9195.

15. Liu, L.; Zachariah, M. R.; Stoliarov, S. I.; Li, J., Enhanced thermal decomposition kinetics of poly(lactic acid) sacrificial polymer catalyzed by metal oxide nanoparticles. *Rsc Adv* **2015,** *5* (123), 101745-101750.

16. (a) Li, S. G.; Jin, W. Q.; Huang, P.; Xu, N. P.; Shi, J.; Lin, Y. S.; Hu, M. Z. C.; Payzant, E. A., Comparison of oxygen permeability and stability of perovskite type $La_{0.2}A_{0.8}Co_{0.2}Fe_{0.8}O_{3-\delta}$ (A = Sr, Ba, Ca) membranes. *Ind Eng Chem Res* **1999,** *38* (8), 2963-2972; (b) Haynes, W. M., *CRC handbook of Chemistry and Physics*. 2007; Vol. 5.

17. Harwig, H. A., On the Structure of Bismuthsesquioxide: The α, β, γ, and δ-Phase. *Z Anorg Allg Chem* **1978,** *444* (1), 151-166.

18. DeLisio, J. B.; Wang, X. Z.; Wu, T.; Egan, G. C.; Jacob, R. J.; Zachariah, M. R., Investigating the oxidation mechanism of tantalum nanoparticles at high heating rates. *J Appl Phys* **2017,** *122* (24).

19. Dawber, M.; Scott, J. F., A model for fatigue in ferroelectric perovskite thin films (vol 76, pg 1060, 2000). *Appl Phys Lett* **2000,** *76* (24), 3655-3655.

20. (a) Mogensen, M.; Lybye, D.; Bonanos, N.; Hendriksen, P. V.; Poulsen, F. W., Factors controlling the oxide ion conductivity of fluorite and perovskite structured oxides. *Solid State Ionics* **2004,** *174* (1-4), 279-286; (b) Lybye, D.; Poulsen, F. W.; Mogensen, M., Conductivity of A- and B-site doped $LaAlO_3$,

LaGaO3, LaScO3 and LaInO3 perovskites. *Solid State Ionics* **2000,** *128* (1-4), 91-103.

21. Pauling, L., The Nature of the Chemical Bond. IV. The Energy of Single Bonds and the Relative Electronegativity of Atoms. *J. Am. Chem. Soc.* **1932,** *54*, 3570-3582.

Chapter 7:

1. Coombe, H. S.; Nieh, S. Polymer Membrane Air Separation Performance for Portable Oxygen Enriched Combustion Applications. *Energy Convers. Manage*. **2007**, *48*, 1499-1505.

2. Baukal, C. E. Jr.; Gershtein, V. Y.; Heffron, J. F.; Best, R. C.; Eleazer, P. B. Method and Apparatus for Reducing NO_x Production During Air-Oxygen-Fuel Combustion. U.S. Patent, 5,871,343. **1999**.

3. Liang, M. S.; Kang, W. K.; Xie, K. C. Comparison of Reduction Behavior of Fe_2O_3, ZnO and $ZnFe_2O_4$ by TPR Technique. *J. Nat. Gas Chem.* **2009**, *18*, 110−113.

4. Richter, H. J.; Knoche, K. F. Reversibility of Combustion Processes. *ACS Symp. Ser.* **1983**, *235*, 71–85.

5. Adánez, J.; de Diego, L. F.; García-Labiano, F.; Gayan, P; Abad, A. Selection of Oxygen Carriers for Chemical-Looping Combustion. *Energy Fuels* **2004**, *18,* 371-377.

6. Liu, L.; Wu, Y.; Hu, J.; Liu, D.; Zachariah, M. R. Zeolite-Supported Iron Oxides as Durable and Selective Oxygen Carriers for Chemical Looping Combustio. *Energy Fuels* **2017**, **31, 11225-11233.**

7. Luo, S.; Zeng, L.; Fan, L. S. Chemical Looping Technology: Oxygen Carrier Characteristics. *Annu. Rev. Chem. Biomol. Eng.* **2015**, *6*, 53−75.

8. Hossain, M. M.; de Lasa, H. I. Chemical-Looping Combustion (CLC) for Inherent CO_2 Separations—A Review. *Chem. Eng. Sci.* **2008**, *63*, 4433-4451.

9. Nandy, A.; Loha, C.; Gu, S.; Sarkar, P.; Karmakar, M. Present Status and Overview of Chemical Looping Combustion Technology. *Renewable Sustainable Energy Rev.* **2016**, *59*, 597-619.

10. Siriwardane, R.; Tian, H.; Richards, G.; Simonyi, T.; Poston, J. Chemical-Looping Combustion of Coal with Metal Oxide Oxygen Carriers. *Energy Fuels* **2009**, *23*, 3885-3892.

11. Piekiel, N. W.; Egan, G. C.; Sullivan, K. T.; Zachariah, M. R. Evidence for the Predominance of Condensed Phase Reaction in Chemical Looping Reactions Between Carbon and Oxygen Carriers. *J. Phys. Chem. C* **2012**, *116*, 24496-24502.

12. Wang, X.; Wu, T.; Zachariah, M. R. Doped Perovskites to Evaluate the Relationship Between Fuel-Oxidizer Thermite Ignition and Bond Energy, Electronegativity and Oxygen Vacancy. *J. Phys. Chem. C* **2017**, *121*, 147-152.

13. Liu, L.; Taylor, D. D.; Rodriguez, E. E.; Zachariah, M. R. Influence of Transition Metal Electronegativity on the Oxygen Storage Capacity of Perovskite Oxides. *Chem. Commun.* **2016**, *52*, 10369-10372.

14. Wang, X.; Zhou, W.; DeLisio, J.; Egan, G.; Zachariah, M. R. Doped δ-Bismuth Oxides to Investigate Oxygen Ion Transport as a Metric for Condensed Phase Thermite Ignition. *Phys. Chem. Chem. Phys.* **2017**, *19*, 12749-12758.

15. Harwig, H. A. On the Structure of Bismuthsesquioxide: The α, β, γ, and δ-Phase. *Z. Anorg. Allg. Chem*. **1978,** *444*, 151-166.

16. Jacobson, A. J. Materials for Solid Oxide Fuel Cells. *Chem. Mater.* **2009**, 22, 660-674.

17. Jung, D. W.; Duncan, K.; Wachsman, E. D. Doubly Doped Bi_2O_3 Electrolytes With Higher Conductivity. *ECS Trans.* **2006**, *1*, 63-71.

18. Takahashi, T.; Iwahara, H. High Oxide Ion Conduction in Sintered Oxides of the System Bi_2O_3-WO_3. *J. Appl. Electrochem*. **1973**, *3*, 65-72.

19. Wachsman, E. D.; Lee, K. T. Lowering the Temperature of Solid Oxide Fuel Cells. *Science* **2011**, *334*, 935-939.

20. Wu, T.; SyBing, A.; Wang, X.; Zachariah, M. R. Aerosol Synthesis of Phase Pure Iodine/Iodic Biocide Microparticles. *J. Mater. Res.* **2017**, *32*, 890-896.

21. Jian, G.; Liu, L; Zachariah, M. R. Facile Aerosol Route to Hollow CuO Spheres and Its Superior Performance as An Oxidizer in Nanoenergetic Gas Generators. *Adv. Funct. Mater.* **2013**, *23,* 1341-1346.

22. Yang, Y.; Romano, M.; Feng, G.; Wang, X.; Wu, T.; Holdren, S.; Zachariah, M. R. Growth of sub-5 nm Metal Nanoclusters in Polymer Melt Aerosol Droplets. *Langmuir* **2018**, *34*, 585-594.

23. Cheary, R. W.; Coelho, A. A. Fundamental Parameters Approach to X-Ray Line-Profile Fitting. *J. Appl. Crystallogr*. **1992**, *25*, 109-121.

24. Toby, B. H.; Von Dreele, R. B. GSAS-II: The Genesis of a Modern Open-Source All Purpose Crystallography Software Package. *J. Appl. Crystallogr*. **2013**,*46*, 544−549.

25. Chupas, P. J.; Chapman, K. W.; Kurtz, C.; Hanson, J. C.; Lee, P. L.; Grey, C. P. A Versatile Sample-Environment Cell for Non-Ambient X-Ray Scattering Experiments. *J. Appl. Crystallogr.* **2008**, *41*, 822−824

26. Lide, D. R. Standard Thermodynamic Properties of Chemical Substances, *CRC handbook of Chemistry and Physics* **2007**, *5*.

27. Hull, S.; Norber, S. T.; Tucker, M. G.; Eriksoon, S. G.; Mohn, C. E.; Stolen, S. Neutron Total Scattering Study of the δ and β Phases of Bi_2O_3. *Dalton Trans*. **2009**, *40*, 8737-8745.

28. Flynn, J. H.; Wall, L. A. General Treatment of the Thermogravimetry of Polymers. *J. Res. Natl. Bur. Stand.* **1966**, *70,* 487-523.

29. Jian, G.; Zhou, L; Piekiel, N. W. Zachariah, M. R. Low Effective Activation Energies for Oxygen Release from Metal Oxides: Evidence for Mass-Transfer Limits at High Heating Rates. *ChemPhysChem*. **2014**, *15,* 1666-1672.

30. Vyazovkin, S.; Burnham, A. K.; Criado, J. M.; Perez-Maqueda, L. A.; Popescu, C.; Sbirrazzuoli, N. ICTAC Kinetics Committee Recommendations for Performing Kinetic Computations on Thermal Analysis Data. *Thermochim. Acta* **2011**, *52,* 1-19.

31. Zhou, W.; DeLisio, J. B.; Wang, X.; Egan, G. C.; Zachariah, M. R. Evaluating Free vs Bound Oxygen on Ignition of Nano-Aluminum Based Energetics Leads to a Critical Reaction Rate Criterion. *J. Appl. Phys.* **2015**, *118,* 114303.

32. Sammes, N. M.; Tompsett, G. A.; Näfe, H.; Aldinera, F. Bismuth Based Oxide Electrolytes-Structure and Ionic Conductivity. *J. Eur. Ceram. Soc.* **1999**, *19*, 1801-1826.

33. Watanabe, A. Polymorphism in $Bi_{14}WO_{24}$: A Monoclinic Low-Temperature Stable Form with β≈90° and Its Displacive Transformation to an Orthorhombic Intermediate Form at About 40° C. *Solid State Ionics* **2005**, *176*, 1281-1289.

34 Resel, R.; Tamas, E.; Sonderegger, B.; Hofbauer, P.; Keckes, J. A Heating Stage Up to 1173 K for X-Ray Diffraction Studies in the Whole Orientation Space. *J. Appl. Crystallogr.* **2003**, *36*, 80-r85.

Chapter 8:

1. (a) Feng, J. Y.; Jian, G. Q.; Liu, Q.; Zachariah, M. R., Passivated Iodine Pentoxide Oxidizer for Potential Biocidal Nanoenergetic Applications. *Acs Appl Mater Inter* **2013,** *5* (18), 8875-8880; (b) Sullivan, K. T.; Piekiel, N. W.; Chowdhury, S.; Wu, C.; Zachariah, M. R.; Johnson, C. E., Ignition and Combustion Characteristics of Nanoscale Al/AgIO3: A Potential Energetic Biocidal System. *Combust Sci Technol* **2011,** *183* (3), 285-302.

2. Setlow, P., Spores of Bacillus subtilis: their resistance to and killing by radiation, heat and chemicals. *J Appl Microbiol* **2006,** *101* (3), 514-525.

3. (a) Zhang, S. S.; Schoenitz, M.; Dreizin, E. L., Iodine Release, Oxidation, and Ignition of Mechanically Alloyed Al-I Composites. *J Phys Chem C* **2010,** *114* (46), 19653-19659; (b) Grinshpun, S. A.; Adhikari, A.; Yermakov, M.; Reponen, T.;

Dreizin, E.; Schoenitz, M.; Hoffmann, V.; Zhang, S. S., Inactivation of Aerosolized Bacillus atrophaeus (BG) Endospores and MS2 Viruses by Combustion of Reactive Materials. *Environ Sci Technol* **2012,** *46* (13), 7334-7341.

4. (a) Xu, X.; Hu, C. L.; Yang, B. P.; Mao, J. G., Syntheses, crystal structures and magnetic properties of three new silver manganese(II) or manganese(III) mixed metal iodates. *Crystengcomm* **2013,** *15* (38), 7776-7782; (b) Huang, C.; Hu, C. L.; Xu, X.; Yang, B. P.; Mao, J. G., Explorations of a Series of Second Order Nonlinear Optical Materials Based on Monovalent Metal Gold(III) Iodates. *Inorg Chem* **2013,** *52* (19), 11551-11562.

5. Phanon, D.; Bentria, B.; Jeanneau, E.; Benbertal, D.; Mosset, A.; Gautier-Luneau, I., Crystal structure of M(IO3)(2) metal iodates, twinned by pseudo-merohedry, with M-II: Mg-II, Mn-II, Co-II, Ni-II and Zn-II. *Z Kristallogr* **2006,** *221* (9), 635-642.

6. (a) Wang, H. Y.; DeLisio, J. B.; Jian, G. Q.; Zhou, W. B.; Zachariah, M. R., Electrospray formation and combustion characteristics of iodine-containing Al/CuO nanothermite microparticles. *Combust Flame* **2015,** *162* (7), 2823-2829; (b) Hu, X. L.; DeLisio, J. B.; Li, X. Y.; Zhou, W. B.; Zachariah, M. R., Direct Deposit of Highly Reactive Bi(IO3)(3)- Polyvinylidene Fluoride Biocidal Energetic Composite and its Reactive Properties. *Adv Eng Mater* **2017,** *19* (1).

7. Rayleigh, L., *Philisophical Magazine* 1882.

8. Taylor, G., Disintegration of water drops in an electric field. *Phys. Sci.* **1964,** *280*, 383-397.

9. Jaworek, A.; Sobczyk, A. T., Electrospraying route to nanotechnology: An overview. *J Electrostat* **2008,** *66* (3-4), 197-219.

10. Phanon, D.; Bentria, B.; Benbertal, D.; Mosset, A.; Gautier-Luneau, I., New potential materials for infrared nonlinear optics. Preparation, characterisation and optical transparency of monometallic and bimetallic iodates. *Solid State Sci* **2006,** *8* (12), 1466-1472.

11. Cushing, B. L.; Kolesnichenko, V. L.; O'Connor, C. J., Recent advances in the liquid-phase syntheses of inorganic nanoparticles. *Chem Rev* **2004,** *104* (9), 3893-3946.

12. Bentria, B.; Benbertal, D.; Bagieu-Beucher, M.; Masse, R.; Mosset, A., Crystal structure of anhydrous bismuth iodate, Bi(IO3)(3). *J Chem Crystallogr* **2003,** *33* (11), 867-873.

13. Wang, H. Y.; Jian, G. Q.; Yan, S.; DeLisio, J. B.; Huang, C.; Zachariah, M. R., Electrospray Formation of Gelled Nano-Aluminum Microspheres with Superior Reactivity. *Acs Appl Mater Inter* **2013,** *5* (15), 6797-6801.

14. Lazarini, F., Thermal Dehydration of Some Basic Bismuth Nitrates. *Thermochim Acta* **1981,** *46* (1), 53-55.

15. Li, M.; Guha, S.; Zangmeister, R.; Tarlov, M. J.; Zachariah, M. R., Method for Determining the Absolute Number Concentration of Nanoparticles from Electrospray Sources. *Langmuir* **2011,** *27* (24), 14732-14739.

16. (a) Hartman, R. P. A.; Brunner, D. J.; Camelot, D. M. A.; Marijnissen, J. C. M.; Scarlett, B., Jet break-up in electrohydrodynamic atomization in the cone-jet mode. *J Aerosol Sci* **2000,** *31* (1), 65-95; (b) Ganan-Calvo, A. M.; Davila, J.; Barrero,

A., Current and droplet size in the electrospraying of liquids. Scaling laws. *J Aerosol Sci* **1997,** *28* (2), 249-275.

17. Schur, M.; Bems, B.; Dassenoy, A.; Kassatkine, I.; Urban, J.; Wilmes, H.; Hinrichsen, O.; Muhler, M.; Schlogl, R., Continuous coprecipitation of catalysts in a micromixer: Nanostructured Cu/ZnO composite for the synthesis of methanol. *Angew Chem Int Edit* **2003,** *42* (32), 3815-3817.

18. (a) Arabgari, S.; Malekfar, R.; Motamedi, K., Parameters effects on the surface morphology and structure of Nd:YAG nanopowders synthesized by co-precipitation method. *J Nanopart Res* **2011,** *13* (2), 597-611; (b) Yin, Y.; Alivisatos, A. P., Colloidal nanocrystal synthesis and the organic-inorganic interface. *Nature* **2005,** *437* (7059), 664-670.

19. Tao, K.; Dou, H. J.; Sun, K., Interfacial coprecipitation to prepare magnetite nanoparticles: Concentration and temperature dependence. *Colloid Surface A* **2008,** *320* (1-3), 115-122.

Chapter 9:

1. Yan, S.; Jian, G. Q.; Zachariah, M. R., Electrospun Nanofiber-Based Thermite Textiles and their Reactive Properties. *Acs Appl Mater Inter* **2012,** *4* (12), 6432-6435.

2. Bragg, W. H., The Structure of Magnetite and the Spinels. *Nature* **1915,** *95*.

3. Heinz, K.; Hammer, L., Epitaxial cobalt oxide films on Ir(100)-the importance of crystallographic analyses. *J Phys-Condens Mat* **2013,** *25* (17).

4. (a) Kang, D.; Kim, T. W.; Kubota, S. R.; Cardiel, A. C.; Cha, H. G.; Choi, K. S., Electrochemical Synthesis of Photoelectrodes and Catalysts for Use in Solar Water Splitting. *Chem Rev* **2015,** *115* (23), 12839-12887; (b) Evdou, A.; Zaspalis, V.; Nalbandian, L., Ferrites as redox catalysts for chemical looping processes. *Fuel* **2016,** *165*, 367-378.